INVESTIGATIONS OF THE FLOW DYNAMICS OF SUPERSONIC MOLECULAR BEAMS AND THE IONIZATION OF MOLECULAR CLUSTERS BY ELECTRON IMPACT

A THESIS PRESENTED FOR THE DEGREE OF
DOCTOR OF PHILOSOPHY
IN CHEMISTRY,
AT THE
UNIVERSITY OF CANTERBURY,
CHRISTCHURCH,
NEW ZEALAND.

by
Brett Russell Cameron
November 1993

To Laura

It is a profound and necessary truth that the deep things in science are not found because they are useful; they are found because it was possible to find them. Robert Oppenheimer

Abstract

A pulsed supersonic molecular beam apparatus has been constructed for the investigation of atomic and molecular van der Waals clusters. The apparatus was characterized by investigating supersonic beam intensities as a function of reservoir pressure and nozzle to skimmer separation, and by measuring supersonic beam speed distributions for various monatomic and diatomic gases and binary monatomic gas mixtures using time–of–flight methods. A new technique for deconvolving badly convoluted time–of–flight data was developed and successfully applied to the deconvolution of time–of–flight waveforms measured for unchopped pulsed supersonic beams of argon, krypton, $CHCl_3$ and CH_3Cl. Size distributions of van der Waals cluster species were investigated for supersonic expansions of pure argon and for seeded helium expansions containing SO_2, N_2O and H_2O, NO and NO_2 and NH_3. Appearance potentials of the cluster ions $(CO_2)_n^+$, $(N_2O)_n^+$ $(2 \leq n \leq 4)$ and $(NH_3)_nH^+$ $(1 \leq n \leq 8)$, and the cluster ion fragments $(N_2O{\cdot}O)^+$ and $(N_2O{\cdot}NO)^+$ have been determined by electron impact ionization of neutral clusters formed in the supersonic beam. The measured appearance potential data were used to estimate cluster ion binding energies, and possible mechanisms for the formation of the cluster fragment ions $(N_2O{\cdot}O)^+$ and $(N_2O{\cdot}NO)^+$ are discussed.

Computational procedures have been developed for the calculation of supersonic beam properties as a function of distance along the expansion axis. Collision frequency, flow velocity, particle density, mean free path, and axial and radial temperatures in supersonic atomic and homonuclear diatomic beams have been calculated for various species using realistic interaction potentials and collision cross sections obtained from scattering theory. A simple approach to the estimation of rotational relaxation times and collision numbers in supersonic expansions was developed and used to calculate rotational relaxation times and rotational collision numbers for H_2, N_2, O_2 and Cl_2. A sophisticated direct simulation Monte Carlo procedure was devised for the investigation of rotational relaxation in small molecules. The devised relaxation model has been used to calculate rotational relaxation data for the homonuclear diatomic molecules H_2, N_2, O_2 and Cl_2, and for the polyatomic species CO_2, OCS, NH_3, CH_4, CH_3Cl and C_2H_4. Results obtained using the Monte Carlo procedure were used to investigate the breakdown of translational and rotational equilibrium in supersonic expansions of CO_2, OCS and CH_3Cl.

Acknowledgements

While many people have, in various ways, assisted me with my Ph.D. research and with the preparation of this thesis, there are some whom I feel deserve a special mention.

I am grateful to my supervisor, Dr. Peter Harland, for his continual guidance, friendship and encouragement, and to my associate supervisor Prof. Leon Phillips for his many useful comments and excellent barbecues.

The Chemistry Department technicians were also most helpful with the construction and development of the molecular beam apparatus. In particular I would like to thank Barrie Wood of the mechanical workshop for his tolerance in the face of my frequent ignorance concerning engineering matters and for the high quality of his workmanship. A similar mention should be made regarding Derek Williams of the electronics workshop.

All of my colleagues deserve special thanks for their friendship and humour over the years that I have known them. In particular I would like to thank Roger Meads for the many and varied discussions and entertaining moments that I have had with him.

Financial support from the Chemistry Department, University of Canterbury and the Computer Services Centre are gratefully acknowledged.

Finally I would like to thank my brother Allan for putting up with me and Dr. Mike Hayes for his friendship and his assistance.

Contents

List of figures

List of tables

Preface

This thesis presents a number of new results concerning investigations of the flow dynamics of supersonic atomic and molecular beams and the detection of atomic and molecular van der Waals clusters by electron impact ionization. The purpose of this preface is to describe how these studies came about and to provide the reader with a short chapter by chapter outline of the thesis.

The initial objective of the research programme was to design and construct a supersonic molecular beam apparatus for the investigation of small atomic and molecular van der Waals clusters by electron impact ionization. The research project was divided into three distinct sections. The first goal of the project was to design and construct the supersonic beam apparatus. The second stage of the research programme was to characterize the supersonic beam and the ion detection system in order to determine the capabilities and limitations of the apparatus, and to verify that the system was operating correctly. The final stage of the project was to investigate the appearance potentials, binding energies, and fragmentation mechanisms of small positive cluster ions produced by electron impact ionization of neutral clusters formed in the supersonic beam. The second stage of the project, however, grew well beyond its initial expectations, and lead to the development of computational procedures for the calculation of supersonic beam properties and the investigation of rotational relaxation phenomena in small molecules. This theoretical work was partially stimulated by the acquisition of extremely good time–of–flight data against which theoretical results could be compared, and partially by the notable lack of literature concerned with the theoretical investigation of collisional properties of supersonic atomic and molecular beams and rotational relaxation processes in supersonic molecular beams.

The design and construction of the supersonic molecular beam apparatus began in January of 1988 and took close to two years to complete. During this time, the actual appearance of the apparatus changed almost continuously as funding was obtained for new vacuum chambers, pumping equipment, and electronics units. Towards the end of 1990, the configuration of the apparatus finally became sufficiently stable to allow the experimental measurements described in Chapter 3 to be performed.[1] I was fortunate in that most of the experiments described in this thesis were able to be performed without any major problems. Signals were invariably large and there was no discernible interference from any periodic noise sources. Random noise was easily handled using signal averaging techniques. The problem of inadequate pumping speed on the expansion chamber meant that it was not initially possible to employ high reservoir pressures, making it difficult to generate significant populations of van der Waals cluster species. This problem was rectified by the timely arrival of a research grant, which facilitated the purchase of a second diffusion pump for the expansion chamber. The measurement of supersonic beam speed distributions described in Section 3.3 was also not without some initial difficulties.

[1] With the exception of the preface, the symbol §is used to denote *Chapter* or *Section* throughout this thesis.

The beam chopper assembly was initially installed with standard bearings and no water cooling facility. The bearings quickly overheated, resulting in excessive bearing noise and serious vibration problems. After several sets of standard bearings had been worn out and replaced, high quality vacuum rated bearings were finally obtained and a water cooled copper jacket was fitted to the chopper motor. Once all mechanical problems had been successfully eliminated, the experimental measurements were performed, and the theoretical side of the research was attacked with some vigour.

The development of the thermal conduction model [Cameron and Harland, 1991] to describe the breakdown of translational and rotational equilibrium in supersonic expansions (Section 4.2) and the application of Monte Carlo methods to the investigation of rotational relaxation in small molecules (Section 4.4) [Cameron and Harland, 1993a] proved to be highly successful and greatly stimulated my interest in the mathematical modelling of complex gas flow phenomena. It was gratifying when the devised theoretical models and experimental measurements combined to yield results that were in excellent agreement with values determined by other workers using different techniques, or when theoretical calculations yielded data not previously reported in the literature. It is hoped that the theoretical work presented in this thesis can be further developed and refined in the near future.

The preceding narrative provides some insight into the principle aims of the research described in this thesis and how this work came about. It is now appropriate to give a chapter by chapter outline of the thesis.

The thesis is written in 5 chapters. Chapter 1 provides an introduction to the basic principles of atomic and molecular beam production, while Chapter 2 briefly describes the main constructional features of the supersonic molecular beam apparatus which was designed and built for the investigation of atomic and molecular cluster species.

The results of all significant experimental work are presented and discussed in Chapter 3. The first few sections of the chapter describe a series of experiments concerned with the characterization of the newly constructed supersonic molecular beam apparatus. In Section 3.2 the intensities of supersonic beams of pure argon are investigated as a function of reservoir pressure and nozzle to skimmer separation in order to determine a set of optimum operating conditions for the apparatus. In Section 3.3 supersonic beam speed distributions are measured for a range of monatomic and homonuclear diatomic species using time–of–flight methods. The measured speed distributions are characterized and compared with the results of other workers in order to verify that the supersonic molecular beam apparatus is functioning correctly. The effects of velocity slip and temperature slip in supersonic expansions of binary gas mixtures are briefly examined in Section 3.5 for supersonic beams of helium seeded with various amounts of neon, argon, or krypton.

Time–of–flight measurements are often greatly complicated by the convolution of the true distribution of particle flight times with the electronic response function of the beam detection system and the gate function associated with the beam modulation device. The effect of these convolutions is to broaden the time–of–flight signal and increase the most probable arrival time. A new and reliable method for deconvolving badly convoluted molecular beam time–of–flight waveforms using Fourier transform and Wiener filtering techniques is presented in Section 3.4 [Cameron and Harland, 1993b]. The mathematical details of the method are discussed and examples of its application to the deconvolution of time–of–flight waveforms measured for unchopped pulsed supersonic beams of argon, krypton, $CHCl_3$ and CH_3Cl are presented.

Having characterized the apparatus and verified that it was operating correctly, attention was shifted to the investigation of weakly bound van der Waals cluster species which

may be formed during the supersonic expansion process. In Section 3.6 cluster size distributions are measured for supersonic expansions of pure argon and for seeded helium expansions containing SO_2, N_2O and H_2O, NO and NO_2 and NH_3. In Section 3.7 appearance potentials of the cluster ions $(CO_2)_n^+$, $(N_2O)_n^+$ $(2 \leq n \leq 4)$ and $(NH_3)_nH^+$ $(1 \leq n \leq 8)$, and the cluster ion fragments $(N_2O{\cdot}O)^+$ and $(N_2O{\cdot}NO)^+$ are determined by electron impact ionization of neutral clusters formed in the molecular beam [Cameron *et al*, 1993]. Results obtained for $(CO_2)_n^+$, $(N_2O)_2^+$ $(2 \leq n \leq 4)$, $(N_2O{\cdot}NO)^+$ and $(NH_3)_nH^+$ $(1 \leq n \leq 3)$ are in general agreement with previously reported appearance potentials for these species while the appearance potentials of $(N_2O{\cdot}O)^+$ and $(NH_3)_nH^+$ $(4 \leq n \leq 8)$ are measured for the first time. The measured appearance potential data were used to determine cluster ion binding energies, and possible mechanisms for the formation of the cluster fragment ions $(N_2O{\cdot}O)^+$ and $(N_2O{\cdot}NO)^+$ are discussed.

The results of all theoretical work are presented and discussed in Chapter 4. In Section 4.2 the thermal conduction model [Cameron and Harland, 1991] is used to describe the supersonic expansion process. Collision frequency, flow velocity, particle density, mean free path, and axial and radial temperatures in supersonic atomic and homonuclear diatomic beams are calculated for various species within the framework of the thermal conduction model using realistic interaction potentials and collision cross sections obtained from scattering theory. The thermal conduction model is extended to include a variable flow velocity, and rotational degrees of freedom are incorporated by the introduction of a rotational–translational coupling parameter. Comparisons between numerical results and measured beam speed distributions are made to estimate values of the rotational–translational coupling parameter for H_2, N_2 and O_2.

A simple approach to the estimation of rotational relaxation times and collision numbers in supersonic expansions based on the use of the thermal conduction model is presented in Section 4.3 [Cameron and Harland, 1993d]. Expressions are derived for the calculation of these quantities, and relaxation times are calculated as a function of mean kinetic temperature and axial distance from the nozzle exit for the homonuclear diatomic species H_2, N_2, O_2 and Cl_2.

The application of a direct simulation Monte Carlo procedure to the investigation of rotational relaxation in homogeneous gases is presented in Section 4.4 [Cameron and Harland, 1993a]. The devised relaxation model assumes that the efficiency of rotational–translational energy transfer may be directly related to the fraction of inelastic collisions experienced by the colliding molecules in terms of an energy dependent rotational–translational coupling parameter. The energy dependence of the coupling parameter is investigated for the homonuclear diatomic molecules H_2, N_2, O_2 and Cl_2, and for the polyatomic species CO_2, OCS, NH_3, CH_4, CH_3Cl and C_2H_4. Rotational collision numbers are calculated for these molecules and the energy dependent coupling parameter is used in thermal conduction model calculations to investigate the breakdown of translational and rotational equilibrium in supersonic expansions of CO_2, OCS and CH_3Cl.

Chapter 5 is the final chapter of this thesis. This chapter gives a summary of the results presented in Chapters 3 and 4 and provides a number of suggestions for possible future research.

Publications

Publications and presentations that were prepared during the course of this research, or are currently under preparation, are listed below:

Cameron, B.R. (1990), August. Monte Carlo methods: What, where, why, how and when. Departmental seminar, Chemistry Department, University of Canterbury.

Cameron, B.R. and Harland, P.W. (1991), 'Flow dynamics of supersonic molecular beams and the measurement of rotational-translational coupling parameters for N_2 and H_2', *J. Chem. Soc. Faraday Trans.*, Vol. 87, No. 8, April, p. 1069.

Cameron, B.R. and Harland, P.W. (1993a), 'Deconvolution of unchopped time–of–flight waveforms', *Rev. Sci. Instrum.* In press.

Cameron, B.R. and Harland, P.W. (1993c), 'Application of the thermal conduction model to rotational relaxation in molecular beams', *J. Chem. Soc. Faraday Trans.*, Vol. 89, No. 12, June, p. 1903.

Cameron, B.R. and Harland, P.W. (1993d), 'Monte carlo calculation of rotational relaxation in small molecules', *J. Chem. Soc. Faraday Trans.* In press.

Cameron, B.R., Aitkin, C.G. and Harland, P.W. (1993), 'Appearance potentials of small cluster ions and their fragments', *J. Chem. Soc. Faraday Trans.* Submitted for publication.

Glossary of terms

AC	alternating current
ATD	arrival time distribution
DC	direct current
DAC	digital–to–analogue converter
DSA	digital storage adaptor
DSMC	direct simulation Monte Carlo
DVM	digital volt meter
FFT	fast Fourier transform
FT	Fourier transform
FWHM	full width at half maximum height
RF	radio–frequency
SNR	signal–to–noise ratio
STP	standard temperature and pressure
TOF	time–of–flight
TTL	transistor–transistor logic

List of symbols

Most of the symbols that are employed throughout this thesis are defined in that part of the text at which they are first invoked. Nevertheless, they are repeated here for ease of reference. Note that some symbols, including subscripts and superscripts, that have application only to a single situation have been omitted from the following list. This applies also to local changes in the meaning of some listed symbols.

§	chapter or section
A	locally specified constant or parameter
$\mathcal{A}$	rotational constant
b	impact parameter
$\mathcal{B}$	rotational constant
χ	angle of deflection
C_p	heat capacity at constant pressure
C_v	heat capacity at constant volume
c_r	relative speed
d_0	nozzle diameter
γ	heat capacity ratio C_p/C_v
K_n	Knudsen number
κ	nozzle peaking factor
k_b	Boltzmann constant
λ	mean free path
m	mass
Ma	Mach number
n	number density
n_0	initial number density
ν	collision frequency
p	locally specified probability function
P_0	source pressure or stagnation pressure
$\mathcal{R}$	number of rotational degrees of freedom
R_f	random deviate
r_0	nozzle radius
ρ	density
σ	collision cross section
t	time
T_0	source temperature or initial temperature
$T_\parallel$	parallel component of the beam temperature
$T_\perp$	perpendicular component of the beam temperature
T_m	mean kinetic temperature
T_r	effective rotational temperature
T_v	effective vibrational temperature

τ_r	rotational relaxation time
u	directed flow velocity
u_∞	flow velocity limiting value
Υ	potential parameter
ω	spectral or rotational frequency
ω_c	cut-off frequency
ω_s	sampling frequency
Ξ	source parameter
ξ	rotational–translational coupling parameter
$\mathcal{Z}_r$	rotational collision number
$\mathcal{Z}_v$	vibrational collision number
z	distance along the molecular beam axis
z_{ns}	nozzle to skimmer separation

Chapter 1

Principles of beam production and detection

1.1 Introduction

The purpose of this chapter is to introduce the basic principles of atomic and molecular beam production. Since the initial development of molecular beam technology in the 1950's, numerous techniques have been devised for the production and detection of atomic and molecular beams [Scoles, 1988]. While a complete description of all of these techniques is well beyond the scope of this thesis, a brief introduction to the principles behind some of the experimental techniques described in §3 may be useful.

1.2 Beam production

A gas contained within a reservoir or source at a constant pressure will have a velocity distribution characterized solely by its molecular weight and the temperature of the source as described by the Maxwell–Boltzmann distribution function [Zemansky, 1984]. For the expansion of such a gas into a region of lower pressure through a small orifice there exist two extreme or limiting situations: the diameter of the orifice may be either *smaller* or *larger* than the mean free path of the atoms or molecules in the source.

When the size of the orifice is smaller than the mean free path of the atoms or molecules in the source, an atom or molecule in the vicinity of the orifice can pass into the low pressure region without undergoing any collisions with the other atoms or molecules in the source. This situation corresponds to an *effusive* expansion, and effusive sources represent the earliest type of molecular beam source [Kennard, 1958]. Since the passage of particles from the source into the low pressure region takes place in the complete absence of any collisions, there is no change in temperature in an effusive expansion. Consequently, in an effusive expansion the velocity distribution of the expanding gas remains largely unchanged,[1] with the gas simply going from a region of high pressure in the source to a region in which the density of the gas is greatly decreased but where its thermal properties are still characterized by the temperature of the source [Ramsey, 1956].

While effusive beams are well understood and easy to characterize, they suffer from a number of disadvantages. Apart from producing beams of low intensity compared to those produced by the supersonic sources discussed below, effusive beams, by virtue of

[1] To some extent there may be a tendency for molecules of higher velocity to dominate the effusive beam as they will undergo more wall collisions within the source than slower moving molecules and are therefore more likely to pass through the orifice into the vacuum.

their means of production, have broad velocity distributions, making them unsuitable for studying the energy dependence of a particular process without the use of an intensity–diminishing velocity selector. Effusive beam sources are, however, the most convenient method for producing beams of non–volatile substances such as alkali metals [Carman Jr., 1986].

In 1951 Kantrowitz and Grey proposed a new method of generating molecular beams which promised to overcome the limitations of the effusive source. They proposed the use of a supersonic nozzle beam source. It was predicted and later verified that the use of such a source would yield beams having intensities several orders of magnitude greater than those attainable using effusive sources. Consequently, since about 1954 supersonic nozzle beam sources have found a large number of applications in chemical physics research and have become a standard tool in molecular beam research [Anderson, 1974].

The supersonic nozzle beam is formed by expanding a gas from a region of high pressure (10^2 Torr to 10^4 Torr) through a small orifice (10^{-4} m to 10^{-5} m diameter) into a low pressure ambient background (10^{-6} Torr to 10^{-8} Torr). The diameter of the nozzle exit is significantly greater than the mean free path of the molecules in the source and consequently the gas molecules will experience a large number of collisions as they pass through the nozzle. In order to obtain a coherent well defined beam a small hyperbolic cone shaped device with a small aperture in its tip is placed in front of the expanding jet. This device is referred to as a *skimmer* and represents what may be the first of several collimating devices along the beam axis. The correct placement of the skimmer in terms of its distance from the nozzle is of crucial importance and is discussed in §3.2.

It is frequently stated that the supersonic expansion of a gas is essentially an isentropic process [Anderson and Fenn, 1965]. While the various degrees of freedom of the gas molecules may remain in equilibrium during the initial stages of the expansion this will almost certainly never be the case at later stages, and in fact three quite distinct regions can be identified within a supersonic expansion. The first is the continuum or hydrodynamic flow region which is characterized by the occurrence of a large number of collisions as the gas molecules pass through the nozzle, and can be adequately described using ordinary fluid mechanics [Douglas *et al*, 1984]. The isentropic nature of the flow is maintained in this region by virtue of the high collision frequency. The second distinct region of the supersonic expansion is referred to as the transition flow regime and is characterized by the breakdown of the isentropic nature of the flow with the various degrees of freedom associated with the expanding gas falling out of equilibrium with one another. This breakdown of equilibrium may begin to occur only a few nozzle diameters beyond the nozzle exit. In the final region of the expansion the populations of all the various degrees of freedom become fixed or *frozen* as the gas density decreases to a point where no further collisions occur and the flow becomes collisionless or *free molecular*.[2]

The effect of a large number of collisions in the vicinity of the nozzle exit is to *monochromatize* the velocity distribution, and since the most effective of these collisions with regard to driving molecules out of the source will be those which have a large component of velocity perpendicular to the nozzle exit, much of the random thermal motion of the molecules in the beam source is converted into directed mass flow along the beam axis [Pauly and Toennies, 1968]. Since most of the thermal energy associated with the

[2]The concept of a truly collisionless flow represents an idealized situation. In practice this will not be the case for a number of reasons. For instance, there will always be collisions occurring between beam molecules and background gas molecules, and even in the absence of such collisions the finite width of the beam velocity distribution means that there is still a small probability of collisions occurring between beam molecules even at low densities. This aspect of the expansion process is examined in §4.2.

molecules is converted into directed kinetic energy, the gas is observed to rapidly cool (as measured by the random motion of the particles in the beam) to very low temperatures as it rarefies, and it is this reduction in temperature that leads to the substantial narrowing of the velocity distribution. The fact that the beam is more axially directed means that there is increased mass flow through the skimmer and thus a greater beam intensity. Supersonic beams are generally observed to have intensities in excess of 10^2 to 10^3 times those of effusive beams.

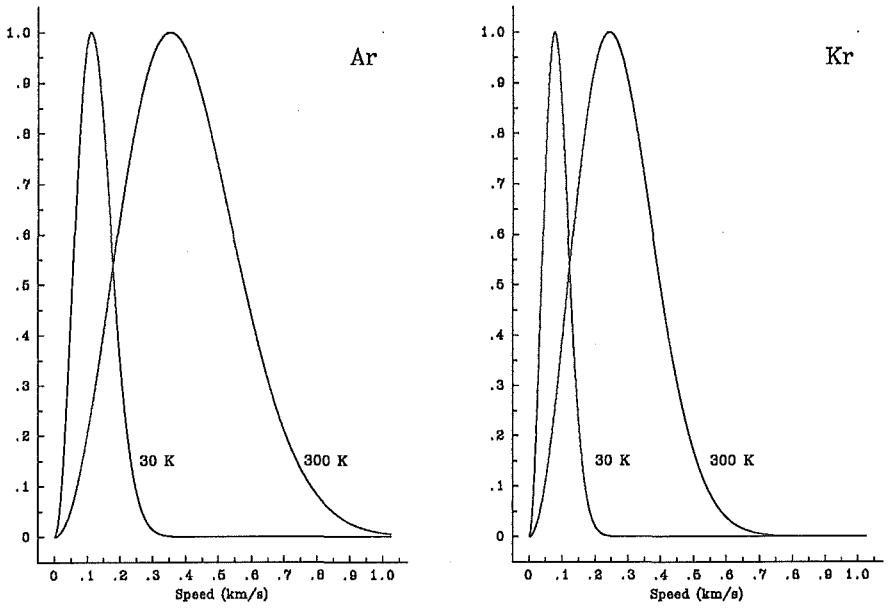

Figure 1.1: Speed distributions for argon and krypton, illustrating the effects of temperature and mass on the width of the distribution.

In addition to the narrowing of the velocity distribution, there is also an increase in the most probable velocity as measured along the flow axis, and it is this increase in velocity accompanied with the decrease in number density which produces the supersonic flow condition. It should be emphasized that the flow is supersonic primarily due to the temperature decrease, which causes a corresponding decrease in the *local sonic velocity*, rather than to the velocity increase. The importance of establishing this supersonic flow condition is that as the gas propagates supersonically, a shock wave is developed around the flow as the result of collisions with slow moving background gas molecules. The effect of this shock wave is to produce a region of high density around the expanding jet which is difficult to penetrate by the warm background gas. The components of this shock wave are referred to as a barrel shock wave and a Mach disc. The barrel shock wave extends outward from the nozzle to the Mach disc, which is a circular shaped shock front lying perpendicular to the direction of the supersonic flow. No such shock waves can be generated in an effusive expansion.

Unfortunately, both the degree of cooling and the gain in intensity obtainable in a supersonic expansion are neither well characterized experimentally or well understood theoretically. Both are complicated functions of many variables such as the source pressure and temperature, and the diameter of the nozzle. It is also necessary to consider effects such as background scattering and skimmer interference. Such effects are discussed in §3.2. Also, as the expansion is a non–equilibrium process, the extent of cooling for translational, rotational, and vibrational degrees of freedom may be quite different. This breakdown of translational and internal equilibrium in the supersonic expansion of a gas into a vacuum represents one of the fundamental experimental and theoretical problems of rarefied gas dynamics and forms the basis for much of the work presented in §4.2. This temperature relaxation has also been exploited for the study of weakly bound clusters, as in §3.6, and to spectroscopically study many complex molecules with high resolution [Hayes, 1987].

The discussion thus far has pertained solely to the expansion of pure gases. For supersonic nozzle sources, however, it is also possible to form supersonic beams of gas mixtures [Anderson *et al*, 1966], and the technique of *seeding* a heavy component into a light *carrier* gas is often used in a variety of supersonic beam experiments for a number of important reasons. In addition to the intensity limitation of effusive beams, there is also the limitation of energy. For an effusive beam, the maximum kinetic energy that can be achieved is totally limited by the temperature of the effusive source. For supersonic expansions of pure gases, however, the situation is only slightly different, since the final kinetic energy of the beam is still essentially dependent upon the temperature of the source. When a binary gas mixture is expanded from a nozzle source in a supersonic expansion such that there are sufficient collisions close to the nozzle exit to maintain energy and momentum equilibrium between the two gases, then both species will attain the same mean velocity and translational temperature. The actual values of the mean velocity and translational temperature will correspond to those of a uniform gas expanded at the same source temperature with molecular weight and heat capacity equal to the concentration–weighted average for the mixture [Anderson, 1974]. In the supersonic expansion of a dilute mixture, the *seed* gas will therefore tend to adopt the characteristics of the carrier gas, and thus, in principle, two quite different gases may be prepared with very similar energies by seeding them in appropriate ratios in a given carrier gas. The important feature of the seeding technique is that the kinetic energy of a given species may be easily changed by changing either the seeding ratio or the carrier gas. In particular, heavy species may be accelerated by seeding them in a light carrier gas to kinetic energies far greater than those attainable for a pure expansion of the heavy species under the same source conditions. An important side–effect of seeding is that of hydrodynamic focussing, in which heavy species seeded into a light carrier gas are preferentially focussed onto the beam axis. This may be understood in terms of pressure diffusion due to the steep pressure gradients observed in supersonic expansions, and has the useful advantage of increasing the concentration of seed gas available for detection by an on–axis detector. Another use of seeding is in the production of clusters, where the addition of a less condensable, inert carrier gas to a pure expansion has been shown in many cases to lead to enhanced cluster formation. This effect and the phenomenon of hydrodynamic focussing are discussed further in sections §3.5 and §3.6, respectively.

Supersonic nozzle sources may be operated in either a continuous or a pulsed mode. If a molecular beam is defined as a collimated stream of molecules moving in an essentially collision–free manner through a vacuum, then a pulsed beam may be viewed as a temporally discrete molecular beam. Such pulses may be produced either by pulsing a supersonic nozzle source or by pulsing open a shutter or *chopper* which interrupts the beam at some

point in time after it has been formed. This latter technique is referred to as *chopping*, and represents a means of generating beam pulses of extremely short duration, such as those required for the accurate determination of the beam speed distributions examined in §3.3.

Pulsed nozzle expansions possess a number of unique features and advantages over continuous sources by virtue of their temporal nature. Much higher source stagnation pressures can be used with only a modest vacuum system through the application of a pulsed nozzle source and the molecular beams produced by such sources can have instantaneous intensities some several orders of magnitude greater than those attainable using a continuous source [Gentry and Giese, 1977]. Pulsed nozzle sources also produce beams with a significantly higher population of atomic and molecular clusters [Liverman *et al*, 1979] while the reduced dependence on expensive high speed differential pumping in pulsed beam experiments means that it is possible to simplify the vacuum system and thereby reduce construction costs.

Despite such advantages over continuous sources, pulsed supersonic nozzle sources suffer from two problems. Firstly, they have a lower duty cycle than a continuous source, although this is generally not of any consequence since many molecular beam experiments make use of pulsed lasers and pulsed detection systems with similarly low duty cycles. A considerably more troubling aspect of pulsed expansions is the fact that beam velocity distributions and cluster size distributions will generally be nonuniform throughout the pulse [Saenger, 1981]. Unfortunately there is little that can be done to overcome this problem.

1.3 Beam detection

A typical beam detection system is schematically illustrated in Figure 1.2. The beam is modulated by the beam source driver, which also provides a reference signal or *trigger* for any detection and monitoring equipment that may require it. The skimmed molecular beam enters the detection region of the apparatus, and the detector produces an output signal which is amplified and sent for analysis to an electronic device such as a computer or an oscilloscope. Beam detectors may be operated in either an analog or a pulse counting mode, and hence some form of signal conversion may be required before the resultant data can be collected. The output of a pulse counting detector consists of a stream of well separated pulses, each of which may be correlated with the detection of a single particle. When the beam flux is too high so that successive pulses cannot be separated, it is not possible to perform measurements using a detector operating in pulse counting mode. Instead it is necessary to operate in an analog mode where the signal output consists of a *continuous* current or voltage.

Atomic and molecular beams may be detected in a number of ways, and a wide variety of beam detectors have been developed [Scoles, 1988]. For the experiments described in this thesis, beam detection was achieved using a commercially available quadrupole mass spectrometer equipped with an electron impact ion source. The use of electron impact ionization followed by mass filtering and ion detection is probably the most common detection method used in molecular beam experiments due to its high sensitivity and applicability to the detection of most chemical species [Lee *et al*, 1969].

Electron impact ionization represents the most universal method of ionizing the components of neutral atomic and molecular beams. Electron impact ionization involves the bombarding of the species to be detected with high energy ($\sim$ 70 eV) electrons. In addi-

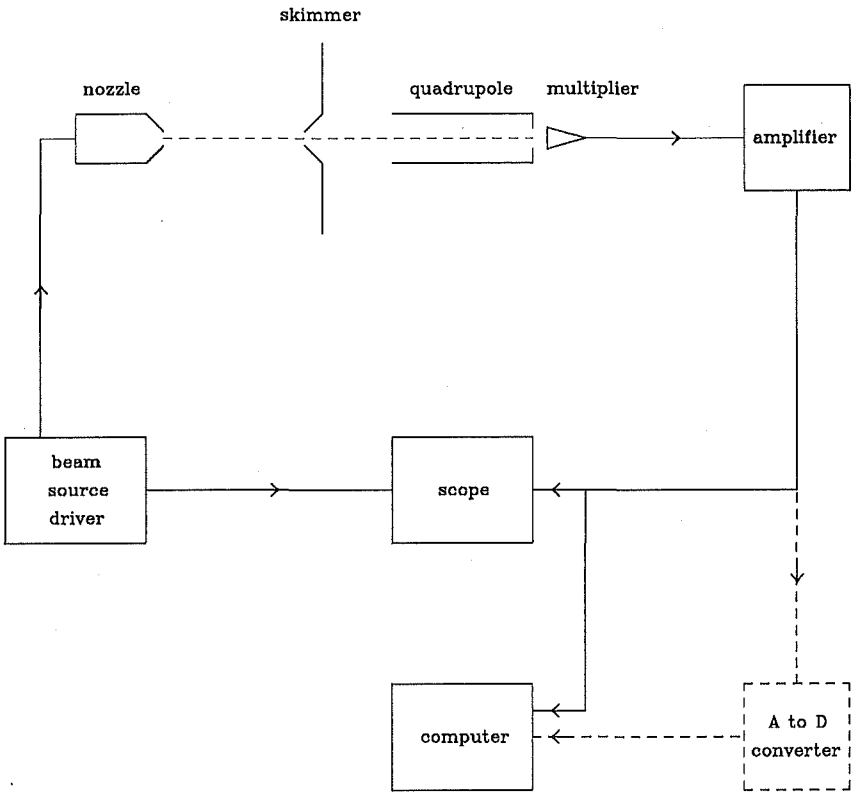

Figure 1.2: Schematic diagram of a typical molecular beam experiment.

tion to being ionized, molecular species are often fragmented as a result of the ionization process. The probability $p(\sigma_i, v)$ of an atom or molecule being ionized while traversing an ionization region of length l is found to be proportional to the electron density j_e, the ionization cross section σ_i, and the residence time of the particle in the electron stream according to the equation

$$p(\sigma_i, v)\mathrm{d}\sigma_i\mathrm{d}v = A\frac{j_e}{e} \cdot \frac{l}{v} \cdot \sigma_i\mathrm{d}\sigma_i\mathrm{d}v, \tag{1.1}$$

where e is the elementary or unit charge (1.609219×10^{-19} C), A is a normalization constant, and v is the speed of the atom or molecule. It should be noted, however, that although the ionization probability depends on both the ionization cross section of the neutral species and the geometry of the ionization region, it is generally found that for most gases the ionization probability curve exhibits a sharp threshold at low electron energies and then rises through a maximum located between 70 eV to 100 eV, thereafter decreasing in a manner approximately proportional to the inverse of the ionizing

electron energy. The sharp threshold observed at low electron energies corresponds to the *appearance potential* or *appearance energy* of the species in question, and forms the basis for the work described in §3.7. Under typical operating conditions, the efficiency of most electron impact ionization sources is generally on the order of 1×10^{-3}. The intrinsic response time of ion sources is limited by the length of the ionization region and the velocity of the atomic or molecular beam entering the source. At high emission currents the response time may also be limited by space charge trapping of ions, resulting in inefficient ion extraction [Carman Jr., 1986].

Following ionization in the ion source of the electron impact mass spectrometer, the ionized species are focussed using a series of ion lenses into a mass filter where they are selected on the basis of their mass–to–charge ratio, with no account being taken of the charge sign. The mechanical structure of the quadrupole mass filter is schematically illustrated in Figure 1.3. It consists ideally of four parallel conductive rods with hyperbolic section to which an electrostatic and a radio frequency potential are simultaneously applied. Ions entering into the filter along the z-direction, perpendicular to the plane of Figure 1.3, experience a potential field $P(x, y, t)$ described by the equation

$$P(x, y, t) = \frac{[U + V \cdot \cos(2\pi f t)]\,(x^2 - y^2)}{r_0^2}, \tag{1.2}$$

where f^{-1} is the period of the radio frequency potential and r_0 is the shortest distance between the quadrupole rods and the z-axis. The electric potential is therefore $+[U + V \cdot \cos(2\pi f t)]$ for the rods lying parallel to the x-z plane and $-[U + V \cdot \cos(2\pi f t)]$ for the rods lying parallel to the y-z plane. The motion of ions through the quadrupole is described by Mathieu's equations, and is highly complicated [Dawson, 1976]. For the present purpose, it is sufficient to note that ions may follow stable trajectories and pass through the quadrupole filter assembly to the detector only if their maximum displacement from the z-axis is sufficiently low to avoid collision with the quadrupole rods. The motion of the ions may be qualitatively understood by considering the separate effects of the positive x-z and negative y-z planes. In the positive plane, ions lie at the bottom of an electrostatic potential well and will oscillate under the action of the radio frequency field. The oscillation amplitude increases with ion mass, and therefore heavy ions are more likely to collide with the quadrupole rods. The function of the positive x-z plane is therefore to act as a low–pass mass filter. Applying an analogous argument, it can be seen that the negative y-z plane acts as a high–pass mass filter. The combination of the two planes is thus to create a band–pass mass filter. A somewhat more quantitative description of the quadrupole operation may be obtained by means of a *stability diagram* such as that illustrated in Figure 1.4. The stability diagram represents the field of stability for solutions of Mathieu's equations as a function of the two parameters

$$a = \frac{2\mathcal{Z}eU}{m(r_0\pi f)^2} \tag{1.3}$$

$$q = \frac{\mathcal{Z}eV}{m(r_0\pi f)^2} \tag{1.4}$$

where e is the unit charge and $\mathcal{Z}$ is an integer value representing the multiplicity of the ionic charge. For certain values of a and q, ionic trajectories through the quadrupole assembly may be unstable in the x-z plane, the y-z plane, or in both the x-z and y-z planes. In addition, there is a well defined region of stability, corresponding to the area bounded by the heavy curve and the x-axis on Figure 1.4. Also shown in Figure 1.4 is the

line a/q = constant, which crosses the stability region at two points corresponding to the upper and lower limits of the mass filter pass band Δm.

It is important to note that real quadrupole systems may differ significantly from ideal systems in terms of both construction and performance. In particular, it should be mentioned that quadrupole rods with hyperbolic section are difficult to manufacture and are generally replaced by cylindrical rods with radius r chosen to obtain the best approximation to the theoretical quadrupole transmission profile. In addition, the performance and mass resolution of real quadrupole systems is generally limited by mechanical and electrical non–idealities.

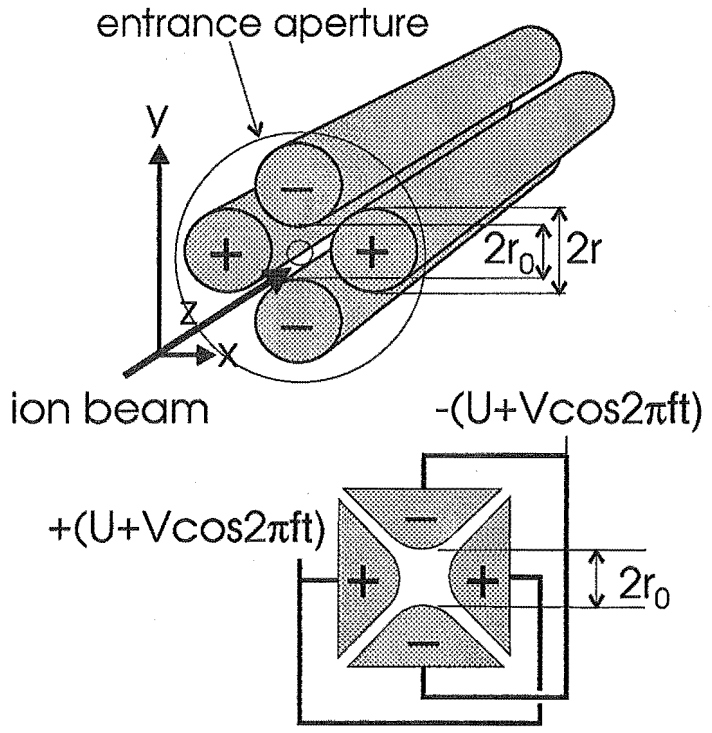

Figure 1.3: Schematic diagram of a quadrupole mass filter.

Ionized beams may be detected in a number of ways. The simplest and most economic means of detection is to use a Faraday cup. While Faraday cups are both cheap and very stable with time, they offer no gain of the detected ion current, are susceptible to noise, which limits their sensitivity, and they often have poor response times.[3] The electron

[3]The Faraday cup is connected to the input stage of an electrometer via a suitable load resistor R_L

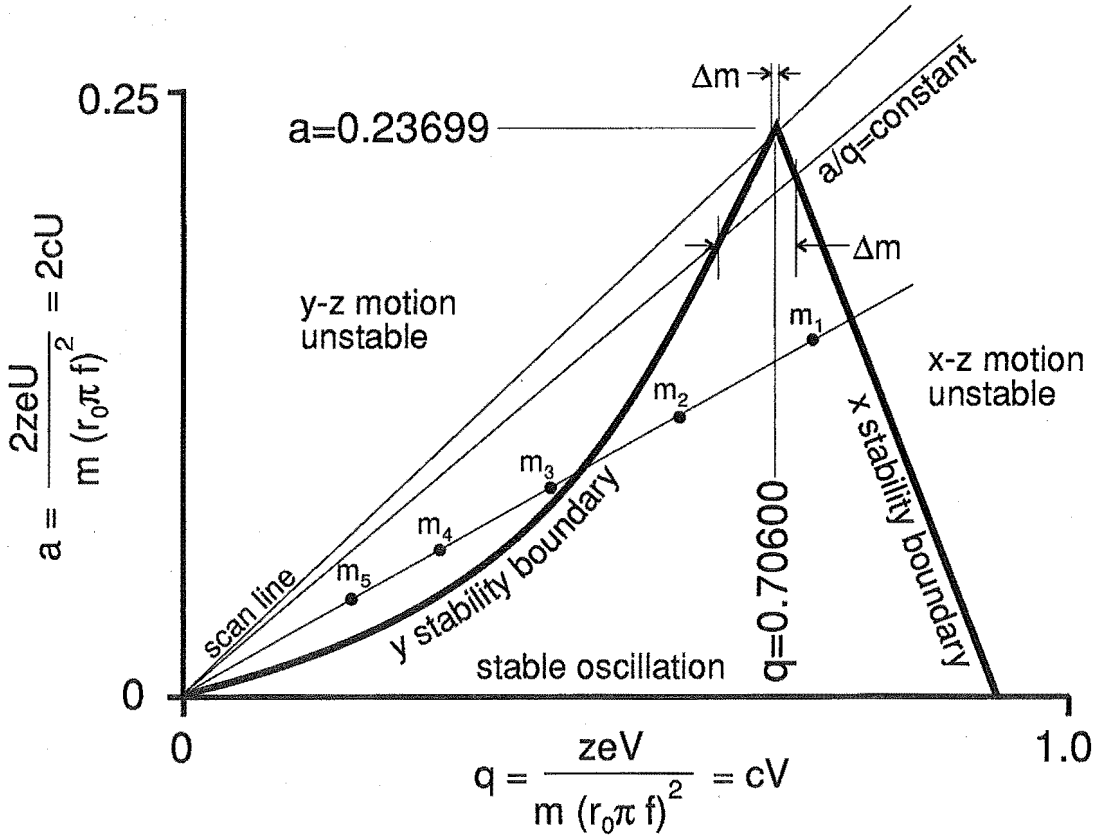

Figure 1.4: Stability diagram for a quadrupole mass filter.

multiplier provides a substantial enhancement in terms of both sensitivity and response time over the Faraday cup detector and is therefore the detector of choice. The electron multiplier works by converting an ion current into an electron current which is further amplified by means of the secondary emission effect. Incident ions induce the liberation of a number of electrons from the resistive surface of the multiplier. The input stage of the multiplier is held at a high negative potential (-1 kV to -3 kV), causing these electrons to flow down the potential gradient towards the collector, which is held at ground potential. As they flow towards the collector, the electrons repeatedly collide with the resistive surface, each time releasing more electrons and so increasing the electron current. The

and is maintained at virtual ground potential. The detection sensitivity of the cup is limited by the noise associated with the load resistor and the noise of the electrometer input stage. Practical values of R_L range from 10^8 Ω to 10^{12} Ω and limit the response time of the detector. The response time is also affected by any stray capacitance associated with the Faraday cup collector and the electrometer input stage.

expected output current i of an electron multiplier is given by the expression

$$i = -e \cdot F \cdot p \cdot G, \tag{1.5}$$

where F is the ion flux impinging on the input stage of the multiplier, p is the ion–electron *conversion probability*, G is the multiplier gain, and e is the unit charge. The detection efficiency of the multiplier is largely determined by the ion–electron conversion probability, which is a measure of the fraction of impinging ions that stimulate the production of primary electrons on the surface of the multiplier. The gain of electron multipliers typically ranges from 10^6 up to 10^8 and is sufficiently high to detect single ions. The intrinsic noise of electron multipliers, on the other hand, may be as low as 10^{-2} counts per second.

Electron multipliers may be operated in both pulse counting and analog modes. In the latter case, the electron current from the multiplier is converted into a voltage signal by means of a load resistor. The resulting voltage waveform may then be amplified and monitored. The output of an electron multiplier is a stream of extremely narrow pulses of different height superimposed on any noise that may be present. When operating in pulse counting mode, this output is sent to an electronic system which amplifies the signal and counts all those pulses with amplitude greater than some prescribed threshold level. In order to be correctly counted, it is necessary for the output pulses to be sufficiently well separated in time. The maximum allowable output pulse rate can be calculated by assuming that the statistical distribution of the output pulses conforms to a Poisson probability distribution, whereupon the probability $p(\Delta t)$ of observing two or more pulses during a time interval Δt is

$$p(\Delta t) = 1 - (1 + \overline{r}\Delta t)\,\mathrm{e}^{-\overline{r}\Delta t}, \tag{1.6}$$

where $\overline{r}$ is the average pulse rate. Assuming that the probability of observing a significant overlap between successive pulses is less than 50%, equation (1.6) suggests a maximum allowable pulse rate of roughly 1×10^6 counts per second.

While the overall sensitivity and efficiency of electron multipliers depends upon many factors, best performance is generally obtained by operating the multiplier in pulse counting mode. Under such conditions the main source of noise is associated with statistical fluctuations of the ionized beam striking the detector such that the signal–to–noise ratio γ is determined by the following expression [Lee *et al*, 1969]:

$$\gamma^2 = \Delta t \frac{S^2}{(S + 2B)}, \tag{1.7}$$

where Δt is the measurement time and S and B are the average number of counts per second arising from the ionized beam and ionized background gas, respectively. In the limit of a negligible background count, the signal–to–noise ratio depends only on S, while for experiments in which the average signal count is significantly lower than that of the background, the signal–to–noise ratio becomes proportional to $S/\sqrt{B}$. For the experiments described in this thesis, it was found that the average signal count was invariably much greater than the background count, and the signal–to–noise ratio was generally more than satisfactory. For example, the appearance potential measurements discussed in §3.7 typically have a measurement time of around three to four hours with a background count rate of not more than 10% of the total count rate. Under such conditions equation (1.7) gives a value for γ of $\sim 10^3$, which is quite acceptable. It should be noted that when the measurement time becomes longer than a few hours consideration must be given to the possibility of long term experimental instabilities affecting the accuracy of the measurement.

Chapter 2

Apparatus

2.1 Introduction

The purpose of this chapter is to briefly describe the important constructional features of the supersonic molecular beam apparatus designed and built for the investigations of atomic and molecular clusters presented in this thesis. Only constructional details are described here. Experimental arrangements and procedures employed for individual experiments are described as and where appropriate in §3. Commercially available electronic and mechanical equipment was often too expensive to purchase or simply failed to meet the exact requirements for a particular application. Consequently many components of the apparatus were designed and constructed within the Chemistry Department with the assistance of technical staff. These components and significant modifications to commercial equipment are described in somewhat greater detail.

2.2 Vacuum system

Two configurations of the supersonic molecular beam apparatus employed for the experimental investigations described in this thesis are illustrated in Figures 2.1 and 2.2. All materials used in the construction of the apparatus were ultra–high vacuum compatible, including type 316 stainless steel, aluminum, OFHC copper, viton o–rings, machineable glass ceramic, and teflon–coated silver wire. The vacuum system was designed in a modular fashion to facilitate ease of maintenance and to allow major modifications of the apparatus (such as the addition of an extra vacuum chamber) to be performed in a relatively straightforward manner. The vacuum chambers were connected via o–ring or copper gasket sealed ConFlat joints. All diffusion pumps were charged with DC705 silicone oil.

The source or expansion chamber consisted of a 15 cm Varian stainless steel cross (four ports). The chamber was differentially pumped by a 3500 l/s (for helium) Varian VHS–6 diffusion pump and a 2000 l/s Varian VHS–4 diffusion pump. Both diffusion pumps were backed by a tandem arrangement of dual stage rotary mechanical pumps, consisting of an Edwards E2M40 (700 litres per minute) and an Edwards EDM20 (342 litres per minute). The VHS–6 diffusion pump was directly attached to the bottom port of the expansion chamber (see Figures 2.1 and 2.2), while the VHS–4 was connected to the expansion chamber via a stainless steel elbow which attached to the top port of the expansion chamber. The diffusion pumps could be isolated from the backing mechanical pumps using valves incorporated into the foreline assembly.

Additional cryogenic pumping of the expansion chamber was provided by three custom

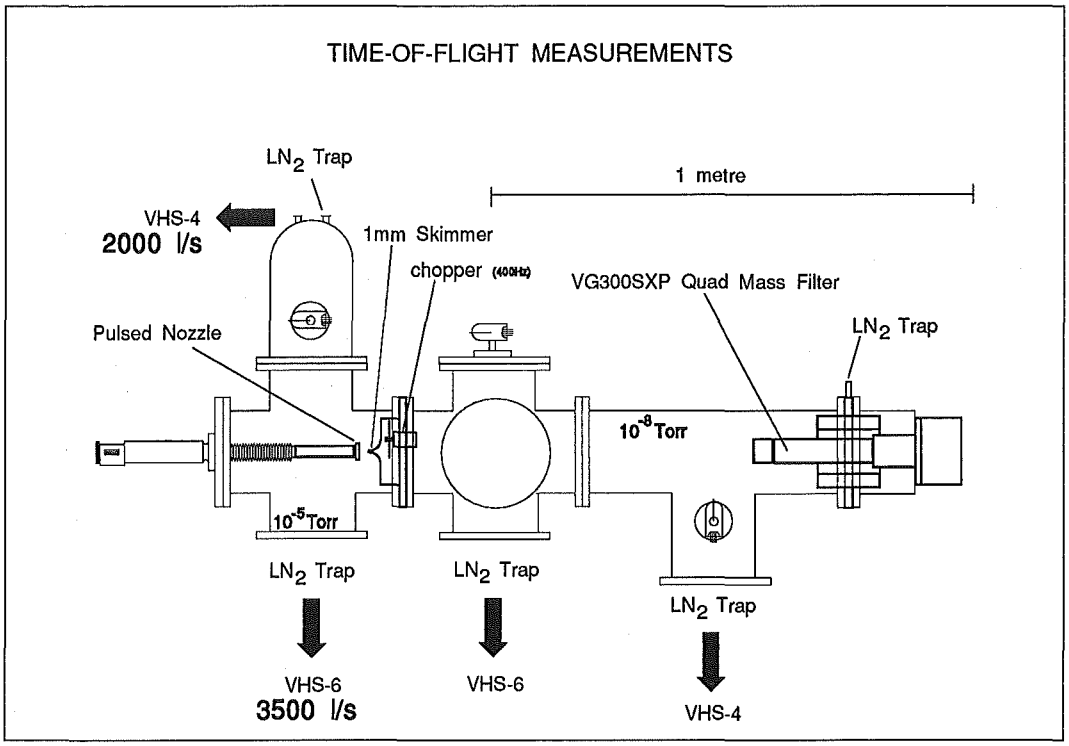

Figure 2.1: Illustration of the experimental apparatus employed for the measurement of supersonic atomic and molecular beam speed distributions.

built stainless steel liquid nitrogen traps. The first trap was located directly above the VHS–4 diffusion pump. The second trap was welded into the stainless steel elbow connecting the VHS–4 diffusion pump to the expansion chamber in a position almost directly above the supersonic nozzle source, while the third trap was sandwiched between the VHS–6 diffusion pump and the bottom port of the expansion chamber. The traps were constructed in the shape of large hollow doughnuts in an attempt to minimize any loss of pumping speed which might be incurred by their location in the vacuum system. This type of trap was found to be extremely effective, and has now become the standard design for any new traps which may be fitted to the apparatus. While not significantly improving the overall quality of the absolute vacuum attainable in the expansion chamber, the liquid nitrogen traps greatly improved the rate of removal of condensible gases from the chamber when the pulsed nozzle was operating. The traps had to be regularly filled during the course of a long experiment due to the high rate of gas condensation onto their surfaces.

The pressure inside the expansion chamber was monitored by a standard ion gauge connected to a MKS–290 ion gauge controller. A background gas pressure of 1×10^{-7} Torr was typical for the expansion chamber when the pulsed nozzle was not operating. When the pulsed nozzle was operating, however, the background pressure could rise to 1×10^{-5} Torr or higher. The foreline pressure associated with the expansion chamber was continuously monitored using a MKS TC1 thermocouple gauge connected to a MKS type 286 controller.

The second vacuum chamber consisted of a 15 cm Varian stainless steel six–way cross.

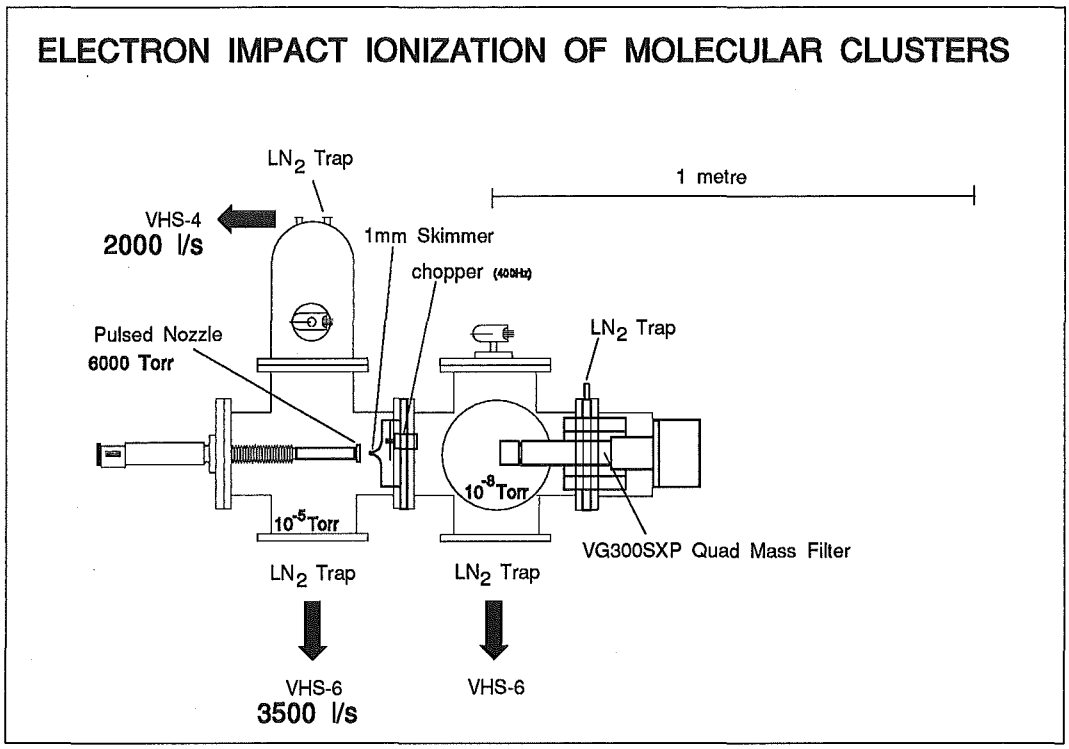

Figure 2.2: Illustration of the experimental apparatus employed for the determination of cluster ion appearance potentials. Note that the beam chopper was not used for these measurements (see §3.7).

The six–way cross was pumped by a 3500 l/s VHS–6 diffusion pump backed by a Varian SD700 mechanical pump (726 litres per minute). The pressure inside the second chamber was monitored using a standard ion gauge connected to a MKS–290 controller, while the foreline pressure was monitored using a MKS TC1 thermocouple gauge and a MKS type 286 controller. The background pressure in the second chamber was typically $\leq 2 \times 10^{-8}$ Torr with the pulsed nozzle not operating. With the pulsed nozzle operating the pressure was generally between 1×10^{-7} Torr and 5×10^{-8} Torr.

An extra vacuum chamber was added to the system for the measurement of supersonic beam speed distributions by time–of–flight methods described in §3.3. This chamber was referred to as the flight–tube, and was pumped by a single 2000 l/s VHS–4 diffusion pump backed by an Alcetal 100 litre per minute mechanical pump. The pressure inside the flight–tube was continuously monitored using a standard ion gauge connected to a MKS–290 ion gauge controller, while the foreline pressure was monitored using a MKS TC1 thermocouple gauge and a MKS type 286 controller. Pressures in the low 10^{-7} Torr to high 10^{-8} Torr range were generally maintained in the flight–tube during normal operation of the pulsed nozzle.

The diffusion pumps were controlled using purpose built time proportional power controller units. The diffusion pumps were protected via an interlock facility provided by the MKS ion gauge and thermocouple gauge controller units. Excessive vacuum or foreline pressure constituted a vacuum failure and resulted in the immediate shutdown

of all diffusion pumps. This protection facility was deactivated when an experiment was being performed as high pressures in the expansion chamber resulting from the operation of the pulsed nozzle could easily trigger a system shutdown. The quadrupole mass filter used to collect experimental data was protected in a similar manner.

2.3 Gas handling system

The gas preparation system consisted of three specially adapted large storage ($\sim 5 \times 10^{-2}$ m^3) freon refrigerant containers along with three glass bulbs (ranging in size from 1 to 5 litres) and vacuum lines to facilitate the preparation of gas mixtures and their delivery to the pulsed nozzle source. The gas handling system was pumped by a liquid nitrogen–trapped Edwards 150 litre per minute mechanical pump (model ES150) and pressure in the line was continuously monitored using a 10000 Torr MKS Baratron capacitance manometer. The large steel storage reservoirs were useful for experiments requiring good pressure stability over long periods of pulsed nozzle operation and for investigations involving the use of high source pressures.

2.4 Supersonic nozzle source

A pulsed supersonic nozzle beam source may be considered to consist of an electromagnetic valve fitted with a supersonic nozzle. Electromagnetic valves of two types were used to accomplish the experimental measurements described in this thesis. A modified Honda Civic fuel–injection valve fitted with a 70 μm nozzle was employed for the beam characterization experiments presented in §3.2, §3.3 and §3.5, while a commercially available pulsed valve supersonic nozzle (General Valve Corporation, model 9-181) was used for the measurements described in §3.4, §3.6 and §3.7. The electromagnetic valves were held in an aluminium housing arrangement referred to as the carriage assembly. The carriage assembly was fitted with vacuum rated precision bearings which allowed it to be mounted onto two parallel stainless steel rods. The mounting rods were friction–fitted into the end flange of the expansion chamber, which supported the skimmer assembly. This mounting arrangement was found to be necessary after initial designs having the mounting rods attached to the front flange of the expansion chamber proved unsatisfactory with respect to the alignment of the nozzle and skimmer. By fitting the mounting rods to the same flange as the skimmer assembly, the alignment between the nozzle and the skimmer was greatly improved. The carriage assembly could be be moved along the mounting rods using a linear motion feedthrough (Huntington Mechanical Laboratories, model VF-156). Using the linear drive mechanism, it was possible to position the supersonic nozzle to a prescribed distance from the skimmer with an accuracy of better than $\pm$ 0.1 mm. To ensure that the pulsed nozzle could not be accidentally driven into the delicate skimmer, a brass stop was attached to one of the carriage assembly mounting rods using a small grub screw. The brass stop was typically positioned so that the minimum possible nozzle to skimmer separation was between 2 mm and 5 mm. The linear drive mechanism was mounted onto the front flange of the expansion chamber through a 2.75 inch ConFlat. An ultra high vacuum electrical feedthrough was used to supply power to the electromagnetic valve solenoid, and all electrical connections were made with vacuum rated teflon–coated silver wire, soldered at each end. The pulsed supersonic nozzle source was connected to the external gas supply via a 1/4 inch diameter flexible stainless steel bellows and a stainless steel Swagelock feedthrough located on the front flange of the expansion chamber.

2.5 Skimmer assembly

The design of the skimmer assembly is illustrated in Figure 2.3. A Beam Dynamics electroformed nickel skimmer was mounted in a machined glass ceramic holder which was secured into the top of an aluminium top–hat. The top–hat arrangement was bolted to the supporting flange separating the first and second vacuum chambers. A skimmer having a 1.0 mm diameter orifice was employed for the beam characterization experiments presented in §3.2 to §3.4 while a skimmer with a 1.5 mm diameter orifice was used in the investigations of atomic and molecular cluster species described in §3.6 and §3.7. Mounting the skimmer in a glass ceramic holder meant that the skimmer was electrically isolated from the rest of the molecular beam apparatus. A length of teflon–coated silver wire was attached to the base of the skimmer. This wire allowed an electric potential to be applied to the skimmer via an electrical feedthrough soldered into the edge of the supporting flange. Some consideration had been given to the possibility of generating ions in the expansion chamber by photon ionization or electrical discharge close to the nozzle exit. With the skimmer electrically isolated from the rest of the apparatus, any ions produced by these methods which hit the skimmer could be detected using a picoammeter.

2.6 Chopper assembly

The construction of the chopper assembly employed for the measurement of supersonic beam speed distributions by time–of–flight methods is illustrated in Figure 2.3. The stainless steel mounting rods used to support the pulsed nozzle carriage assembly passed through into the second vacuum chamber of the apparatus and were also used to mount the chopper assembly. The chopper unit was firmly held in place on the mounting rods by two small grub screws which could be easily accessed to facilitate the removal of the unit from the apparatus. A 1.5 mm diameter skimmer (Beam Dynamics) was fitted to the front of the chopper assembly to further collimate the beam and to prevent beam particles striking the front of the unit from being reflected back onto the beam axis. The skimmer was mounted on the front flange of the chopper assembly using a glass ceramic holder similar to that described previously for the primary skimmer located in the expansion chamber. The rotating beam chopper consisted of a 1.5 mm thick stainless steel disc with two diametrically opposed slits of width 2 mm. The diameter of the chopper disc was 70 mm. The beam transmission radius of the disc was approximately 30 mm and the depth of the chopper slits was 10 mm.

The chopper disc was rotated by a 400 Hz AC hysteresis motor (TRW Electronic Components, Globe Motors) which was powered by a custom built power amplifier and variable frequency oscillator. The motor was fitted with high temperature vacuum rated bearings and cooling of the chopper motor was achieved by flowing water through a copper block that was tightly fastened to the motor housing. A threaded hole drilled into the motor shaft was used to attach the chopper disc to the motor. The rotation of the chopper disc was monitored by a slotted optical switch (Monsanto, model MCT8) driven by an external power supply and amplifier circuit. The optical switch was positioned directly below the point of beam transmission to minimize any errors associated with measuring the time at which the supersonic beam passed through the chopper slits. The chopper disc was able to locked in an open position using a solenoid–driven locking pin and large holes were machined through both of the stainless steel mounting flanges of the chopper assembly to facilitate efficient pumping of the chopping region.

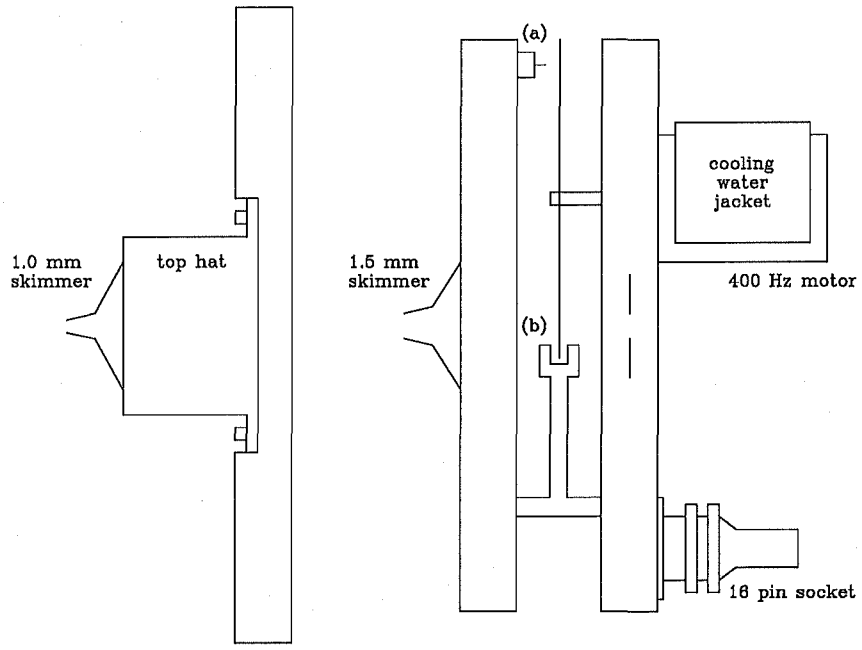

Figure 2.3: Skimmer and chopper assembly ((a) Solenoid and chopper locking pin; (b) Optical switch assembly). The stainless steel mounting rods used to support the chopper and the pulsed nozzle carriage assembly are not shown.

2.7 Mass spectrometer

A Vacuum Generators SXP300 quadrupole mass filter was used to collect all of the experimental data presented in this thesis. Although a detailed description of the mass filter is not provided here, a number of important modifications were made to the instrument and these will be discussed. The basic operating principles of the quadrupole mass filter were described in §1.3.

The mass filter assembly was removed from its original housing and mounted in a stainless steel top–hat (see Figures 2.1 and 2.2) in order to improve the efficiency of pumping around the quadrupole rods and the electron multiplier. A doughnut–shaped liquid nitrogen trap similar to those fitted to the expansion chamber was used to further improve pumping in the vicinity of the mass filter. The trap was mounted in a stainless steel flange sandwiched between the top–hat and the second vacuum chamber (or the flight–tube), and totally surrounded the middle section of the mass filter assembly.

The small signal amplifier supplied with the SXP300 quadrupole mass filter for the amplification of output pulses from the channeltron electron multiplier had a minimum response time of 1 ms. This response time was found to be unsatisfactory for the accurate measurement of beam speed distributions (see §3.3), and an alternative amplifier with a shorter response time was constructed. The new amplifier was inverting[1] with a gain of 5, and utilized video line–driver circuitry to achieve a response time of ~ 1 μs. The use of video line–driver circuitry also ensured a reasonably flat frequency response across the entire bandwidth of the amplifier (~ 1 MHz). It was somewhat frustrating that the gain of the new amplifier was so low. Unfortunately there was little that could be done to overcome this problem, as the maximum gain of the circuit was effectively limited by the experimental requirements of high speed and low input impedance. The design of the circuit therefore represented something of a compromise, with high gain being sacrificed for high speed, low input impedance, and a flat frequency response. It should be mentioned that operational amplifiers designed for video applications generally have a limited or fixed gain anyway, with further increases in gain being achieved by the addition of extra stages of amplification.

Due to the great acceleration of beam particles following electron impact ionization, the flight time of the ionized supersonic beam through the quadrupole mass filter to the detector is often assumed to be negligible in time–of–flight measurements of supersonic beam speed distributions. When the distance between the beam chopper and the ionization region of the mass filter is short (< 1 m), however, the time taken for the ionized beam particles to traverse the mass filter may become significant and should be taken into account. For the time–of–flight measurements described in §3.3, the length of the molecular beam flight path from the chopper disc to the ionization region of the mass filter assembly was only 89 cm. To measure distributions of ion flight times through the mass filter, a fast switching circuit was incorporated into the mass spectrometer controller unit. The switch was triggered by an external 5 V pulse and could be used to modulate the potential applied to the mass filter ion focussing plate from ground potential to -90 V DC. With the focus plate at ground potential, no ions were transmitted. By pulsing the potential applied to the focus plate it was possible to accurately measure distributions of ion flight times through the mass filter and thus apply suitable corrections to the time scales of measured time–of–flight waveforms. Disconnection of the switching circuit and reconnection of the normal -90 V focus plate supply was achieved via a toggle switch mounted in the back of

[1]The output pulses from an electron multiplier are negative–going and are generally inverted by the signal processing circuitry to simplify interpretation.

the mass spectrometer controller unit.

The experimental procedure described in §3.7 for the collection of cluster ion appearance potential data was entirely computer controlled via custom written interfacing software. Control of the electron energy scale and mass selection was achieved by incorporating custom built 12-bit digital–to–analogue converters into the mass spectrometer controller unit. The digital–to–analogue converters employed opto–coupled devices to improve stability and were connected to a commercial driver card installed in the laboratory computer (10 MHz 286 IBM-AT) via 2 m lengths of ribbon cable. It should be mentioned that although the SXP300 mass filter was designed for the detection of species having mass–to–charge ratios $m/z \leq 300$, species could be observed with adequate resolution up to $m/z \leq 350$. This *extra* feature of the instrument proved most useful in the investigations of atomic and molecular cluster species presented in §3.6 and §3.7.

The final change made to the mass spectrometer involved modifying the ion source so that the quadrupole mass filter assembly could be mounted at 90 degrees to the direction of the molecular beam. This was achieved by drilling a 5 mm hole through the ion source mounting block perpendicular to the quadrupole axis. A home–made aluminium skimmer with a 4 mm diameter orifice was fitted to the hole to prevent any scattering of beam particles from the edges of the hole.

2.8 Custom built electronics units

In addition to commercially obtained electronic equipment, a number of purpose built electronics units were used to achieve many of the measurements presented in this thesis. The most important of these units were the beam source driver unit and the chopper motor controller and pulse processing unit, which are briefly described below. Other custom built electronics units included a 2 MHz notch filter used to eliminate radio frequency pick–up from the quadrupole mass filter driver circuitry (see §3.7) and a simple pulse rejection circuit which was used to reject pulses emitted by the chopper optical switch to yield a lower frequency that could be used to trigger the pulsed supersonic nozzle via the beam source driver (see §3.3).

2.8.1 Beam source driver unit

The frequency and duration of beam pulses was controlled by a custom built beam source driver unit. The beam source driver was capable of providing variable length 12 V or 24 V pulses to the pulsed supersonic nozzle solenoid. The frequency and duration of the pulses could be independently varied in order to obtain the best beam signal. The frequency of beam pulses was controlled by a three position rotary switch and a ten–turn potentiometer. Using the three position switch, the pulse frequency could be changed by an order of magnitude (10^0, 10^1, 10^2). The ten–turn potentiometer could then be used to finely adjust the pulse frequency to any desired value within the selected order of magnitude. The pulse frequency was continuously monitored via a digital display fitted to the front of the beam source driver unit. The maximum pulse frequency attainable was 1 kHz. The duration of the 12 V or 24 V pulses produced by the beam source driver unit could be finely adjusted using another ten–turn potentiometer. The minimum and maximum pulse lengths were 200 μs and 2.2 ms, respectively.

For most of the experiments described in this thesis, pulsed supersonic nozzles were operated at 24 V, with a pulse frequency of close to 10 Hz. The time required for a pulsed nozzle to become fully open is proportional to the electric potential (energy) applied to the

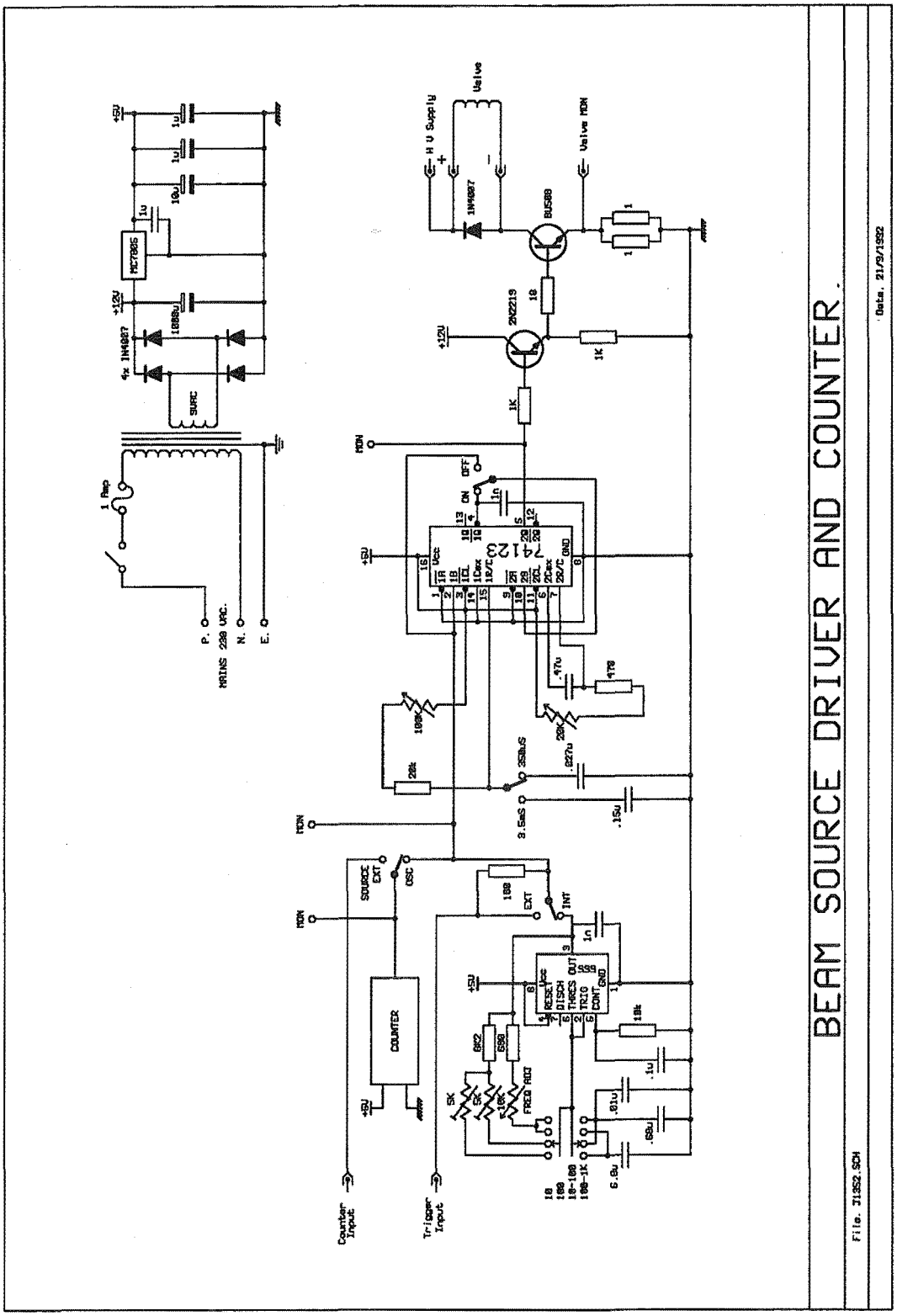

Figure 2.4: Beam source driver circuit diagram. Note that this circuit diagram corresponds to a later version of the beam source driver unit to that described in the text. The circuit illustrated provides greater control of the pulse frequency and allows the input of an external voltage to operate the electromagnetic valve. Details of the variable delay facility are not shown.

electromagnetic valve solenoid. The use of 24 V pulses ensured faster opening of the pulsed nozzle and also allowed the use of shorter pulse durations ($\sim$ 2 ms). Pulse frequencies of greater than $\sim$ 10 Hz were rarely employed. At high pulse frequencies, the increased flow of gas through the pulsed nozzle could lead to a substantial pressure increase in the expansion chamber, resulting in a degradation of the supersonic beam due to an increase in the number of collisions between beam species and background gas particles.

It should be mentioned that some care was required when setting the frequency and duration of pulses produced by the beam source driver unit. It was possible to set these two variables in a completely independent manner, and it was important to ensure that the product of these quantities did not ever equal or exceed unity. The result of such a condition was to lock the pulsed nozzle in an open state, allowing gas to flow continuously into the expansion chamber. Depending on the source pressure and the diameter of the nozzle, a continuous flow of gas into the expansion chamber could very easily cause serious damage to many components of the molecular beam apparatus. In addition to overloading the pumping system fitted to the expansion chamber, the resultant pressure increase could damage ion gauges or cause considerable damage to the quadrupole mass filter. A sudden increase in the pressure differential between the expansion chamber and the second vacuum chamber of the apparatus could easily damage the thin walled skimmer separating the two chambers.

For most experiments, the beam source driver was used to provide a 5 V trigger pulse to all other electronic equipment requiring synchronization. For experiments in which an alternative method of synchronization was required, the beam source driver could be triggered by an external 5 V pulse. The beam source driver was equipped with a variable delay facility which could be used to provide a delay between the receipt of an external 5 V trigger pulse and the issuing of the 12 V or 24 V pulse to the electromagnetic valve solenoid. The length of the delay was controlled by a ten–turn potentiometer and could be varied from 2 ms to 5 ms. The variable delay facility was used for the time–of–flight measurements described in §3.3 to synchronize the opening of the pulsed nozzle with the beam chopper.

2.8.2 Chopper motor controller and pulse processing unit

The chopper motor controller and pulse processing unit was used to power the rotating beam chopper and to shape the output pulses from the optical switch mounted on the chopper assembly (see Figure 2.3). The 400 Hz synchronous motor used to rotate the chopper disc was powered by a 180 V power supply and a variable frequency oscillator. The frequency of the motor could be accurately varied from 200 Hz to 400 Hz by adjusting a ten–turn potentiometer located on the front panel of the controller unit. This frequency adjustment was generally used only when powering up or powering down the chopper motor. The chopper was usually operated at maximum speed (400 Hz) but, to reduce the risk of damage to the chopper system, the chopper motor was started at 200 Hz and gradually brought up to maximum speed over a period of several minutes by adjusting the potentiometer. The motor was powered down in a similar manner. The motor controller and pulse processing unit also housed the power supply for the chopper disc locking mechanism. To align one of the chopper slits with the solenoid–activated locking pin, a push–button switch was provided, which allowed the chopper motor to be pulsed around in small steps until the chopper disc was in the correct position. A toggle switch was used to insert and retract the locking pin.

Chapter 3

Experimental results and discussion

3.1 Introduction

The results of all significant experimental work are presented and discussed in this chapter. The first few sections of the chapter present a series of experiments concerned with the characterization of the newly constructed supersonic molecular beam apparatus. In §3.2 the intensities of supersonic beams of pure argon are investigated as a function of reservoir pressure and nozzle to skimmer separation in order to determine a set of optimum operating conditions for the apparatus. In §3.3 supersonic beam speed distributions are measured for a range of monatomic and diatomic species using time–of–flight methods [Young, 1973]. The measured speed distributions are characterized in terms of a mean flow velocity and a parallel translational temperature. Fitted values of the flow velocity and translational temperature are compared with the results of other workers in order to verify that the supersonic molecular beam apparatus is functioning correctly. The effects of velocity slip and temperature slip in supersonic expansions of binary gas mixtures are briefly examined in §3.5 for supersonic beams of helium seeded with various amounts of neon, argon, or krypton.

Time–of–flight methods are often greatly complicated by the convolution of the true distribution of particle flight times with the electronic response function of the beam detection system and the gate function associated with the beam modulation device [Young, 1973]. The effect of these convolutions is to broaden the time–of–flight signal and increase the most probable arrival time. A reliable method for deconvolving badly convoluted molecular beam time–of–flight waveforms using Fourier transform and Wiener filtering techniques is presented in §3.4. The devised deconvolution method places no restrictions on the functional form of any factors affecting the shape of the measured time–of–flight distribution, but rather uses an accurately determined speed distribution to estimate an overall response function for the system. The estimated response function may then be used to deconvolve any convoluted time–of–flight waveform measured under similar experimental conditions. The mathematical details of the method are discussed and examples of its application to the deconvolution of time–of–flight waveforms measured in unchopped pulsed supersonic beams of argon, krypton, $CHCl_3$ and CH_3Cl are presented.

Having characterized the apparatus and verified that it is operating correctly, attention is shifted to the investigation of weakly bound van der Waals cluster species which may be formed during the supersonic expansion process. In §3.6 cluster size distributions are measured for supersonic expansions of pure argon and for seeded helium expansions containing SO_2, N_2O and H_2O, NO and NO_2, and NH_3. In §3.7 appearance potentials of

the cluster ions $(CO_2)_n^+$, $(N_2O)_n^+$ $(2 \leq n \leq 4)$ and $(NH_3)_nH^+$ $(1 \leq n \leq 8)$, and the cluster ion fragments $(N_2O{\cdot}O)^+$ and $(N_2O{\cdot}NO)^+$ are determined by electron impact ionization of neutral clusters formed in the molecular beam. Results obtained for $(CO_2)_n^+$, $(N_2O)_2^+$ $(2 \leq n \leq 4)$, $(N_2O{\cdot}NO)^+$ and $(NH_3)_nH^+$ $(1 \leq n \leq 3)$ are in general agreement with previously reported appearance potentials for these species while the appearance potentials of $(N_2O{\cdot}O)^+$ and $(NH_3)_nH^+$ $(4 \leq n \leq 8)$ are measured for the first time. Binding energies deduced from appearance potential measurements for the $(CO_2)_n^+$ $(2 \leq n \leq 4)$ and $(N_2O)_2^+$ cluster ions are observed to be in accord with results obtained using ion–molecule equilibrium methods. Proton solvation energies and the proton affinity of ammonia derived using the appearance potentials of $(NH_3)_nH^+$ $(1 \leq n \leq 8)$ are found to be in considerable disagreement with values obtained using high pressure ion–molecule techniques, indicating that electron impact methods fail to measure the adiabatic threshold for the generation of protonated ammonia clusters from their neutral precursors. Possible mechanisms for the formation of the cluster fragment ions $(N_2O{\cdot}O)^+$ and $(N_2O{\cdot}NO)^+$ are discussed.

3.2 Beam intensity measurements

3.2.1 Introduction

A supersonic atomic or molecular beam source essentially consists of a nozzle assembly, a skimmer, and an expansion chamber held at sufficiently low pressure to ensure a supersonic expansion. The nozzle flow rate is determined by the properties of the gas, the reservoir conditions and the shape of the nozzle. The nozzle shape is of critical importance with regard to determining the angular variation of the beam flux and the number of intermolecular collisions occurring in the vicinity of the nozzle exit, thus having an affect on the axial flux and on condensation [Murphy and Miller, 1984]. The skimmer transmits only the central core of the expanding jet, and its shape represents a compromise between minimizing deleterious shock structure effects upstream while maximizing the conductance downstream [John, 1969]. The jet density at the skimmer orifice influences whether thermalizing collisions between beam particles and the walls of the skimmer will dominate the resultant beam properties.

Ideally, the flux of a supersonic beam and its degree on monoenergeticity are determined only by the reservoir conditions and the design of the nozzle. In practice, however, interactions of beam molecules with mechanical components and background gas particles usually lead to significant departures from ideal behaviour. For example, the intensity of a supersonic beam should increase in a linear manner with increasing reservoir pressure. Experimentally, the range of linear behaviour is found to depend upon the nozzle to skimmer separation and is also limited by the speed and capacity of the pumping system fitted to the expansion chamber.

In this section, the intensities of supersonic beams of pure argon are measured as a function of the reservoir pressure P_0 and the nozzle to skimmer separation z_{ns} to determine an approximate set of optimum operating conditions for the apparatus. The intensity of a supersonic beam may vary by more than an order of magnitude over a moderate range of nozzle to skimmer separations. It is therefore necessary to determine the optimum nozzle to skimmer separation in order to maximize the beam flux through the skimmer and thus improve the signal–to–noise ratio for a particular experiment. Maximizing the beam flux in this manner is particularly important for cluster experiments in which the cluster population may represent only a small fraction of the total beam pressure, or in hexapole transmission measurements where the species under investigation may be seeded

in trace amounts into a light carrier gas and suffer considerable depreciation through the hexapole assembly due to many of the molecules being in unfocussed rotational states.

It is important to emphasize that the overall intensity of a supersonic beam is not only dependent on the reservoir pressure and the nozzle to skimmer separation. The intensity also depends on the properties of the gas or gas mixture under study and upon many other factors peculiar to the geometry of the apparatus and the conditions employed for a particular experiment. The results and discussion presented in this section are by no means definitive, but merely serve to illustrate the optimization procedure and to define the phenomena responsible for the observed trends in beam intensity.

3.2.2 Experimental arrangement

The experimental arrangement used to investigate the variation of beam intensity as a function of stagnation pressure and nozzle to skimmer separation is illustrated schematically in Figure 3.1. The gas under study was expanded into the first of two differentially pumped vacuum chambers through a modified Honda Civic fuel–injection valve fitted with a cylindrical 70 μm nozzle. The central core of the pulsed supersonic expansion was sampled by a 1 mm diameter skimmer (Beam Dynamics) and allowed to pass through the second differentially pumped chamber before entering the ion source of the quadrupole mass filter (Vacuum Generators, SXP300). The pulsed valve was mounted on a moveable carriage assembly to facilitate the positioning of the nozzle relative to the skimmer. Movement of the carriage assembly was achieved using a calibrated linear motion vacuum feedthrough (Huntington Mechanical Incorporated, model VF–156). Using the motion drive mechanism it was possible to manually vary the nozzle to skimmer separation from 2 mm to 70 mm with an accuracy of $\pm$ 0.1 mm. The output current from the mass filter channeltron electron multiplier was converted into a voltage waveform and amplified using the preamplifier supplied as part of the mass filter controller unit. Amplified waveforms were monitored on a 20 MHz oscilloscope and averaged using a boxcar integrator. The relative position of the boxcar sampling window was fixed over the arrival time distribution of the pulsed supersonic beam and its length carefully adjusted to window the entire waveform. The output voltage from the boxcar was stabilized by the application of a suitably long time constant and monitored on a small digital volt meter. The observed voltage was recorded and taken as an average measure of the relative beam intensity. The frequency and duration of beam pulses were controlled by the custom built beam source driver unit, which also served to provide the necessary triggering for the boxcar and the oscilloscope. During normal operation of the pulsed nozzle, background pressures on the order of 10^{-5} Torr and 10^{-8} Torr were maintained in the expansion chamber and the mass spectrometer chamber, respectively.

3.2.3 Results and discussion

Supersonic beam intensities were measured as a function of source pressure and nozzle to skimmer separation for beams of pure argon using the experimental arrangement described above. The source pressure was varied from 300 Torr to 3000 Torr in 300 Torr steps and intensities were measured at 25 equally spaced nozzle to skimmer separations between 68 and 500 nozzle diameters for each pressure. Measurements were repeated several times at each nozzle to skimmer separation in order to obtain an average intensity value with an acceptable standard error. All data were recorded for a source temperature of 300 K. The pulsed nozzle was operated at 10 Hz, with an estimated open time of not more than 2 ms.

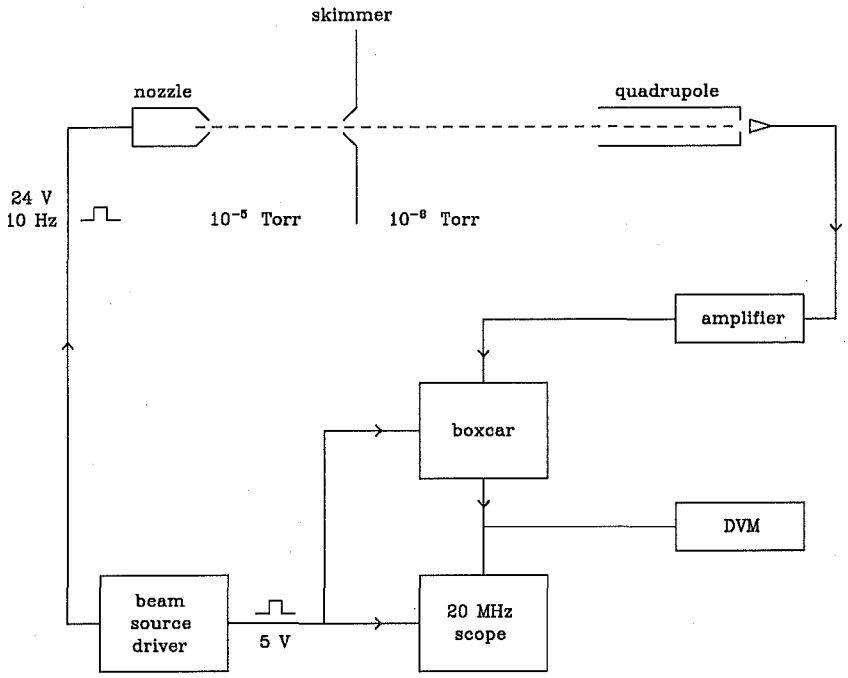

Figure 3.1: Experimental arrangement employed for the collection of beam intensity data.

An electron energy of 70 eV was used to ionize the neutral argon beams.

Beam intensities measured at each pressure are plotted as a function of nozzle to skimmer separation in Figures 3.2 and 3.3. The nozzle to skimmer separation is expressed in nozzle diameters z_{ns}/d_0, where d_0 is the diameter of the nozzle and z_{ns} is the distance between the nozzle exit and the skimmer. For all of the source pressures considered, the beam intensity was observed to rise rapidly with increasing nozzle to skimmer separation before passing through a local maximum between approximately 200 and 300 nozzle diameters. Beyond this maximum the intensity curves gradually declined with increasing separation. These trends for the variation of beam intensity with nozzle to skimmer separation are well known [Anderson *et al*, 1966] and may be attributed to a combination of skimmer interference effects and the scattering of beam particles by background gas in the expansion chamber.

There may be appreciable attenuation of the beam intensity due to collisions between atoms or molecules in the expanding jet and background gas particles in the expansion

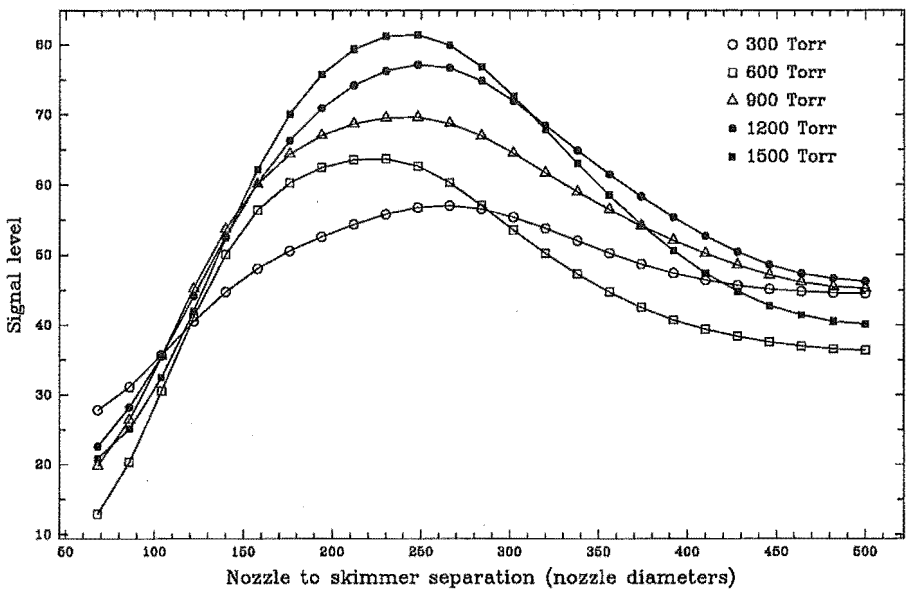

Figure 3.2: Beam intensity as a function of nozzle–skimmer distance for argon at several source pressures.

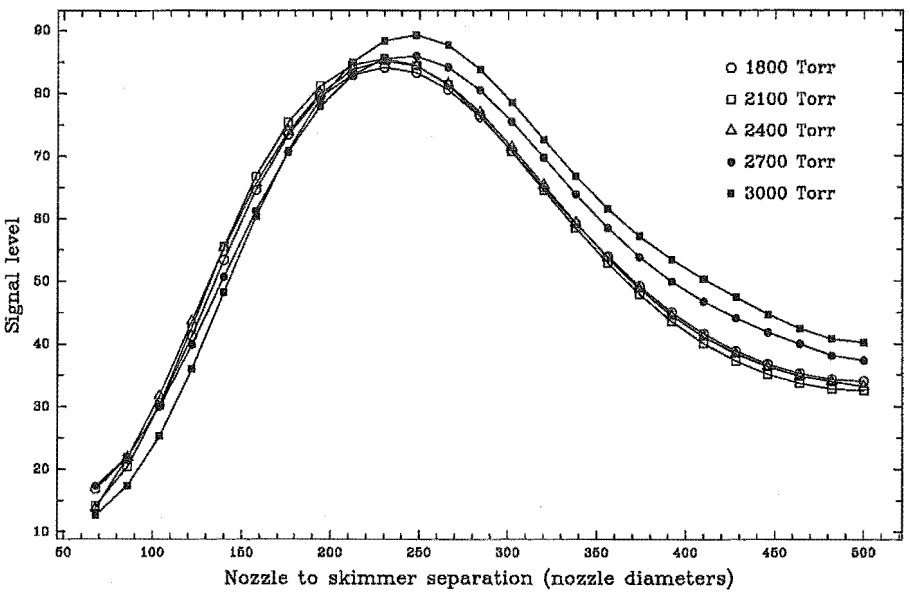

Figure 3.3: Beam intensity as a function of nozzle–skimmer distance for argon at several source pressures.

chamber. The effect of background gas pressure in the expansion chamber is to either decelerate the jet particles in strong shock waves which form at high jet densities, or to simply scatter them at low jet densities. At high jet densities, a barrel shock wave is formed around the edges of the expanding jet. The barrel shock wave extends outwards from the nozzle and merges with a second shock wave referred to as the Mach disc, which lies perpendicular to the direction of the supersonic flow. These features of the supersonic expansion are illustrated in Figure 3.4. While the location of the Mach disc is observed to be relatively independent of the reservoir to background pressure ratio, both the Mach disc and the barrel shock wave become progressively thicker and more diffuse with increasing total pressure. As stated in §1.2, the effect of the barrel shock wave is to produce a region of high density around the expanding jet that is difficult to penetrate by thermalized background gas particles. Unless this shock wave becomes attached to the skimmer, however, it will combine with the Mach disc to thermalize and scatter atoms or molecules in the expanding jet, resulting in a severely degraded supersonic beam. The position of the skimmer within the supersonic flow field is therefore of considerable importance. In order to ensure attachment of the barrel shock wave, the skimmer must be positioned upstream of the Mach disc in the zone of silence [Campargue, 1984].

At large nozzle to skimmer separations, the variation of beam intensity with increasing separation may begin to take the form of the classical scattering equation [Levine and Bernstein, 1974]:

$$I = I_0 \mathrm{e}^{-n\sigma_{eff} z_{ns}}, \tag{3.1}$$

where n is the number density of the background gas particles in the expansion chamber, σ_{eff} is the effective scattering cross section, z_{ns} is the length of the scattering region, and I and I_0 are the observed and ideal beam intensities, respectively. The magnitude of σ_{eff} depends upon the interaction potential and the relative velocity of the colliding particles, and may also be influenced to some extent by the geometry of the apparatus.[1]

In addition to scattering collisions with background gas particles in the expansion chamber, the expanding jet may suffer considerable attenuation due to a variety of skimmer interference effects. While supersonic expansions are capable of producing high intensity beams with high mean flow velocities and a narrow velocity spread, such capabilities will not be fully realized unless the skimmer meets a number of rather exacting requirements [Bird, 1976b]. Apart from an orifice with as sharp an edge as possible, the ideal skimmer should have an exterior angle that is as small as possible in order to reduce the flux of particles impinging on its surface and to minimize the density of reflected molecules immediately upstream of the skimmer entrance. In contrast to the requirement of a small exterior angle, the interior angle of the skimmer should be sufficiently large in order to minimize scattering losses inside the skimmer. The basic requirements for the internal and external angles of an ideal skimmer are therefore in conflict with one another, and practical skimmer designs must consequently involve a compromise between these two angular requirements [Gentry and Giese, 1975].

Skimmer interference can lead to significant losses in beam intensity, and manifests itself in the scattering of jet particles either in front of the skimmer inlet or within it, depending upon the density of the expanding jet. Ideally, the gas passing through the skimmer orifice will represent an undisturbed sample of the supersonic flow field at the location of the skimmer entrance. This situation is referred to as ideal skimming and will only be achieved when the flow at the skimmer entrance is essentially collision–free in

[1]The effective scattering cross section depends in part on the angular deflection required to remove a particle from the beam and hence will be somewhat design specific.

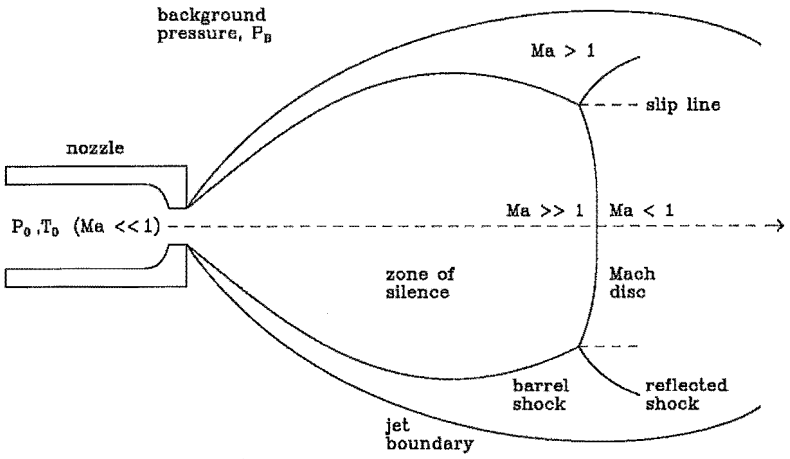

Figure 3.4: Features of the supersonic expansion. The Mach number Ma is defined as the ratio of the flow velocity u to the local speed of sound.

nature. This requirement may be expressed in the following form:

$$K_n = \frac{\lambda}{d_s} \gg 1, \tag{3.2}$$

where K_n is the Knudsen number, d_s is the diameter of the skimmer orifice, and λ is the mean free path of the atoms or molecules in the supersonic expansion at the skimmer entrance. When the Knudsen number is much greater than unity, the flow at the skimmer may be regarded as almost collision free. As K_n decreases towards unity, however, collisions between undisturbed jet particles and atoms or molecules reflected from the external walls of the skimmer may cause significant departures from ideal flow. For low jet densities, K_n will be large enough to ensure that jet particles will pass through the skimmer orifice without significant interaction with reflected atoms or molecules. Under such conditions, atoms or molecules hitting the external surface of the skimmer may be reflected back into the expanding jet, but their density will be so low that collisions with approaching jet species will be quite negligible. As jet density is increased, the density of reflected atoms or molecules will increase and cause the scattering of jet particles in front of the skimmer entrance. With a further increase in jet density, the reflected and scattered particles will both begin to contribute to the density of the scattering region in front of the skimmer. This scattering region appears to have some of the characteristics of a diffuse shock wave [Anderson *et al*, 1966], and may cause considerable degradation of the supersonic beam. For still higher jet densities such that $K_n \ll 1$, the jet flux at the skimmer may be so high that reflected atoms or molecules are driven downstream by the approaching jet. Under these conditions, the diffuse shock structure will no longer be present in front of the skimmer, but disturbance of the supersonic flow within the skimmer may now occur due to the formation of an oblique shock wave extending inward from

the skimmer tip to the beam axis [Bird, 1976b]. In extreme cases this can result in the skimmer acting as a virtual effusive source.

Unfortunately, there is little that can be done to avoid skimmer interference. Increasing the nozzle to skimmer separation reduces the density of the jet in the vicinity of the skimmer but subjects it to the possibility of increased attenuation due to scattering collisions with background gas particles in the expansion chamber. At extremely short nozzle to skimmer separations ($z_{ns}/d_0 \leq 1$), the skimmer will begin to act as a virtual source, transmitting virtually all of the gas issuing from the nozzle into the detection chamber whereupon it will undergo expansion. Although this may result in a sharp increase in the beam signal, the resultant unskimmed free jet will be poorly defined and partially thermalized due to destruction of the supersonic flow by shock waves formed in the supersonic expansion process that would normally attach to the skimmer. Species with large collision cross sections are more likely to be disturbed by the tip of the skimmer and are therefore more susceptible to skimmer interference. While skimmer interference may also be more significant for skimmers with a small orifice, larger orifices may result in a less well defined supersonic beam.

The effects of skimmer interference and background scattering on beam intensity may be summarized as follows. At small nozzle to skimmer separations skimmer interference is generally the predominant factor. The rapid drops in beam intensity often observed at such separations for high jet densities may be attributed to the formation of a shock–like structure at the skimmer inlet which may scatter and thermalize particles in the expanding jet. The density of this shock structure is proportional to the particle density at the skimmer and therefore becomes progressively more diffuse with increasing nozzle to skimmer separation. Consequently, the intensity of the supersonic beam is observed to rise to a maximum value at some intermediate separation before decreasing again due to increased attenuation from scattering collisions with background gas particles. For all of the source pressures considered here, the optimum nozzle to skimmer separation was observed to lie between approximately 200 and 300 nozzle diameters.

The effects of source pressure on the intensity of the supersonic beam are more clearly illustrated in Figure 3.5, which shows measured intensities as a function of source pressure at several nozzle to skimmer separations. Ideally the beam intensity should increase in a linear fashion with increasing source pressure. In practice, however, this is rarely found to be the case. Instead, the range of linear behaviour, if any, is generally observed to be highly dependent upon the nozzle to skimmer separation and the speed of the pumping system associated with the expansion chamber. As can be seen from Figure 3.5, the range of linear behaviour is greatest at large nozzle to skimmer separations. At small separations, shock waves may form in front of the skimmer even at very low source pressures. As the nozzle to skimmer separation is increased, the beam pressure required for this shock wave formation increases, and the range of linear intensity behaviour with source pressure increases accordingly. The speed of the pumping system fitted to the expansion chamber was not considered to be a limiting factor for any of the measurements presented here.

Although similar trends to those illustrated in Figures 3.2, 3.3, and 3.5 may be expected for gases other than argon, it is important to note that the nozzle flow rate is inversely proportional to mass. A lighter gas will have a higher flow rate through the pulsed nozzle and hence may be expected to produce a more intense supersonic beam. Depending upon the efficiency of the pumping system associated with the expansion chamber, however, the background particle density in the expansion chamber may be higher, and the atoms or molecules in the expanding jet may therefore be subjected to a greater number of collisions with background gas particles, thereby lowering the intensity of the resultant su-

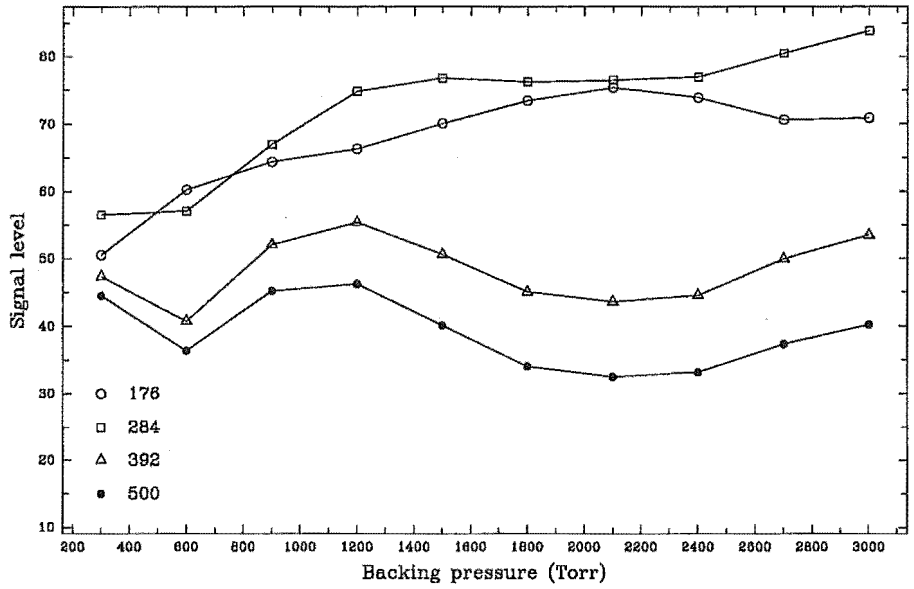

Figure 3.5: Beam intensity as a function of source pressure for argon at several nozzle–skimmer distances.

personic beam and increasing its velocity spread.[2] Different ionization cross sections may also complicate the comparison of beam intensities measured for several species under identical experimental conditions using an electron impact ionization mass filter. Despite these points, it represents little difficulty to determine the optimum nozzle to skimmer separation for a particular gas at any set of source conditions using the method described in this section. Such measurements may be readily performed in a routine manner at the start of any molecular beam experiment in order to optimize the beam flux through the skimmer and thus maximize the signal–to–noise ratio for the experiment.

3.2.4 Conclusion

The intensities of supersonic beams of pure argon were measured as a function of source pressure and nozzle to skimmer separation in order to deduce a set of optimum operating conditions for the molecular beam apparatus. The beam intensity was observed to be strongly dependent upon the nozzle to skimmer separation, with the observed trends being attributed to a combination of skimmer interference effects and the scattering of jet particles by background gas in the expansion chamber. For all of the source pressures considered, the optimum nozzle to skimmer separation was found to lie between 200 and 300 nozzle diameters. Similar behaviour may be expected for gases other than argon, although further work would be required to confirm this prediction. There is little that can be done to reduce skimmer interference, but rather its effects must be minimized by way of experiment. While the results presented in this section are by no means definitive, it is a straightforward matter to determine an optimum nozzle to skimmer separation for any

[2]Light jet particles are more likely to have their momentum changed and be scattered off the jet axis through collisions with background gas particles.

gas under any set of source conditions using the methods described. The necessary measurements may be routinely performed at the start of any investigation to maximize the beam flux through the skimmer and thus optimize the signal–to–noise ratio for the experiment. Such measurements were performed at the beginning of all subsequent experimental investigations presented in this chapter.

3.3 Measurement of beam speed distributions

3.3.1 Introduction

In 1951, Kantrowitz and Grey proposed that the flow field of the conventional effusive beam source be replaced by a supersonic jet. It was predicted that supersonic jets would yield atomic and molecular beams with intensities several orders of magnitude greater than those attainable from an effusive source. This prediction was verified in 1954 by Becker and Bier who conclusively demonstrated the effectiveness of supersonic nozzle jets as molecular beam sources. Such sources may be used to generate intense, almost monoenergetic atomic and molecular beams. Since the pioneering work of Kantrowitz and Grey, supersonic beam sources have found a large number of important applications in chemical physics research [Scoles, 1988]. During the supersonic expansion process leading to the formation of a supersonic nozzle beam, a great deal of translational and internal relaxation occurs as the energy associated with these degrees of freedom is converted into directed axial motion. Researches have exploited this relaxation to study the formation and structure of weakly bound van der Waals clusters [Scoles, 1988] and to spectroscopically study a wide range of complex molecules with high resolution [Hayes, 1987].

The feasibility of pulsing the flow of a supersonic expansion in order to reduce pumping requirements was demonstrated by Hagena in the mid 1960's [Hagena, 1964] and during the past decade the use of pulsed supersonic expansions has become widespread in atomic and molecular beam studies [Scoles, 1988]. The large instantaneous fluxes characteristic of pulsed expansions makes them ideally suited to pulsed laser experiments having inherently low duty cycles, while the pulsed temporal nature of these expansions allows higher stagnation pressures and greater nozzle diameters to be employed with only modest pumping systems.

In this section, supersonic beam speed distributions are investigated for the monatomic species He, Ne, Ar and Kr, and for the homonuclear diatomic species H_2 and N_2 using a synchronous time–of–flight technique [Young, 1973]. The measured speed distributions are characterized in terms of a mean flow velocity u and a translational temperature $T_{||}$ parallel to the beam axis. Values of u and $T_{||}$ deduced for the monatomic species are compared with the experimental and theoretical results of other workers in order to verify that the supersonic beam apparatus is operating correctly. The values of u and $T_{||}$ obtained for H_2 and N_2 are employed in §4.2 and §4.3 for the determination of rotational–translational coupling parameters and rotational relaxation times, respectively.

3.3.2 Mathematical considerations

Supersonic atomic and molecular beam speed distributions are generally determined using some form of time–of–flight analysis. The basis of the time–of–flight technique is well established. The beam is modulated by a narrow slit located on a rotating chopper disc and the modulated beam signal is monitored by a detector located at some fixed distance L from the disc. By measuring the time t required for a beam particle to travel from the

chopper disc to the detector, and repeating this measurement over a suitably wide range of flight times, it is possible to determine the distribution of flight times $g(t)$ and thus the distribution of atomic or molecular speeds $f(v)$, where

$$v = \frac{L}{t}. \tag{3.3}$$

In practice, however, the situation is not nearly so simple, since the true distribution of flight times will invariably be convolved with the electronic response function of the detection system and the gate function describing the shape of the chopper slit [Young, 1973]. The effect of these convolutions is to broaden the time–of–flight signal and increase the most probable arrival time [Cameron and Harland, 1993b]. In order to extract reliable information from measured time–of–flight waveforms it is therefore necessary to eliminate these potential sources of distortion from the experiment or to correctly take them into account when analyzing results. Unfortunately, it is generally not practical or even possible to completely eliminate such factors from time–of–flight measurements. The idealized model of an impulsive gate function may be approached but never fully realized. Similarly, it is not possible to construct a detector or an electronic circuit having a zero response time. Consequently, any time–of–flight measurement must involve some degree of compromise between resolution and performance.

The speed distribution function $f(v)$ of a supersonic atomic or molecular beam is generally considered to be well described by the distribution function

$$f(v)\mathrm{d}v = Av^2\mathrm{e}^{-m(v-u)^2/2k_bT_{\|}}\mathrm{d}v. \tag{3.4}$$

The distribution is characterized by the two parameters u and $T_{\|}$, which represent the flow velocity and parallel translational temperature of the beam, respectively. The symbols m and k_b in equation (3.4) have their usual meanings, and A is simply a normalization constant defined such that

$$\int_{\infty}^{\infty} f(v)\mathrm{d}v = 1. \tag{3.5}$$

It is important to note that the speed distribution function described by equation (3.4) represents a purely semi-empirical expression having little theoretical basis. It is a simple expression which is easy to apply. In the absence of a better model, the principle reason for its continued use is that it generally describes experimental data with sufficiently high accuracy to afford considerable confidence in the reliability of the determined values of u and $T_{\|}$.

In order to apply equation (3.4) to the analysis of measured time–of–flight waveforms it is necessary to transform the measured time domain signal into a distribution of speeds. From equation (3.3), it follows that the Jacobian for the transformation from velocity space to the time domain is given by the expression

$$\mathrm{d}v = -\frac{L}{t^2}\mathrm{d}t, \tag{3.6}$$

and the distribution of flight times is therefore

$$g(t)\mathrm{d}t = -\frac{L}{t^2}f\left(\frac{L}{t}\right)\mathrm{d}t. \tag{3.7}$$

The minus sign in this expression and the normalization constant A in equation (3.4) are generally ignored when analyzing time–of–flight data since only proportionality need be considered. Once the parameters u and $T_{\|}$ have been determined by fitting the experimental data to equation (3.4), the distribution of beam speeds has been characterized.

3.3.3 Experimental arrangement

The experimental arrangement used to collect chopped pulsed nozzle time–of–flight waveforms is illustrated schematically in Figures 3.6 and 3.7. A modified Honda Civic fuel–injection valve fitted with a cylindrical 70 μm diameter nozzle was employed for these measurements. The central core of the pulsed supersonic expansion was sampled by a 1 mm diameter skimmer (Beam Dynamics) positioned approximately 300 nozzle diameters (21 mm) downstream from the nozzle exit and allowed to pass into a differentially pumped flight tube housing the beam chopper assembly and terminated with a quadrupole mass filter (Vacuum Generators SXP300). The skimmed supersonic beam was chopped at high frequency ($\sim$ 800 Hz) by a 70 mm diameter chopper wheel. The chopper wheel, with two diametrically opposed slits of width 2 mm, was rotated by a water cooled 400 Hz synchronous motor (TRW Electronic Components, Globe Motors) fitted with high quality vacuum rated precision bearings. A photodiode residing diametrically opposed to the beam axis was used to monitor the rotation of the chopper wheel. The photodiode emitted a pulse train having twice the rotational frequency of the chopper wheel. The frequency of the pulse train was reduced using a custom built pulse rejection unit to yield a resultant frequency that was sufficiently low ($\sim$ 10 Hz) to trigger the pulsed nozzle via the beam source driver. The chopped gas pulse was allowed to evolve in time over a fixed flight path of length 0.89 m before entering the ion source of the quadrupole mass filter assembly. The output current of the mass filter channeltron electron multiplier generated by the ion beam was converted into a voltage waveform using an external load resistor and amplified using a suitably fast ($\sim$ 1 μs) custom built circuit. Amplified waveforms were monitored on a 20 MHz oscilloscope and sampled using a transient digitizer capable of averaging repetitive waveforms (LeCroy 8837F). The resultant averaged data were stored on the hard disk of a personal computer. The open time of the pulsed nozzle was controlled by the beam source driver unit, which also served to provide the necessary trigger pulses for the transient digitizer and the oscilloscope. During normal operation of the pulsed nozzle, background pressures of approximately 10^{-5} Torr and 10^{-8} Torr were maintained in the expansion chamber and the flight tube, respectively.

3.3.4 Results and discussion

It is important to emphasize that what is being measured in a time–of–flight experiment is in fact a distribution of atomic or molecular speeds $f(v)$ as opposed to a distribution of velocities $f(\mathbf{v})$. This point is rarely mentioned in papers on the subject and can lead to considerable confusion. The speed and velocity of an object are simply related by the expression

$$v = |\mathbf{v}| = \left(v_x^2 + v_y^2 + v_z^2\right)^{1/2}, \tag{3.8}$$

where v_x, v_y, and v_z represent the individual components of velocity in the x, y, and z direction respectively.[3] Velocity is a vector quantity and as such has associated with it a direction and a magnitude. It is the magnitude of the velocity vector which is determined in a time–of–flight experiment. Individual components of the velocity vector cannot be determined for individual atoms or molecules using the time–of–flight technique.

It should also be mentioned that velocity components perpendicular to the beam axis may be assumed to contribute little to the overall speed of the atoms or molecules in a

[3]Throughout this thesis the molecular beam is assumed to propagate parallel to the z–axis in the Cartesian coordinate system.

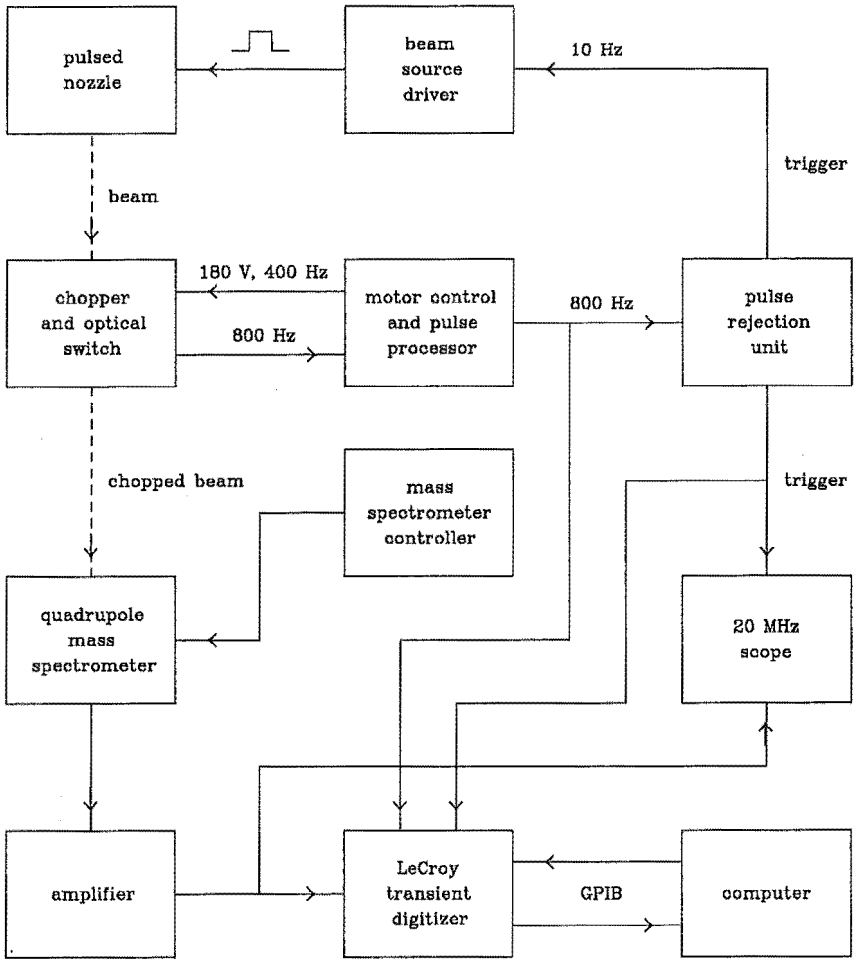

Figure 3.6: Experimental arrangement employed for the collection of chopped pulsed nozzle time–of–flight waveforms.

supersonic beam. While the translational temperature $T_{||}$ associated with kinetic motion parallel to the beam axis is observed to freeze and remain essentially constant beyond a certain distance from the nozzle exit [Beijerinck and Verster, 1981; Cameron and Harland, 1991], the translational temperature $T_{\perp}$ associated with the components of velocity perpendicular to the beam axis continues to decrease at a rate roughly proportional to $z^{-4/3}$, where z is the distance from the nozzle exit [Hamel and Willis, 1966]. Depending upon the source conditions and the composition of the beam, the perpendicular translational temperature will generally be two or three orders of magnitude lower than the parallel translational temperature at the location of the beam detector, and the translational energy component of the supersonic beam perpendicular to the beam axis will therefore be quite negligible compared to the parallel component.

Chopped pulsed nozzle time–of–flight waveforms were recorded for He, Ne, Ar, Kr, H_2, and N_2 using the experimental arrangement described in the previous section. A stagna-

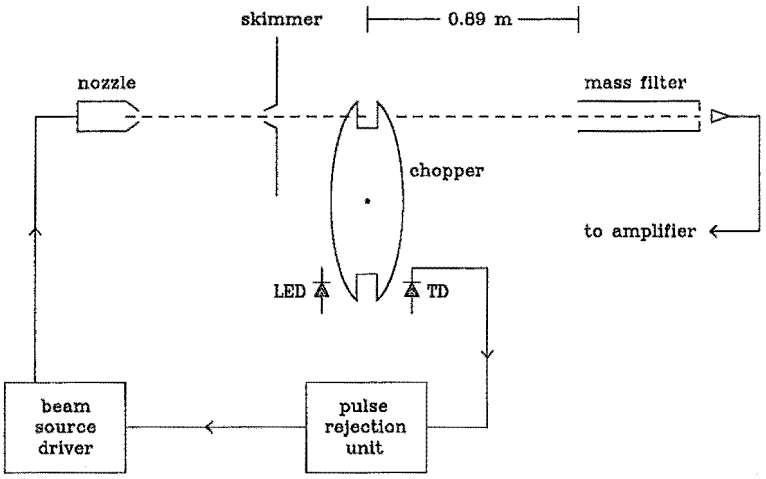

Figure 3.7: Schematic illustration of the synchronous pulsed nozzle time–of–flight technique.

tion pressure of 4 atm was employed for the measurement of H_2 time–of–flight waveforms. All other data were recorded for a source pressure of 1 atm at a temperature of 300 K. The chopper motor was operated at 400 Hz, resulting in a chopper open time of approximately 25 μs at the radius of beam transmission. The pulsed nozzle was operated at a frequency of 10 Hz, with an estimated open time of not more than 2 ms. The output of the LeCroy transient digitizer used to collect the chopped time–of–flight waveforms was 4096 regularly spaced points. The time base of the digitizer was set to 20 ms for all measurements, corresponding to a sampling frequency of approximately 200 kHz. Waveform averaging was performed to improve the signal–to–noise ratio of the recorded data, with 256 averages being more than sufficient in all cases. The pulse train emitted by the photodiode employed to monitor the rotation of the chopper wheel was simultaneously recorded on a separate channel of the transient digitizer and used to establish the time at which the supersonic beam was transmitted by the chopper. This situation is illustrated in Figure 3.8, which shows a typical time–of–flight waveform recorded for argon and the corresponding pulse train emitted by the photodiode. It should be noted that the photodiode pulses have been shaped and lengthened by the pulse rejection unit. The pulse rejection unit did not alter the position or rise-time of the leading edge of the photodiode pulses, however.

Deconvolution of the measured chopped time–of–flight waveforms to remove the effects of the chopper gate function and the response function of the detection electronics was considered to be unnecessary. Due to the high frequency response of the small signal amplifier (1 MHz) and the transient digitizer (> 20 MHz) employed for these measurements, it is most unlikely that the recorded signals were distorted in any way by the signal amplification and data collection circuitry. A more probable source of distortion was represented by the gate function describing the time dependent transmission of the chopper slit. Young has suggested that the effect of the gate function is negligible if the ratio of the chopper

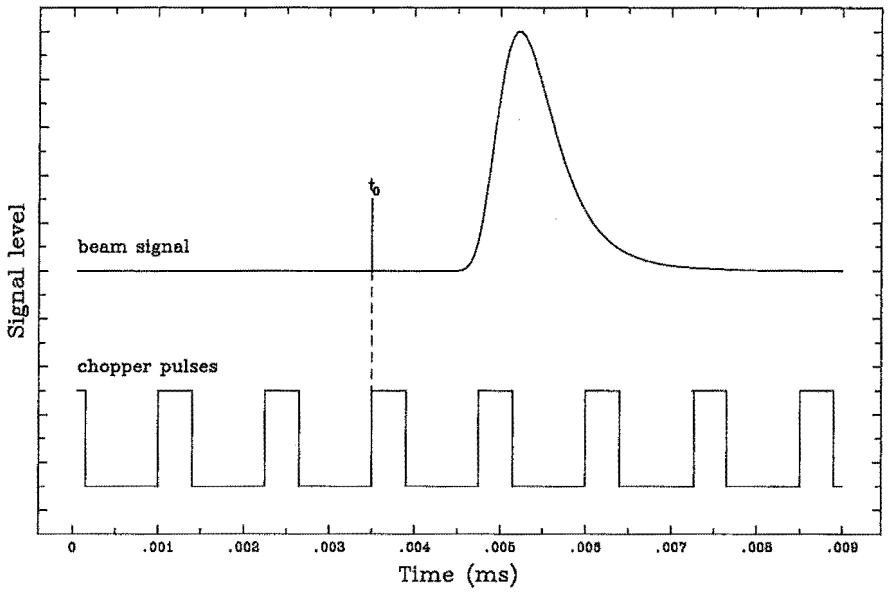

Figure 3.8: Typical time–of–flight and chopper pulse signals recorded by the transient digitizer. The photodiode pulses have been shaped and lengthened by the pulse rejection unit. The leading edge position and rise-time of the pulses was not affected, however.

open time to the most probable arrival time is less than 0.01 [Young, 1973]. Although this condition was not met for any of the systems examined, there were no obvious signs of distortion on the recorded time–of–flight waveforms arising from the gate function. It is interesting to note that the results obtained by Young indicate that the effect of the gate function on the shape of time–of–flight signals is generally less significant than the effect of an electronic response function having the same characteristic time. The reasons for this observation, however, were not explained. The gate function is symmetrical and often approximated by a sinusoidal or a trapezoidal function, while the response function of an electronic circuit with linear RC response is usually well described by an exponential decay curve. The mean and variance of a function $g(t)$ formed by the convolution of n functions $f_1(t), \ldots, f_n(t)$ are identical to the sums of the individual means and variances of the n functions, respectively [Bracewell, 1986]. Since the variance of an exponential function will in general be greater than that of a sinusoidal or trapezoidal gate function with the same mean, the electronic response function will have a more pronounced affect on the width of the time–of–flight signal.

Owing to the great acceleration of beam particles following electron impact ionization, the length of the molecular beam flight path is generally taken to be the distance from the chopper disc to the ionization region of the mass filter assembly, and the flight time of the ionized supersonic beam through the filter is assumed to be negligible. When the length of the molecular beam flight path is short (< 1 m), however, the time taken for the ionized particles to traverse the mass filter and reach the detector may become significant and should be taken into account. By pulsing the DC potential applied to the mass filter ion focussing plate using a suitably fast switching circuit, it was possible to accurately

Ion	H_2^+	He^+	Ne^+	N_2^+	Ar^+	Kr^+
Correction (μs)	5.0	7.0	15.7	18.3	22.1	31.9

Table 3.1: Mean flight times of ions through the mass filter assembly at an ion energy of 15 eV.

measure distributions of ion flight times for all of the species investigated here and thus apply suitable corrections to the time scales of the recorded time–of–flight waveforms.

In order to correctly account for the distribution of ion flight times through the mass filter assembly, it is necessary to deconvolve this distribution from the corresponding time–of–flight signal. The recorded distributions of ion flight times were all observed to be extremely narrow (2 μs to 10 μs full width at half maximum signal level) and were therefore considered most unlikely to have an appreciable effect on the width of the measured time–of–flight signals. Consequently, numerical deconvolution was again considered to be unnecessary. Instead, mean ion flight times were simply subtracted from the time scales of the recorded time–of–flight waveforms. Mean ion flight times were determined as a function of ion energy from 5 eV to 15 eV. Time–of–flight waveforms were generally measured using an ion energy of 15 eV, and the mean ion flight times determined at this energy are listed in Table 3.1. In situations where it is not possible to experimentally determine the average flight times of ions through the mass filter, a good approximation is given by the expression

$$\bar{t}_f = l_f \left(\frac{2E_i}{m} \right)^{-1/2}, \tag{3.9}$$

where l_f and E_i are the length of the mass filter and the ion energy, respectively. In order to calculate mean ion flight times to a higher degree of accuracy, it is necessary to consider the trajectories of the ions through the quadrupole assembly as described by Mathieu's equations [Dawson, 1976]. This is a non–trivial task, and from a practical point of view quite unnecessary.

Corrected time–of–flight waveforms were transformed from the time domain into velocity space and fitted to the speed distribution function described by equation (3.4). By noting that $v^{-2}f(v)$ is a Gaussian distribution function with mean u and standard deviation $(m/k_bT_{||})^{1/2}$, it is a straightforward matter to directly determine u from a plot of $v^{-2}f(v)$ versus v and to calculate $T_{||}$ from a plot of $\ln|v^{-2}f(v)|$ versus $(v-u)^2$ using a simple linear least squares algorithm. Values of u and $T_{||}$ determined in this manner for the monatomic species He, Ne, Ar and Kr, and for the homonuclear diatomic species H_2 and N_2 are presented in Tables 3.2 and 3.3, respectively. The quality of the obtained fits was generally observed to be excellent, resulting in linear least squares correlation coefficients for the determination of $T_{||}$ of better than 0.96 in all cases. The fitted values of u and $T_{||}$ were found to be reproducible to within $\pm$ 3% and $\pm$ 5%, respectively. The high degree of correlation between the experimental and fitted curves is clearly illustrated in Figures 3.9 and 3.10 which show typical experimental time–of–flight waveforms for H_2 and N_2, and the curves fitted to them using equation (3.4).

Values of u and $T_{||}$ determined for H_2 and N_2 under identical conditions to those employed here could not be found in the literature, although the results obtained for N_2 are in reasonable agreement with the calculations of Randeniya and Smith [Randeniya and Smith, 1990] for an expansion from 800 Torr through a 0.03 cm diameter nozzle at 300 K. The values of u and $T_{||}$ listed in Table 3.2 for He, Ne, Ar, and Kr are all in excellent accord with the the theoretically predicted values of Cameron and Harland [Cameron and Harland, 1991] and the experimental results of Beijerinck and Verster [Beijerinck and

Gas	P_0 (atm)	T_0 (K)	u (m/s)	$T_\parallel$ (K)	u_∞ (m/s)
He	1	300	1740	5.5	1766
Ne	1	300	773	3.2	786
Ar	1	300	552	1.3	558
Kr	1	300	381	1.1	394

Table 3.2: Source conditions, fitted values of u and $T_\parallel$, and thermodynamic limiting flow velocities for He, Ne, Ar, and Kr.

Gas	P_0 (atm)	T_0 (K)	u (m/s)	$T_\parallel$ (K)	u_∞ (m/s)
H_2	4	300	2659	4.4	3010
N_2	1	300	753	13.1	804

Table 3.3: Source conditions, fitted values of u and $T_\parallel$, and thermodynamic limiting flow velocities for H_2 and N_2.

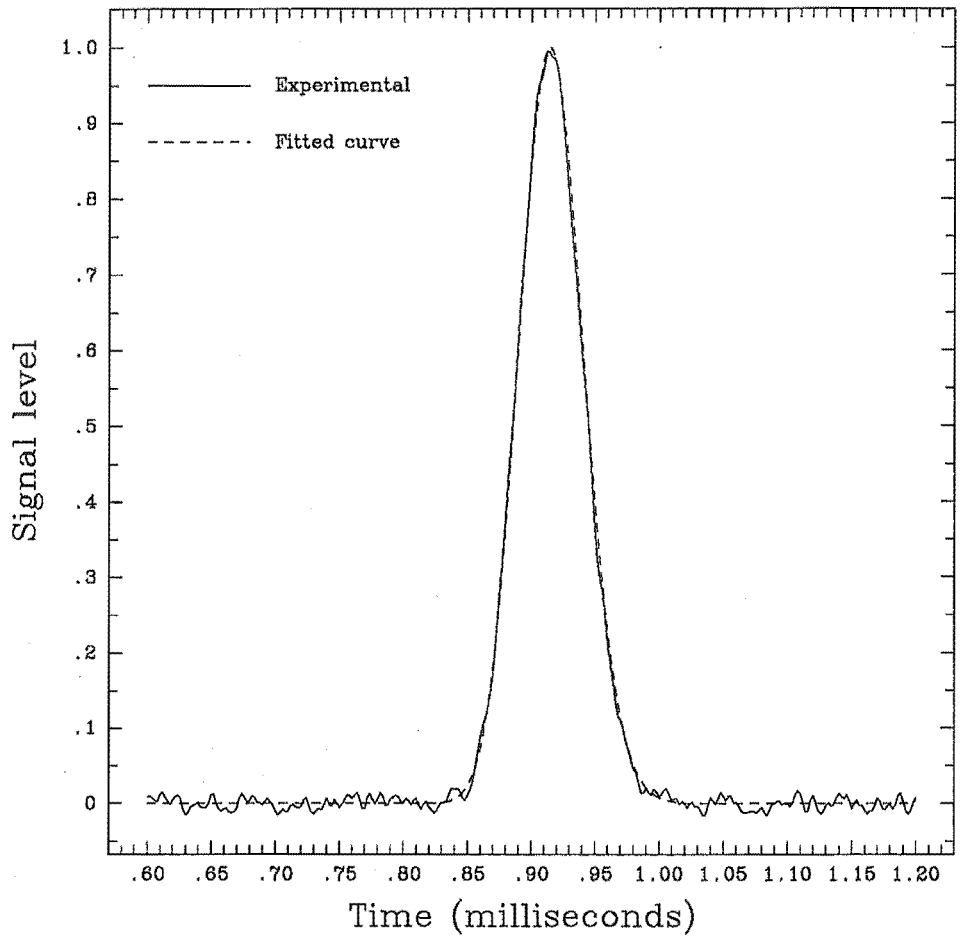

Figure 3.9: Experimental and fitted time–of–flight waveforms for N_2.

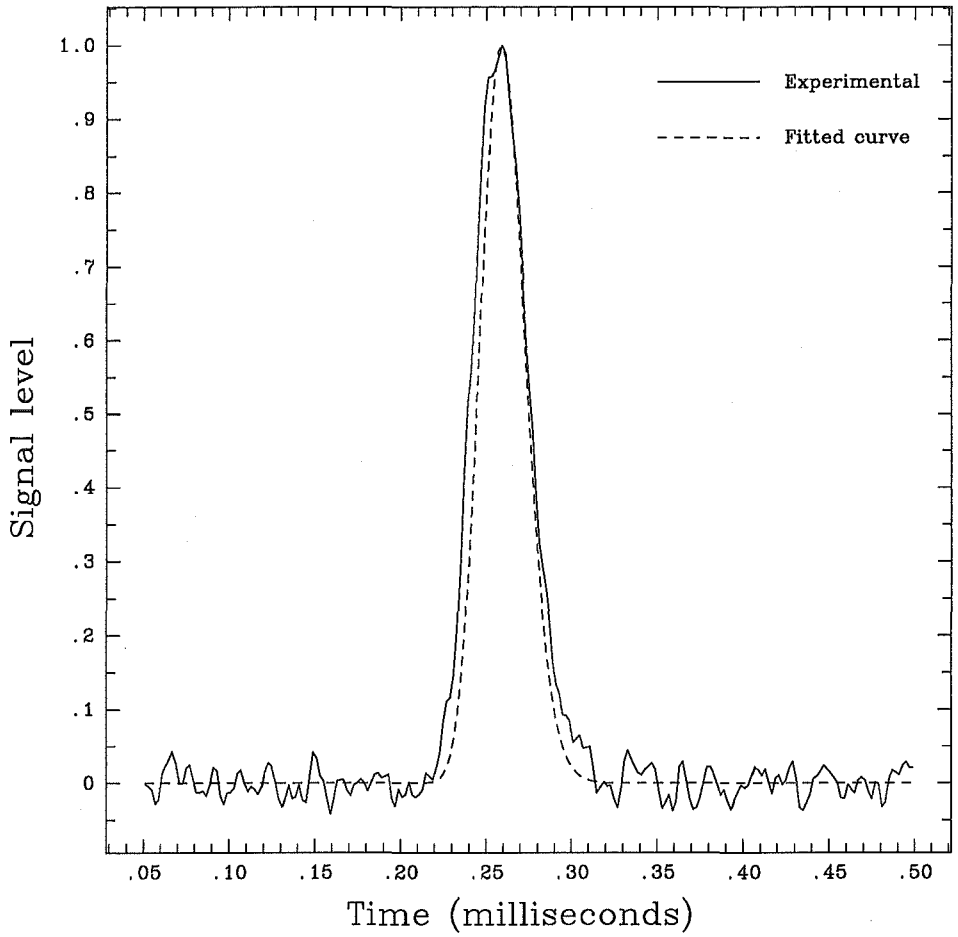

Figure 3.10: Experimental and fitted time–of–flight waveforms for H_2.

Verster, 1981]. In view of this good agreement, it is reasonable to assume that the values of u and $T_{||}$ determined for H_2 and N_2 are also reliable.

It is interesting to note that the terminal parallel translational temperatures measured for the monatomic species decrease with increasing mass. This is presumably due to the fact that translational relaxation, and thus the conversion of translational energy into directed kinetic energy, is more efficient for the more polarizable species of higher mass. For diatomic and polyatomic species, the situation is greatly complicated by the presence of internal degrees of freedom, each of which may have a distinct relaxation rate, and no simple trend in the variation of $T_{||}$ with mass may be observed [Cameron and Harland, 1993d]. Rotational and vibrational relaxation processes are usually much less efficient than translational relaxation. Consequently, the terminal rotational and vibrational temperatures of a supersonic molecular beam are generally higher than the terminal parallel translational temperature and will attain an essentially constant value considerably earlier in the expansion [Cameron and Harland, 1991]. Also listed in Tables

3.2 and 3.3 are thermodynamic limiting values u_∞ of the directed flow velocity calculated according to the equation

$$u_\infty = \left(\frac{\gamma}{\gamma - 1}\right)^{1/2} \left(\frac{2k_b T_0}{m}\right)^{1/2}, \tag{3.10}$$

where γ is the heat capacity ratio C_p/C_v and T_0 is the source temperature. The flow velocity can never attain its thermodynamic limiting value, since to do so would require the conversion of all the random thermal energy of the beam particles into the kinetic energy associated with the directed mass flow of the supersonic beam. Due to the freezing of the translational and internal temperatures during the expansion process, total conversion of all the thermal energy does not occur. As can be seen from Tables 3.2 and 3.3, the flow velocities measured for the monatomic species are only slightly less than their thermodynamic limiting value, while those measured for H_2 and N_2 are significantly lower due to the freezing of the vibrational and rotational modes.

3.3.5 Conclusion

Speed distributions have been measured for supersonic beams of He, Ne, Ar, Kr, H_2, and N_2 using time–of–flight methods. The measured distributions were characterized in terms of a mean flow velocity u and a translational temperature $T_{||}$ by fitting them to an assumed form of the speed distribution function. Values of u and $T_{||}$ determined for the monatomic species were observed to be in excellent accord with theoretical predictions and the experimental results of other workers, indicating that the molecular beam apparatus was operating correctly with regard to the production of well defined, narrow velocity distributions. Flow velocities determined for the monatomic species were observed to be close to their thermodynamic limiting value, while those obtained for H_2 and N_2 were considerably lower than the limiting value due to the presence of internal degrees of freedom. For the monatomic species, the degree of translational cooling was observed to be inversely proportional to mass, suggesting that translational relaxation of atoms becomes more efficient with increasing molecular weight.

3.4 Deconvolution of unchopped time–of–flight waveforms

3.4.1 Introduction

Time–of–flight techniques have been extensively used to determine speed distributions of atoms and molecules in molecular beam experiments for more than three decades. The importance and popularity of these methods is due not only to the simplicity and compactness of the experimental arrangements involved, but also to the wide range of experiments to which they are applicable. For example, time–of–flight techniques may be used for the characterization of molecular beam sources [Carman Jr., 1986], the investigation of inelastic scattering by energy loss methods [van den Bergh *et al*, 1973], or for the determination of reactant energy distributions in reactive scattering experiments [Schafer *et al*, 1970].

How accurately the measured time–of–flight signal actually represents the true distribution of atomic or molecular speeds in a molecular beam has often been questioned [Alcalay and Knuth, 1969; Young, 1973]. In a time–of–flight experiment, the molecular beam must be modulated in some manner and the measured time–of–flight signal will therefore depend upon the geometry and frequency of the modulating device according

to some modulator or *gate* function. Furthermore, since the beam signal is measured using an electronic circuit with a non–zero response time, the measured distribution of flight times may be distorted by the dynamic response of the electronic system. Due to these problems, it is often necessary to perform some kind of deconvolution on measured time–of–flight data in order to extract a more accurate representation of the true speed distribution. There are essentially three approaches which may be adopted to handle this problem. Apart from applying direct numerical deconvolution, it is possible to use moment methods, or to fit convolutions and transformations of empirical speed distribution functions to time–of–flight data.

Using Laplace transform methods, Alcalay and Knuth [Alcalay and Knuth, 1969] derived expressions for the moments of typical speed distributions and gate functions. By evaluating moments of the measured time–of–flight data and subtracting those of the gate function, moments of the true speed distribution can be found. In principle, any function can be characterized to any degree by considering a sufficient number of moments. In practice, however, noise in the data generally limits the number of usable moments to only a few. The process is also time consuming and makes possibly invalid assumptions regarding the exact form of the gate function.

A quite general method for deconvolving time–of–flight data is to approach the problem from the reverse direction by fitting a parameterized convolution to the experimental data [Kay *et al*, 1986]. This approach is somewhat artificial and the solution derived in terms of the various parameters used may not be unique. Such an approach is also time consuming from a computational point of view, as numerically fitting the measured or observed signal in this manner for some assumed set of parameters may require many iterations in order to minimize the sum of the squares of the deviations between the experimental and fitted distributions.

While it may be necessary to make some assumptions regarding the form of the speed distribution in a supersonic molecular beam, it is not at all necessary to make any such assumptions regarding the form of the gate function or the electronic response function. Also, apart from these functions there may be any number of other factors that distort the time–of–flight waveform which cannot be adequately described in terms of any empirically derived expression. All of these factors combine to give an overall system response function which must be deconvolved from the measured time–of–flight signal in order to obtain the true distribution of flight times. In our laboratory, the situation is made worse by the fact that for some experiments it is not possible to fit a chopper assembly into the molecular beam apparatus to modulate the beam in an acceptable manner. It is therefore necessary to estimate flow velocities and parallel translational temperatures from highly convoluted time–of–flight waveforms measured in unchopped pulsed supersonic expansions.

In this section, the use of Fourier transform and Wiener filtering techniques to reliably deconvolve measured time–of–flight waveforms is illustrated. It is shown how an accurately measured, or theoretical, time–of–flight distribution may be deconvolved from a badly convolved distribution to estimate an overall response function for the system. This response function may then be used to deconvolute any time–of–flight distribution measured under similar experimental conditions. The form of the system response function is briefly discussed and illustrative results obtained using the deconvolution procedure are presented for argon, krypton, $CHCl_3$ and CH_3Cl. The use of direct numerical deconvolution in this manner is made computationally efficient through the use of the fast Fourier transform algorithm [Cooley and Tukey, 1965], and problems associated with high frequency noise components in the experimental data are reduced by the application of a simple low-pass filtering function.

3.4.2 Mathematical considerations

The affect of most factors that contribute to the distortion of time–of–flight waveforms may be expressed in terms of the convolution integral

$$g(t) = \int_0^t h(t)f(t-\tau)\mathrm{d}\tau = \int_0^t h(t-\tau)f(t)\mathrm{d}\tau, \tag{3.11}$$

where $g(t)$ is the measured time–of–flight signal, $f(t)$ is the true time–of–flight waveform, and $h(t)$ is some function which describes the dynamic response of the experimental apparatus at time t. Given sufficient knowledge regarding the form of the response function, Fourier transform techniques may be used to solve equation (3.11) to obtain $f(t)$ through the application of the convolution theorem, which states that the transform of the convolution is equal to the product of the transforms.

Defining the forward Fourier transform of a function $f(t)$ to be $F(\omega)$ such that

$$F(\omega) = \int_{\infty}^{\infty} f(t)\mathrm{e}^{2\pi i\omega t}\mathrm{d}t, \tag{3.12}$$

and the inverse Fourier transform as[4]

$$f(t) = \int_{\infty}^{\infty} F(\omega)\mathrm{e}^{-2\pi i\omega t}\mathrm{d}\omega, \tag{3.13}$$

the convolution theorem gives that

$$G(\omega) = H(\omega)F(\omega). \tag{3.14}$$

The significance of the convolution theorem is that the process of convolution in the time domain is simplified to mere multiplication in the Fourier, or frequency, domain. Deconvolution of equation (3.11) to determine the true time–of–flight waveform therefore amounts to the calculation of $G(\omega)$ and $H(\omega)$ for a given $g(t)$ and $h(t)$, respectively, followed by the evaluation of $F(\omega)$ according to the equation

$$F(\omega) = \frac{G(\omega)}{H(\omega)}. \tag{3.15}$$

Equation (3.13) may then be used to obtain $f(t)$. Despite the formal simplicity of this approach, considerable difficulties may arise in practice due to noise in the measured signal or the presence of zeros in $H(\omega)$.

It is a common problem that deconvolution will frequently result in the amplification of noise. Noise in the measured signal will produce high frequency components in $G(\omega)$, causing $F(\omega)$ to diverge at high frequencies. Any such high frequency components may be removed from the measured signal through the application of low–pass filtering, in which $G(\omega)$ is multiplied by some filtering function $L(\omega)$ with cut-off frequency ω_c. All components beyond the cut-off value will be removed, while those below ω_c may or may not be attenuated, depending upon the functional form of $L(\omega)$. The simplest low–pass filter is the rectangle function,

$$\Pi(\omega) = \begin{cases} 1 & |\omega| \leq \omega_c \\ 0 & |\omega| > \omega_c \end{cases} \tag{3.16}$$

[4]It should be noted that some authors [Bracewell, 1986] define the forward transform with the minus sign, and the inverse transform without. This is of little consequence so long as consistency is maintained.

which leaves all components of the filtered function unaltered for $|\omega| \leq \omega_c$. The use of rectangular filters, however, can frequently lead to the manifestation of undesirable features such as *ringing* in the corresponding time domain signal, and should therefore be applied with some caution. In this investigation, experimentally measured time–of–flight signals were low–pass filtered, when necessary, using a filter consisting of a rectangle function multiplied by a single cosine lobe,

$$L(\omega) = \Pi(\omega) \cdot \cos\left(\frac{\pi\omega}{\omega_c}\right), \tag{3.17}$$

to provide a gradually increasing attenuation of $G(\omega)$ up to the chosen cut-off frequency. It was found that, with careful choice of ω_c, this filter was generally quite adequate for the removal of high frequency noise components from measured time–of–flight waveforms, although in many applications involving more complicated signals a considerably more sophisticated filtering function would probably be required.

Filtering of the measured time–of–flight signal may not always be required and it is advisable to examine the Fourier transform of the measured signal to determine exactly what frequency components are present. Ideally the measured signal should be sufficiently smooth to avoid the need for any filtering, but obtaining a suitably smooth signal may often require a considerable amount of signal averaging, particularly if the signal is small. In order to improve the signal–to–noise ratio by a factor of k the number of averages must be increased by k^2. If filtering is considered necessary the choice of a suitable ω_c is, to some extent, a matter of trial and error. If the cut-off frequency is too low, then information about $f(t)$ may be lost, while if it is too high, no improvement in the quality of $F(\omega)$, and hence the deconvolved signal, may be gained. The transform of a measured signal may be compared with that of a perfectly smooth fitted curve, evaluated at *identical* time intervals, to estimate a reasonable lower limit for ω_c applicable to a series of experiments recorded with the same sampling frequency.

To deconvolve the experimental time–of–flight signal and obtain $f(t)$, it is necessary to know the form of the system response function, $h(t)$. The system response function will contain contributions from a large number of sources, many of which may be unknown. It is therefore impossible to predict the shape of this function with any real degree of accuracy. Instead, a reliable estimate, $\hat{h}(t)$, may be obtained by deconvolving an accurately measured, or theoretical, time–of–flight distribution from a convoluted distribution. This estimate of the system response function may then be applied to the deconvolution of other convoluted distributions measured in the *same* apparatus under *similar* experimental conditions. It is important to emphasize that a response function estimated in this manner will contain features peculiar to the apparatus in which the convoluted distribution was measured and may therefore not be applicable to results obtained using another apparatus. Further, the estimated response function will also depend to some extent upon the experimental conditions employed for a particular measurement, and care should be taken to ensure that pressures, temperatures, and detector settings are roughly the same for all measurements to which the estimated response function is to be applied.

In some cases it may be possible to make direct use of equations (3.12), (3.13), and (3.15) to determine $f(t)$ using the estimated response function. Frequently, however, the Fourier transform of the response function will contain one or more points which are exactly zero, causing $F(\omega)$ to be undefined at those points. In such situations, an acceptable deconvolution can generally be obtained through the application of Wiener filtering [Bracewell, 1986], in which equation (3.15) is rewritten as

$$F(\omega) \approx G(\omega)\hat{W}(\omega), \tag{3.18}$$

where

$$\hat{W}(\omega) = \frac{\hat{H}^*(\omega)}{\left|\hat{H}(\omega)\right|^2 + \phi}. \tag{3.19}$$

In this expression, $\hat{H}^*(\omega)$ and $|\hat{H}(\omega)|$ are the complex conjugate and modulus of $\hat{H}(\omega)$, respectively, and ϕ is an adjustable parameter roughly equal to the noise–to–signal ratio associated with $g(t)$ such that

$$\phi \approx \frac{\sum c^2}{\sum f^2}, \tag{3.20}$$

for a signal with noise component $c(t)$. By improving the signal–to–noise ratio, the ϕ term in the Wiener filter can be made very small, resulting in a more highly resolved deconvolution. Unfortunately it is not always possible to make use of equation (3.20) and, as with the choice of low–pass filter cut-off frequency, the best choice of ϕ is to some extent a matter of trial and error. The optimum value of ϕ represents something of a compromise, as a value which is too small will cause $\hat{W}(\omega)$ to diverge for very small values of $|\hat{H}(\omega)|$, while a value that is too large will dominate $\hat{W}(\omega)$, resulting in a poor deconvolution. When it is difficult to estimate ϕ using equation (3.20), a simple and generally successful approach is to take ϕ as some small fraction ($\sim 10^{-6}$) of the maximum signal amplitude.

3.4.3 Experimental arrangement

The experimental arrangement used to collect unchopped pulsed nozzle time–of–flight waveforms is illustrated schematically in Figure 3.11. A commercially available pulsed valve nozzle (General Valve Corporation, model 9–181) was employed for these measurements. The valve was modified to have a nominal nozzle diameter of 70 μm. The central core of the pulsed supersonic expansion was sampled by a 1 mm diameter skimmer (Beam Dynamics) positioned approximately 15 mm downstream from the nozzle exit. The skimmed supersonic beam was then allowed to pass through a differentially pumped flight–tube before entering the ion source of a Vacuum Generators SXP300 quadrupole mass filter. The output current of the channeltron electron multiplier generated by the resultant ion beam was converted into a voltage waveform and amplified using a custom designed circuit having a gain of 5 and a flat frequency response across a bandwidth of 1 MHz. Amplified waveforms were monitored on a 20 MHz oscilloscope and sampled using a 20 MHz Thurlby digital storage adaptor. Digitized waveforms were stored on the hard disk of a personal computer. The frequency and duration of beam pulses was controlled by the beam source driver unit, which also provided the necessary trigger pulses for the digital storage adaptor and the oscilloscope. During operation of the pulsed nozzle, background pressures of 10^{-5} Torr and 10^{-8} Torr were maintained in the expansion chamber and the flight tube, respectively.

3.4.4 Results and discussion

A number of special considerations apply to the measurement of time–of–flight waveforms in unchopped pulsed molecular beams. In particular, it is important to be aware of the time dependent nature of the nozzle conductance, which implies that the speed distribution of an element of gas within a pulse is a function of the time at which that element passed through the nozzle. The width of the speed distribution will be relatively constant during the time that the pulsed nozzle is fully open. During the opening and closing of the nozzle, however, the width of the speed distribution will generally be somewhat greater,

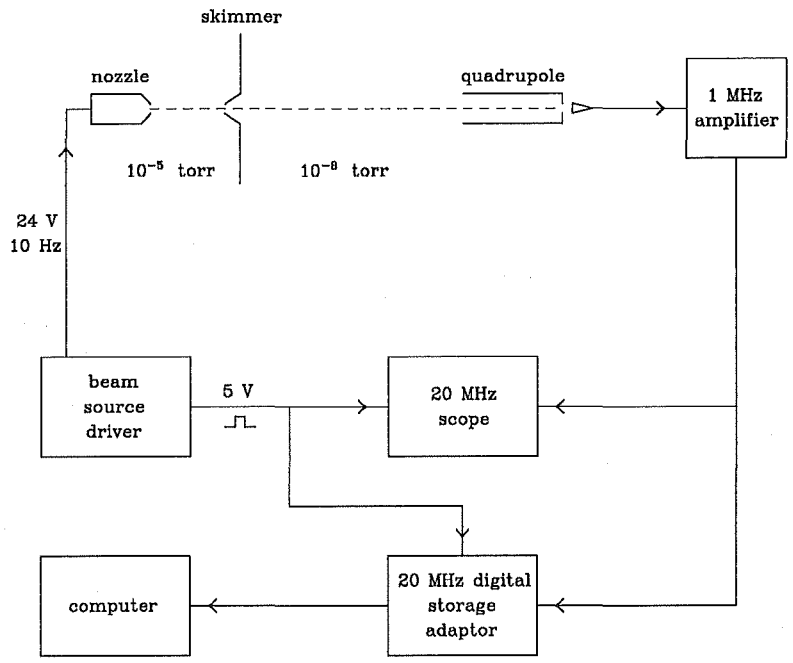

Figure 3.11: Experimental arrangement employed for the collection of unchopped time–of–flight waveforms.

and time dependent. Because of this intrinsic time dependence, time–of–flight analysis of unchopped pulsed molecular beams is considerably more difficult than the analysis of well chopped beams, in which the speed distribution is separable from the beam modulating function.

It is also important to be aware of a number of points concerning the use of fast Fourier transform algorithms to convolve and deconvolve data. The fast Fourier transform algorithm used to obtain the results presented in this section was that of Cooley and Tukey [Cooley and Tukey, 1965]. This algorithm may be used to perform discrete Fourier transforms on complex one, two, or three dimensional data, requiring the number of points in each dimension to be a power of 2. It is a common feature of most fast Fourier transform algorithms that the number of data elements be a power of 2 for reasons of computational efficiency [Bracewell, 1986], although there are algorithms available that place no such restriction upon the number of elements [Press *et al*, 1986]. The output of the Thurlby

digital storage adaptor used to collect the unchopped time–of–flight waveforms presented here was 1024 regularly spaced samples, allowing direct use of the Cooley–Tukey algorithm. In situations where the number of elements is not a power of 2, the measured data may be packed with an appropriate number of leading and trailing zeros to increase the number of samples to a suitable power of 2. Zero–packing of the data in this manner results in an interpolation effect in the Fourier domain [Bracewell, 1986] which may often improve the resolution of spectral features. Indeed, in some instances, it may prove advantageous to perform zero–packing on data sets already consisting of 2^N points for this very reason. It should be noted, however, that in some instances zero–packing will be detrimental and therefore should not be applied in an indiscriminate manner [Bracewell, 1986]. No packing was performed on any of the data presented here.

The fast Fourier transform algorithm provides a discrete approximation of equations (3.12) and (3.13), and assumes that the input is periodic with period equal to the number of data elements. The integration limits of equations (3.12) and (3.13) extend from $-\infty$ to $+\infty$, while the fast Fourier transform is performed on waveforms which are discretely sampled within some window of finite size. If the sampled data does not adequately represent at least one entire period of the waveform, then spectral features pertaining to the shape of the window will be observed in the spectrum produced by the fast Fourier transform. This is of little consequence when performing simple deconvolutions such as those described in this investigation, but is of considerable importance to experimental techniques, such as Fourier transform infrared spectroscopy, where detailed spectral analysis is required.

Unchopped pulsed nozzle time–of–flight waveforms were recorded for argon, krypton, CH_3Cl, and $CHCl_3$ using the experimental arrangement described above. All data were recorded for a source pressure of 1 atm at a temperature of 300 K. The pulsed nozzle was operated at a frequency of 10 Hz, with an estimated open time of not more than 2 ms. The time base of the Thurlby digital storage adaptor was set at 50 ms, corresponding to a sampling frequency of 20 kHz. Waveform averaging was performed to improve the signal–to–noise ratio of the recorded data, with 64 averages generally being sufficient to reduce the amplitude of any random noise superimposed on the observed signal to an acceptable level. Due to the high frequency response of the amplifier and the digital storage adaptor employed for these measurements, it is unlikely that any distortion of the recorded signals was caused by the signal amplification and collection circuitry.

An overall response function for the system was estimated by deconvolving an accurate argon time–of–flight waveform determined in a previous study under identical source conditions (see §3.3) from the corresponding unchopped argon distribution measured in the present study. As will be discussed later, a theoretical speed distribution could have been used in place of the accurately measured argon time–of–flight waveform to estimate the response function, but it was felt that the use of experimental data would provide a more severe test of the proposed deconvolution method. The chopped and unchopped argon waveforms are illustrated in Figures 3.12(a) and 3.12(b), respectively. The width of the unchopped waveform is considerably greater than that of the chopped waveform, and the rise-time of the unchopped signal, from the base of the leading edge to the most probable arrival time, is approximately twice that of the accurately measured curve. The greater width of the unchopped signal is a direct result of the long duration of the beam pulse, while the difference in rise-times may be attributed to the finite time required for the pulsed nozzle to become fully open. The 2 ms duration of the beam pulse produced by the pulsed nozzle was approximately 55 times longer than that of the chopped beam. It can also be seen from Figure 3.12 that the most probable arrival time for the unchopped signal is some 4 ms greater than that of the chopped distribution. Apart from the time

required for the pulsed nozzle to become fully open, there were a number of other factors responsible for this difference. In particular, the length of the flight path for the unchopped beam was approximately 1.2 m, while that of the chopped beam was only 0.89 m. The beam source driver unit used to control the pulsed nozzle and trigger the digital storage adaptor was the other major contributing factor to the observed difference in most probable arrival times, with there being a fixed delay of exactly 2 ms between the 5 V trigger pulse and the 24 V pulse supplied to the electromagnetic valve of the pulsed nozzle.

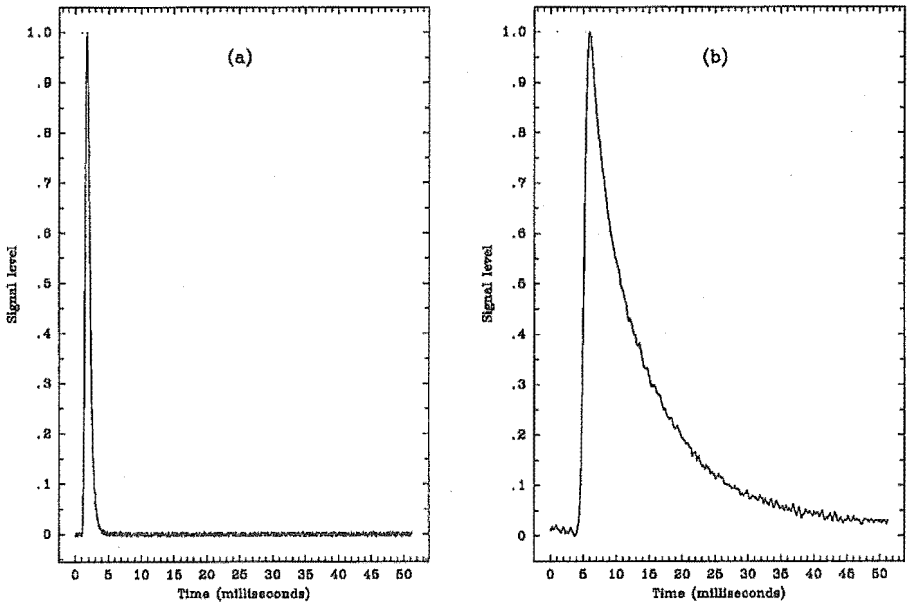

Figure 3.12: Time–of–flight distributions for argon measured (a) with and (b) without a chopper.

Despite the high signal–to–noise ratios observed for the chopped and unchopped waveforms shown in Figure 3.12, both sets of data were low-pass filtered, prior to calculating the system response function, to remove any frequency components above 5 kHz. Examination of the Fourier transforms of both the chopped and unchopped waveforms indicated the presence of noise components down to a frequency of approximately 1 kHz. It was found, however, that components below about 2.5 kHz could not be removed using the low-pass filter described by equation (3.17) without introducing considerable ringing into the corresponding time domain signal. This effect is clearly illustrated in Figures 3.13(a) and 3.13(b), which show the chopped argon signal after the application of low-pass filtering according to equation (3.17), with cut-off frequencies of 500 Hz and 1 kHz, respectively. The period of the ringing is equal to the reciprocal of the filter cut-off frequency, while the amplitude of the introduced oscillations increases with decreasing cut-off frequency. This ringing is due to both the shape and cut-off frequency of the filtering function. It is important to realize that the act of filtering in the frequency domain corresponds to

performing a convolution in the time domain. If the low-pass filter cut-off frequency is too low or the attenuation of frequency components up to the cut-off value is too rapid, then features of the filtering function will contribute significantly to the shape of the filtered signal in the time domain. In general, any abrupt attenuation performed in the frequency domain will produce ringing in the time domain. A raised cosine filter of the form

$$L(\omega) = \frac{\Pi(\omega)}{2}\left[1 + \cos\left(\frac{2\pi\omega}{\omega_c}\right)\right] \tag{3.21}$$

may be used instead of the filter described by equation (3.17) to provide a considerably more gradual attenuation of frequency components up to the desired cut-off value. Results obtained using equation (3.17) with a cut-off frequency of 5 kHz were more than satisfactory, however, and the use of an alternative filter, such as that described by equation (3.21) was not considered necessary.

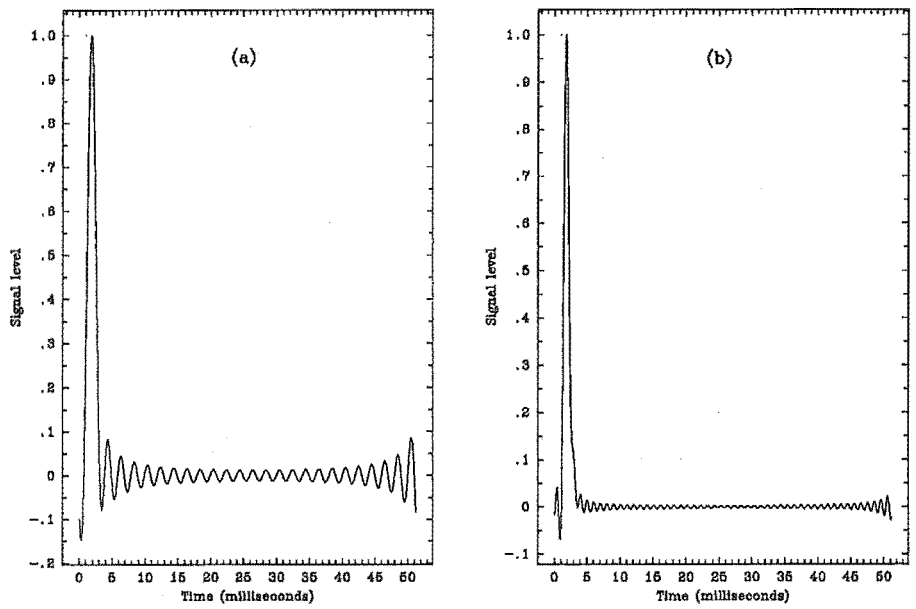

Figure 3.13: Effect of badly chosen low–pass filter cut–off frequency ((a) w_c=500 Hz; (b) w_c=1 kHz).

The deconvolution of the low-pass filtered chopped argon time–of–flight waveform from the filtered unchopped waveform to obtain the system response function was performed using a Wiener filter with an estimated noise–to–signal ratio of 3×10^{-4}. The spectrum of the resulting response function is illustrated in Figure 3.14. It was observed that the value of ϕ, in this instance, was not particularly critical, with values ranging from 1×10^{-3} to 1×10^{-6} having an indiscernible effect of the shape of the estimated response function. The symmetry of Figure 3.14 is due to the fact that we are working with purely real

data. The Fourier transform of a real function is Hermitian [Bracewell, 1986], and the real component of a Hermitian function is even. The sharp spike in the spectrum at 0 kHz was caused by the presence of a significant DC offset on the measured unchopped waveform; the Fourier transform of a constant function being the impulse function, $\delta(\omega)$. This offset is not reflected in Figure 3.12(b) or any other plots of unchopped time–of–flight waveforms presented here, as the y-scales of these graphs have all been adjusted to range from 0 to 1. The frequency components of the response function between $1 \leq |\omega| < 5$ kHz are due to noise which was not successfully filtered from the chopped and unchopped waveforms. As can be seen, the noise level is observed to increase with increasing $|\omega|$ up to about 4.5 kHz, after which it drops rapidly, reaching zero at the low-pass filter cut-off frequency of 5 kHz. If no low-pass filtering had been performed on the data, the level of this noise would have continued to increase with $|\omega|$, resulting in a response function which could not be applied to the deconvolution of unchopped signals without introducing considerable noise, or amplifying existing noise. The observation that the noise level increases with increasing frequency suggests that high frequency noise components were less effectively attenuated by the signal averaging process, and may be due to the existence of a timing instability between the internal clock of the digital storage adaptor and the internal clock of the beam source driver used to trigger the digital storage adaptor. By operating the system at higher frequencies, the effect of any such instability may be reduced, resulting in a more uniform attenuation of the noise components by the signal averaging process. The maximum operating frequency of the system is, however, restricted by the period of the waveform being measured. From Figure 3.12(b), it can be seen that the period of the unchopped argon waveform is at least 50 ms, indicating that the system cannot be operated at above 20 Hz without significantly undersampling the waveform. A more precise value for the maximum operating frequency is given by the bandwidth of the system. The bandwidth may be estimated from the power spectrum,

$$\hat{P}(\omega) = \hat{H}(\omega) \cdot \hat{H}^*(\omega), \tag{3.22}$$

of the response function, being roughly equal to the full width at half maximum power. The power spectrum of Figure 3.14 yielded a bandwidth of approximately 18.5 Hz.

The estimated response function was then used to deconvolve the unchopped argon signal. A comparison between the original and deconvolved unchopped signals is shown in Figure 3.15. The deconvolved signal contains little or no noise, and appears identical to the chopped time–of–flight waveform in terms of rise-time, width, and most probable arrival time. Deconvolution of the unchopped krypton signal also resulted in a considerable narrowing of the time–of–flight waveform and a similar shift of the most probable arrival time. As with argon, very little noise was observed on the deconvolved krypton signal.

The deconvolved argon and krypton signals were converted from the time domain into velocity space and least squares fitted to the speed distribution function

$$f(v)\mathrm{d}v = Av^2 \mathrm{e}^{-m(v-u)^2/2k_bT_\parallel}\mathrm{d}v, \tag{3.23}$$

where u and $T_\parallel$ represent the mean flow velocity and parallel translational temperature of the supersonic beam, respectively, and A is a normalization constant. Since deconvolution using the estimated response function adjusts the arrival times of the unchopped waveforms to correspond to those expected for chopped beams measured over a shorter flight path in the absence of any delaying effects introduced by the beam source driver and the action of the pulsed nozzle, speeds used in the fitting of the deconvolved waveforms were determined using the flight path of 0.89 m associated with the measurement of the chopped

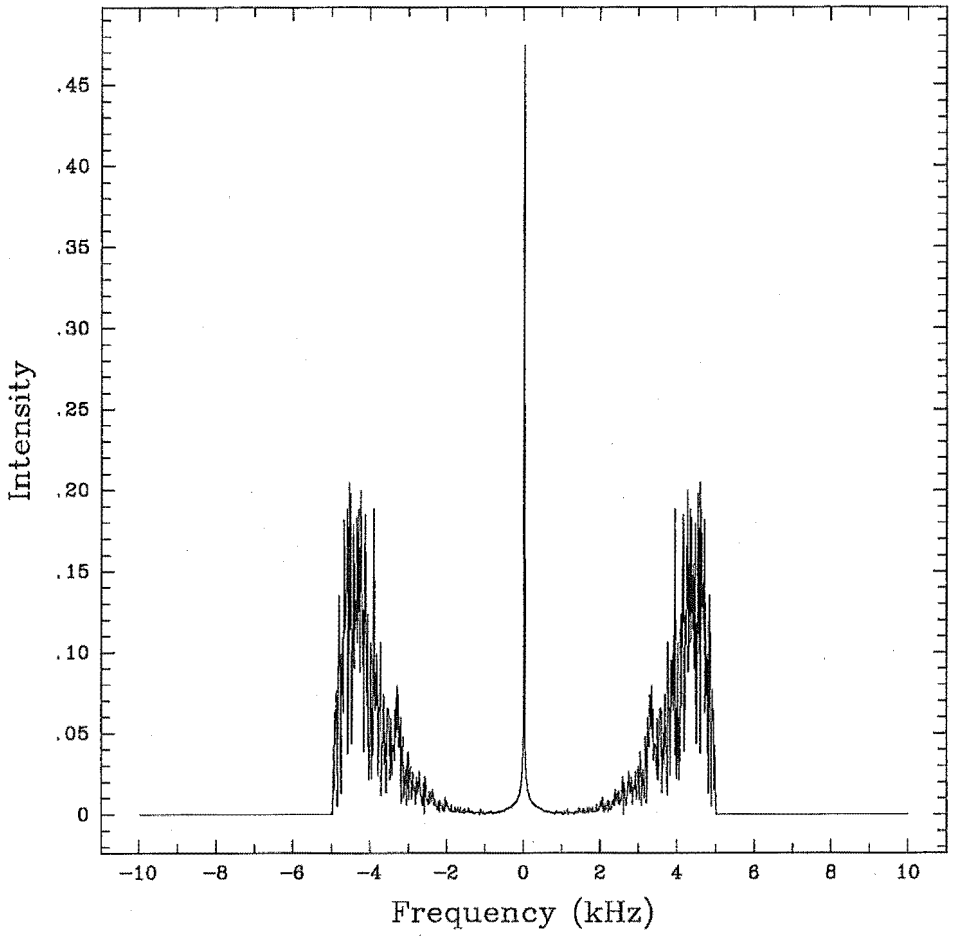

Figure 3.14: Spectrum of the estimated system response function.

argon signal. The fitted values of u and $T_{||}$, along with those obtained for the accurately measured argon and krypton distributions, are presented in Table 3.4. The values of u and $T_{||}$ calculated for the deconvolved argon signal were found to be virtually identical to those determined for the chopped data. Correspondingly good agreement was observed between the values of u and $T_{||}$ determined for the accurately measured and the deconvolved krypton time–of–flight waveforms, providing considerable confidence in the validity of the proposed deconvolution strategy.

The estimated system response function was also used to deconvolve the unchopped time–of–flight waveforms measured for CH_3Cl and $CHCl_3$. The original unchopped and deconvolved signals for these species are illustrated in Figures 3.16 and 3.17. The deconvolved distributions obtained for CH_3Cl and $CHCl_3$ were fitted to the speed distribution described by equation (3.23), and the resulting values of u and $T_{||}$ are given in Table 3.4. While accurate speed distribution measurements have not been performed in our laboratory for either of these species, the values of u and $T_{||}$ obtained from the deconvoluted data

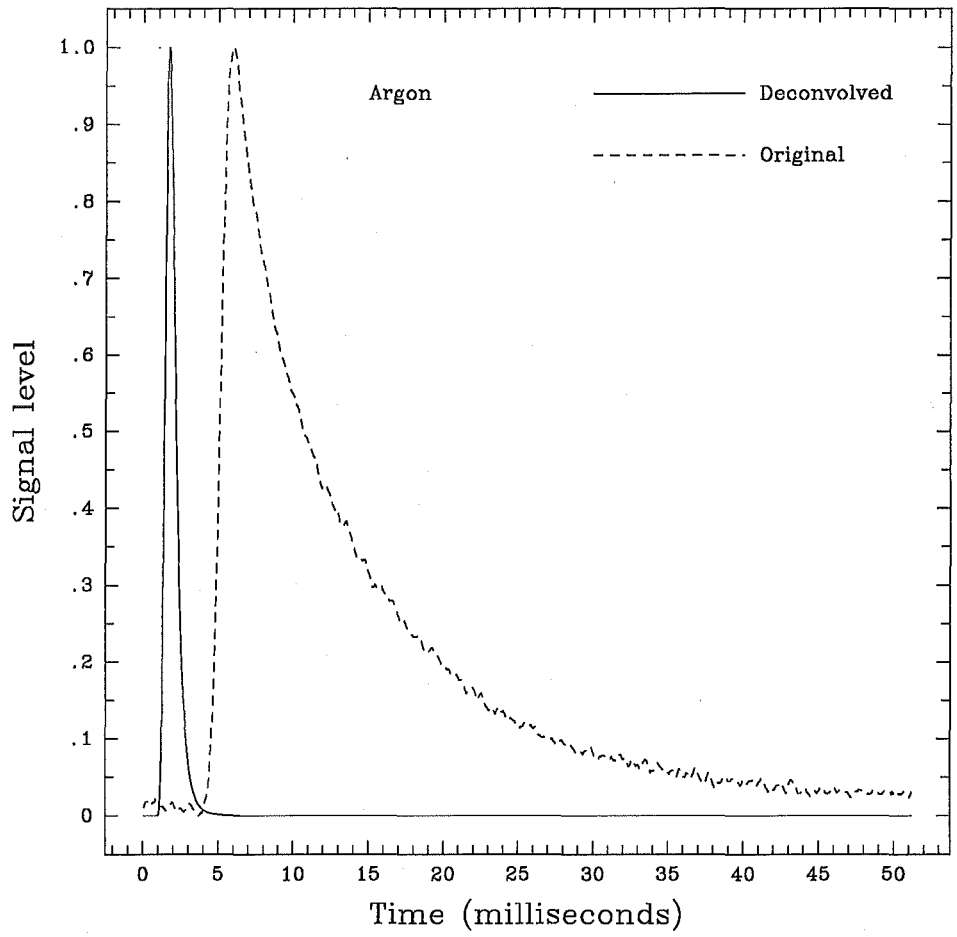

Figure 3.15: Unchopped argon time–of–flight waveforms before and after deconvolution.

	Chopped		Deconvoluted unchopped	
System	u (m s^{-1})	$T_{\|\|}$ (K)	u (m s^{-1})	$T_{\|\|}$ (K)
Ar	552	1.4	552	1.4
Kr	381	1.1	381	1.2
$CHCl_3$	—	—	397	21.4
CH_3Cl	—	—	543	29.0

Table 3.4: Estimated mean flow velocities and parallel translational temperatures for chopped and deconvolved unchopped time–of–flight signals.

appear reasonable. The values obtained for $CHCl_3$ are in good agreement with the predictions of thermal conduction model calculations [Cameron and Harland, 1993c], assuming a rotational–translational coupling parameter of unity.

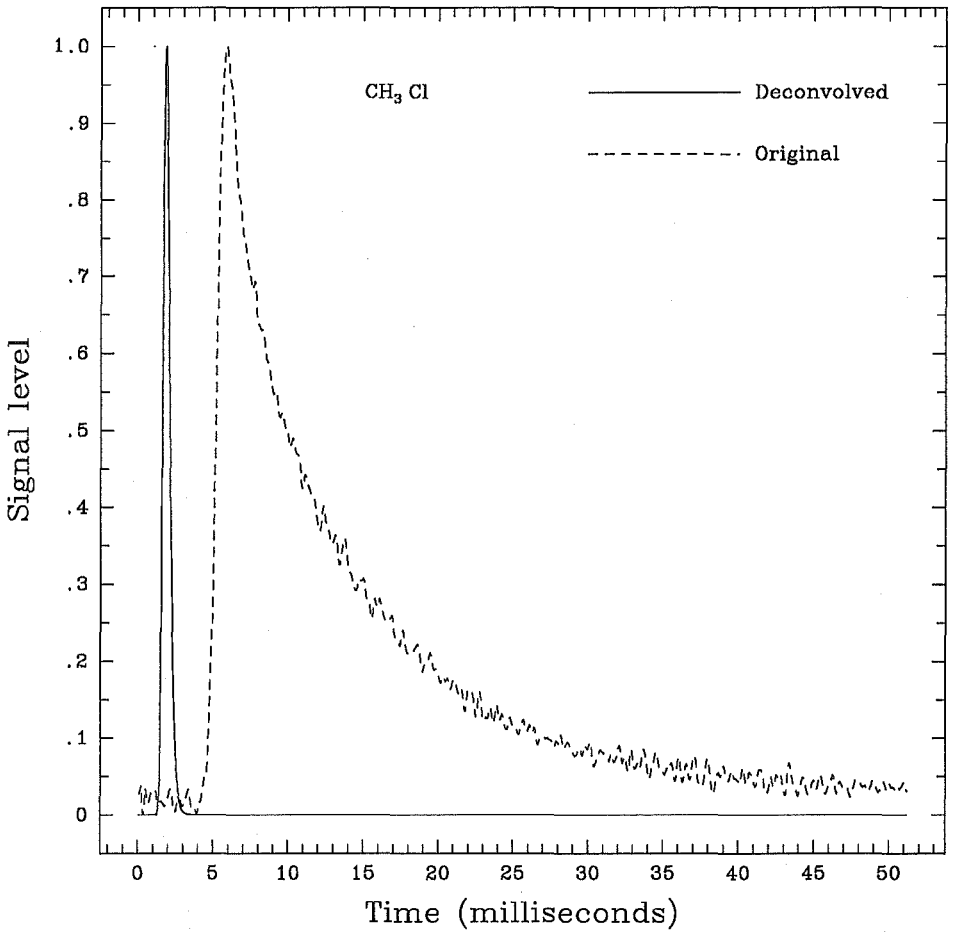

Figure 3.16: Unchopped CH_3Cl time–of–flight waveforms before and after deconvolution.

A response function was also estimated using a theoretical argon time–of–flight waveform calculated according to the time domain equivalent of equation (3.23) using the fitted values of u and $T_{||}$ given in Table 3.4. The response function determined in this manner was found to produce identical deconvolutions to those obtained using the response function determined with the accurate experimental waveform. This result is of considerable importance with regard to the success of the deconvolution strategy, as accurate experimental time–of–flight data may not always be available for the estimation of the system response function, while theoretical terminal speed distributions may be reliably predicted for atomic species such as argon, neon, and krypton for any set of source conditions [Cameron and Harland, 1991].

In applying the same response function to the deconvolution of unchopped time–of–

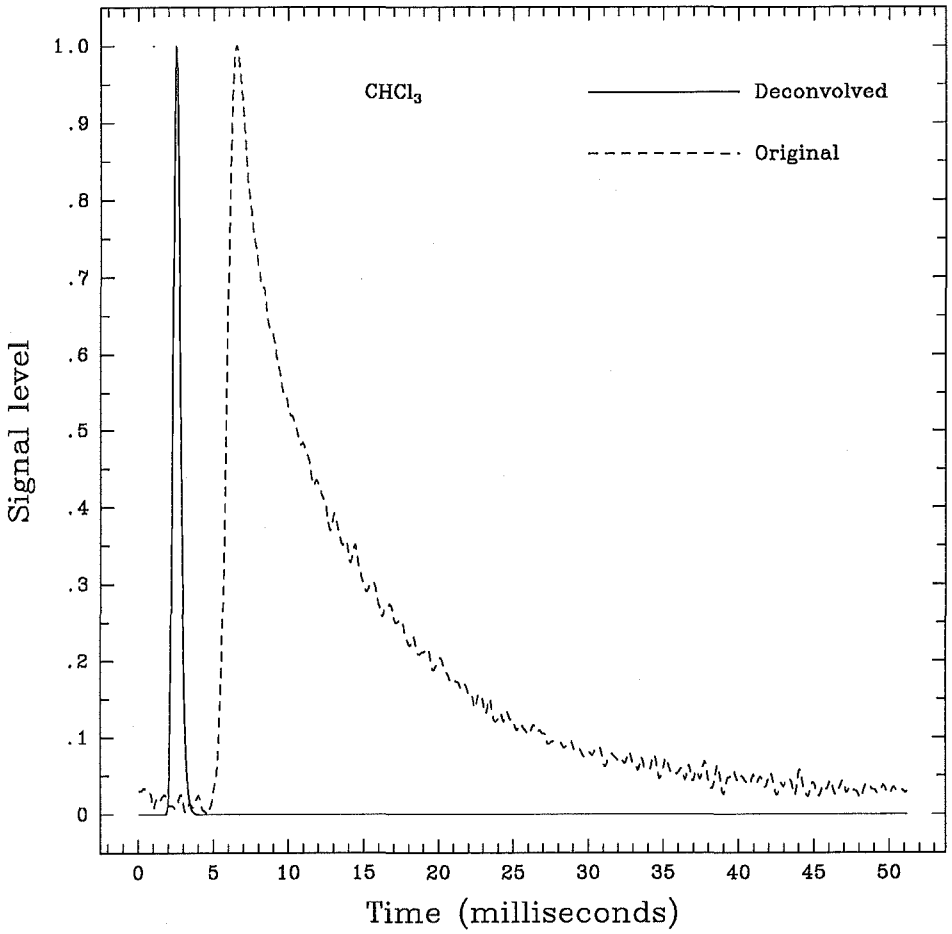

Figure 3.17: Unchopped $CHCl_3$ time–of–flight waveforms before and after deconvolution.

flight waveforms measured for a range of species, under identical experimental conditions, it has been assumed that the influence of factors such as viscosity and the scattering of beam particles through collisions with background gases have a negligible effect on the shape of the measured time–of–flight waveform. For moderate source pressures ($P_0 \sim 1$ atm), it is reasonable to assume that the times required for the pulsed nozzle to fully open and to fully close are not significantly affected by the viscosity of the gas. Such an assumption may not be strictly valid at high source pressures ($P_0 > 10$ atm), and will depend considerably upon the design and, in particular, the force constant of the pulsed nozzle. The scattering of beam particles through collisions with background gases will result in a narrowing of the speed distribution due to the preferential elimination of particles with lower momentum from the beam. The background pressures maintained in the apparatus used for the measurements described here were sufficiently low to ensure that background scattering did not significantly affect the shape of the measured time–of–flight waveforms. It should also be recognized that as certain components of the system

age, their characteristics and those of the system response function may change. This is particularly true of components such as electromagnetic values. More work is clearly required in order to determine the dependence of the system response function on both the experimental conditions and the nature of the gas.

3.4.5 Conclusion

A quite general method for deconvolving badly convoluted supersonic molecular beam time–of–flight waveforms using Fourier transform and Wiener filtering techniques has been presented. The method makes no possibly invalid assumptions regarding the exact functional form of convolutions such as the chopper gating function or the response function of any detection electronics, but rather employs an overall system response function, estimated using accurate time–of–flight data, for the deconvolution of convoluted signals. The method was successfully applied to the deconvolution of highly distorted argon, krypton, CH_3Cl, and $CHCl_3$ time–of–flight waveforms measured in an unchopped pulsed supersonic molecular beam, affording considerable confidence in the reliability of the devised approach, although more work is required to determine the dependence of the estimated response function on experimental conditions. The use of direct numerical deconvolution in the manner described is considerably more efficient than the use of moment methods or the fitting of a parameterized convolution to experimental data. The problem of noise superimposed on the measured signal may be negated through the use of Wiener filtering and the application of a simple low–pass filter.

3.5 Velocity and temperature slip in supersonic expansions of binary mixtures

3.5.1 Introduction

At high jet densities such that the product of the stagnation pressure P_0 and the nozzle diameter d_0 is greater than about 2 Torr cm, it can generally be assumed that the supersonic flow field of an expanding gas mixture will be virtually identical to that of a pure gas with molecular weight and heat capacity equal to the weighted average for the mixture [Anderson, 1974]. In principle it is therefore possible to produce supersonic beams in which the velocity distributions and translational temperatures of several very different species are almost identical simply by seeding them in the correct ratio into a suitable carrier gas. A heavy species may be accelerated by seeding it into a light carrier gas, or a light species may be decelerated by seeding it into a heavy carrier gas. It is possible to finely tune the kinetic energy of a particular beam constituent with considerable accuracy simply by adjusting its mole fraction in the expanding gas mixture.

At somewhat lower values of the product $P_0 d_0$, a number of important non–equilibrium effects may occur during the supersonic expansion of a gas mixture. One important result of the seeding technique is the phenomenon of hydrodynamic focussing. This effect leads to the diffusive separation of the different beam constituents such that heavy species are preferentially focussed onto the beam axis. The primary cause of diffusive separation is the occurrence of pressure diffusion in the expansion chamber. Under the steep pressure gradients which prevail in expanding free jets, heavier gas species tend to migrate to regions of higher pressure along the axis of the expansion.[5] A less significant source of

[5]Since the streamlines in a supersonic expansion initially curve away from the axis, the heavy species are concentrated along the expansion axis.

diffusive separation is caused by interactions between species in the expanding jet and the walls of the skimmer. Although the fractional composition of the expanding jet at the skimmer inlet may be almost identical to that of the source for suitably large values of P_0, the on–axis composition of the resultant supersonic beam downstream from the skimmer at the detector will invariably favour heavier beam species. Assuming near continuum or free molecular flow conditions at the skimmer inlet, all species in the expanding jet will have nearly the same flow velocity and translational temperature. In the subsequent free molecular flight beyond the skimmer, lighter beam species will have a lower perpendicular speed ratio $u/(2k_bT_\perp/m)^{1/2}$ and a larger perpendicular component of translational motion, causing more lateral spreading than would be the case for a heavier component.

Different scattering cross sections for collisions between beam species and background gases may also play some part in causing diffusive separation. It is important to note, however, that the extent to which this and the factors discussed above contribute to the hydrodynamic focussing of various beam components along the beam axis is highly dependent upon the design of the molecular beam apparatus and may vary from one laboratory to another. As a general guide, it has been found that the concentration of a heavy seed gas along the axis at the detector will be greater than that in the source by a factor approximately equal to the ratio of the seed mass to the carrier mass. This fact is particularly useful with regard to cluster experiments as, although cluster concentrations generally drop with increasing size, heavier clusters will be focussed along the axis of the beam, thereby increasing their concentration at the detector.

Two other important non–equilibrium effects observed in the supersonic expansion of gas mixtures are the phenomena of velocity slip and temperature slip. Velocity slip is the difference between the terminal flow velocities of each beam species and temperature slip is the difference between the terminal parallel translational temperatures. These effects are generally observed in expansions from low stagnation pressures ($\sim$ 760 Torr) with heavy to light mass ratios greater than about 5 and arise as a result of the different translational relaxation rates of each species in the expanding gas mixture [Scoles, 1988]. In this section, the effects of velocity and temperature slip are examined using time–of–flight methods for supersonic beams of helium seeded with various amounts of neon, argon or krypton. The results presented here are by no means conclusive, but simply serve to provide some indication of the magnitude of these effects which may be expected under various experimental conditions.

3.5.2 Results and discussion

Seeded supersonic beams were produced by expanding binary gas mixtures containing between 5 Torr and 100 Torr of neon, argon, or krypton made up to 1000 Torr with helium through a 70 μm nozzle at a source temperature of 300 K. Chopped pulsed nozzle time–of–flight waveforms were measured for both helium and the seed gas for each binary mixture using the experimental arrangement and procedures outlined in §3.3.3. The recorded time–of–flight waveforms were transformed from the time domain into velocity space and fitted to the speed distribution function described by equation (3.4). The average values of u and $T_{||}$ determined from four runs with each gas mixture are listed in Table 3.5 and plotted as a function of mole fraction X_i in Figures 3.18 and 3.19, respectively. The fitted values of u and $T_{||}$ were found to be highly reproducible, and the average values presented for these quantities in Table 3.5 are considered accurate to within $\pm$ 5%. Also listed in Table 3.5 are values of the velocity slip Δu and the temperature slip $\Delta T_{||}$ observed in each case.

System	X_L	X_H	$T_{\parallel,L}$ (K)	u_L (m/s)	$T_{\parallel,H}$ (K)	u_H (m/s)	$\Delta T_\parallel$	Δu
He–Ne	0.900	0.100	6.7	1492	12.5	1447	-5.8	45
	0.920	0.080	6.4	1538	12.0	1494	-5.6	44
	0.940	0.060	6.2	1580	11.5	1537	-5.3	43
	0.960	0.040	6.0	1638	11.1	1596	-5.1	42
	0.980	0.020	5.7	1697	10.6	1656	-4.9	41
	0.995	0.005	5.6	1747	10.3	1707	-4.7	40
He–Ar	0.900	0.100	6.1	1301	16.8	1233	-10.7	68
	0.920	0.080	6.0	1370	15.9	1303	-9.9	67
	0.940	0.060	5.9	1437	15.0	1372	-9.1	65
	0.960	0.040	5.8	1523	14.2	1460	-8.4	63
	0.980	0.020	5.6	1628	13.4	1566	-7.8	62
	0.995	0.005	5.6	1718	12.8	1657	-7.2	61
He–Kr	0.900	0.100	2.6	1027	4.5	1016	-1.9	11
	0.920	0.080	2.9	1098	4.3	1087	-1.4	11
	0.940	0.060	3.3	1194	4.2	1183	-0.9	11
	0.960	0.040	3.7	1314	4.1	1303	-0.4	11
	0.980	0.020	4.4	1496	4.0	1485	0.4	11
	0.995	0.005	5.2	1680	3.9	1670	1.3	10

Table 3.5: Summary of velocity slip and temperature slip data for helium–neon, helium–argon, and helium–krypton mixtures. The subscripts H and L refer to the heavy and light species, respectively.

In order to verify the accuracy of the time–of–flight measurements used to obtain the data presented in Table 3.5, an energy balance was performed with the average values of u and $T_\parallel$ determined for each gas mixture. Ignoring the effects of diffusive separation, the energy balance equation for an n-component monatomic gas mixture is given by the expression [Scoles, 1988]

$$\frac{5}{2}k_b T_0 = \sum_{i=1}^{n} X_i \left(\frac{1}{2} m_i u_i^2 + \frac{3}{2} k_b T_{\parallel,i} + \frac{2}{2} k_b T_{\perp,i} \right), \tag{3.24}$$

where T_0 is the source temperature and X_i is the mole fraction of component i in the source.[6] Assuming the perpendicular component of the translational energy to be negligible compared to the parallel component, the left and right hand sides of equation (3.24) were found to be in agreement to within $\pm$ 2% in all cases, indicating that the time–of–flight measurements were highly accurate.

It should be mentioned that it was not possible to reliably determine values of u and $T_\parallel$ for helium from time–of–flight measurements with gas mixtures containing more than about 12% of argon or krypton. For such mixtures, the signal–to–noise ratio associated

[6]The reason that the $T_\parallel$ term in equation (3.24) is weighted more than one might expect is that it includes the *flow work* term $k_b T_\parallel$ along the streamline in question.

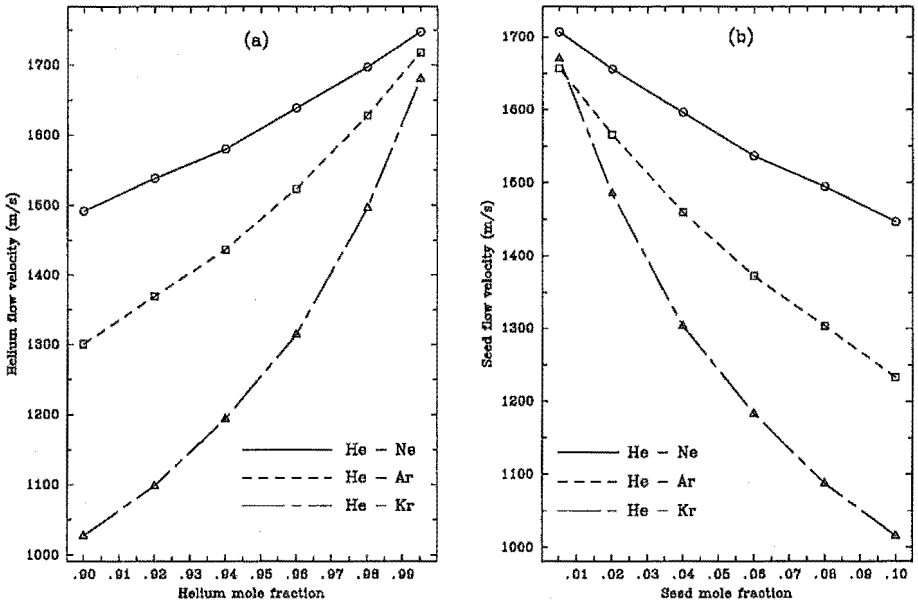

Figure 3.18: Velocity slip in supersonic expansions of helium–neon, helium–argon, and helium–krypton mixtures.

with the helium signal was too low to allow an accurate fit of the measured helium time–of–flight waveforms even after extensive waveform averaging. The low signal levels observed for helium in these mixtures may be attributed to a number of factors. In particular, the transmission efficiency of quadrupole mass filters is generally poor for very light species such as hydrogen and helium. It is usually possible to re-tune the mass filter to improve the transmission efficiency of these species, but only at the expense of adversely affecting the transmission of higher masses [Scoles, 1988]. In addition, helium has an extremely small ionization cross section and therefore exhibits a low ionization probability. The electron impact ionization probability of helium relative to N_2 is approximately 0.15 while the ionization probabilities of argon and krypton relative to N_2 are 1.2 and 1.9, respectively [Flaim and Ownby, 1971]. Argon and krypton are therefore roughly an order of magnitude more likely than helium to be ionized in the ion source of the quadrupole mass filter employed for these measurements. Depreciation of the helium signal due to increased hydrodynamic focussing with increasing argon or krypton mole fraction may also be an important factor.

The possibility of measuring helium time–of–flight waveforms for gas mixtures containing mole fractions of neon greater than those listed in Table 3.5 was not investigated. By re-tuning the mass filter to favour the transmission of lower mass species it should be possible to successfully measure helium time–of–flight waveforms using the present experimental arrangement for binary mixtures containing mole fractions of neon well in excess of those examined here. It should also be mentioned that since the atomic mass of neon

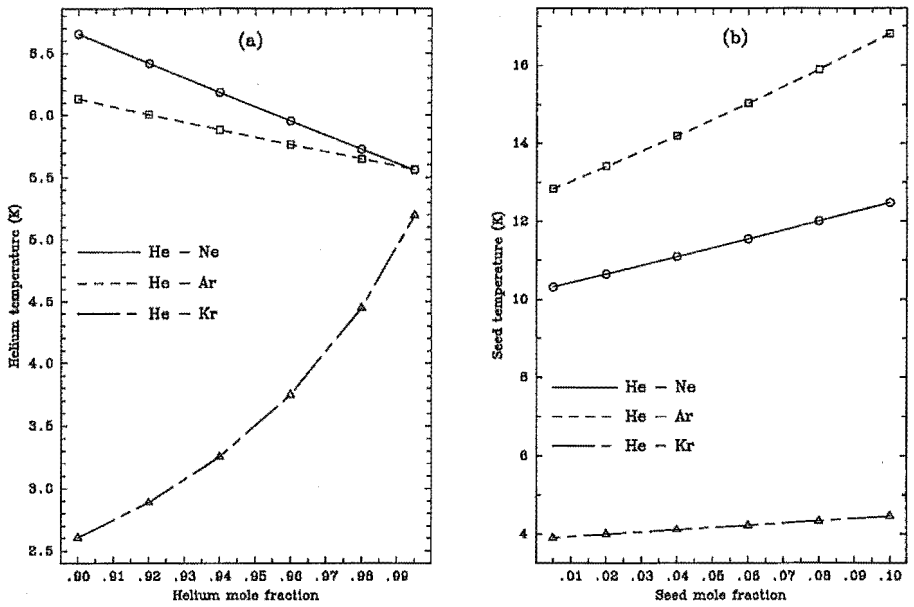

Figure 3.19: Temperature slip in supersonic expansions of helium–neon, helium–argon, and helium–krypton mixtures.

is less than that of either argon or krypton, diffusive separation in helium–neon mixtures will have a less significant effect on the amplitude of the helium signal.

The trends observed in Figure 3.18 for the variation of helium and seed gas flow velocity with mole fraction may be explained in terms of the efficiency of momentum transfer in collisions between the seed and carrier gas species [Abuaf *et al*, 1967]. Increasing the mole fraction X_H of the seed gas was observed to decrease the mean helium flow velocity. This decrease in flow velocity may be attributed to an increase in the number of collisions between the heavy seed gas and the light helium carrier with increasing seed mole fraction during the initial stages of the supersonic expansion, close to the nozzle exit. The effect of these collisions is to lower the momentum and thus the velocity of the helium atoms in the resultant supersonic beam. As can be seen, the magnitude of this decelerating effect may be quite significant even at low seed mole fractions, and increases in an almost linear fashion with increasing seed mass. As the mole fraction of the seed gas approaches zero, the mean flow velocity of the helium atoms tends to the value of 1740 m s^{-1} expected for a pure helium expansion at the same source temperature and pressure [Cameron and Harland, 1991]. The flow velocities of the seed gases were all observed to increase with increasing helium mole fraction. For higher seed mole fractions than those considered here, the flow velocities of the seed gases would be expected to rapidly approach their respective pure expansion values, with an accompanying decrease in the helium flow velocity.

The variations of helium and seed gas parallel translational temperature illustrated in Figure 3.19 are somewhat surprising. The parallel translational temperature of the

helium atoms was observed to increase with increasing neon or argon mole fraction and to decrease with increasing krypton concentration over the range of mole fractions examined. From Figure 3.18a, it can also be seen that for helium–krypton mixtures, the slope of the helium temperature curve steadily increases with increasing helium mole fraction, while for mixtures containing either neon or argon, the variation of helium temperature with mole fraction is distinctly linear. As the mole fraction of the seed gas tends to zero, the parallel translational temperature of the helium approaches the value of 5.5 K expected for a pure helium expansion under identical source conditions [Cameron and Harland, 1991]. The variation of seed gas temperature with mole fraction was distinctly linear for all three seed gases over the range of mole fractions considered. For seed gas mole fractions greater than those considered here, the temperature curves for the seed species would be expected to change slope with increasing seed mole fraction and gradually approach values indicative of pure seed expansions.

The results obtained for the helium-argon mixtures are in reasonable agreement with the theoretical predictions of Cooper and Bienkowski [Cooper and Bienkowski, 1966] and the experimental results of Abuaf *et al* [Abuaf *et al*, 1966]. Values of Δu and $\Delta T_{||}$ determined for helium–neon and helium–krypton mixtures under identical experimental conditions to those employed here could not be found in the literature, although the results obtained for the helium–krypton mixtures exhibit similar trends to those observed by Haberland *et al* [Haberland *et al*, 1972] for helium–xenon mixtures under comparable conditions. Considering the high accuracy of the time–of–flight measurements, however, it is reasonable to assume that all the velocity slip and temperature slip data presented in Table 3.5 are reliable.

The increase in flow velocity experienced by a heavy gas seeded into a light carrier gas such as helium is inversely proportional to the mass of the seed species, and hence, for different gas mixtures with the same carrier gas and seed mole fraction, it is reasonable to assume that the velocity slip Δu will increase with increasing seed mass. The magnitude of Δu may also be expected to increase with increasing seed mole fraction. As can be seen from Table 3.5, Δu increases with increasing seed mole fraction for each of the helium–seed combinations examined, in accordance with the expected result. For mixtures containing the same seed mole fraction, however, the magnitude of Δu does not continue to increase with increasing seed mass. Instead, the smallest values of Δu were observed for the helium–krypton mixtures. Similar behaviour was observed for $\Delta T_{||}$, with the smallest values again being observed for the helium–krypton mixtures. It can also be seen that for krypton mole fractions less than or equal to 0.02, the translational temperature of the krypton atoms was less than that of the helium carrier gas. This somewhat surprising behaviour may be explained in terms of the efficiency of translational relaxation for the different seed gases. It was noted in §3.3 that $T_{||}$ for supersonic expansions of pure monatomic gases decreased with increasing atomic mass[7], suggesting that translational relaxation, and thus the conversion of translational energy into directed kinetic energy, becomes more efficient with increasing mass for monatomic species. Relating this observation to the velocity slip and temperature slip data presented in Table 3.5, it would appear that for the helium–neon and helium–argon mixtures examined, the mass of the seed gas is the most important factor influencing the magnitude of Δu and $\Delta T_{||}$ while for the helium–krypton mixtures the mass effect is dominated by the high efficiency of translational relaxation for krypton.

[7]It should be noted that this trend may not always be the case. For large values of the product $P_0 d_0$ (> 50 Torr cm), helium expansions are known to exhibit strong quantum effects, leading to extremely low parallel translational temperatures (< 0.14 K), and flow velocities close to the their thermodynamic limiting value.

It must be emphasized that the above explanation for the observed trends in velocity slip and temperature slip is somewhat speculative, and may not be totally correct. There are considerable discrepancies between many existing sets of results to be found in the literature [Abuaf *et al*, 1966; Haberland *et al*, 1972; Miller and Andres, 1968], indicating that further experimental and theoretical work is required in order to formulate a complete understanding of the phenomena of velocity slip and temperature slip in supersonic expansions of gas mixtures. It is also important to emphasize that the results and discussion presented in this section pertain to supersonic expansions of monatomic gas mixtures and may not be applicable to expansions of mixtures containing diatomic or polyatomic molecules, the analysis of which will be greatly complicated by the presence of internal degrees of freedom.

3.5.3 Conclusion

The phenomena of velocity slip and temperature slip in supersonic expansions of gas mixtures were investigated for helium–neon, helium–argon and helium–krypton mixtures using time–of–flight methods. The observed trends were tentatively explained in terms of competing mass and translational relaxation effects. The results presented here serve to illustrate that both velocity slip and temperature slip may be important effects, even for low seed mole fractions. It would be interesting to perform similar measurements for helium–xenon mixtures and for mixtures containing diatomic or polyatomic molecules. It would also be interesting to examine the behaviour of Δu and $\Delta T_{\|}$ for somewhat less dilute mixtures than those considered here.

The kinetic theory analysis of velocity slip and temperature slip in binary gas mixtures is highly complicated, largely due to the possibility of three distinct binary collision types, each requiring a separate interaction potential. For gas mixtures containing more than two components, the situation will become still more complicated, with the number of possible binary collision types increasing in an almost exponential manner with increasing number of components.[8] Consequently, although several reasonable semi-empirical expressions have been proposed to describe the observed behaviour, no generally valid correlation exists. The possibility of examining the phenomena of velocity and temperature slip using direct simulation Monte Carlo techniques [Bird, 1976b] with realistic interaction potentials is currently being investigated. Chatwani and Fieberg [Chatwani and Fieberg, 1981] have performed calculations of this type for monatomic binary mixtures using hard sphere and inverse ninth power law interaction potentials to describe the collision dynamics. The use of such potentials cannot be considered particularly realistic, however, and their results are probably not reliable.

3.6 Measurement of cluster size distributions

3.6.1 Introduction

During the supersonic expansion of a pure gas or gas mixture into a vacuum from a high pressure reservoir, temperatures in the vicinity of the nozzle exit may become low enough while particle densities and collision frequencies remain sufficiently high that the expanding gas particles may condense to form clusters, bound together by weak van der Waals forces. This process was first reported by Becker [Becker *et al*, 1956], who observed the formation

[8] To be precise, the number of possible binary collision types increases according to the algebraic series $n(n+1)/2$, where n is the number of distinct chemical species.

of clusters in supersonic expansions of pure monatomic gases. It was soon realized that other gases could be seeded into an inert carrier gas to produce a wide variety of exotic cluster species, and it is now possible to produce clusters of practically any pure substance or mixture of substances [Levy, 1981; Bartell, 1966]. Furthermore, by careful choice of carrier gas, seed mole fraction and source conditions, it is possible to accurately control the size distributions of the cluster species produced in the expanding jet. It is possible to produce clusters that range in size from simple dimers through to species containing many hundreds or thousands of monomer units [Hagena, 1981]. Following their availability for study, there has been a great amount of interest in these species, which serve to bridge the gap between single atoms or molecules and the macroscopic condensed state.

Unfortunately, the quantification of clustering in supersonic expansions has proven to be an extremely non–trivial task. The most commonly applied technique to the investigation of cluster size distributions over the past three decades of cluster research has been electron impact mass spectrometry. Work performed in recent years has brought to light the rather frustrating realization that extensive fragmentation of most cluster species occurs following electron impact ionization [Milne *et al*, 1972]. Furthermore, cluster size distributions measured using mass spectrometric techniques may be biased due to a variety of instrumental effects, and may in fact bear little resemblance to the true neutral cluster size distribution being investigated. The cluster size distribution also depends upon which region of the supersonic expansion is being sampled, since separation of beam constituents may occur as a result of hydrodynamic focussing, leading to a concentration of heavier cluster species along the centerline axis of the molecular beam. This effect may be enhanced by the presence of skimmers and other collimating devices. Finally, it is important to note that many cluster species are relatively unstable and may loose one or more monomer units during the flight time from their point of formation to the detector.

In this section, cluster size distributions are examined for supersonic expansions of pure argon and for seeded helium expansions containing SO_2, N_2O and H_2O, NO and NO_2, and NH_3. This work was performed prior to commencing the appearance potential measurements discussed in §3.7 in order to to ascertain exactly what types of cluster species could be readily produced in sufficient concentration to allow accurate appearance potential measurements to be performed. The measurement of cluster size distributions is, however, of significant interest for a number of reasons. For example, such measurements are of importance with regard to the characterization and development of cluster beam sources. Measurements of cluster size distributions may also provide valuable information concerning the nucleation and condensation processes occurring during the course of the supersonic expansion. Interest in cluster size distributions has been intensified further in recent years by the observation of intensity anomalies at specific cluster sizes [Shinohara *et al*, 1988; Lifshitz and Louage, 1989]. Such anomalies can be quite dramatic and have been attributed to the existence of particularly stable geometric or electronic structures in the neutral clusters, kinetic effects during the nucleation process, and to special stabilities of fragment ions formed upon ionization of neutral cluster species.

3.6.2 Experimental arrangement

The experimental arrangement employed for the cluster size distribution measurements presented in this section is illustrated schematically in Figure 3.20. The gas or gas mixture under study was expanded from a high pressure reservoir through a commercial electromagnetic pulsed valve (General Valve Corporation, model 9-181) into the first of two differentially pumped vacuum chambers. The high pressure reservoir consisted of one or

more specially adapted large capacity ($\sim 5.0 \times 10^{-2}$ m^{-3}) freon refrigerant containers. The electromagnetic valve was modified by the inclusion of a small stagnation volume between the 0.8 mm orifice of the valve and a 50 μm shaped orifice in the exit plane. This arrangement was found to produce considerably higher cluster densities than those attainable using a conventional 50 μm nozzle. The central core of the pulsed supersonic expansion was sampled by a 1.5 mm diameter skimmer (Beam Dynamics) located approximately 300 nozzle diameters from the nozzle exit. The resultant skimmed supersonic beam was allowed to enter the ion source of a Vacuum Generators SXP300 quadrupole mass filter located 10 cm downstream from the skimmer assembly in the second differentially pumped vacuum chamber. The output current from the mass filter channeltron electron multiplier was converted into a voltage using a suitable load resistor and amplified using the preamplifier supplied with the mass filter controller unit. Amplified signals were monitored on a 20 MHz oscilloscope and averaged using custom written software via a 14-bit analogue-to-digital converter. Averaged signals were stored on the hard disk of the laboratory personal computer as a function of cluster ion mass–to–charge ratio. Mass selection was performed manually. The frequency and duration of beam pulses were controlled by the beam source driver unit, which also served to provide the necessary triggering for the oscilloscope and the mass spectrometer controller unit. The pulsed nozzle was operated at a frequency of 10 Hz, with an estimated open time of not more than 2 ms. During operation of the pulsed nozzle, background pressures of 10^{-5} Torr and 10^{-8} Torr were maintained in the expansion chamber and the mass spectrometer chamber, respectively. All measurements were performed with an electron energy of 25 eV in an effort to reduce any fragmentation of the cluster species following electron impact ionization. Multiplier voltages of between 2.3 kV and 2.5 kV were employed in all cases. It is estimated from the standard deviation of the averaged signals that the experimental error associated with the use of this experimental arrangement was approximately $\pm$ 15% in all cases.

3.6.3 Results and discussion

The production of supersonic cluster beams has been discussed in detail in several excellent review articles [Hagena, 1981; Stein, 1985; Hayes, 1987]. The cluster content of a supersonic beam is found to be most significantly influenced by the geometry of the nozzle, the stagnation pressure, and the initial temperature of the gas sample. It is generally found that both the cluster concentration and the average cluster size increase with increasing stagnation pressure and nozzle diameter, and decrease with increasing reservoir temperature. The onset of clustering in a supersonic expansion may be qualitatively described in terms of a simple macroscopic picture. During the supersonic expansion process, the density and temperature of the expanding jet continue to decrease with increasing distance from the nozzle exit until the supersonic flow becomes *collisionless* and the temperatures associated with the various degrees of freedom of the atoms or molecules in the jet become fixed. The supersonic expansion is a non–equilibrium process, and there may be regions of the expansion zone that are characterized by local pressures greater than the corresponding vapour pressure of the species in the expanding jet. This supersaturation may lead to cluster formation if the time remaining until the flow becomes collision–free is sufficiently long. As stated by Kern *et al* [Kern *et al*, 1985], the formation of a stable cluster entity involves the collisional transfer of all or some of the energy of cluster formation to other jet particles. These stabilizing collisions will raise the kinetic temperature of the resultant supersonic beam and increase its angular divergence.

Clustering may often be enhanced by application of the seeding technique discussed

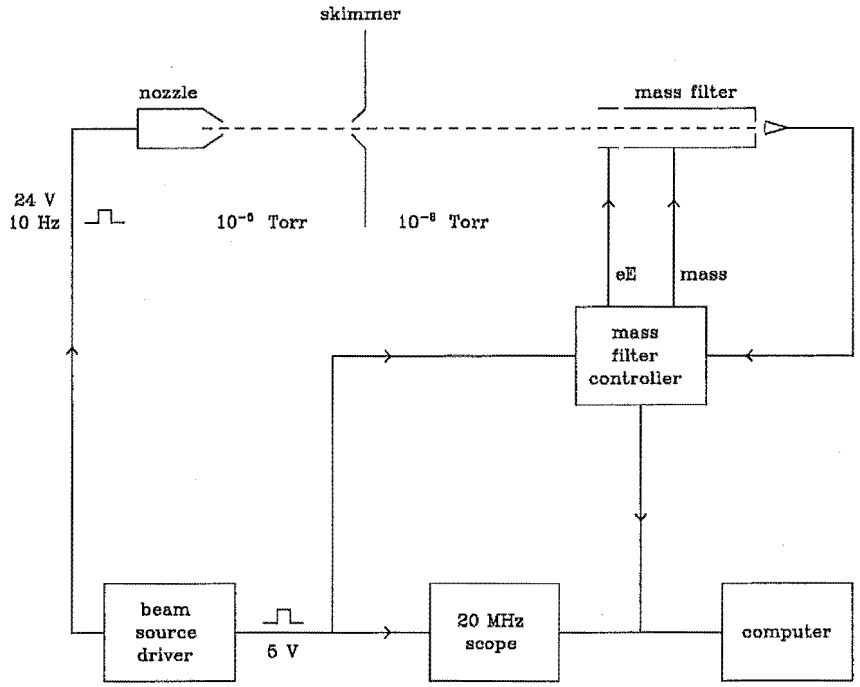

Figure 3.20: Experimental arrangement employed for the measurement of cluster size distributions.

in §1.2 and §3.5. For example, it has been found that seeding a molecular gas M into a less condensible, inert carrier gas such as helium, frequently leads to considerably higher concentrations of clusters M_x than those attainable from expansions of pure M alone. This observation may be explained in terms of more efficient removal of the condensation energy of the cluster species through collisions with the carrier gas. Increasing the carrier gas mole fraction decreases the number of potentially destructive collisions between the M_x cluster species. Eventually this dilution effect will become dominant over any additional cooling, however, and no further gains in total cluster intensity will be achieved by the addition of more carrier gas.

In recent years it has become increasingly clear that cluster ion distributions determined by electron impact ionization mass spectroscopic methods are often severely distorted with respect to the cluster size distribution of the neutral parent beam. The primary cause of this distortion is the often severe fragmentation of the weakly bound

clusters upon ionization [Milne *et al*, 1972], although each of the three major components of the mass spectrometer system (ionizer, mass filter and detector) may contribute to the distortion of the mass spectrum. For example, Buck and Meyer [Buck and Meyer, 1984] have determined that the fragmentation probability of the argon dimer is at least 0.4, and that the argon trimer is detected almost totally as Ar_2^+ following electron impact ionization, as opposed to Ar_3^+. They also found that higher Ar_n clusters were predominantly detected as Ar_2^+.

Argon clusters represent something of an extreme example, but similar trends have been observed for many other species [Ng, 1983], indicating that fragmentation is clearly of considerable significance. Two factors are predominantly responsible for this extensive fragmentation; namely the occurrence of large geometrical changes upon ionization, and the effect of any excess energy incurred as a result of the ionization process. The ground state geometric configuration of a neutral cluster represents a Franck–Condon region of highest transition probability to the ionized cluster ground state potential surface. If the minimum energy geometry of the ionized cluster is significantly different to that of the neutral cluster, the ion will be produced with an excess of vibrational energy. If this excess vibrational energy exceeds the binding energy of the cluster ion in its lowest energy dissociation channel, then fragmentation of the cluster ion will occur.

For rare gas cluster ions such as Ar_n^+, fragmentation simply results in the loss of one or more atoms from the cluster. For clusters of diatomic and polyatomic molecules the situation may be far more complicated. Ionization of these clusters is believed to initially involve the ionization of a single molecule within the cluster, whereupon the cluster may undergo both intramolecular and intermolecular configurational changes. Both types of configurational change may be substantial, but generally only one type will predominate. If intramolecular changes dominate, homolytic fragmentation may be observed, in which a single monomer unit is expelled from the cluster:

$$M_n^+ \longrightarrow M_{n-1}^+ + M$$

If intermolecular configurational changes dominate upon ionization then dissociative ion–molecule reactions of several types may occur, depending upon the chemical composition of the cluster [Ng, 1983]. For clusters of polar hydrogen–containing compounds such as NH_3, H_2O and HCl, *proton transfer ionization* may occur. Proton transfer ionization involves the loss of a neutral atomic or molecular fragment from the cluster, and the protonation of the remaining cluster entity:

$$(HX)_n^+ \longrightarrow (HX)_{n-1}H^+ + X$$

For clusters of a number of molecules (NH_3), proton transfer ionization is exoergic, while for clusters of other species (H_2O) the reaction is endoergic but dominant because of favourable Franck–Condon factors [Tomoda and Kimura, 1983]. For clusters of molecules which do not contain hydrogen, *chemiionization* may occur, in which the initially formed cluster ions may fragment, often via several different reaction channels, to produce a variety of cluster ion fragments and neutral species [Ng, 1983].

There is a common experimental problem in producing low energy electron beams with narrow energy distributions for electron impact ionization, and consequently it is difficult to avoid fragmentation of cluster ions using electron impact sources. Besides fragmentation, another potential cause of distortion to cluster size distributions measured using electron impact quadrupole mass spectrometry arises from the fact that the transmission of ions through a quadrupole mass filter is not necessarily of uniform efficiency

m/z	80	120	160	200	240	280	320
Ion(s)	Ar_2^+	Ar_3^+	Ar_4^+	Ar_5^+	Ar_6^+	Ar_7^+	Ar_8^+

Table 3.6: Mass peak assignments for the argon cluster ion mass spectrum.

over the entire mass range of the instrument [Dawson, 1976]. The mass spectrum of a cluster distribution may also be distorted to some extent by the electron multiplier, since the gain of the multiplier is related to the mass of the resultant ion [Lee *et al*, 1969]. It is generally observed that the gain of an electron multiplier decreases as the square root of the ion mass. Since the quadrupole mass filter is sensitive to both particle momentum and energy, the speed distributions of individual cluster species should also be taken into consideration in any serious attempt to estimate the relative concentrations of neutral van der Waals cluster species formed in supersonic molecular beams. The relative intensities of the neutral clusters could be calculated from a knowledge of the relative ionization cross sections and ion fragmentation patterns of the respective cluster species. Since neither of these two factors are known for most of the system examined here, no attempt has been made to estimate the neutral cluster distributions.

3.6.3.1 Argon clusters

Neutral argon clusters were produced by expanding pure argon at a stagnation pressure of 6600 Torr at 300 K. The resulting argon cluster mass spectrum is illustrated in Figure 3.21 and the various cluster ion peak assignments are listed in Table 3.6. It was possible to detect argon cluster ions up to the maximum mass–to–charge ratio afforded by the SXP300 quadrupole mass filter. As can be seen from Figure 3.21, the mass spectrum was dominated by the Ar_2^+ dimer ion peak at m/z 80. The signal level recorded for Ar_3^+ was observed to be approximately 60% less than that of the dimer ion, in reasonable agreement with the observations of Buck and Meyer [Buck and Meyer, 1984]. Beyond the argon trimer ion a gradual decrease in the Ar_n^+ signal with increasing n was observed, although the Ar_6^+ signal was found to be slightly lower than the Ar_7^+ signal. This small anomaly is most probably related to experimental uncertainty as opposed to the existence of any particularly stable geometric or electronic configuration for the Ar_7^+ ion or its neutral precursor. The stabilities of Ar_n and Ar_n^+ species have been examined by a number of workers [McGinty, 1970; Hiraoka and Mori, 1989], and no stability anomalies have been reported.

3.6.3.2 Ammonia clusters

Neutral NH_3 clusters were prepared by expanding a gas mixture containing 500 Torr of NH_3 and 3400 Torr of helium at a reservoir temperature of 300 K. Using this gas mixture it was possible to measure signal levels for the protonated ammonia cluster ions $(NH_3)_n{\cdot}NH_4^+$ across the entire mass range of the quadrupole mass filter. The resulting cluster ion mass spectrum and the corresponding mass spectrum peak assignments are shown in Figure 3.22 and Table 3.7, respectively. It is well known that ionization of neutral ammonia clusters causes the initially formed cluster ions to undergo the following *proton transfer ionization* reaction

$$(NH_3)_n^+ \longrightarrow (NH_3)_{n-2} \cdot NH_4^+ + NH_2, \tag{3.25}$$

leading to the loss of a neutral NH_2 fragment from the cluster and the formation of an NH_4^+ ion within the remaining cluster entity. The extent of this reaction was such that it was not

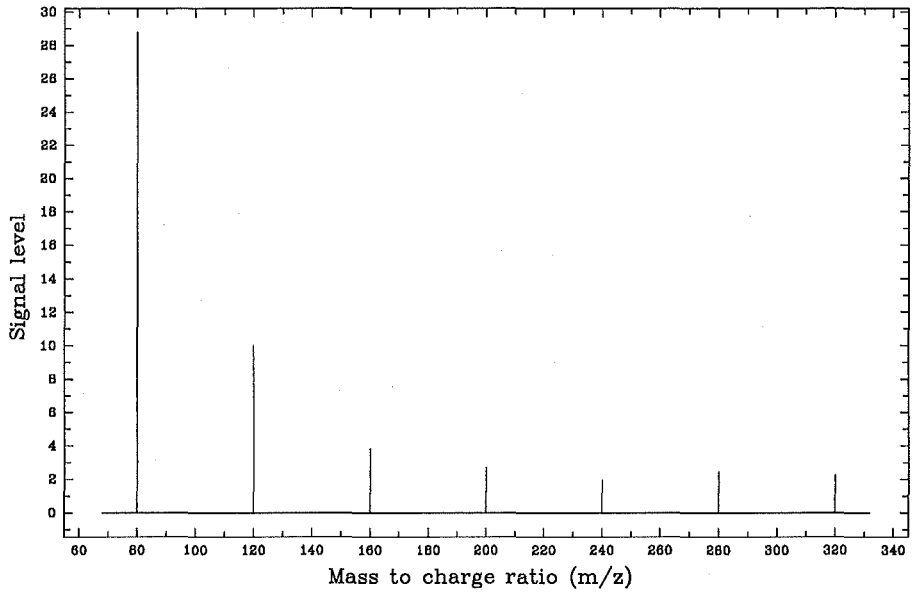

Figure 3.21: Mass spectrum of argon clusters Ar_2 to Ar_8.

possible to detect signals corresponding to the unprotonated $(NH_3)_n^+$ ions using the same amplification to that employed for measurement of the $(NH_3)_n{\cdot}NH_4^+$ data. In addition to the internal ion–molecule process described by reaction (3.25), ammonia clusters may also undergo the following unimolecular fragmentation process [Coolbaugh *et al*, 1989]:

$$(NH_3)_n^+ \longrightarrow (NH_3)_{n-1} \cdot NH_2^+ + H \tag{3.26}$$

This reaction is not favoured under most conditions, however, and no species corresponding to the general formula $(NH_3)_n{\cdot}NH_2^+$ were detected in the present study. It should be noted that the NH_3 used for these measurements was not of particularly high quality and contained a small quantity (3% to 5%) of H_2O. While mixed clusters of NH_3 and H_2O have been observed by a number of workers [Shinohara *et al*, 1988], no such species were detected in this investigation.

Unless there are particularly stable geometric or electronic configurations at specific clusters sizes, it is generally observed that the signals for a particular cluster type, M_x, gradually decrease with increasing cluster size. This gradual decrease in signal level may be attributed to decreasing neutral cluster concentrations with increasing cluster size and to increased fragmentation following ionization of the neutral species with increasing neutral cluster size. The high signal level observed in Figure 3.22 for $(NH_3)_4{\cdot}NH_4^+$ at m/z 86 suggests that this species is a particularly stable ion. This intensity anomaly has been reported by a number of workers [Wei *et al*, 1990a] and may be attributed to the high stability afforded by the presence of a complete solvation shell of four NH_3 molecules about the central ammonium ion. Further small intensity anomalies which are apparent on Figure 3.22 at higher mass are somewhat more difficult to explain and may be due simply to experimental error. The slight increase observed for the $(NH_3)_{11}{\cdot}NH_4^+$ ion at m/z 205 is consistent with the results of Wei *et al* [Wei *et al*, 1990a], however, who

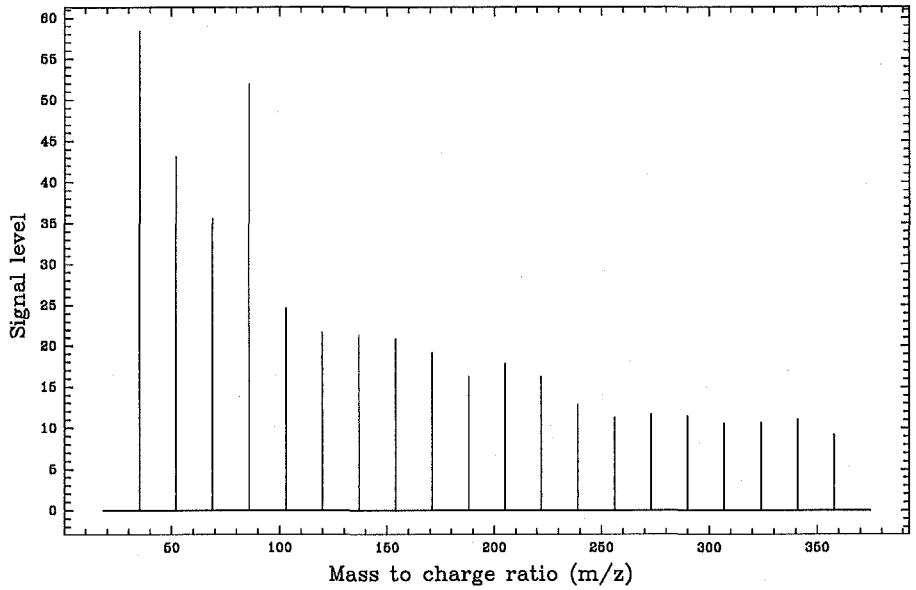

Figure 3.22: Mass spectrum of protonated ammonia clusters.

m/z	Ion(s)	m/z	Ion(s)
35	$NH_3{\cdot}NH_4^+$	205	$(NH_3)_{11}{\cdot}NH_4^+$
52	$(NH_3)_2{\cdot}NH_4^+$	222	$(NH_3)_{12}{\cdot}NH_4^+$
69	$(NH_3)_3{\cdot}NH_4^+$	239	$(NH_3)_{13}{\cdot}NH_4^+$
86	$(NH_3)_4{\cdot}NH_4^+$	256	$(NH_3)_{14}{\cdot}NH_4^+$
103	$(NH_3)_5{\cdot}NH_4^+$	273	$(NH_3)_{15}{\cdot}NH_4^+$
120	$(NH_3)_6{\cdot}NH_4^+$	290	$(NH_3)_{16}{\cdot}NH_4^+$
137	$(NH_3)_7{\cdot}NH_4^+$	307	$(NH_3)_{17}{\cdot}NH_4^+$
154	$(NH_3)_8{\cdot}NH_4^+$	324	$(NH_3)_{18}{\cdot}NH_4^+$
171	$(NH_3)_9{\cdot}NH_4^+$	341	$(NH_3)_{19}{\cdot}NH_4^+$
188	$(NH_3)_{10}{\cdot}NH_4^+$	358	$(NH_3)_{20}{\cdot}NH_4^+$

Table 3.7: Protonated ammonia cluster mass spectrum peak assignments.

m/z	Ion(s)	m/z	Ion(s)
96	$[SO_2{\cdot}S]^+$, $[SO_2{\cdot}O_2]^+$	224	$[(SO_2)_3{\cdot}S]^+$, $[(SO_2)_3{\cdot}O_2]^+$
112	$[SO_2{\cdot}SO]^+$	240	$[(SO_2)_3{\cdot}SO]^+$
128	$(SO_2)_2^+$	256	$(SO_2)_4^+$
160	$[(SO_2)_2{\cdot}S]^+$, $[(SO_2)_2{\cdot}O_2]^+$	288	$[(SO_2)_4{\cdot}S]^+$, $[(SO_2)_4{\cdot}O_2]^+$
176	$[(SO_2)_2{\cdot}SO]^+$	304	$[(SO_2)_4{\cdot}SO]^+$
192	$(SO_2)_3^+$	320	$(SO_2)_5^+$

Table 3.8: Sulphur dioxide cluster ion mass spectrum peak assignments.

determined that the binding energy of $(NH_3)_{11}{\cdot}NH_4^+$ is approximately 50 meV greater than that of $(NH_3)_{10}{\cdot}NH_4^+$ or $(NH_3)_{12}{\cdot}NH_4^+$.

3.6.3.3 Sulphur dioxide clusters

Neutral sulphur dioxide clusters were produced by expanding a gas mixture containing 250 Torr of SO_2 and 3700 Torr of helium at a reservoir temperature of 300 K. The resulting cluster ion mass spectrum is illustrated in Figure 3.23 and possible formulae for the ions corresponding to the various peaks observed on the mass spectrum are listed in Table 3.8. The mass spectrum measured for the sulphur dioxide system was found to be characterized by a distinctive fragmentation pattern whereby for each $(SO_2)_n^+$ $(2 \leq n \leq 5)$ parent cluster ion peak there were two additional considerably smaller peaks at lower m/z which may be attributed to the cluster fragment ions $[(SO_2)_n{\cdot}S]^+$, $[(SO_2)_n{\cdot}O_2]^+$, and $[(SO_2)_n{\cdot}SO]^+$. The various fragmentation processes leading to the formation of these species may be summarized as follows:

$$(SO_2)^+(SO_2)_{n-1} \longrightarrow [(SO_2)_{n-1} \cdot S]^+ + O_2 \quad (3.27)$$

$$\longrightarrow [(SO_2)_{n-1} \cdot O_2]^+ + S \quad (3.28)$$

$$\longrightarrow [(SO_2)_{n-1} \cdot SO]^+ + O \quad (3.29)$$

Considering the relative amplitudes of the fragment ion peaks, it is clear that reaction (3.29) represents the most favourable fragmentation process. The products of reactions (3.27) and (3.28) have identical masses and could not easily be distinguished using the present experimental arrangement.[9] It is likely, however, that both reaction (3.27) and reaction (3.28) occur to some extent. It is interesting to note that little work has been done on SO_2 clusters, which is somewhat surprising, considering the important role of SO_2 in atmospheric pollution.

It should be mentioned that it was necessary to remove and thoroughly clean the nozzle assembly and the gas inlet system prior to performing the measurements described here for the SO_2 cluster species. Initial attempts to produce SO_2 clusters resulted in the nozzle becoming partially blocked. Blockage of the nozzle was indicated by a substantial decline in the beam signal over a short period of pulsed nozzle operation. Both the nozzle and the gas inlet system were found to contain traces of a fine white powder, believed to be $(NH_4)_2SO_4$ or $(NH_4)_2SO_3$ formed by reaction of the SO_2 gas with residual NH_3 and H_2O in the inlet system which had not been successfully flushed away following the completion of

[9] Sulphur has a naturally occurring isotope of mass 34 amu with 4.2% abundance. It may be possible to distinguish between the products of reactions (3.27) and (3.28) using a somewhat more sensitive experimental technique than that employed here by checking for species containing this sulphur isotope.

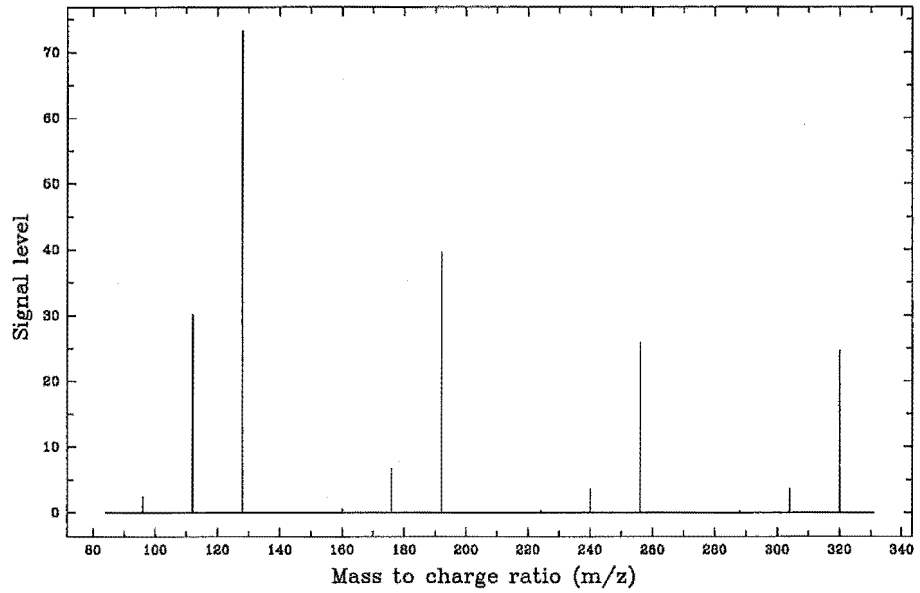

Figure 3.23: Mass spectrum of $(SO_2)_n$ clusters.

the preceeding investigation of NH_3 clusters. Affected components were carefully washed with distilled water followed by pure ethanol to remove the offending material. Removing and cleaning the nozzle assembly was a frustrating and time consuming exercise and consequently extra care was taken following this incident to ensure that the inlet system was completely free of any potentially reactive species prior to commencing work with a new gas mixture.

3.6.3.4 Mixed clusters of N_2O and H_2O

Clusters of N_2O and mixed clusters of N_2O and H_2O were produced by expanding a gas mixture containing 500 Torr of N_2O and approximately 30 Torr of water vapour made up to a total pressure of 3500 Torr with helium at a reservoir temperature of 300 K. The resulting cluster ion mass spectrum is illustrated in Figure 3.24 and the species responsible for the various peaks on the mass spectrum are listed in Table 3.9. Using the specified gas mixture it was possible to detect the cluster ions $(N_2O)_n^+$ $(2 \leq n \leq 8)$ and the cluster ion fragments $[(N_2O)_n{\cdot}NO]^+$ $(1 \leq n \leq 7)$ along with the mixed cluster ions $[(N_2O)_n{\cdot}H_2O]^+$ $(1 \leq n \leq 7)$ and $[(N_2O)_n{\cdot}(H_2O)_2]^+$ $(1 \leq n \leq 7)$. No pure or protonated water cluster ions were detected, although such species have been investigated by a number of workers [Dreyfuss and Wachman, 1982]. Failure to observe these species in the present study may be attributed to the low H_2O concentration in the expanded gas mixture. At such a low concentration, the number of collisions between H_2O molecules will be small compared to the number of collisions between H_2O and N_2O or helium.

The amplitude of the $(N_2O)_3^+$ cluster ion signal was found to be slightly lower than both the $(N_2O)_4^+$ and $(N_2O)_5^+$ signals. This intensity anomaly is most probably due to experimental error, since it has been found that the binding energy of $(N_2O)_n^+$ cluster ions decreases monotonically with increasing n [Cameron *et al*, 1993]. Significant contributions

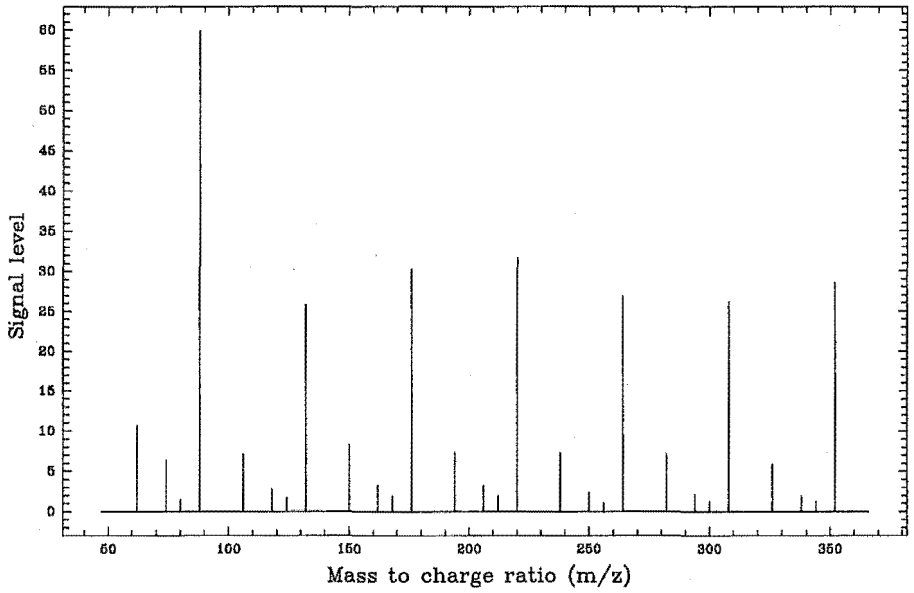

Figure 3.24: Mass spectrum obtained from N_2O–H_2O mixture.

m/z	Ion(s)	m/z	Ion(s)
62	$[N_2O{\cdot}H_2O]^+$	212	$[(N_2O)_4{\cdot}(H_2O)_2]^+$
74	$[N_2O{\cdot}NO]^+$	220	$(N_2O)_5^+$
80	$[N_2O{\cdot}(H_2O)_2]^+$	238	$[(N_2O)_5{\cdot}H_2O]^+$
88	$(N_2O)_2^+$	250	$[(N_2O)_5{\cdot}NO]^+$
106	$[(N_2O)_2{\cdot}H_2O]^+$	256	$[(N_2O)_5{\cdot}(H_2O)_2]^+$
118	$[N_2O{\cdot}NO]^+$	264	$(N_2O)_6^+$
124	$[(N_2O)_2{\cdot}(H_2O)_2]^+$	282	$[(N_2O)_6{\cdot}H_2O]^+$
132	$(N_2O)_3^+$	294	$[(N_2O)_6{\cdot}NO]^+$
150	$[(N_2O)_3{\cdot}H_2O]^+$	300	$[(N_2O)_6{\cdot}(H_2O)_2]^+$
162	$[(N_2O)_3{\cdot}NO]^+$	308	$(N_2O)_7^+$
168	$[(N_2O)_3{\cdot}(H_2O)_2]^+$	326	$[(N_2O)_7{\cdot}H_2O]^+$
176	$(N_2O)_4^+$	338	$[(N_2O)_7{\cdot}NO]^+$
194	$[(N_2O)_4{\cdot}H_2O]^+$	344	$[(N_2O)_7{\cdot}(H_2O)_2]^+$
206	$[(N_2O)_4{\cdot}NO]^+$	352	$(N_2O)_8^+$

Table 3.9: Possible N_2O–H_2O cluster ion mass spectrum peak assignments.

to the $(N_2O)_4^+$ and $(N_2O)_5^+$ signals from fragmentation of higher $(N_2O)_n^+$ ions cannot be discounted however.

In addition to forming stable species or undergoing homolytic fragmentation, initially formed $(N_2O)_n^+$ cluster ions must be expected to undergo the following fragmentation processes:

$$(N_2O)^+(N_2O)_{n-1} \longrightarrow [(N_2O)_{n-1} \cdot NO]^+ + N \quad (3.30)$$

$$\longrightarrow [(N_2O)_{n-1} \cdot N]^+ + NO \quad (3.31)$$

$$\longrightarrow [(N_2O)_{n-1} \cdot O]^+ + N_2 \quad (3.32)$$

The species $[(N_2O)_n \cdot N]^+$ and $[(N_2O)_n \cdot O]^+$ were not detected, indicating that reaction (3.30) represents the most energetically favourable fragmentation channel for the initially formed $(N_2O)_n^+$ species. It is most likely, however, that reactions (3.31) and (3.32) will occur to some extent, and failure to observe the products of these reactions may be due to the low sensitivity of the experimental arrangement employed for the measurements described here. Mixed clusters containing more than two H_2O molecules were also not observed, presumably due to the low concentration of H_2O in the expanded gas mixture. In addition, no mixed cluster ion fragments such as $[(H_2O)_2 \cdot NO]^+$ or $[(N_2O)_n \cdot H_3O]^+$ were detected, suggesting that fragmentation involving the loss of an entire H_2O molecule may represent the most favourable fragmentation process for the mixed cluster ions $[(N_2O)_n \cdot H_2O]^+$ and $[(N_2O)_n \cdot (H_2O)_2]^+$.

3.6.3.5 Mixed clusters of NO and NO_2

Mixed clusters of NO and NO_2 were formed by expanding a gas mixture containing 400 Torr of NO and 100 Torr of NO_2 made up to a total pressure of 3900 Torr with helium at a reservoir temperature of 300 K. The resulting cluster ion mass spectrum is illustrated in Figure 3.25 and possible formulae for species which may be assigned to the various peaks observed on the mass spectrum are listed in Table 3.10. With the exception of the first two peaks on the mass spectrum, the signal levels recorded for this system were somewhat low in comparison to those obtained for most of the other cluster systems examined in this section and, in contrast to the SO_2 and N_2O–H_2O systems, no consistent fragmentation patterns were observed. The majority of the species detected were either mixed cluster ions or cluster ion fragments, with $(NO)_2^+$ being the only homogeneous cluster ion possibly observed. Despite the low concentration of NO_2 in the expanded gas mixture relative to NO, no mixed cluster ions having the general formula $[(NO_2)_m \cdot (NO)_n]^+$ were observed with $m < n$. It was not possible to unambiguously assign some of the peaks seen on the mass spectrum to a single cluster ion, although at mass–to–charge ratios where two ions have been specified in Table 3.10, it is most likely that both species partially contribute to the overall signal. While no valid assumptions can be made regarding individual contributions to the signals measured at m/z 60, 76, and 106, it is reasonable to expect that the strong signal observed at m/z 46 was largely due to NO_2^+.

The species $[(NO)_n \cdot X]^+$ (where X is N or O) and $[(NO_2)_n \cdot N]^+$ may be produced by fragmentation of the homogeneous cluster ions $(NO)_n^+$ and $(NO_2)_n^+$, respectively, or by fragmentation of the mixed cluster ions $[(NO_2)_m \cdot (NO)_n]^+$. Initially formed $[(NO_2)_m \cdot (NO)_n]^+$ $(m, n \geq 1)$ mixed cluster ions may be anticipated to form stable species or undergo a variety of fragmentation processes, which may be summarized as follows:

$$[(NO_2)_m \cdot (NO)_n]^+ \longrightarrow [(NO_2)_{m-1} \cdot (NO)_n \cdot N]^+ + O_2 \quad (3.33)$$

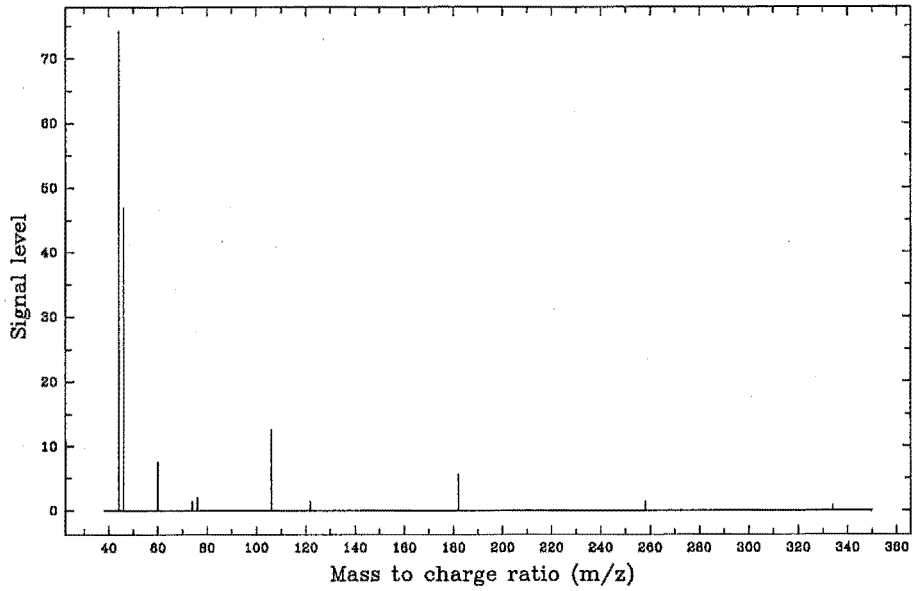

Figure 3.25: Mass spectrum obtained from NO–NO_2 mixture.

m/z	Ion(s)	m/z	Ion(s)
44	$(NO{\cdot}N)^+$	106	$[(NO)_3{\cdot}O]^+$, $[(NO_2)_2{\cdot}N]^+$
46	NO_2^+, $(NO{\cdot}O)^+$	122	$[(NO_2)_2{\cdot}NO]^+$
60	$(NO)_2^+$, $(NO_2{\cdot}N)^+$	182	$[(NO_2)_3{\cdot}NO{\cdot}N]^+$
74	$[(NO)_2{\cdot}N]^+$	258	$[(NO_2)_4{\cdot}(NO)_2{\cdot}N]^+$
76	$[(NO)_2{\cdot}O]^+$, $[NO_2{\cdot}NO]^+$	334	$[(NO_2)_5{\cdot}NO]^+$

Table 3.10: Possible NO–NO_2 cluster ion mass spectrum peak assignments.

$$\longrightarrow [(NO_2)_{m-1}\cdot(NO)_n\cdot O]^+ + NO \quad (3.34)$$
$$\longrightarrow [(NO_2)_{m-1}\cdot(NO)_n\cdot O_2]^+ + N \quad (3.35)$$
$$\longrightarrow [(NO_2)_{m-1}\cdot(NO)_n]^+ + NO_2 \quad (3.36)$$
$$\longrightarrow [(NO_2)_m\cdot(NO)_{n-1}\cdot N]^+ + O \quad (3.37)$$
$$\longrightarrow [(NO_2)_m\cdot(NO)_{n-1}\cdot O]^+ + N \quad (3.38)$$
$$\longrightarrow [(NO_2)_m\cdot(NO)_{n-1}]^+ + NO \quad (3.39)$$

The species $[(NO_2)_m{\cdot}(NO)_n{\cdot}O_2]^+$ were not observed, indicating that reaction (3.35) is not energetically favourable. As stated above, $(NO)_2^+$ was the only homogeneous cluster ion that was possibly observed in the present study. It is likely, however, that fragmentation processes of both homogeneous and mixed cluster ions contribute to the formation of the cluster ion fragments $[(NO)_n{\cdot}N]^+$, $[(NO)_n{\cdot}O]^+$ and $[(NO_2)_n{\cdot}N]^+$. It is similarly reasonable to expect that the species $[(NO_2)_n{\cdot}NO]^+$ ($n = 1, 2, 5$) may be formed by stabilization of initially formed mixed cluster ions as well as by reactions (3.36) and (3.39). Failure to observe homogeneous cluster ions other than possibly $(NO)_2^+$ suggests that such species

are highly unstable and readily undergo fragmentation.

The strong signal observed at m/z 44 is somewhat difficult to explain. It is possible that the cluster ion fragments $[(NO)_n \cdot (NO_2)_m \cdot N]^+$ produced by reactions (3.33) and (3.37) are not particularly stable for some m and n and may undergo rearrangement and further fragmentation, resulting in the formation of $(NO \cdot N)^+$. Observation of the $(NO)_2 \cdot N^+$ and $(NO_2)_m(NO)_n N^+$ cluster fragment ions lends some support to this assignment.

3.6.4 Conclusion

Cluster ion mass spectra have been examined for supersonic expansions of pure argon and for expansions of seeded helium expansions containing SO_2, N_2O and H_2O, NO and NO_2, and NH_3. The recorded mass spectra indicated that most of the cluster species formed in the expanding jet incurred extensive fragmentation following electron impact ionization. Fragmentation of ammonia clusters resulted in the formation of the protonated species $(NH_3)_n \cdot NH_4^+$ while for the SO_2 and mixed cluster systems a variety of cluster ion fragments were detected in addition to non–fragmented species. Intensity anomalies were observed for the species $(NH_3)_4 \cdot NH_4^+$ and $(NH_3)_{11} \cdot NH_4^+$, indicating that particularly stable geometric or electronic configurations exist for these ions. It should be mentioned that cluster ion mass spectra were also briefly examined for several other gas mixtures. Using a gas mixture containing 500 Torr of CO_2 and 3500 Torr of helium it was possible to detect the cluster ions $(CO_2)_n^+$ $(2 \leq n \leq 8)$ while for a mixture containing 200 Torr of HCl and 3300 Torr of helium, only the $(HCl)_2^+$ dimer ion was detected. It is important to emphasize that the results presented in this section cannot be used to obtain quantitative information regarding neutral cluster size distributions or to estimate the extent of any of the fragmentation processes described in this study. The purpose of the present study was simply to determine the types of clusters and cluster ions which may be prepared in the molecular beam apparatus prior to an investigation of cluster ion appearance potentials and fragmentation mechanisms.

3.7 Appearance potentials of small cluster ions and their fragments

3.7.1 Introduction

Atomic and molecular clusters have been the subject of extensive experimental and theoretical research activity for more than thirty years. The fundamental aim of this research effort has been to gain an improved understanding of the evolution from the atomic or molecular properties of a system to its bulk phase properties with increasing cluster size. For example, atomic and molecular clusters represent small, isolated systems which may be used to test and further our understanding of amorphous solids, catalysis, liquid structure and solvation effects. Despite the intensive research activity involved, however, the characterization of cluster species is still in its early stages. Considerably more particle specific information will be required in order to develop a complete understanding of the mechanisms of cluster formation and to elucidate the exact nature of various factors governing the structure and stability of such species. The use of supersonic molecular beams to generate cluster species which are rotationally and vibrationally cooled represents an excellent means of obtaining this important information. The essentially collision–free environment of the molecular beam allows clusters formed in the supersonic expansion to be studied in the absence of any further aggregation, and problems related to particle

specificity may be largely resolved through the application of ionization and mass filtering techniques.

In this section, the appearance potentials of the cluster ions $(CO_2)_n^+$, $(N_2O)_n^+$ $(2 \leq n \leq 4)$ and $(NH_3)_nH^+$ $(1 \leq n \leq 8)$, and the cluster ion fragments $(N_2O{\cdot}O)^+$ and $(N_2O{\cdot}NO)^+$ are investigated using electron impact ionization. The chemistry of CO_2 cluster ions is of considerable interest in ionospheric studies of the predominantly CO_2 containing atmospheres of Mars and Venus [Mautner and Field, 1977] while ammonia clusters are of interest with regard to the energetics of gas phase proton solvation. The N_2O molecule is isoelectronic with CO_2 and its clusters may therefore be expected to exhibit similar binding and fragmentation characteristics to those of CO_2. Accurate appearance potentials are required for the determination of binding energies and enthalpy changes associated with various steps in cluster formation. A knowledge of cluster ion appearance potentials may also be used to obtain valuable information about rearrangement processes and internal cluster ion–molecule reactions which may occur following electron impact or photon ionization. Appearance potentials for $(CO_2)_n^+$ $(2 \leq n \leq 4)$, $(N_2O)_2^+$ $(2 \leq n \leq 4)$, $(N_2O{\cdot}NO)^+$ and $(NH_3)_nH^+$ $(1 \leq n \leq 3)$ have been previously reported by a number of workers [Klots and Compton, 1978; Jones and Taylor, 1978; Linn and Ng, 1981; Stephan *et al*, 1982a; Kamke *et al*, 1989; Stephan *et al*, 1982b; Ceyer *et al*, 1979] while those determined for $(N_2O{\cdot}O)^+$ and $(NH_3)_nH^+$ $(4 \leq n \leq 8)$ represent new results.

3.7.2 Experimental arrangement

The experimental arrangement used to collect the ionization efficiency curve data presented in this investigation is illustrated schematically in Figure 3.26. The gas mixture under study was expanded from a high pressure stagnation reservoir through a commercial electromagnetic valve (General Valve Corporation, model 9-181) into the first of two differentially pumped vacuum chambers. The valve was modified by the inclusion of a small stagnation volume between the 0.8 mm orifice in the valve and a 50 μm shaped orifice in the exit plate. This arrangement gave higher cluster densities than those obtained from a valve fitted with a 50 μm orifice alone. The high pressure ($\sim$ 4000 Torr) reservoir consisted of a specially adapted large capacity ($\sim 5.0 \times 10^{-2}$ m^3) freon refrigerant container. The central core of the pulsed supersonic expansion was sampled by a 1.5 mm skimmer (Beam Dynamics) located approximately 300 nozzle diameters (15 mm) from the nozzle exit. The skimmed supersonic beam was allowed to enter the ion source of a Vacuum Generators SXP300 quadrupole mass filter located 10 cm downstream from the skimmer assembly in the second differentially pumped chamber. Output pulses from the channeltron electron multiplier associated with the mass filter were passed through a high-Q 2 MHz notch filter to remove any pick–up introduced by the mass spectrometer radio frequency generator and amplified with a fast preamplifier followed by an amplifier and pulse amplitude discriminator combination.

In order to distinguish between the beam signal and background pulses, a simple gating arrangement was employed. The output from the pulse counting preamplifier was split and fed into two and-gates, as shown in Figure 3.27. Using a pulse generator and a custom built pulse delay unit, two windows of identical width were positioned over different regions of the signal pulse envelope as viewed on a 20 MHz oscilloscope. The first window was carefully placed over the arrival time distribution of the supersonic beam while the second was positioned somewhat later in time, windowing only background noise. The windowing pulses provided the other input to each of the two and-gates. The output of the first and-gate (gate 1) therefore consisted of both beam signal and background

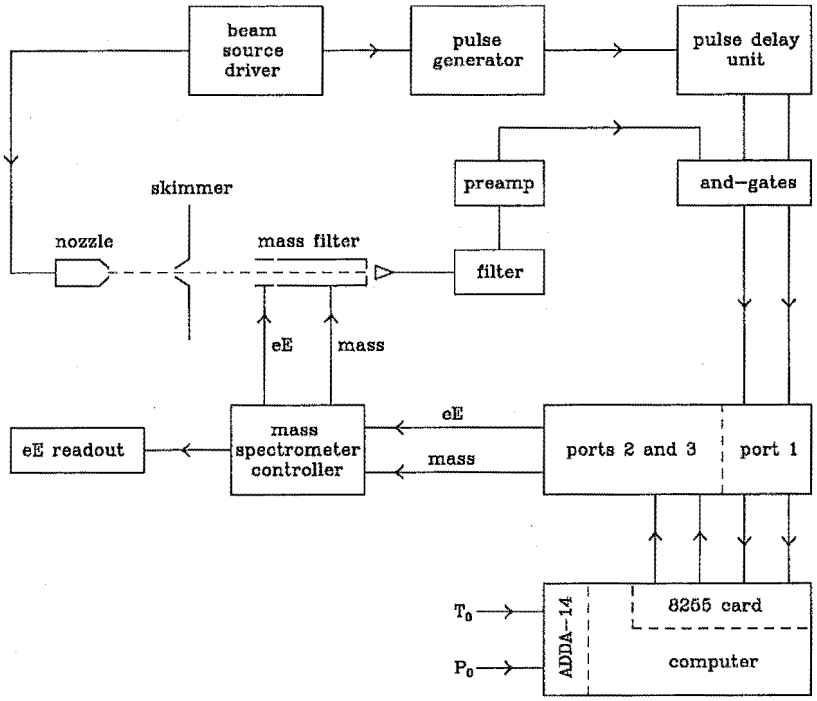

Figure 3.26: Experimental arrangement employed for the collection of ionization efficiency curve data.

pulses and the output of the second and-gate (gate 2) consisted of background pulses only. Output pulses from the two and-gates were counted using a counter–timer card and recorded via custom written interfacing software. Computer control of electron energy and mass selection was achieved using custom built 12-bit digital–to–analogue converters incorporated into the mass spectrometer controller unit. The selected mass was displayed on the front panel of the controller and the electron energy was monitored using a digital volt meter.

The frequency and duration of beam pulses was controlled by the beam source driver unit, which also served to provide the necessary triggering for the pulse generator. The pulsed nozzle was generally operated at a frequency of 10 Hz, with an estimated open time of not more than 2 ms. During normal operation of the nozzle, background pressures of 10^{-5} Torr and 10^{-8} Torr were maintained in the expansion chamber and the mass spectrometer chamber, respectively. The temperature of the nozzle was monitored using

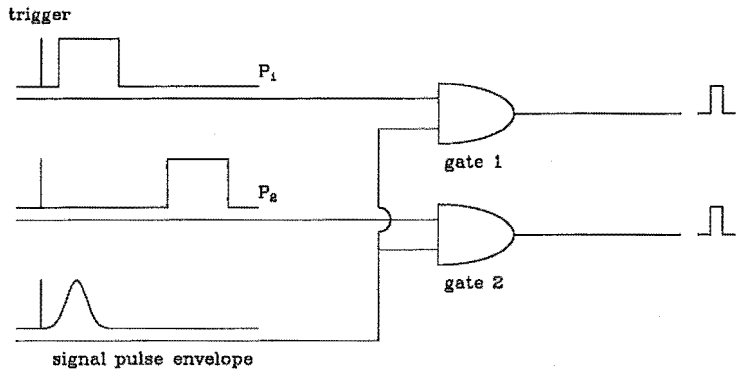

Figure 3.27: Gating arrangement employed to distinguish between beam signal and background pulses.

a thermocouple attached to the body of the valve. The potential difference across the thermocouple was calibrated and amplified using a simple fixed gain circuit, the output of which was supplied to one of sixteen 14-bit analogue–to–digital conversion channels monitored by the interfacing software. The reservoir pressure was monitored using a MKS Baratron (10000 Torr) connected to a MKS type 286 controller. The calibrated 0 V to 10 V output of the MKS controller was periodically checked by the data acquisition software via one of the 14-bit analogue–to–digital conversion channels.

3.7.3 Results and discussion

Neutral CO_2, N_2O and NH_3 clusters were produced by expanding gas mixtures containing 100 Torr of argon and 500 Torr of CO_2, N_2O, or NH_3 made up to a total pressure of approximately 4000 Torr with helium at a reservoir temperature of 295 K. These mixtures were found to produce supersonic beams of sufficiently high cluster content for the reliable determination of appearance potentials for the cluster ions $(CO_2)_n^+$, $(N_2O)_n^+$ $(2 \leq n \leq 4)$ and $(NH_3)_nH^+$ $(1 \leq n \leq 8)$. For the N_2O mixture it was also possible to estimate the appearance potentials of the cluster ion fragments $(N_2O{\cdot}O)^+$ and $(N_2O{\cdot}NO)^+$. Additional ionization efficiency curves were measured for any ions which may be observed from the fragmentation of the respective monomers following electron impact ionization. While monomer and cluster speed distributions were not measured, the parallel translational temperature of the cluster beams may be expected to be close to the value of approximately 6 K predicted for a pure helium beam under the same source conditions [Cameron and Harland, 1991]. The extent of rotational cooling which occurs during the supersonic expansion of these gas mixtures is unclear and will depend greatly upon the efficiency of rotational to translational energy transfer in collisions between the molecules and clusters

and the rare gas atoms. It is tentatively suggested that the terminal rotational temperatures of the molecules and clusters will be less than 40 K in all cases. No clusters containing helium or argon atoms were observed for any of the gas mixtures examined.

Ion counts were measured at up to 100 points, scanning from high to low electron energy in 0.1 eV steps. Ions were typically counted for a period of 5 s at each electron energy and this operation was repeated some 15 to 20 times to obtain an average count with an acceptable standard error. Average ion counts were also recorded at an electron energy of 70 eV at the beginning and end of each run. Depending upon the number of ions examined, a run could take up to three or four hours to complete and it was therefore necessary to consider any potential sources of long term experimental instability which may adversely affect the accuracy of the measurements. In particular, it is well known that the cluster content of supersonic molecular beams is highly sensitive to variations in source pressure and temperature [Scoles, 1988], and these variables were carefully monitored throughout each run. Due to the small flow of gas through the 50 μm nozzle, the reservoir pressure was observed to drop by not more than 2% or 3% over a four hour period of continuous pulsed nozzle operation. No change in nozzle temperature was detected. The gas inlet system was flushed with helium and thoroughly pumped prior to commencing measurements with a new gas mixture.

Electron impact ionization techniques have been widely used for over fifty years in experiments directed towards the investigation of ionization and fragmentation energetics. Despite their extensive use, electron impact techniques do suffer from two main problems, and it is important to be aware of these potential sources of error. The energy spread of the ionizing electron beam is often significant,[10] and the actual mean energy of the electron beam may differ considerably from the nominal electron energy expected from the applied electrode potentials. It is therefore vitally important to suitably account for the spread of the ionizing electron beam and to accurately calibrate the energy scale by performing concurrent measurements with one or more reference gases for which the quantity of interest is accurately known. If the distribution of electron energies is known or can be accurately measured, then in some situations it may be possible to deconvolve the energy distribution from the measured ion signal [Morrison, 1963; Harland *et al*, 1970]. In the case of appearance potential measurements, numerical deconvolution is generally not satisfactory, especially close to the ionization threshold where the signal–to–noise ratio is low. Consequently it is usually necessary to resort to somewhat more conventional methods such as threshold extrapolation for the determination of appearance potentials. There are a variety of accurate extrapolation methods which may be used to correct for the finite width of the electron energy distribution by careful comparison of the unknown and calibrant ion signals in the threshold region of the ionization efficiency curves [McDowell, 1963; Kiser, 1965]. The semi-log plot method [McDowell, 1963; Kiser, 1965] was used to determine the cluster ion appearance potentials presented in this investigation with an estimated accuracy of $\pm$ 0.1 eV in all cases. This error limit includes both statistical and systematic errors. Although nominally less accurate than photon ionization methods, this precision is sufficient to allow critical comparisons to be made between the present results and those of previous experimental and theoretical investigations. Argon was used as the electron energy calibrant for all of the appearance potential measurements, and the appearance potential of Ar^+ was taken to be 15.76 $\pm$ 0.01 eV [Dibeler and Reese, 1966]. Corrections to the energy scale based on the known appearance potential of Ar^+ were typically on the order of 0.2 eV to 0.5 eV.

[10] The spread of the ionizing electron beam employed for the measurements described here was estimated to be approximately 850 meV FWHM.

Ion	A.P. (eV)	Ion	A.P. (eV)	Ion	A.P. (eV)
$(CO_2)_2^+$	13.1	$(N_2O{\cdot}O)^+$	14.6	NH_4^+	9.7
$(CO_2)_3^+$	12.8	$(N_2O{\cdot}NO)^+$	14.3	$(NH_3)_2H^+$	9.2
$(CO_2)_4^+$	12.6		17.0	$(NH_3)_3H^+$	9.0
		$(N_2O)_2^+$	12.3	$(NH_3)_4H^+$	8.9
		$(N_2O)_3^+$	12.1	$(NH_3)_5H^+$	8.9 (8.85)
		$(N_2O)_4^+$	12.0	$(NH_3)_6H^+$	8.8 (8.81)
				$(NH_3)_7H^+$	8.8 (8.78)
				$(NH_3)_8H^+$	8.7 (8.72)

Table 3.11: Summary of measured appearance potentials. All data were reproducible within ± 0.1 eV or better.

Illustrative examples of ionization efficiency curves measured for $(CO_2)_2^+$, $(CO_2)_3^+$ and $(CO_2)_4^+$ are shown in Figure 3.28, where the observed ion count is plotted as a function of the uncorrected ionizing electron energy. Calibration of the electron energy scale was achieved by concurrently measuring the appearance potential for Ar^+, and corrected values of the measured $(CO_2)_2^+$, $(CO_2)_3^+$ and $(CO_2)_4^+$ appearance potentials are presented in Table 3.11. These appearance potentials may be directly compared with values obtained in several previous investigations. In an early study, Klots and Compton [Klots and Compton, 1978] reported that they could detect only marginal differences between the appearance potentials of the CO_2 monomer, dimer and trimer positive ions using a retarding potential difference technique with 0.1 eV resolution. In a slightly more recent photon ionization study of CO_2 clusters formed in a supersonic molecular beam, Linn and Ng [Linn and Ng, 1981] determined appearance potentials of 13.32 ± 0.02 eV, 13.24 ± 0.02 eV and 13.18 ± 0.02 eV for $(CO_2)_2^+$, $(CO_2)_3^+$ and $(CO_2)_4^+$, respectively. In another photon ionization study, Jones and Taylor [Jones and Taylor, 1978] obtained an appearance potential of 13.40 eV for $(CO_2)_2^+$, while Stephan *et al* [Stephan *et al*, 1982a] determined a value of 13.1 ± 0.2 eV for the same ion using electron impact ionization methods and linear extrapolation [McDowell, 1963; Kiser, 1965]. In contrast to Klots and Compton, a significant difference between the appearance potentials of the CO_2 monomer and cluster ions was observed here, and the appearance potentials of the CO_2 cluster ions determined in the present study were seen to decrease with increasing cluster size, in qualitative agreement with the results of Linn and Ng.

As can be seen from Table 3.11, the appearance potential of $(CO_2)_2^+$ determined in the present study using electron impact ionization is identical to the value obtained by Stephan *et al* [Stephan *et al*, 1982a] using the same technique. This value is considerably smaller than the values obtained in either of the photon ionization studies referenced above and suggests that the two methods of ionization may in fact yield different results. The value obtained by Jones and Taylor [Jones and Taylor, 1978] using synchrotron radiation as the light source is also significantly greater than that obtained by Linn and Ng [Linn and Ng, 1981]. It was concluded by Jones and Taylor that their value did not represent the true adiabatic ionization potential of the dimer ion. As stated by Linn and Ng [Linn and Ng, 1981], the major problem associated with the use of synchrotron radiation as the photon source in photon ionization studies of appearance potentials is the difficulty of eliminating the effects of refracted higher order vacuum ultraviolet light from the experiment. At the ionization threshold ionization cross sections tend to zero and ions produced

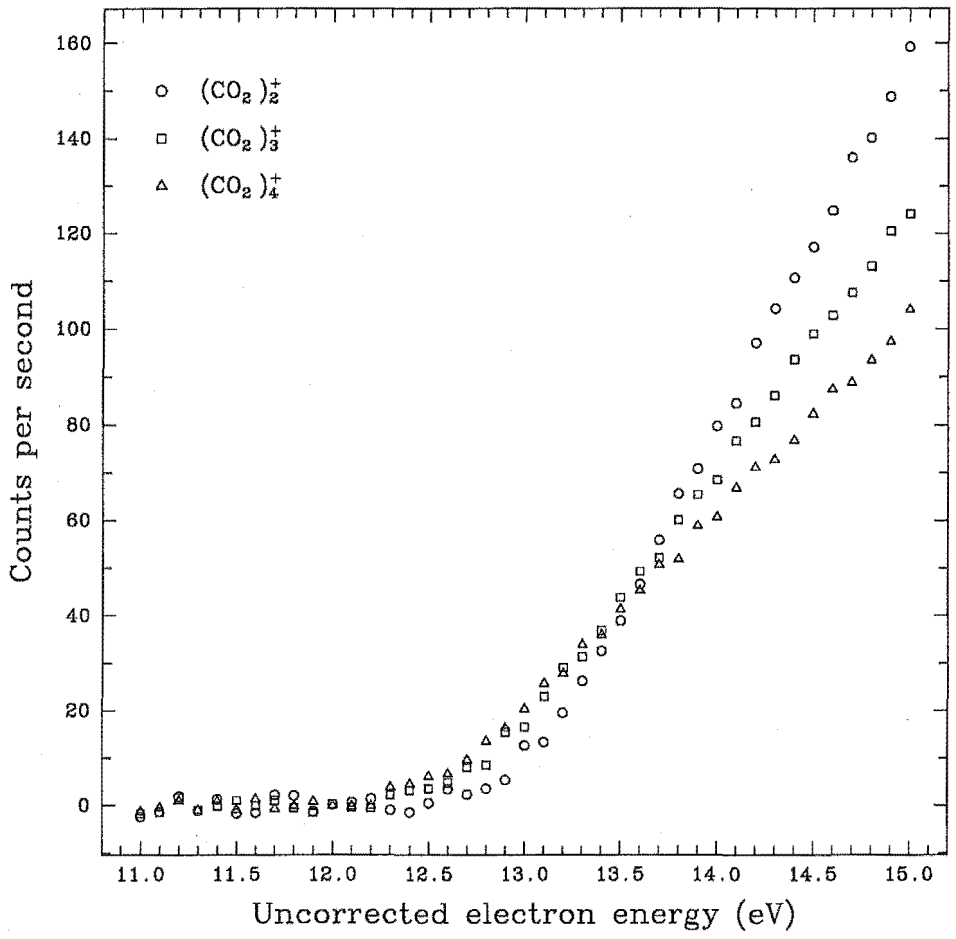

Figure 3.28: Measured ionization efficiency curves for $(CO_2)_2^+$, $(CO_2)_3^+$ and $(CO_2)_4^+$. Note that only every second point has been plotted on this and all other ionization efficiency curves presented in this section for reasons of clarity.

by the higher order vacuum ultraviolet radiation may make the identification of the true appearance potential extremely difficult. A discharge light source in conjunction with a vacuum ultraviolet monochrometer was employed for the measurements performed by Linn and Ng [Linn and Ng, 1981; Ono *et al*, 1980].

There was some concern that contributions to the $(CO_2)_2^+$ ionization efficiency curve from the fragmentation of larger cluster ions may effect the ionization threshold of the dimer. It is well known that extensive fragmentation of most cluster species occurs following most types of ionization [Scoles, 1988]. By performing measurements at lower reservoir pressures ($\sim$ 2000 Torr) such that negligible amounts of the trimer and tetramer species were present in the beam, no change in the $(CO_2)_2^+$ appearance potential or the shape of the ionization efficiency curve could be observed. Similar measurements were performed for the N_2O and NH_3 systems with analogous results. This result is somewhat surprising since fragmentation processes involving the loss of one or more neutral monomer units from a cluster ion to yield an ion of smaller size may be expected to introduce pronounced changes of slope, or *breaks*, into the ionization efficiency curve of the smaller cluster ion, corresponding to the appearance potentials of the larger ions. The failure to observe such features on any of the $(CO_2)_n^+$, $(N_2O)_n^+$ and $(NH_3)_nH^+$ ionization efficiency curves may be largely due to the relatively low resolution of the experimental arrangement employed for these measurements. It is hoped that work currently being pursued in our laboratory using a near–monochromatic electron gun [Harland and McIntosh, 1985] will help to clarify this situation.

Ionization efficiency curves obtained for $(N_2O)_n^+$ $(2 \leq n \leq 4)$ and the cluster ion fragments $(N_2O{\cdot}O)^+$ and $(N_2O{\cdot}NO)^+$ are illustrated in Figures 3.29 and 3.30. The appearance potentials determined for these species are summarized in Table 3.11. The value of 12.3 eV determined for the appearance potential of $(N_2O)_2^+$ is in excellent agreement with the photon ionization results of 12.35 $\pm$ 0.02 eV and 12.394 $\pm$ 0.015 eV reported by Linn and Ng [Linn and Ng, 1981] and Kamke *et al* [Kamke *et al*, 1989], respectively. It can be seen from Figure 3.30 that the shape of the ionization efficiency curve measured for the $(N_2O{\cdot}NO)^+$ cluster ion fragment is significantly different to the shape of the curves obtained for any of the other ions illustrated in Figures 3.28 to 3.32. Apart from the ionization threshold at 14.3 eV, there is a sharp change of slope at approximately 17.0 eV, suggesting the presence of a second threshold for the formation of this ion. The shape of this curve was found to be totally reproducible in repeat experiments. The $(N_2O{\cdot}NO)^+$ ion was also observed by Linn and Ng [Linn and Ng, 1981], who estimated an appearance potential of 14.01 eV, in reasonable accord with the lowest energy threshold of 14.3 eV determined in the present study. A second threshold at approximately 17.2 eV is also clearly apparent on the $(N_2O{\cdot}NO)^+$ photon ionization efficiency curve recorded by Linn and Ng, supporting the present observation of a second, higher energy threshold. The appearance potential of $(N_2O{\cdot}O)^+$ has not been previously reported in the literature. In view of the good agreement observed between the appearance potentials of $(N_2O)_2^+$ and $(N_2O{\cdot}NO)^+$ determined in the present study and those obtained by Linn and Ng using photon ionization, it is reasonable to expect that the appearance potentials of 12.1 eV, 12.0 eV and 14.6 eV obtained for $(N_2O)_3^+$, $(N_2O)_4^+$ and $(N_2O{\cdot}O)^+$, respectively, are equally as reliable.

The appearance potentials for $(N_2O)_3^+$ and $(N_2O)_4^+$ reported in the photon ionization study of Kamke *et al* [Kamke *et al*, 1989] were 12.29 $\pm$ 0.02 eV and 12.26 $\pm$ 0.04 eV, respectively. These values are approximately 0.2 eV higher than the electron impact values determined in the present study. Although photon ionization should in principle yield more accurate ionization threshold data with lower experimental uncertainty than electron

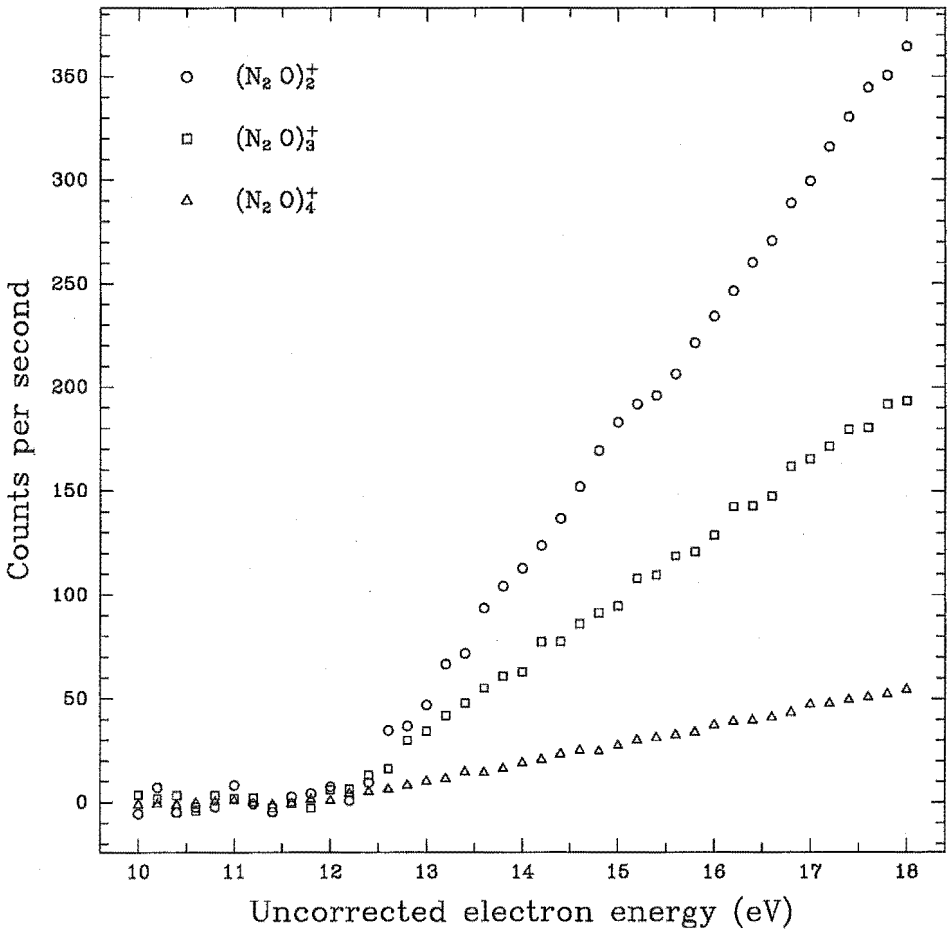

Figure 3.29: Measured ionization efficiency curves for $(N_2O)_2^+$, $(N_2O)_3^+$ and $(N_2O)_4^+$.

impact methods, this is frequently not the case. The appearance potentials determined by Kamke *et al* for the $(N_2O)_n^+$ $(2 \leq n \leq 8)$ cluster ions were reported with experimental uncertainties ranging from $\pm$ 0.015 eV for $n = 2$ to $\pm$ 0.04 eV for $n = 8$. However, inspection of the experimental data presented in Figure 1 of [Kamke *et al*, 1989] shows little correspondence between the reported appearance potential values and the thresholds anticipated by visual inspection of the data. The threshold regions appear smeared and noisy, and the shape of the ionization efficiency curves varies considerably from $n = 1$ and $n = 8$. The reported thresholds and their associated uncertainties were the result of an empirical multiparameter fitting procedure, which *cannot* guarantee a unique solution. Consequently, despite quoting appearance potential values to two or three decimal places with uncertainties in the 10 meV range, some consideration must be given to the data treatment employed by Kamke *et al*. Electron impact ionization thresholds invariably return reliable appearance potential values within the stated uncertainty, although it must be acknowledged that recoil energy and internal excitation in the ionization process may

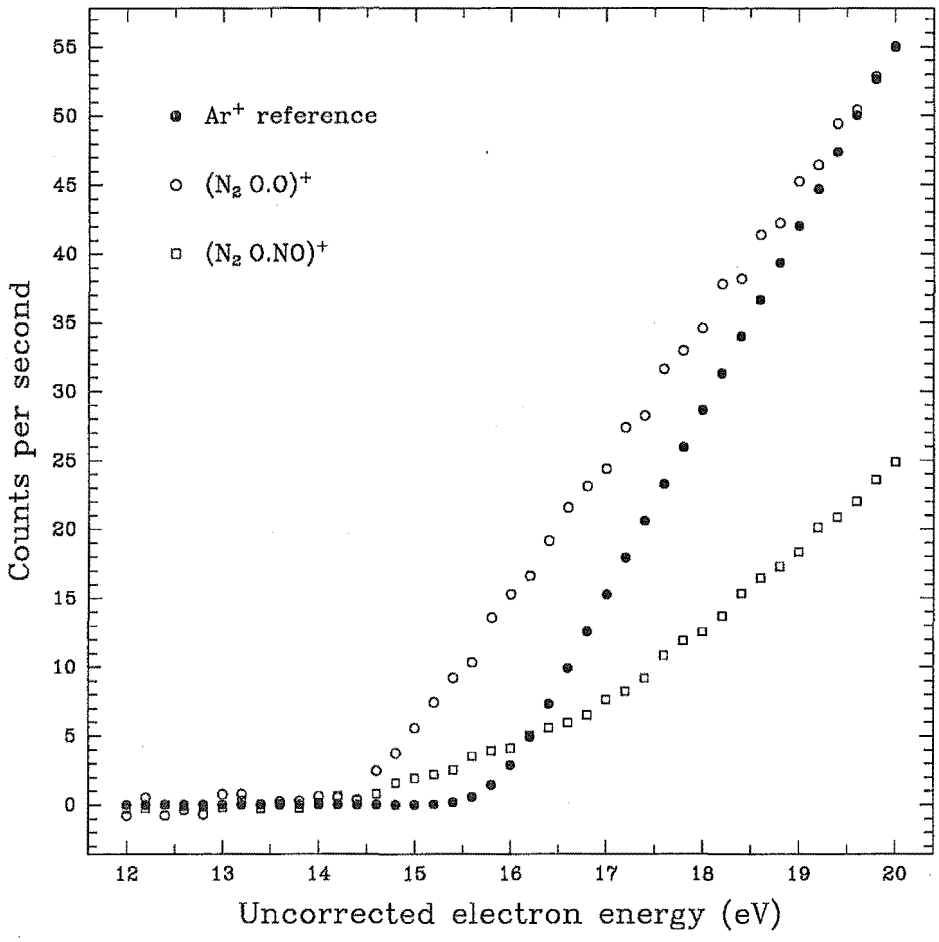

Figure 3.30: Measured ionization efficiency curves for $(N_2O{\cdot}O)^+$ and $(N_2O{\cdot}NO)^+$. The (scaled) Ar^+ reference curve is also shown.

contribute to the absolute values determined using either technique.

Ionization efficiency curves for the protonated ammonia cluster ions are illustrated in Figures 3.31 and 3.32. The appearance potentials listed in Table 3.11 for $(NH_3)_nH^+$ $(1 \leq n \leq 3)$ may be compared with those reported in two previous investigations. Using photon ionization, Ceyer *et al* [Ceyer *et al*, 1979] determined appearance potentials of 9.59 ± 0.02 eV, 9.15 ± 0.04 eV and 9.03 ± 0.04 eV for NH_4^+, $(NH_3)_2H^+$ and $(NH_3)_3H^+$, respectively. In an electron impact study, Stephan *et al* [Stephan *et al*, 1982b] obtained the somewhat less accurate values of 9.95 ± 0.3 eV, 9.50 ± 0.3 eV and 9.20 ± 0.03 eV for the same respective quantities. Within experimental error, the present data are in general agreement with the results of Ceyer *et al*. It was also possible to determine the appearance potentials of $(NH_3)_nH^+$ $(4 \leq n \leq 8)$. There do not appear to be any previously reported values for the appearance potentials of these species.

It should be noted that is was not possible to measure ionization efficiency curves

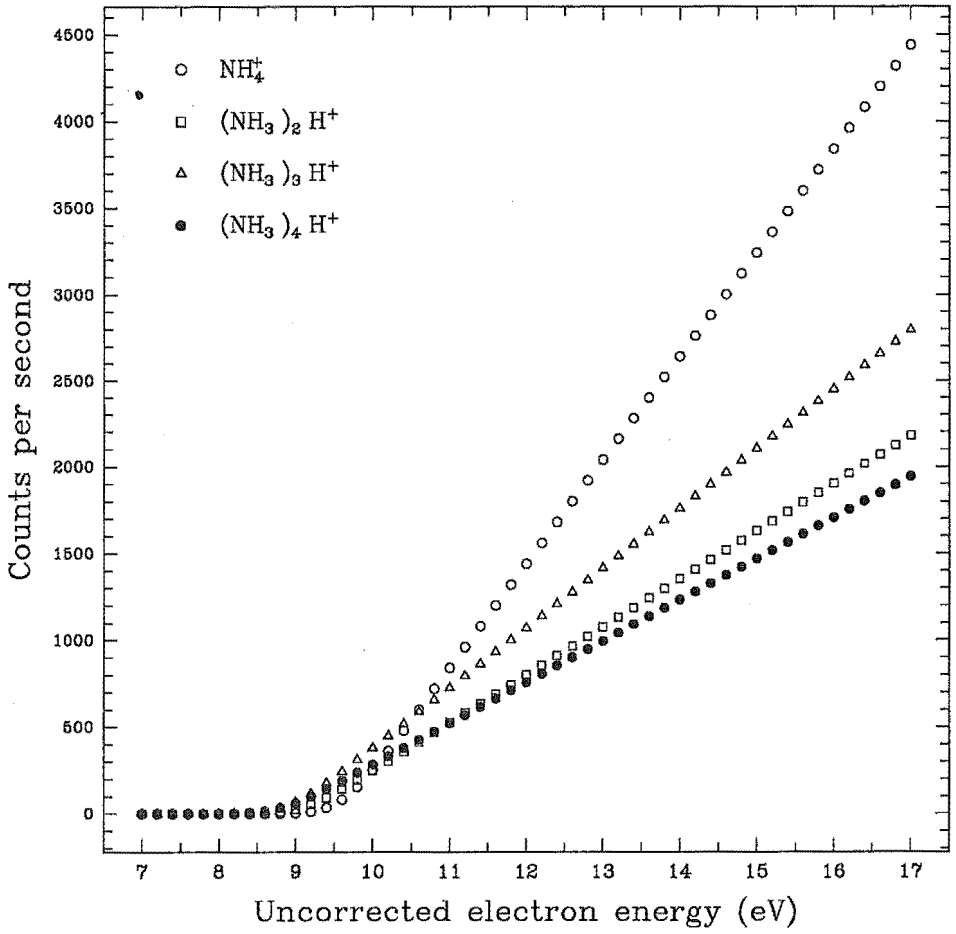

Figure 3.31: Measured ionization efficiency curves for $(NH_3)H^+$, $(NH_3)_2H^+$, $(NH_3)_3H^+$ and $(NH_3)_4H^+$.

for any of the unprotonated ammonia cluster ions, $(NH_3)_n^+$ $(2 \leq n \leq 8)$. Ionization of neutral ammonia clusters invariably causes the clusters to undergo an internal ion–molecule reaction resulting in the loss of NH_2 and the formation of a NH_4^+ core [Wei *et al*, 1990a; Wei *et al*, 1990b]. This process may be described by the reactions

$$(NH_3)_n + e^- \longrightarrow NH_3^+(NH_3)_{n-1} + 2e^- \tag{3.40}$$

$$NH_3^+(NH_3)_{n-1} \longrightarrow NH_4^+(NH_3)_{n-2} + NH_2 \tag{3.41}$$

and is generally observed to occur to such an extent that virtually no ammonia clusters are detected as $(NH_3)_n^+$ [Stephan *et al*, 1982b; Wei *et al*, 1990a]. In the present study, ion counts for the unprotonated ammonia clusters were observed to be several orders of magnitude smaller than those of the protonated cluster ions at an electron energy of 70 eV. Ion counts in the threshold region (< 20 eV) were too low to facilitate an accurate determination of appearance potentials for the unprotonated species while counts for the

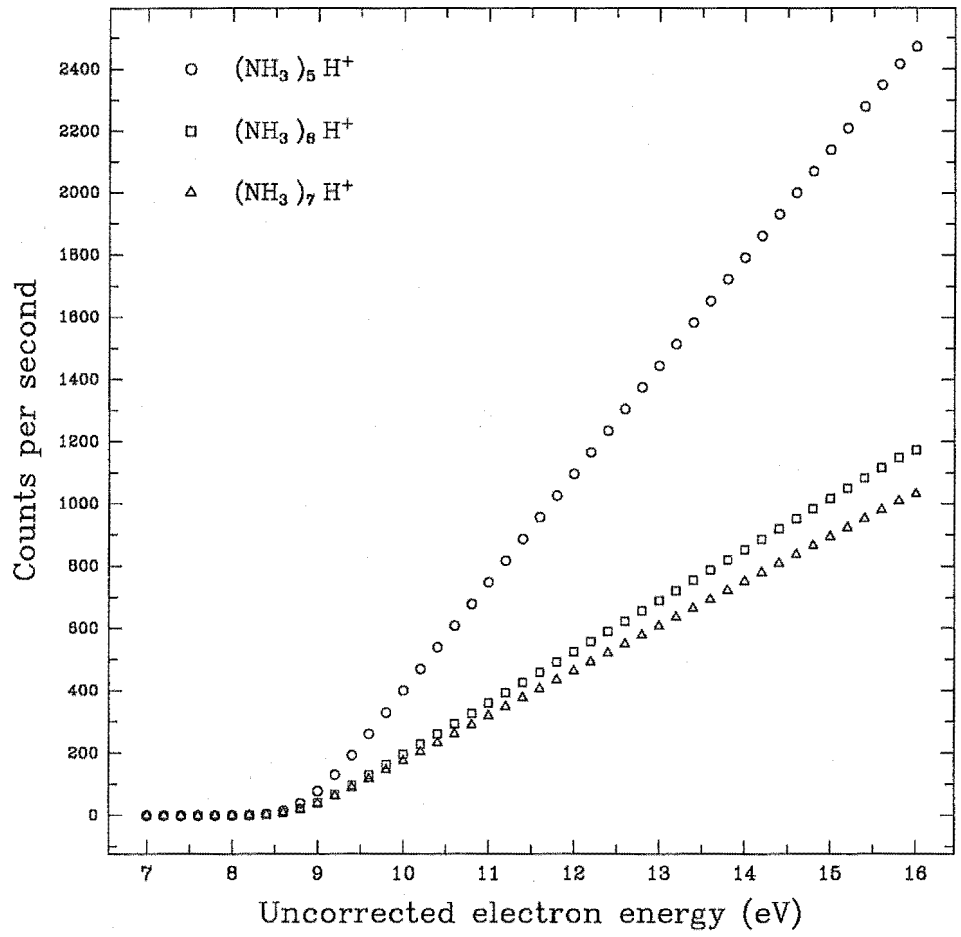

Figure 3.32: Measured ionization efficiency curves for $(NH_3)_nH^+$ $(5 \leq n \leq 8)$. The ionization efficiency curve for $(NH_3)_8H^+$ would be superimposed on that measured for $(NH_3)_7H^+$ and has therefore been omitted. The higher signal level observed for $(NH_3)_5H^+$ over the $(NH_3)_3H^+$ and $(NH_3)_4H^+$ ions reflects the higher stability of the pentamer structure (see §3.6).

$(NH_3)_nH^+$ species were substantially higher than those for the corresponding $(CO_2)_n^+$ and $(N_2O)_n^+$ cluster ions.

The discrepancies observed between some of the previously reported cluster ion appearance potentials discussed in the preceding paragraphs has led to the suggestion that photon and electron impact ionization studies fail to yield the true adiabatic ionization potentials of these weakly bound species [Klots and Compton, 1978; Stephan *et al*, 1982a]. Klots and Compton [Klots and Compton, 1978] suggested that the equilibrium geometry of van der Waals cluster ions produced by electron impact or photon ionization may be considerably different from the equilibrium geometry of the neutral precursor. In such situations the Franck–Condon factors near the true adiabatic ionization threshold may be so small that the observation of the adiabatic threshold is rendered virtually impossible. It has been suggested that small Franck–Condon factors near threshold are not a particularly serious problem in the ionization of atomic rare gas clusters due to the close spacing of many Rydberg levels throughout the region between the adiabatic and the direct ionization thresholds which may decay via autoionization [Ng *et al*, 1977; Ceyer *et al*, 1979]. Rydberg states with lifetimes greater than 50 μs and principal quantum numbers $55 \leq n \leq 75$ have been reported for CO_2 clusters by Campbell and Tittes [Campbell and Tittes, 1990]. Such long lived high Rydberg states can only be observed if there are some states for which non–radiative mechanisms of decay, such as autoionization and electronic predissociation, are significantly slower than radiative decay. It has been shown [Tarr *et al*, 1981] that predissociation rates of molecular Rydberg states are considerably greater for states of low principal quantum number and while autoionization is the most probable non–radiative decay mechanism, the apparent absence of states with principal quantum number less than 55 observed in the experiment performed by Campbell and Tittes indicates that predissociation may also be an important mechanism. It is therefore possible that lower Rydberg states of molecular clusters may in fact predissociate instead of decaying to levels of lower energy via the autoionization process. For this reason, unfavourable Franck–Condon factors may not be completely compensated for in the ionization of molecular cluster species, making the observation of their true adiabatic ionization potentials extremely difficult.

In order to determine whether or not cluster ion appearance potentials obtained from photon and electron impact ionization studies are close to their true adiabatic values, it is necessary to compare thermochemical data deduced from these measurements with that obtained from ion–molecule equilibrium experiments using techniques such as high pressure mass spectrometry, ion flow tubes and ion cyclotron resonance. Ion–molecule equilibrium measurements provide a direct means of determining the Gibbs free energy change ΔG° for a reaction, which may be used to determine the heat of reaction ΔH° and the entropy of reaction ΔS° via the van't Hoff equation [Illies, 1988]. For the generalized association reaction

$$A^+ + B + M \rightleftharpoons BA^+ + M, \tag{3.42}$$

the dissociation energy of the B–A^+ bond is equivalent to the enthalpy change for the reaction and may therefore be directly measured using ion–molecule equilibrium methods. The dissociation energy may also be obtained via the appearance potential of BA^+ according to the equation

$$D_{BA^+} = AP_{A^+} - AP_{BA^+} + D_{AB}, \tag{3.43}$$

where AP_{BA^+} is the appearance potential of BA^+, D_{BA^+} and D_{AB} are the dissociation energies of BA^+ and AB, respectively, and AP_{A^+} is the appearance potential of A^+. Determination of the dissociation energy in this manner represents an indirect measurement,

requiring an independent estimation of the neutral AB binding energy and a knowledge of the appearance potential for A^+. If a considerable geometry change occurs following ionization, the appearance potential determined for BA^+ may be too large, resulting in an underestimation of the dissociation energy.

In order to calculate the bond dissociation energy of $(CO_2)_2^+$, it is necessary to know the binding energy of the neutral CO_2 dimer and the appearance potentials of CO_2^+ and $(CO_2)_2^+$. The appearance potential of CO_2^+ is accurately known, and spectroscopic values for a number of electronic states are given by Rosenstock *et al* [Rosenstock *et al*, 1977]. Although the dissociation energy of the neutral CO_2 dimer has, to the best of the author's knowledge, never been directly measured, a number of theoretical investigations of this species have been performed. In an early investigation Stogryn and Hirschfelder [Stogryn and Hirschfelder, 1959] calculated an intermolecular well depth of about 0.016 eV. In a more recent calculation Kiode and Kihara [Kiode and Kihara, 1974] used second virial coefficients, polarizabilities parallel and perpendicular to the molecular axis, and the electronic quadrupole moment to determine well depths of 0.059 eV and 0.039 eV for the staggered parallel and *t*–shaped CO_2 dimer structures, respectively. The results of Kiode and Kihara are supported by the *ab initio* calculations of Illies *et al* [Illies *et al*, 1987], who determined that the staggered dimer structure was bound by 0.056 eV and the *t*–shaped dimer by 0.048 eV. Molecular beam deflection studies of the neutral CO_2 dimer indicate that it is a nonpolar species, thus precluding the *t*–shaped geometry or any other nonsymmetric configurations which may be possible. McKee [McKee, 1990] concluded that of all the possible geometries for which symmetry demands a zero dipole moment, the staggered parallel configuration is the most probable. In view of the fact that the staggered parallel configuration also possess the largest binding energy, it would seem reasonable to assign a binding energy of 0.056 eV to the reaction

$$(CO_2)_2 \longrightarrow CO_2 + CO_2 \tag{3.44}$$

Using the appearance potential value of 13.1 eV determined in the present study for $(CO_2)_2^+$ along with the spectroscopic value of 13.769 eV for the appearance potential of $CO_2^+(X^2\Pi_{3/2g})$ and the value of 0.056 eV calculated by Illies *et al* for the binding energy of the neutral CO_2 dimer, the bond dissociation energy of $(CO_2{\cdot}CO_2)^+$ was calculated to be 0.73 eV. Considering the degree of translational and rotational cooling which occurs during the supersonic expansion process, it seems reasonable to assume that this value will be close to the negative enthalpy change at 0 K for the association reaction

$$CO_2^+ + CO_2 \longrightarrow CO_2^+ \cdot CO_2 \tag{3.45}$$

Positively charged CO_2 dimers produced by this reaction have been observed by a number of authors using high pressure mass spectrometry [Schildcrout and Franklin, 1969; Paulson *et al*, 1964; Kasper and Franklin, 1972], and several values for the enthalpy change of this process have been reported. The value of 0.73 eV determined in this investigation is in good agreement with the figure of 0.675 eV reported by Keesee and Castleman [Keesee and Castleman, 1986], and in reasonable accord with the value of 0.563 eV given by Mautner [Mautner and Field, 1977]. It should be noted that these latter two values have been corrected to 0 K by Linn and Ng [Linn and Ng, 1981] and are therefore lower than the original values stated by the respective authors. This correction was made by accounting for the temperature dependent differences in heat capacity $\Delta C_p(T)$ between the reactants and products of the above association reaction such that

$$\Delta H_0^\circ = \Delta H_{T_{expt}}^\circ - \int_0^{T_{expt}} \Delta C_p(T)\mathrm{d}T, \tag{3.46}$$

where ΔH_0° is the enthalpy change corrected to 0 K and $\Delta H_{T_{expt}}^\circ$ is the enthalpy change observed at the experimental temperature T_{expt}. The accurate calculation of ΔH_0° using equation (3.46) requires detailed information regarding the rotational constants, vibrational frequencies and electronic degeneracies of the reactants and products. Much of this information is not available for many clusters of interest and must usually be estimated. Sufficient data is available for the $(CO_2)_2^+$ cluster ion [Illies, 1988], and the corrections made by Linn and Ng are considered to be reliable.

Although the cluster binding energies of the neutral CO_2 trimer and tetramer species are not known, it is reasonable to assume that they will be similar to the binding energy of the neutral dimer.[11] Assuming this to be the case, the dissociation energies of $(CO_2)_2^+ \cdot CO_2$ and $(CO_2)_3^+ \cdot CO_2$ were calculated to be 0.36 eV and 0.26 eV, respectively. The value of 0.26 eV estimated for the binding energy of $(CO_2)_3^+ \cdot CO_2$ is in reasonable accord with the value of 0.22 eV reported by Hiraoka *et al* [Hiraoka *et al*, 1988] for the negative enthalpy change of the association reaction

$$(CO_2)_2 \cdot CO_2^+ + CO_2 \longrightarrow (CO_2)_4^+ \tag{3.47}$$

The binding energy of 0.36 eV determined for $(CO_2)_2^+ \cdot CO_2$ is in good agreement with the ion–molecule result of 0.32 eV given by Keesee and Castleman [Keesee and Castleman, 1986] (see also [Illies *et al*, 1987]).

Using the appearance potential value of 12.3 eV measured for $(N_2O)_2^+$ along with the known appearance potential of 12.886 ± 0.002 eV for N_2O^+ [Rosenstock *et al*, 1977] and the estimated intermolecular binding energy of 0.02 eV [Johnston and McCloskey, 1940] for the neutral dimer, the bond dissociation energy of $(N_2O \cdot N_2O)^+$ was calculated to be 0.61 eV, in good agreement with the value of 0.56 eV obtained by Linn and Ng [Linn and Ng, 1981] and the value of 0.57 eV determined by Illies using ion–molecule methods [Illies, 1988]. It should be mentioned, however, that this latter value pertains to a measurement of ΔH° for the association reaction of N_2O and N_2O^+ at 481 K and therefore may not be directly comparable. The $(N_2O)_2^+$ binding energy calculated using the photon ionization data reported by Kamke *et al* [Kamke *et al*, 1989] is 0.512 eV, which seems a little low. Assuming the same binding energy of 0.02 eV for $(N_2O)_3$ and $(N_2O)_4$, bond dissociation energies of 0.22 eV and 0.12 eV were calculated for $(N_2O)_2^+ \cdot N_2O$ and $(N_2O)_3^+ \cdot N_2O$, respectively, compared to values of 0.124 eV and 0.05 eV calculated using the photon ionization data of Kamke *el al*.

The appearance potential of 14.6 eV determined for the $(N_2O \cdot O)^+$ cluster ion fragment is observed to be 2.3 eV greater than that of $(N_2O)_2^+$, in apparent agreement with the difference of 2.4 eV between the appearance potential of N_2O^+ from N_2O (12.886 eV) and the appearance potential of O^+ from N_2O (15.29 eV) [Rosenstock *et al*, 1977]. One possible means of interpreting this observation may be to write the structure of $(N_2O \cdot O)^+$ as $O^+ \cdot N_2O$ and to postulate the formation of this species as involving the ionization and fragmentation of one of the N_2O monomer units in $(N_2O)_2$ without any significant perturbation of the accompanying cluster molecule. It is interesting to note that a similar situation was found for the species $(CO \cdot CO_2)^+$ and $(NH_2 \cdot NH_3)^+$ observed by Stephan *et al* [Stephan *et al*, 1982a; Stephan *et al*, 1982b]. An alternative mechanism proposed by

[11] It is reasonable to assume that neutral cluster binding energies will remain essentially constant in the initial growth stages of cluster formation. This will be particularly true for the dimer, trimer and tetramer species considered in this communication, where the binding energy results from relatively weak van der Waals forces and should be approximately additive. The relatively weak binding energies of these species also suggests that their vibrational energy is quite low and therefore not liable to influence the shape of the ionization efficiency curves.

them for the formation of these cluster fragment ions involves the occurrence of an internal cluster ion–molecule reaction. If the ion within the $(N_2O)_2$ cluster is initially formed in some electronically excited state N_2O^{+*}, then the $(N_2O{\cdot}O)^+$ ion may be produced by the following sequence of reactions:

$$(N_2O)_2 + e^- \longrightarrow N_2O \cdot N_2O^{+*} + 2e^- \longrightarrow N_2O_2^+ + N_2 + 2e^- \qquad (3.48)$$

The $N_2O_2^+$ species produced in this manner would be expected to have an appearance potential greater than that of $(N_2O)_2^+$ by at least the additional energy required for the electronic excitation of the parent ion. Irrespective of whichever mechanism applies, the appearance potential of 14.6 eV measured for $(N_2O{\cdot}O)^+$ may be used along with the thermochemical threshold of 15.29 eV for the formation of O^+ from N_2O [Rosenstock *et al*, 1977] and the binding energy of 0.02 eV for $(N_2O)_2$ [Johnston and McCloskey, 1940] to estimate a lower bound of 0.71 eV for the bond dissociation energy of $(N_2O{\cdot}O)^+$.

The lowest energy threshold observed for the formation of $(N_2O{\cdot}NO)^+$ corresponds to an appearance potential of 14.3 eV while the break at higher electron energy equates to an ionization threshold of approximately 17.0 eV. The differences of 2.0 eV and 4.7 eV observed between these thresholds and the appearance potential of 12.3 eV obtained for $(N_2O)_2^+$ correspond very well to the differences of 2.124 eV and 4.854 eV between the appearance potential of 12.886 eV for N_2O^+ and the thermochemical thresholds of 14.19 eV and 17.76 eV for the fragmentations processes

$$N_2O + e^- \longrightarrow N_2O^+ + 2e^- \longrightarrow NO^+(X^1\Sigma^+) + N(^4S) + 2e^- \qquad (3.49)$$

and

$$N_2O + e^- \longrightarrow N_2O^+ + 2e^- \longrightarrow NO^+(X^1\Sigma^+) + N(^2P) + 2e^-, \qquad (3.50)$$

respectively [Rosenstock *et al*, 1977]. Employing the same argument applied to $(N_2O{\cdot}O)^+$, it seems reasonable to write the structure of $(N_2O{\cdot}NO)^+$ as $NO^+{\cdot}N_2O$ and to describe the formation of this species as involving the ionization and fragmentation of one of the N_2O molecules in the neutral dimer without any significant perturbation of the other. Realistically, the molecules making up a cluster must exert an influence on one another. This might well be expected to include a lowering of the ionization potential with increasing cluster size, as observed in this and other studies. This adds support to the mechanism of cluster ionization described above. Linn and Ng [Linn and Ng, 1981] observed that the photon ionization efficiency curve they measured for $(N_2O{\cdot}NO)^+$ had essentially the same profile as that of NO^+ produced from the fragmentation of N_2O^+. Such an observation clearly indicates that fragmentation N_2O^+ and $(N_2O)_2^+$ to form NO^+ and $(N_2O{\cdot}NO)^+$, respectively, follow similar reaction pathways, further supporting the notion that ionization of the neutral N_2O dimer occurs on a single monomer unit to form $N_2O^+{\cdot}N_2O$. The neutral monomer in $N_2O^+{\cdot}N_2O$ then acts simply as a spectator in the fragmentation process leading to the formation of $(N_2O{\cdot}NO)^+$. An alternative mechanism for the formation of $(N_2O{\cdot}NO)^+$ via an internal ion–molecule reaction similar to that described by equation (3.48) cannot be discounted however. It should be mentioned that N_2O^+ may undergo another fragmentation process, leading to the formation of $NO^+(X^1\Sigma^+)$ and $N(^2D)$. The thermochemical threshold for NO^+ produced by this process is 16.57 eV [Rosenstock *et al*, 1977], suggesting that another break in the ionization efficiency curve of $(N_2O{\cdot}NO)^+$ may be expected between 14.3 eV and 17.0 eV. It was not possible to detect this break in the present study, although there was some evidence for such a feature on the photon ionization efficiency curve measured by Linn and Ng [Linn and Ng, 1981]. Failure to observe this feature may be attributed to the low resolution of the instrument employed for

Ion	Binding energy (eV)	Ion	Binding energy (eV)
$CO_2^+ \cdot CO_2$	0.73	$N_2O^+ \cdot N_2O$	0.61
$(CO_2)_2^+ \cdot CO_2$	0.36	$(N_2O)_2^+ \cdot N_2O$	0.22
$(CO_2)_3^+ \cdot CO_2$	0.26	$(N_2O)_3^+ \cdot N_2O$	0.12

Table 3.12: Summary of $(CO_2)_n^+ \cdot CO_2$ and $(N_2O)_n^+ \cdot N_2O$ $(1 \leq n \leq 3)$ binding energies determined in this study.

the present study. The fragmentation of $N_2O^+ \cdot N_2O$ may be viewed as a set of competing unimolecular reactions, and it would appear that reactions analogous to processes (3.49) and (3.50) are the most probable channels for the formation of $(N_2O \cdot NO)^+$.

From a knowledge of the H_2N–H bond strength and the appearance potentials of H^+ and NH_4^+ it is possible to calculate the proton affinity of ammonia. The strength of the H_2N–H bond was determined by Bohme *et al* [Bohme *et al*, 1973] to be 4.60 eV while the spectroscopic value for the appearance potential of H^+ is 13.598 eV. Using these values and the value of 9.7 eV determined in the present study for the appearance potential of NH_4^+, the proton affinity of ammonia was estimated to be 8.5 eV at 0 K, or approximately 8.6 eV at 298 K. This latter value is in fair agreement with the generally accepted value of 8.96 ± 0.08 eV at 298 K [Lias *et al*, 1980], although some debate still appears to surround the correct value of this quantity. Photoelectron spectroscopy studies [Houle and Beauchamp, 1979], when combined with a carefully calibrated scale of proton affinities established using high pressure mass spectrometry [Yamdagni and Kebarle, 1976] and ion cyclotron resonance [Wolf *et al*, 1977], suggest a value of 9.02 ± 0.06 eV while theoretical calculations have produced values of 8.89 eV [Goodliffe *et al*, 1971] and 9.01 eV [Tann and Linnett, 1976].

The binding energy of the neutral ammonia dimer has been accurately determined from virial coefficient, lattice energy and molecular beam scattering measurements [Duquette *et al*, 1978], leading to a value of 0.15 ± 0.04 eV. Using this value along with the value of 10.166 eV for the appearance potential of NH_3^+ and the value of 9.7 eV determined in the present study for the appearance potential of NH_4^+, a negative enthalpy change ΔH_0° of 0.62 eV was calculated for the hydrogen abstraction reaction

$$NH_3^+ + NH_3 \longrightarrow NH_4^+ + NH_2 \tag{3.51}$$

This value is in reasonable accord with those of 0.45 ± 0.3 eV and 0.74 ± 0.4 eV deduced by Stephan *et al* [Stephan *et al*, 1982b] and Ceyer *et al* [Ceyer *et al*, 1979], respectively, from appearance potential measurements. All of these values are, however, in considerable disagreement with the ion–molecule figure of 1.08 eV at 298 K estimated by Stephan *et al* [Stephan *et al*, 1982b] from the proton affinity of ammonia and the heats of formation of NH_3, NH_2 and H^+ [Rosenstock *et al*, 1977]. Assuming that only rotational and translational degrees of freedom are active at 298 K, a correction of approximately 0.08 eV should be subtracted from the ion–molecule result to obtain ΔH_0°, thus slightly reducing, but not eliminating, the discrepancy between the enthalpies deduced from the two types of experiment. Considering the ion–molecule result to be reliable, the enthalpies determined from appearance potential measurements are clearly too low, indicating that none of the measured NH_4^+ appearance potentials correspond to the true adiabatic ionization threshold.

The binding energy of 0.15 eV and the appearance potentials listed in Table 3.11 for the higher protonated clusters $(NH_3)_nH^+$ $(2 \leq n \leq 8)$ may be used to calculate the solvation

	$(NH_3)_n \cdot NH_4^+ \rightleftharpoons (NH_3)_{n-1} \cdot NH_4^+ + NH_3$	
$n, n-1$	ΔH_0° (eV) (this study)	ΔH_{298}° (eV) (literature)
1, 0	-0.65	-0.797[a]
		-0.931[b]
		-1.074[c]
		-1.169[d]
2, 1	-0.35	-0.701[b]
		-0.758[c]
		-0.736[d]
3, 2	-0.25	-0.550[e]
		-0.610[b]
4, 3	~ -0.2	-0.525[e]
5, 4	~ -0.2	-0.290[e]
6, 5	~ -0.2	-0.250[e]
7, 6	~ -0.2	-0.235[e]

Table 3.13: Summary of proton solvation energy data ((a) Reference [Wincel, 1972], (b) Reference [Arshadi and Futrell, 1974], (c) Reference [Payzant *et al*, 1973], (d) Reference [Searles and Kebarle, 1968], (e) Reference [Wei *et al*, 1990b]).

energy of an ammonium ion by one to seven ammonia molecules. The calculated solvation energies are presented in Table 3.13 along with known literature values determined using ion–molecule techniques such as high pressure mass spectrometry. It is clear from Table 3.13 that the agreement between the solvation energies determined in the present study and those obtained using ion–molecule equilibrium methods is not good, even after the adjustment of the latter to 0 K [Stephan *et al*, 1982b]. The enthalpy changes determined on the basis of appearance potential measurements are again too low, suggesting that the measured appearance potential values are too high.

It is the opinion of the author that the proton affinity of ammonia and the solvation energies deduced from ion–molecule measurements are reliable. Similarly, the appearance potential of NH_3^+ and the binding energy of the neutral ammonia dimer are well established quantities. It must therefore be concluded that both electron impact and photon ionization measurements fail to yield the true adiabatic ionization threshold for the generation of protonated ammonia clusters from their respective neutral precursors. The inability of these techniques to correctly sample the thermochemical threshold may be related to geometric changes that are required for the proton transfer reaction channel, and hence to unfavourable Franck–Condon factors. Competition between dissociation channels and formation of the protonated species by reaction (3.41) may therefore be important also.

3.7.4 Conclusion

Appearance potentials have been determined for the van der Waals cluster ions $(CO_2)_n^+$, $(N_2O)_n^+$ $(2 \leq n \leq 4)$ and $(NH_3)_nH^+$ $(1 \leq n \leq 8)$, and the cluster ion fragments $(N_2O{\cdot}O)^+$ and $(N_2O{\cdot}NO)^+$ using electron impact ionization. The appearance potentials obtained for $(CO_2)_n^+$, $(N_2O)_n^+$ $(2 \leq n \leq 4)$, $(N_2O{\cdot}NO)^+$ and $(NH_3)_nH^+$ $(1 \leq n \leq 3)$ were all found to be in general agreement with previously reported values while the appearance potentials of $(N_2O{\cdot}O)^+$ and $(NH_3)_n^+$ $(4 \leq n \leq 8)$ were examined for the first time. In contrast to the $(CO_2)_n^+$ and $(N_2O)_n^+$ systems, dissociation energies of the $(NH_3)_nH^+$ ions deduced from appearance potential measurements were observed to be in considerable disagreement with those obtained by ion–molecule methods, indicating that electron impact ionization measurements fail to sample the true adiabatic ionization thresholds of the latter species. Some knowledge of Franck–Condon factors for van der Waals clusters may therefore be required for the reliable interpretation of cluster ion appearance potentials. The most probable mechanism for the formation of the cluster fragment ions $(N_2O{\cdot}O)^+$ and $(N_2O{\cdot}NO)^+$ would appear to involve the ionization and fragmentation of one of the N_2O molecules in the neutral N_2O dimer without any significant perturbation of the accompanying molecule, although alternative mechanisms cannot be discounted. However, electron impact ionization efficiency curves provide significant mechanistic information where breaks are found and where comparisons with monomer measurements and data collected using other techniques are available. It is hoped that work currently being pursued in our laboratory using a more accurate instrument than that employed for the measurements described in this investigation will help to clarify this situation.

Chapter 4

Theoretical results and discussion

4.1 Introduction

In addition to the experimental work discussed in the previous chapter, a significant quantity of theoretical work was also performed during the course of the research presented in this thesis. The initial motivation for this theoretical work came from a desire to be able to predict reliably the collision frequency and particle density of a supersonic molecular beam at any point along the expansion axis, and to gain some insight into the breakdown of rotational and translational equilibrium during the initial stages of the supersonic expansion process. The development of theories to model the expansion process and to accurately predict the terminal properties of a supersonic beam from a knowledge of the source conditions and the properties of the gases involved has been an area of considerable interest for several decades [Hamel and Willis, 1966; Willis *et al*, 1972]. Experiments designed to measure quantitative parameters in atomic and molecular beams rely on a knowledge of the beam density and collisional quantities such as collision frequency and mean free path. Such quantities cannot be routinely measured in the laboratory and it is therefore desirable to have reliable theories which may be used to calculate this information.

In §4.2 the thermal conduction model developed by Beijerinck and Verster [Beijerinck and Verster, 1981] is used to describe the supersonic expansion process. Collision frequency, flow velocity, particle density, mean free path, and axial and radial temperatures in supersonic atomic and homonuclear diatomic beams are calculated for various species within the framework of the thermal conduction model using realistic interaction potentials and collision cross sections obtained from scattering theory. The thermal conduction model is extended to include rotational degrees of freedom by the introduction of a rotational–translational coupling parameter. Comparisons between numerical results and measured beam speed distributions are made to estimate values of the rotational–translational coupling parameter for H_2, N_2 and O_2.

A simple approach to the estimation of rotational relaxation times and collision numbers in supersonic expansions based on the use of the thermal conduction model is presented in §4.3. Expressions are derived for the calculation of these quantities, and relaxation times are calculated as a function of mean kinetic temperature and axial distance from the nozzle exit for the homonuclear diatomic species H_2, N_2, O_2 and Cl_2. The devised model provides a convenient means of estimating rotational relaxation times in a supersonic expansion and is found to produce results that are in general accord with those of similar studies for most of the species considered.

The calculations presented in §4.2 and §4.3 assume that the value of the rotational–translational coupling parameter for a particular collision system is independent of all other

collision parameters. This assumption is somewhat naive and open to improvement. In order to determine the dependence of the coupling parameter on other collision variables it is necessary to simulate the rotational relaxation process under a wide range of conditions for which reliable experimental relaxation data are available and to vary the value of the coupling parameter until agreement between theory and experiment is obtained in each case. The application of a direct simulation Monte Carlo procedure to the investigation of rotational relaxation in homogeneous gases is presented in §4.4. The devised relaxation model assumes that the efficiency of rotational–translational energy transfer may be directly related to the fraction of inelastic collisions experienced by the colliding molecules in terms of an *energy dependent* rotational–translational coupling parameter. The energy dependence of the coupling parameter is investigated for the homonuclear diatomic molecules H_2, N_2, O_2 and Cl_2, and for the polyatomic species CO_2, OCS, NH_3, CH_4, CH_3Cl and C_2H_4. Rotational collision numbers are calculated for these molecules and the energy dependent coupling parameter is used in thermal conduction model calculations to investigate the breakdown of translational and rotational equilibrium in supersonic expansions of CO_2, OCS and CH_3Cl.

4.2 Flow dynamics of supersonic molecular beams and the determination of rotational–translational coupling parameters for H_2, N_2 and O_2

4.2.1 Introduction

A frequently cited property of supersonic molecular beams is the collision–free nature of the flow far downstream from the nozzle exit. The beam may be considered to consist simply of a stream of molecules moving along parallel paths in the complete absence of any collisions. To the extent that this is a valid description of the true situation, it facilitates the preparation of state–selected and oriented species for the investigation of scattering processes [Harland *et al*, 1990; Carman Jr. *et al*, 1986], and the investigation of radiationless processes in large isolated molecules. In reality, the supersonic flow will only approach a collision–free situation [Hamel and Willis, 1966]; free molecular flow will never actually occur due to the finite width of the velocity distribution, causing some molecules to overtake and collide with others.

Since the development and use of molecular beams as a research tool some three or four decades ago, a number of workers have addressed the problem of calculating collision rates within such systems. Probably the first in this regard was Troitskii [Troitskii, 1962], who reported that the collision frequency of molecules at any point in an effusive beam was approximately one–third that found in a bulk gas of the same number density. Using a similar formalism Lubman *et al* [Lubman *et al*, 1982] developed general expressions for the collision frequency in effusive and supersonic molecular beams. Their calculations showed that, when characterized by the same density and temperature, the collision rates in an effusive beam, supersonic beam, and a bulb are approximately in the ratio of 1 : 1.5 : 3, indicating that the directionality of the supersonic nozzle beam source does little to reduce the collision frequency by any more than a factor of two below that in a gas bulb.

While exact for the case of an effusive beam, the expressions given by Lubman *et al* pertaining to the supersonic system were obtained using a greatly simplified treatment of the expansion process and, although completely general, cannot be considered particularly accurate. Velocity components perpendicular to the beam axis were assumed to contribute

little to the overall number of collisions and were neglected in Lubman's analysis.

In this section, the thermal conduction model [Beijerinck and Verster, 1981] is used to provide a more realistic description of the expansion process. The model has been modified to incorporate a variable flow velocity and extended using Klots approach [Klots, 1980] to include rotational degrees of freedom. Results obtained from the thermal conduction model are used in conjunction with accurately calculated collision cross sections to derive theoretical values of collision frequency as a function of distance from the nozzle exit for supersonic beams of the monatomic species He, Ne, Ar and Kr, and the homonuclear diatomic species H_2, N_2 and O_2. Values of Klots rotational–translational coupling parameter are determined for H_2, N_2 and O_2 by fitting parameters calculated using the thermal conduction model to experimental data determined by time–of–flight methods. The value of the coupling parameter determined for N_2 is in excellent accord with previously published results [Randeniya and Smith, 1990] and the value obtained for H_2 is consistent with the expectations of previous investigations [Gallagher and Fenn, 1974].

4.2.2 Theoretical considerations

The free expansion of a gas into a vacuum is one of the fundamental theoretical and experimental problems of rarefied gas dynamics. Accordingly, many theories have been developed to explain the dynamics of the expansion process, ranging in sophistication from a simple hard sphere treatment of the collision dynamics [Anderson and Fenn, 1965] through to the incorporation of subtle quantum effects [Toennies and Winkelmann, 1977]. At an intermediate level one finds the collision dynamics treated solely in terms of long range van der Waals forces, generally assuming an interaction potential of the form

$$V(r) = -C_6 r^{-6}. \tag{4.1}$$

One such model which has been employed by a number of workers in recent years is the thermal conduction model, originally proposed by Habets [Habets, 1977] and Beijerinck and Verster [Beijerinck and Verster, 1981] to describe the breakdown of translational equilibrium in free jet expansions of monatomic gases. The model has been extended by Klots [Klots, 1980] to include rotational degrees of freedom through the application of unimolecular dissociation theory which, as applied to collision complexes, provides a natural means for describing the coupling between rotational and translational modes. In this model, the rate of energy exchange associated with the breakdown of translational and rotational equilibrium during the expansion process is assumed to be proportional to the thermal conductivity associated with the various degrees of freedom. The thermal conduction model is particularly appealing both from the point of view of its relatively simple form and because of its ability to produce results which are in good agreement with those obtained by experiment. The major difficulty in solving the thermal conduction model lies in the calculation of the coefficients of thermal conductivity using realistic interaction potential data.

It should be noted that the thermal conduction model was originally proposed from a purely intuitive basis as opposed to being derived in some possibly dubious manner from the Boltzmann equation. Most other models of the supersonic expansion process, such as that devised by Randeniya and Smith [Randeniya and Smith, 1990], use the method of moments to *solve* the Boltzmann equation for an assumed energy distribution function. Both sides of the Boltzmann equation are multiplied by some function of velocity and internal energy to produce an equation which for some set of properties $\psi_i(\mathbf{v})$, $(i = 1, \ldots, N)$ may be integrated over velocity space and summed over available internal states

γ	5/3	7/5	8/6	9/7
κ	1.98	1.38	1.08	1.10

Table 4.1: Nozzle peaking factors for various values of the heat capacity ratio γ.

to obtain a set of N moment equations. The different moment methods differ in their choice of the set ψ_i and the arbitrary input for the distribution function. Their common feature is that the distribution function is chosen to contain N undetermined parameters, meaning that it is necessary to solve N simultaneous moment equations. It is hoped that for sufficiently small N and a judicious choice of distribution function that accurate results can be obtained. The thermal conduction model makes no such assumptions regarding the exact form of the distribution function and therefore represents a somewhat less contrived description of the true situation.

In common with most other models of the supersonic expansion process, the thermal conduction model assumes that the local number density in the core of the expansion at a distance z from the nozzle exit is given by the expression

$$n(z) = n_0 \left(\frac{z}{z_0}\right)^{-2} \left(\frac{u}{u_\infty}\right)^{-1}, \tag{4.2}$$

where n_0 is the stagnation number density and z_0 is related to the nozzle throat radius according to the expression

$$z_0^2 = r_0^2 \kappa \left[\left(\frac{\gamma-1}{\gamma+1}\right)^{1/2} \left(\frac{2}{\gamma+1}\right)^{1/(\gamma-1)}\right],$$

where γ is the heat capacity ratio C_p/C_v and κ is the nozzle peaking factor. The nozzle peaking factor is a complicated function of the heat capacity ratio and values calculated by Beijerinck and Verster [Beijerinck and Verster, 1981] for several heat capacity ratios are listed in Table 4.1. The value of u_∞ is given by the expression

$$u_\infty = \left(\frac{\gamma}{\gamma-1}\right)^{1/2} \left(\frac{2k_bT_0}{m}\right)^{1/2}, \tag{4.3}$$

and represents the thermodynamic limiting value of the mean flow velocity u.

In order to simplify the solution to the expansion problem, Beijerinck and Verster introduced the non–dimensional source parameter Ξ. The source parameter is a function of the reservoir parameters and the interaction potential only, and is determined according to the expression

$$\Xi = \frac{16}{15} n_0 z_0 c_{2,2} \left(\frac{2k_bT_0}{m}\right)^{1/2} \left(\frac{C_6}{k_bT_0}\right)^{1/3} \frac{1}{u_\infty}; \quad c_{2,2} \approx 2.99.$$

Introducing the reduced variables

$$\tau = \frac{T}{T_0} \Xi^{6(\gamma-1)/(\gamma+2)}$$

and

$$\zeta = \frac{z}{z_0} \Xi^{-3/(\gamma+2)},$$

the appropriate set of differential equations to be solved under the thermal conduction model for the attractive C_6 potential are

$$\frac{d\tau_\perp}{d\zeta} = -\frac{2\tau_\perp}{\zeta} + p(\tau_\perp, \tau_\parallel, \tau_r)\frac{\tau_m^{1/6}}{2\zeta^2} \times \left[\frac{1}{2}(\tau_\parallel - \tau_\perp)(1+\xi\alpha) + \xi\beta(\tau_r - \tau_m)\left[1 - \frac{1}{18}\left(\frac{\tau_\parallel - \tau_\perp}{\tau_m}\right)\right]\right] \tag{4.4}$$

$$\frac{d\tau_\parallel}{d\zeta} = -p(\tau_\perp, \tau_\parallel, \tau_r)\frac{\tau_m^{1/6}}{\zeta^2} \times \left[(\tau_\parallel - \tau_\perp)(1+\xi\beta) - \xi\beta(\tau_r - \tau_m)\left[1 + \frac{1}{9}\left(\frac{\tau_\parallel - \tau_\perp}{\tau_m}\right)\right]\right] \tag{4.5}$$

$$\frac{d\tau_r}{d\zeta} = -p(\tau_\perp, \tau_\parallel, \tau_r)\frac{3\xi\beta}{\mathcal{R}}\frac{\tau_m^{1/6}}{\zeta^2}(\tau_r - \tau_m) \tag{4.6}$$

$$\tau_m = \frac{2\tau_\perp + \tau_\parallel}{3},$$

where $\tau_\parallel$, $\tau_\perp$ and τ_r pertain to the parallel, perpendicular and rotational temperatures, respectively, $\mathcal{R}$ is the number of rotational degrees of freedom, and ξ relates to the efficiency of rotational to translational energy transfer, as discussed below. The coefficients α and β are defined as

$$\alpha = \frac{1}{\Gamma}\frac{3}{80}\left(\frac{\mathcal{R}}{\mathcal{R}+1}\right)$$

and

$$\beta = \frac{1}{\Gamma}\frac{9}{16}\left(\frac{\mathcal{R}}{\mathcal{R}+1}\right)$$

respectively, with $\Gamma \approx 0.5813$ for the C_6 potential.

As something of an aside, it is interesting to note that it is possible to solve the thermal conduction model for any inverse power law potential having the general form

$$V(r) = -C_n r^{-n}.$$

For this generalized form of the interaction potential, the corresponding set of differential equations in terms of reduced variables for an atomic system are

$$\frac{d\tau_\perp}{d\zeta} = -2\frac{\tau_\perp}{\zeta}\tau_m^\varrho + p(\tau_\perp, \tau_\parallel, \tau_r)\frac{\tau_m^\varrho}{2\zeta^2}\left(\tau_\parallel - \tau_\perp\right) \tag{4.7}$$

$$\frac{d\tau_\parallel}{d\zeta} = -p(\tau_\perp, \tau_\parallel, \tau_r)\frac{\tau_m^\varrho}{\zeta^2}\left(\tau_\parallel - \tau_\perp\right) \tag{4.8}$$

where

$$\varrho = \frac{1}{2} - \frac{2}{n}.$$

To the extent that a real system is properly represented by the inverse power law model of the interaction potential, the effective value of n is generally in the range $6 \leq n \leq 9$, with the special cases of hard sphere ($n = \infty$) and Maxwell molecules ($n = 4$) representing limiting cases of *hard* and *soft* collision systems, respectively. All of the calculations presented in this section employ the C_6 potential function in the solution of the thermal conduction model equations.

In all previous studies involving the use of the thermal conduction model, it has been assumed that the directed flow velocity u reaches its thermodynamic limiting value only a

few nozzle diameters downstream of the nozzle exit, leading to the following simplification of equation (4.2)

$$n(z) = n_0 \left(\frac{z}{z_0}\right)^{-2}.$$

In fact, the flow velocity can never attain its thermodynamic limiting value, since to do so would require the conversion of all the energy associated with the translational and internal modes of the particles into the kinetic energy $\frac{1}{2}mu^2$ of the directed mass flow. Rather, u asymptotically approaches its limiting value as the expansion proceeds. Assuming that the expansion is a truly isentropic process, conservation of energy gives that [Haberland *et al*, 1985]

$$\frac{5}{2}k_bT_0 + \frac{\mathcal{R}}{2}k_bT_0 = \frac{3}{2}k_bT_{\|} + \frac{2}{2}k_bT_{\perp} + \frac{\mathcal{R}}{2}k_bT_r + \frac{1}{2}mu^2, \tag{4.9}$$

assuming $\frac{1}{2}k_bT$ per rotational degree of freedom and neglecting all vibrational contributions. In equations (4.4) to (4.6), $p(\tau_{\perp}, \tau_{\|}, \tau_r)$ represents the ratio u/u_{∞}, which can be simply determined from equation (4.9) to be

$$p(\tau_{\perp}, \tau_{\|}, \tau_r) = \left[\frac{(\mathcal{R}+5)\tau_0 - 3\tau_{\|} - 2\tau_{\perp} - \mathcal{R}\tau_r}{(\mathcal{R}+5)\tau_0}\right]^{1/2}. \tag{4.10}$$

The rotational–translational coupling is described in terms of the single parameter ξ, which represents the fraction of capture collisions (those pertaining to classical capture cross sections) that lead to a quasiequilibrium distribution of energy [Klots, 1980]. Although somewhat naive, the assumption that ξ is independent of all other collision parameters is made attractive by its simplicity and the success of equations (4.4) to (4.6) to yield results which are in excellent agreement with those obtained by experiment. While equations (4.4) to (4.6) do allow solutions for $\xi > 1$, it is most unlikely that rotational relaxation will ever be more efficient than translational relaxation and it would therefore appear reasonable to suggest that $\xi = 1$ represents a lower limit to the terminal rotational temperature obtainable in a given expansion.

In order to calculate the mean collision rate, the local velocity distribution of the atoms or molecules in the beam must be known or approximated. The most frequently used velocity distribution function is an ellipsoidal function of the form

$$f(\mathbf{v})\mathrm{d}\mathbf{v} = \frac{1}{\pi^{3/2}}\left(\frac{m}{2k_bT_{\perp}}\right)\left(\frac{m}{2k_bT_{\|}}\right)^{1/2} \mathrm{e}^{-mv_x^2/2k_bT_{\perp}}\mathrm{e}^{-mv_y^2/2k_bT_{\perp}}\mathrm{e}^{-m(v_z-u)^2/2k_bT_{\|}}\mathrm{d}\mathbf{v}, \tag{4.11}$$

where v_x and v_y are the velocity components perpendicular to the beam axis and v_z is the velocity component parallel to the beam axis. The use of this ellipsoidal model has become a standard technique in many theoretical and experimental studies of the supersonic expansion process [Willis *et al*, 1972; Engelhardt *et al*, 1985] as it simplifies the analysis of the parallel and perpendicular profiles by allowing their characterization in terms of separate uncoupled Maxwellian velocity distribution functions.

Assuming that all molecules in the beam have a normalized velocity distribution given by (4.11), the mean collision rate for a single atom or molecule was calculated by averaging the product $n\sigma c_r$ over all classes of the relative speed c_r

$$\begin{aligned} \nu &= n\int_0^{\infty} \sigma(c_r)c_r g(c_r)\mathrm{d}c_r \qquad (4.12)\\ &= n\overline{\sigma(c_r)c_r}, \end{aligned}$$

where g is the relative speed distribution function derived from equation (4.11). Mean free paths were calculated in an analogous manner according to the equation

$$\lambda = \left[n \int_0^\infty \sigma(c_r) g(c_r) dc_r \right]^{-1}.$$

The collision cross sections were calculated according to the integral

$$\sigma^l(c_r) = 2\pi \int_0^\infty b(1 - \cos^l \chi) \mathrm{d}b \tag{4.13}$$

for $l = 2$, where b is the impact parameter and χ is the classical deflection angle. Evaluations of the integral (4.13) were performed using the numerical quadrature techniques described by O'Hara and Smith [O'Hara and Smith, 1970; O'Hara and Smith, 1971]. Lennard–Jones (12,6) interaction potentials were used in the calculation of collision cross sections for the diatomic species using the potential parameters given by Hirschfelder *et al* [Hirschfelder *et al*, 1954], while for the monatomic species a modified Buckingham potential was employed [Tang and Toennies, 1977].

4.2.3 Computational procedure

The computational procedure for the calculation of supersonic beam properties using the thermal conduction model was primed with the source temperature and pressure, a tabulated interaction potential, the molecular mass of the gas, the heat capacity ratio γ, the nozzle peaking factor κ, and the Lennard–Jones C_6 potential parameter. For molecular species, the number of rotational degrees of freedom and the rotational–translational coupling parameter ξ were also specified. The tabulated interaction potential was used for the calculation of collision cross sections and consisted of up to 100 points sampled at regular intervals along the potential curve for the species of interest. Cubic spline interpolation [Conte and de Boor, 1980] was then used to evaluate the interaction potential at any intermolecular separation from the supplied list of points. Extrapolation of the supplied potential data was performed when necessary by fitting appropriate inverse power functions to each end of the interpolating function.[1] The radius of the nozzle exit and the range of the calculation were set at 35 μm and 5×10^{-2} m, respectively, for all of the calculations presented in this section. The number of equally spaced points along the expansion axis for which beam temperatures and collisional data were sampled was set to 1024.

Equations (4.4) to (4.6) were solved in terms of the reduced variables τ_i ($i = \perp, \parallel, r$) and ζ using a fourth order Runge–Kutta algorithm [Press *et al*, 1986] with an integration step size of 1×10^{-6} reduced distance units. Boundary conditions for the solution of the thermal conduction model equations were determined by assuming that departures from equilibrium are negligible for $z \leq z_0$. The flow velocity and temperature components of the supersonic beam were evaluated at appropriate intervals along the expansion axis and used to determine the mean collision cross section, mean collision frequency, mean free path and beam density. Mean collisional quantities were calculated by averaging 1024 individual values determined at energies sampled with appropriate probability from the relative speed distribution function related to equation (4.11). An energy balance was performed at each sampling interval to obtain an estimate for any errors associated with the numerical integration of equations (4.4) to (4.6). Energy was conserved to within $\pm$ 0.01 K for all of the calculations presented in this section.

[1] A more detailed description of the procedures employed for the interpolation and extrapolation of tabulated interaction potential data may be found in §4.4.

Gas	P_0 (atm)	T_0 (K)	u_{expt} (m/s)	$T_{\|\|,expt}$ (K)	u_{calc}	$T_{\|\|,calc}$	$T_{r,calc}$	ξ
H_2	4	300	2659	4.4	2493	5.9	154.7	0.015
N_2	1	300	753	13.1	753	14.6	26.9	0.39
O_2	1	300	—	—	708	13.8	22.8	0.41

Table 4.2: Experimental and calculated flow parameters for diatomic species. Experimental values presented previously in Table 3.3 are reproduced here for convenience.

Gas	P_0 (atm)	T_0 (K)	u_{expt} (m/s)	$T_{\|\|,expt}$ (K)	u_{calc}	$T_{\|\|,calc}$
He	1	300	1740	5.5	1745	5.8
Ne	1	300	773	3.2	781	3.3
Ar	1	300	552	1.3	557	1.4
Kr	1	300	381	1.1	385	1.1

Table 4.3: Experimental and calculated flow parameters for monatomic gases. Experimental values presented previously in Table 3.2 are reproduced here for convenience.

4.2.4 Results and discussion

The experimental measurement of u and $T_{||}$ using time–of–flight techniques was described in §3.3. A comparison between the experimentally determined values of u and $T_{||}$ presented in §3.3 and values calculated under identical source conditions using the thermal conduction model is illustrated in Tables 4.2 and 4.3. Time–of–flight measurements were not performed for O_2 due to the risk of oxidizing the filament in the mass spectrometer ion source. The calculated and experimental values of u and $T_{||}$ were in excellent agreement for all of the monatomic species examined. Due to the occurrence of decelerating collisions between the atoms or molecules in the supersonic beam and background gas particles in the expansion chamber, the experimentally determined flow velocities were observed to be slightly lower than the calculated values in all cases.

For the monatomic species, fast cooling was observed, with the flow velocity reaching its terminal value within a distance of only a few nozzle diameters from the nozzle exit and being nearly equal to the thermodynamic limiting value predicted by equation (4.3). The overall relaxation rate was somewhat slower for the diatomic species due to the presence of the rotational energy reservoir, resulting in a larger distance from the nozzle exit before the beam acceleration became negligible. The terminal flow velocities obtained for the diatomic species were also observed to differ considerably from the corresponding thermodynamic limiting values.

A comparison between the measured parallel translational temperatures and numerical results obtained using the thermal conduction model gave values for the rotational–translational coupling parameter ξ of 0.015 for H_2 and 0.39 for N_2. The value of 0.41 listed in Table 4.2 for O_2 was estimated using the experimental results of Anderson and Fenn [Anderson and Fenn, 1965]. Flow velocities and parallel translational temperatures calculated for H_2, N_2 and O_2 using values of ξ exceeding about $\pm$ 5% difference from the values listed in Table 4.2 were in considerable disagreement with the experimental data. A maximum uncertainty of $\pm$ 10% is suggested for all values of ξ determined in this study.

Figures 4.1 and 4.2 illustrate calculated temperature profiles for H_2 with $\xi = 0.015$ and N_2 with $\xi = 0.39$ under the experimental conditions specified in Table 4.2. The rotational temperature very rapidly approaches a nearly constant value for both species,

with the final rotational temperatures being 154.7 K and 26.9 K for H_2 and N_2, respectively. The rotational temperature approaches a nearly constant value with increasing distance from the nozzle exit as a result of the diminishing number of collisions with increasing distance which forces disequilibrium with the translational degrees of freedom. A further decrease in the number of collisional events leads to a freezing of the parallel translational temperature, while the perpendicular translational temperature component continues to drop in a geometric fashion due to the perpetual narrowing of the perpendicular velocity distribution [Hamel and Willis, 1966].

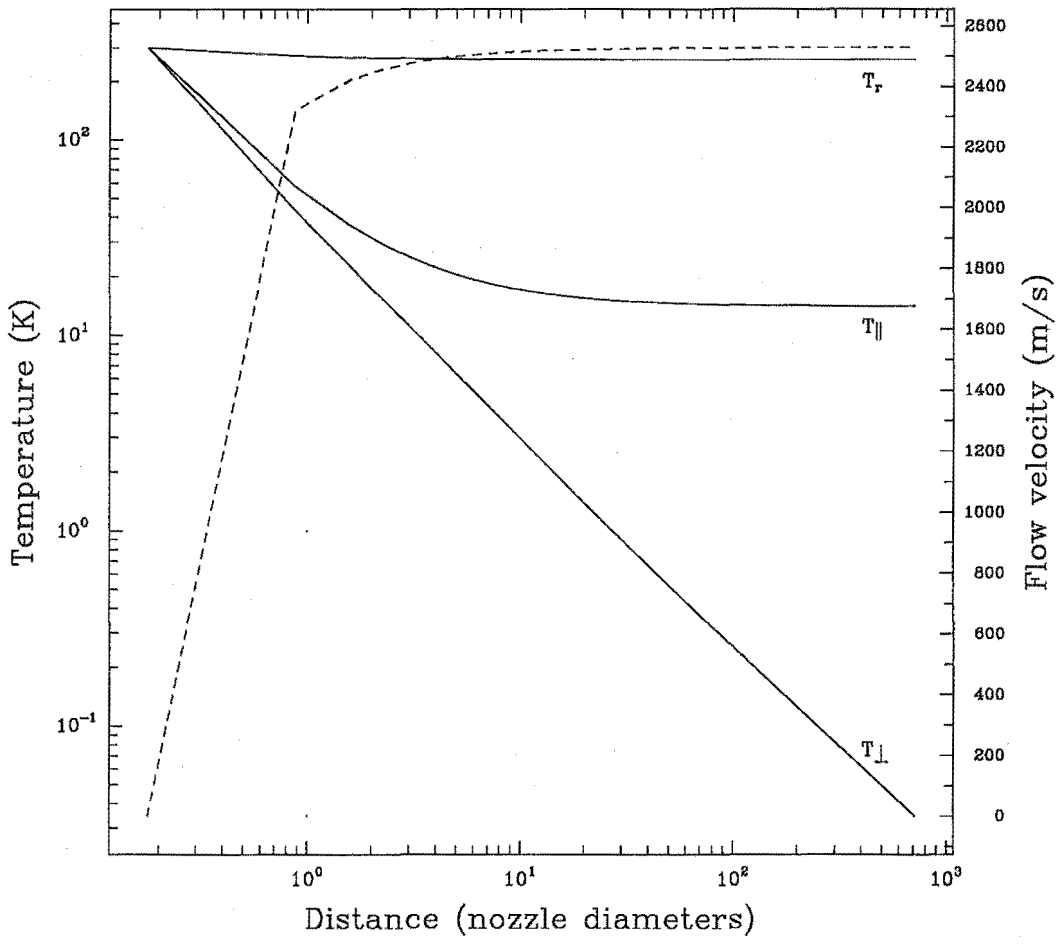

Figure 4.1: Calculated rotational and translational temperature profiles for H_2.

The rotational–translational coupling parameter value of 0.39 determined for N_2 is in excellent accord with the value of 0.41 calculated by Randenyia and Smith [Randeniya *et al*, 1989]. The low value of ξ determined for H_2 appears reasonable and indicates that rotational relaxation in H_2 is an extremely inefficient process. This is well known to be the case, with high collision numbers having been determined for both vibrational–translational and rotational–translational relaxation in H_2. The value of 154.7 K calculated

for the final rotational temperature of H_2 is in good agreement with the results of Gallagher and Fenn [Gallagher and Fenn, 1974]. In view of this result and the good agreement observed between the rotational–translational coupling parameter determined for N_2 in the present study and that obtained by Randeniya and Smith, it seems reasonable to assume that the values determined for H_2 and O_2 are reliable.

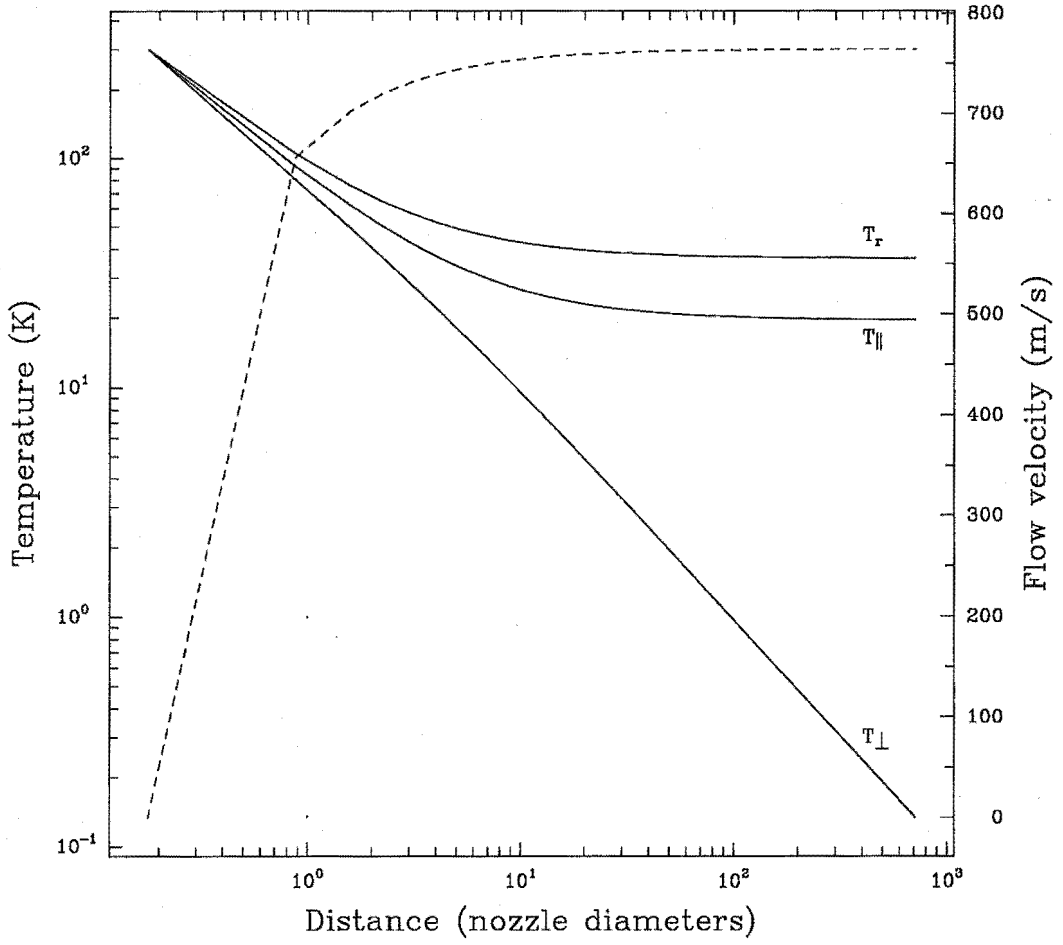

Figure 4.2: Calculated rotational and translational temperature profiles for N_2.

The calculations performed in this investigation suggest that the total number of binary collisions experienced by an atom or molecule during the supersonic expansion process[2] is typically between 10^2 and 10^3. Any kinetic process requiring this number of collisions will be subject to relaxation effects during the course of the expansion and may *freeze*. The vibrational relaxation of simple diatomic molecules typically requires

[2]The total number of binary collisions experienced by an atom or molecule during the course of the supersonic expansion was estimated by numerically integrating the collision frequency with respect to time over the entire range of the calculation. Time intervals Δt for the integration process were calculated according to the expression $\Delta t = 2(z_2 - z_1)/(u_1 + u_2)$.

in excess of 10^4 collisions, indicating that the vibrational modes of such species do not participate in the expansion. The explicit consideration of vibrational degrees of freedom has therefore been ignored in the present analysis, the assumption being that either these modes very rapidly freeze out or that they contain insufficient energy to significantly alter any flow characteristics. Under conditions of thermal equilibrium at a nozzle temperature of 300 K, statistical thermodynamical considerations indicate a negligible population of anything but the ground vibrational level for all of the diatomic systems considered in this study. The vibrational collision numbers of large polyatomic molecules and the rotational collision numbers of most diatomic species are of the order 1 to 100, so that such modes can exchange energy and cool to some extent during the initial stages of the supersonic expansion before freezing.

Figures 4.3 to 4.5 present a set of curves showing the variation of collision frequency and mean free path as a function of axial distance for several species at various source conditions. From these curves it is evident that even at large distances from the nozzle exit the collision frequency within the beam remains quite high. Molecular beams are commonly considered to be collision free, but in fact such a situation can only be true in the limit of zero particle density or zero velocity dispersion. Even in a well collimated molecular beam, collisions will occur as faster molecules approach and overtake slower ones. Figure 4.3 shows a set of curves calculated for argon at three reservoir pressures and illustrates the point that, for a fixed nozzle diameter, the collision frequency is directly proportional to P_0.

The variation of normalized beam density as a function of axial distance from the nozzle exit calculated using equation (4.2) is shown for helium and nitrogen in Figure 4.6. For the experimental arrangement described in §3.3, the axial particle density for a helium beam at a distance of 3.9 cm from the nozzle exit corresponds to a beam pressure of approximately 3×10^{-3} Torr for a stagnation pressure of 1 atm. Recent measurements performed in our laboratory [Aitken *et al*, 1993] indicate that beam densities calculated in this manner are generally quite accurate. Realistic values of beam density as a function of axial distance are an essential prerequisite for the reliable determination of collision cross sections from crossed beam experiments.

Collision frequencies in a bulb were calculated in an analogous manner to those in a supersonic beam according to the integral (4.12), using a Maxwellian speed distribution function for $g(c_r)$. A plot of the ratio ν_{beam}/ν_{bulb} as a function of the mean kinetic temperature T_m is given in Figure 4.7 for argon. The oscillations in the curve result only from the integration procedure employed for the calculation and also reflect the greater density of points calculated for the lower temperatures. The collision frequency in the beam is always lower than that in the bulb, although the ratio does not remain constant at a value of approximately 1/2 as originally suggested by Lubman *et al* [Lubman *et al*, 1982]. The major reason for this difference comes from the use of realistic energy dependent collision cross sections in the present study in place of the constant hard sphere values employed by Lubman *et al*. Calculations indicate that the size of the mean collision cross section may change by up to an order of magnitude during the course of a typical supersonic expansion starting at room temperature. The reason that ν_{beam} is always less than ν_{bulb} may be attributed to the fact that the magnitude of the relative velocity between two particles in a supersonic beam is significantly less than that between two particles in a bulb. Quite clearly atoms and molecules can never be taken as being completely isolated in a supersonic beam simply because of the finite width of the velocity distribution, causing some particles to overtake and collide with others. What is of importance, however, is

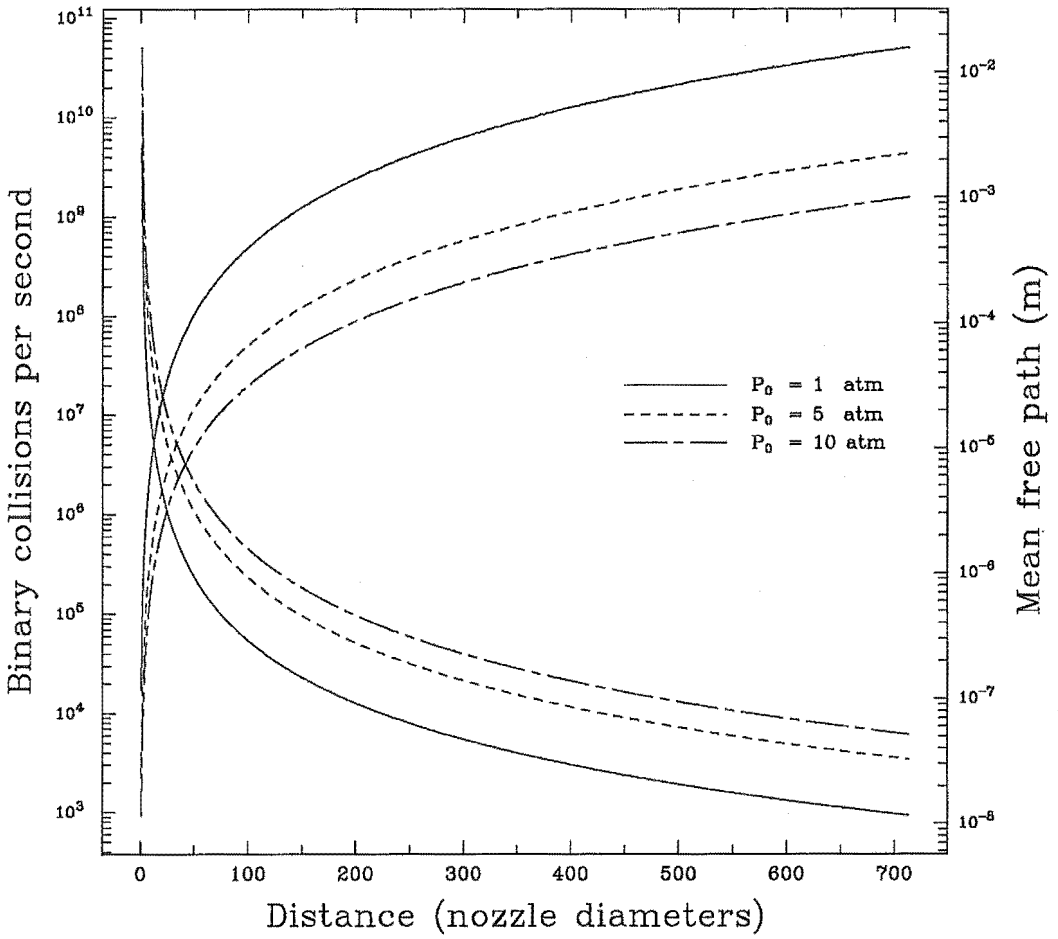

Figure 4.3: Collision frequencies and mean free paths as a function of stagnation pressure for beams of argon with a source temperature of 300 K.

whether or not the beam species are suitably well isolated on the time scale relevant to the experiment of interest.

4.2.5 Conclusion

The thermal conduction model has been used to investigate the flow dynamics of supersonic beams for the monatomic species He, Ne, Ar and Kr, and the diatomic species H_2, N_2 and O_2. The model was modified to incorporate a variable flow velocity by the inclusion of an energy balance term. Temperature and flow velocity data obtained using the thermal conduction model were used to calculate collision frequencies and beam densities as a function of distance from the nozzle exit. Rotational–translational coupling parameters were determined for the diatomic species by fitting calculated values of u and $T_{\|}$ to experimental time–of–flight data. The excellent agreement obtained between the experimentally determined and calculated time–of–flight parameters for all of the species examined and

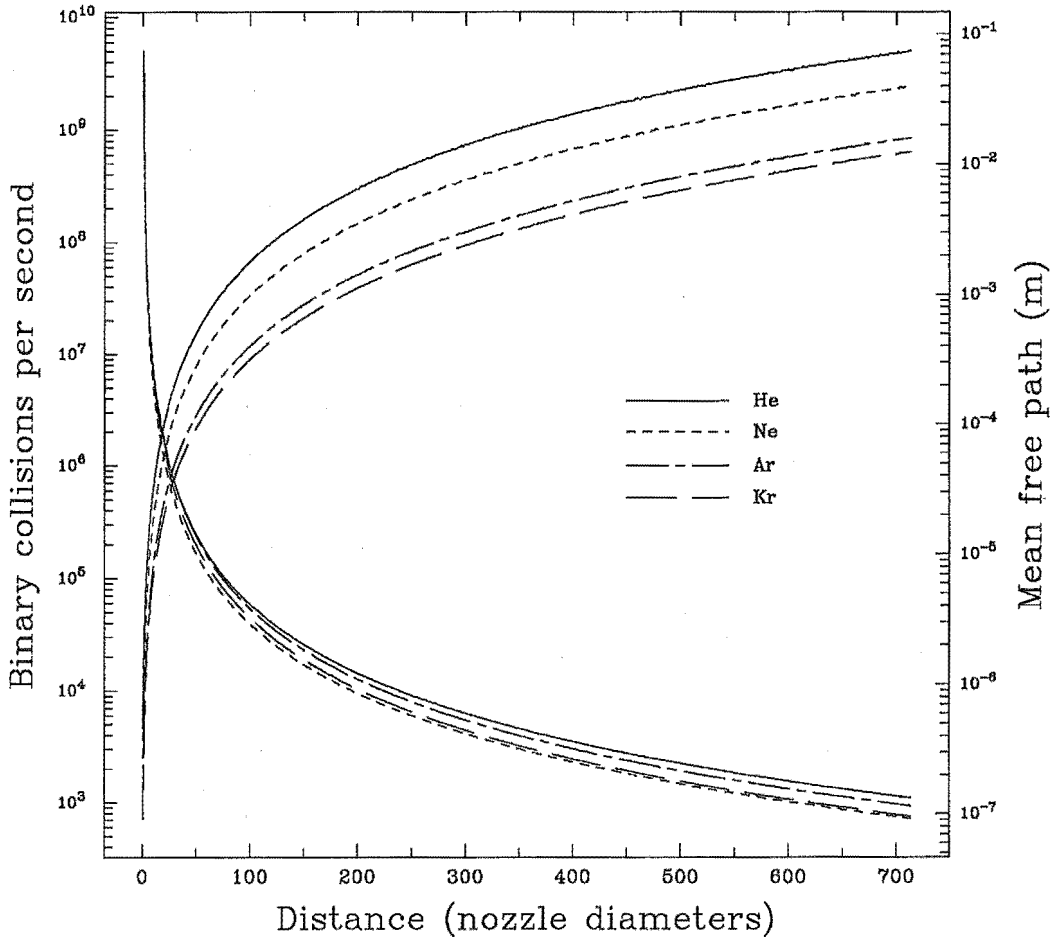

Figure 4.4: Calculated collision frequencies and mean free paths for several noble gases ($P_0 = 1$ atm, $T_0 = 300$ K).

the good agreement of the rotational–translational coupling parameter for N_2 determined in the present study with that obtained by Randeniya and Smith [Randeniya *et al*, 1989] afford some confidence that the collision frequencies and particle densities calculated from the thermal conduction model using realistic collision cross sections and interaction potentials closely reflect the characteristics of a skimmed supersonic beam along the expansion axis. A more detailed theoretical investigation into the rotational relaxation of small molecules in supersonic molecular beams is presented in the following section, while the possibility of extending the thermal conduction model to investigate supersonic expansions of simple gas mixtures is being pursued.

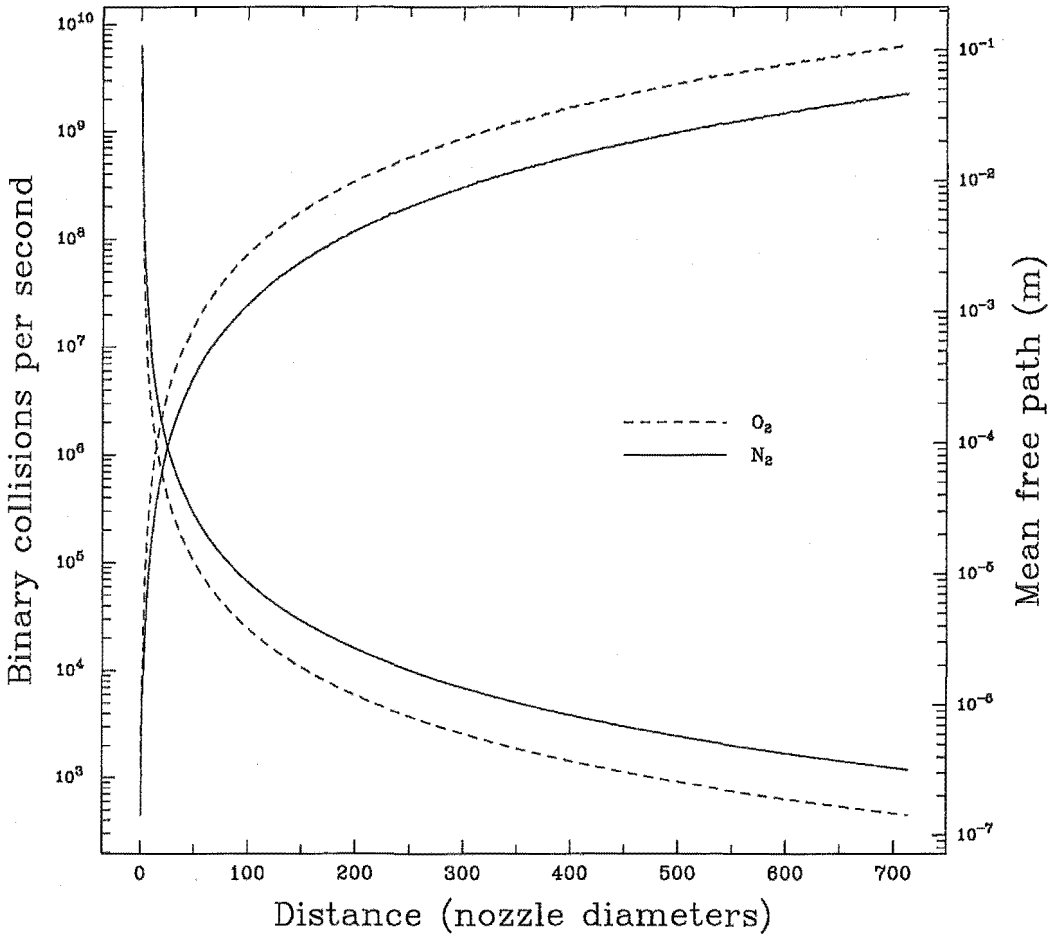

Figure 4.5: Calculated collision frequencies and mean free paths for the diatomic species O_2 and N_2.

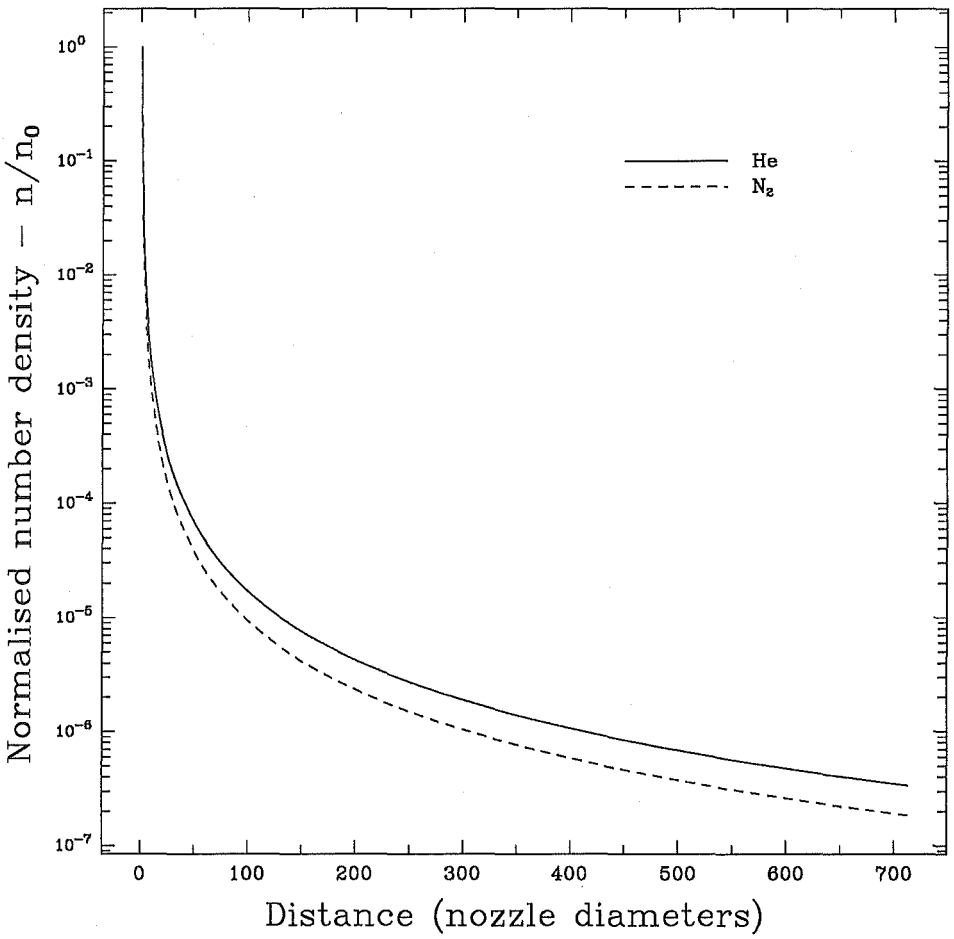

Figure 4.6: Normalized number density profiles for helium and nitrogen.

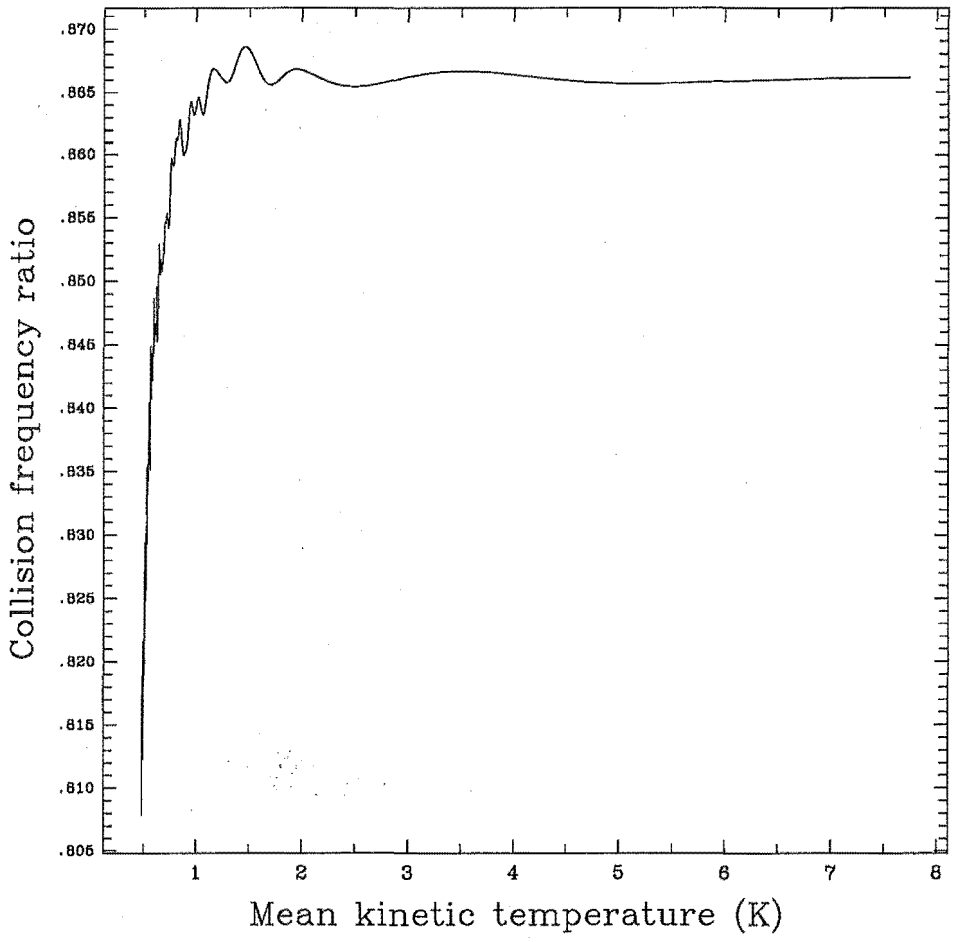

Figure 4.7: Collision frequency ratio (ν_{beam}/ν_{bulb}) for argon as a function of the mean kinetic temperature.

4.3 Application of the thermal conduction model to rotational relaxation in molecular beams

4.3.1 Introduction

Until recently, supersonic or nozzle molecular beam sources were the exclusive domain of the molecular dynamicist. Once it was recognised that these devices provided a new technique for the generation of cooled molecules through seeding, such sources became a valuable tool in the study of the spectroscopy of polyatomic molecules and for the study of ion–molecule chemistry at low temperatures. Experiments such as these which are designed to measure quantitative parameters in molecular beams rely on a knowledge of the beam density, collision frequency and temperature of the species involved as a function of distance from the nozzle exit. The thermal conduction model and the extensions described in this section provide a convenient means by which these properties may be estimated. Such parameters cannot be routinely measured in the laboratory and rigorous solution of the Boltzmann equation results in expressions which cannot be easily applied.

The translational temperature of a molecular gas undergoing a supersonic expansion may decrease so rapidly that the rotational degrees of freedom of a molecule do not have sufficient time to relax completely [Cameron and Harland, 1991]. It is these relaxation *lags* which are observed experimentally in the form of a difference between the terminal rotational temperature and the terminal parallel translational temperature of a supersonic molecular beam. An analysis of these rotational relaxation lags is useful for the study of energy transfer processes between rotational and translation degrees of freedom and for the prediction of the internal states of molecules in molecular beams produced by supersonic expansion techniques. It would for example be desirable to be able to predict with some degree of accuracy the final distribution of rotational states of symmetric top molecules used in molecular beam experiments employing a supersonic nozzle source in association with an upper Stark state selector [Harland *et al*, 1991].

A number of workers have analysed the relaxation kinetics in supersonic expansions on the basis of the so-called *Landau–Teller* model [Yamazaki *et al*, 1981] with the inherent assumption that the characteristic bulk rotational relaxation rate is approximately constant throughout the entire duration of the expansion. On the basis of experimental results this assumption is quite clearly incorrect. Consequently, for any theoretical model to realistically describe the relaxation kinetics of supersonic expansions it must allow for the variation of the rotational relaxation time as a function of both the mean translational temperature and the rotational temperature. It is shown here that the thermal conduction model may be used to provide the required functionality in both a straightforward and reliable manner.

4.3.2 Theoretical considerations

The differential equation used to describe the rate of change of the rotational temperature as a function of distance in the adaptation of the thermal conduction model presented in §4.2 has much in common with the following expression which has been frequently used for many years [Klots, 1980] to describe rotational relaxation phenomena:

$$\frac{\mathrm{d}T_r}{\mathrm{d}t} = \frac{1}{\tau_r}(T_m - T_r). \tag{4.14}$$

In this equation, τ_r is the mean rotational relaxation time, T_r is the rotational temperature at time t and T_m is the mean equilibrium temperature of the translational reservoir.

Equation (4.14) has generally been applied to the analysis of bulk systems under thermodynamic equilibrium and has proven somewhat difficult to justify at the molecular level. Gallagher and Fenn [Gallagher and Fenn, 1974] recognised, however, that the evolution of a distinct rotational temperature in a supersonic expansion is essentially a relaxation process having much in common with such bulk equilibrium processes. Comparing equation (4.14) with equation (4.6) of §4.2, which describes the change in rotational temperature as a function of reduced distance along the expansion axis, it can be shown that the expression for the inverse rotational relaxation time according to the thermal conduction model is

$$\tau_r^{-1} = u\frac{3\xi\beta}{\mathcal{R}}p(T_\perp, T_{||}, T_r)\Xi\left(\frac{T_m}{T_0}\right)^{1/6}\frac{z_0}{z^2} \tag{4.15}$$

$$= \frac{16}{15}\frac{3\xi\beta}{\mathcal{R}}p(T_\perp, T_{||}, T_r)^3 n(z)\left(\frac{2k_bT_m}{m}\right)^{1/2} c_{2,2}\left(\frac{C_6}{k_bT_m}\right)^{1/3}. \tag{4.16}$$

It is important to note that this expression is only applicable to the evaluation of rotational relaxation times in an expanding jet, and that it is only valid at distances from the nozzle exit greater than or equal to the boundary condition value, z_0. The function $p(T_\perp, T_{||}, T_r)$ has the following form (see §4.2.2):

$$p(T_\perp, T_{||}, T_r) = \left[\frac{(\mathcal{R}+5)T_0 - 3T_{||} - 2T_\perp - \mathcal{R}T_r}{(\mathcal{R}+5)T_0}\right]^{1/2}, \tag{4.17}$$

and must be evaluated using the variant of the thermal conduction model described in §4.2. In this expression T_0 is the source temperature, $T_\perp$ and $T_{||}$ are the translational temperature components perpendicular and parallel to the beam axis, respectively, and $\mathcal{R}$ is the number of rotational degrees of freedom of the molecule. All other quantities in equations (4.16) and (4.17) are defined in §4.2.

The expression for the rotational relaxation time given in equation (4.16) is similar in form to equation (26) of [Randeniya and Smith, 1990] derived by Randeniya and Smith, but with one important difference. In contrast to the expression derived by them, equation (4.16) accounts for the dependence of the rotational relaxation time on the translational and the rotational temperature of the system. The expression used by Randeniya and Smith includes only one temperature variable and essentially assumes that the function $p(T_\perp, T_{||}, T_r)$ is a constant value. They go to considerable lengths to derive a set of moment equations from the generalized Boltzmann equation to predict the properties of a supersonic expansion and criticise the thermal conduction model for its failure to properly account for the total energy of the expanding jet as a result of fixing the flow velocity of the beam at its thermodynamic limiting value at all points in the expansion. Subsequent to Randeniya and Smith's publication, the function $p(T_\perp, T_{||}, T_r)$ was introduced by Cameron and Harland [Cameron and Harland, 1991] as a simple and effective means of incorporating a variable flow velocity into the thermal conduction model using basic conservation of energy principles. While it is true that $p(T_\perp, T_{||}, T_r)$ rapidly tends to a constant value for most systems, it is by no means independent of temperature. In assuming a constant function for $p(T_\perp, T_{||}, T_r)$, Randeniya and Smith have effectively incorporated into their model the point of their criticism regarding the thermal conduction model.

From equation (4.16) it follows that the inverse rotational collision number is given by the expression

$$Z_r^{-1} = \frac{16}{15}\frac{3\xi\beta}{\mathcal{R}}p(T_\perp, T_{||}, T_r)^3, \tag{4.18}$$

which, like equation (4.16), is also a function of both the translational and rotational temperature of the expanding jet. In the approach adopted by Randeniya and Smith this quantity is assumed to be a constant value, independent of the rotational and translational energy of the system during the course of the expansion. The rotational collision number is defined as the product of the rotational relaxation time and the mean collision frequency. The collision number is therefore independent of pressure and dependent only upon T_r, T_m, and the degree of non–equilibrium between the translational and rotational modes of the molecule.

The distribution of rotational energies of molecules in an expanding jet may exhibit distinctly non–Boltzmann character [Marrone, 1967]. Although the thermal conduction model and the approach used by Randenyia and Smith [Randeniya and Smith, 1990] to describe the expansion process freely use the term *rotational temperature*, this does not imply that a unique rotational temperature and, by inference, a well defined rotational state distribution exists in an expanding jet [Klots, 1980]. The rotational temperature is merely a convenient shorthand notation used to describe the average rotational energy of the system.

It is important to note that the approach described here represents only a first order approximation of the rotational relaxation process in molecular beams and will become progressively less accurate with increasing distance from the nozzle exit. The inclusion of higher order terms in the rate expression would require a knowledge of the exact state–to–state cross sections for the rotational to translational energy transfer process. A complete evaluation of the differential cross sections as a function of scattering angle and initial relative velocity would be necessary to properly evaluate the relaxation time. The use of full scale trajectory calculations for the evaluation of such detailed information is currently being pursued for the case of atomic–homonuclear diatomic systems. The application of a simple direct simulation Monte Carlo algorithm to the calculation of rotational relaxation data for larger non–polar polyatomic systems is presented in §4.4. The method described here is also not applicable to polar molecules for which the interaction potential is decidedly non–spherical.

4.3.3 Results and discussion

Rotational relaxation times calculated using equation (4.16) for the homonuclear diatomic species N_2, O_2, Cl_2 and H_2 are plotted in Figure 4.8 as a function of the mean kinetic temperature T_m and in Figure 4.9 as a function of axial distance expressed in nozzle diameters. All data were calculated for a source pressure of 1 atm at a temperature of 300 K and a nozzle diameter of 7×10^{-5} m. The values of the rotational–translational coupling parameters ξ used for these calculations are given in Table 4.4. The Lennard–Jones C_6 potential parameters were taken from [Hirschfelder *et al*, 1954]. The values of ξ for H_2, N_2 and O_2 were taken from §4.2 while the value of 0.58 for Cl_2 was estimated from the experimental data of [Anderson and Hornig, 1958] using the iterative Monte Carlo procedure described in §4.4, in which it is assumed that the amount of energy transferred between the rotational and translational degrees of freedom of each molecule in a binary collision is equal to a constant fraction multiplied by the difference in energy between the rotational and translational modes. The value of the constant fraction is varied in an iterative manner such that the calculated rotational relaxation time converges to the specified experimental figure. It can be shown that this fraction is to good approximation directly proportional to ξ [Cameron and Harland, 1993c]. Given suitably reliable experimental rotational relaxation data, this technique provides a useful approach to estimating ξ for

System	H_2	N_2	O_2	Cl_2
ξ	0.015	0.39	0.41	0.58

Table 4.4: Rotational–translational coupling parameters used for the calculation of relaxation times and collision numbers. Values presented previously in Table 4.2 are reproduced here for convenience.

any system.

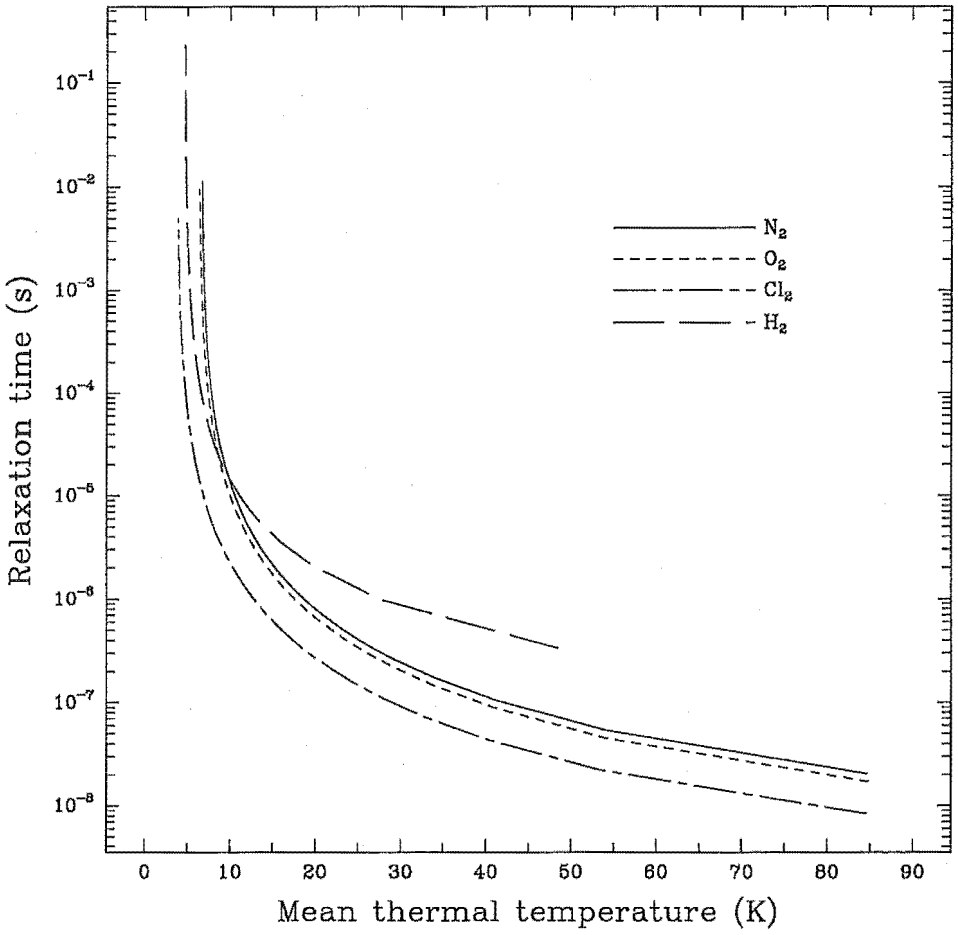

Figure 4.8: Rotational relaxation times as a function of mean kinetic temperature for N_2, O_2, Cl_2 and H_2 calculated for a source pressure of 1 atm at 300 K.

The variation of rotational collision number as a function of distance from the nozzle exit is illustrated for the species considered in Figure 4.10. It can be seen that the absolute change in rotational collision number during the course of the expansion is small but significant. For all the systems considered, the collision number is observed to decrease slightly during the expansion and then become essentially constant as the rotational and

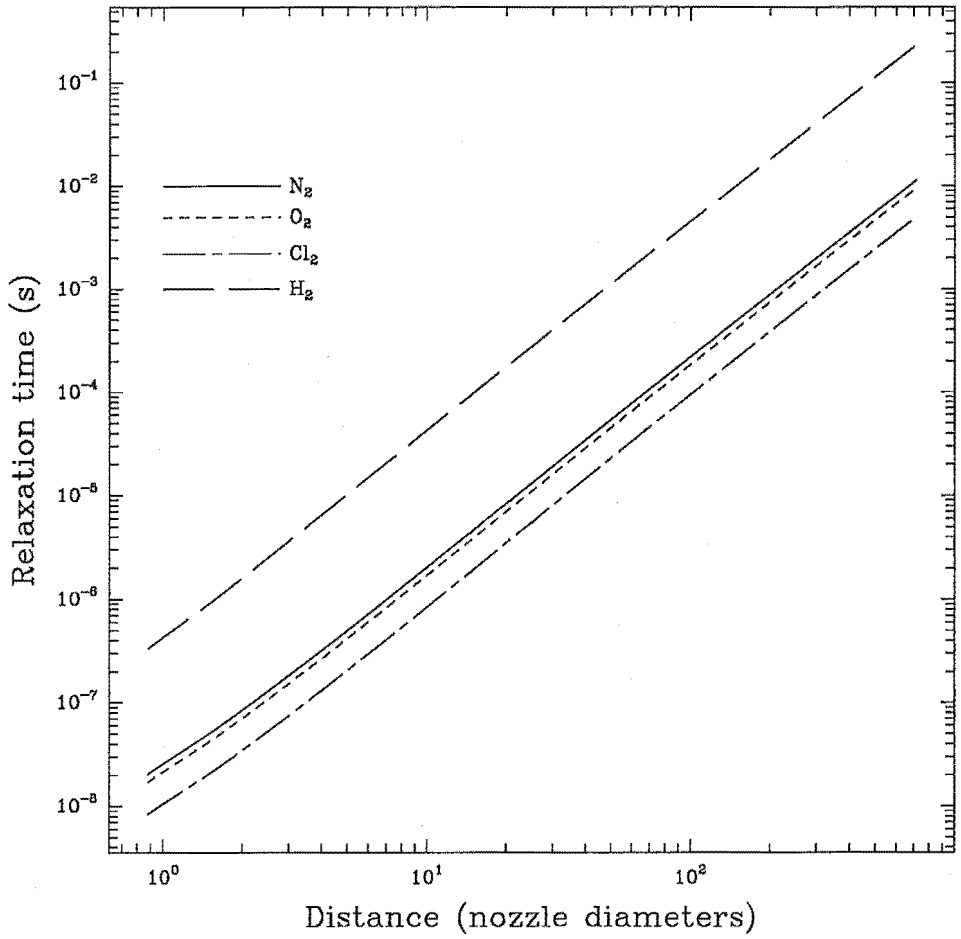

Figure 4.9: Rotational relaxation times as a function of distance from the nozzle exit for N_2, O_2, Cl_2 and H_2.

parallel translational temperature components begin to freeze out. The rotational collision number represents the average number of collisions required for a molecule to establish equilibrium between its rotational and translational degrees of freedom. As the rotational and parallel translational temperature components of the expanding jet freeze out, so too will the rotational collision number. It is of course true that the perpendicular component of the translational temperature does not freeze out but rather continues to decrease towards zero with increasing distance from the nozzle exit. However, the perpendicular temperature is so small compared to the parallel temperature at the point in the expansion where the parallel component becomes frozen that its effect on the collision number will be quite negligible beyond that point.

The behaviour of the N_2, O_2 and Cl_2 systems is quite similar, with the rotational collision numbers becoming almost constant at approximately the same point within the expansion. Rotational relaxation in H_2 is a far less efficient process with the rotational

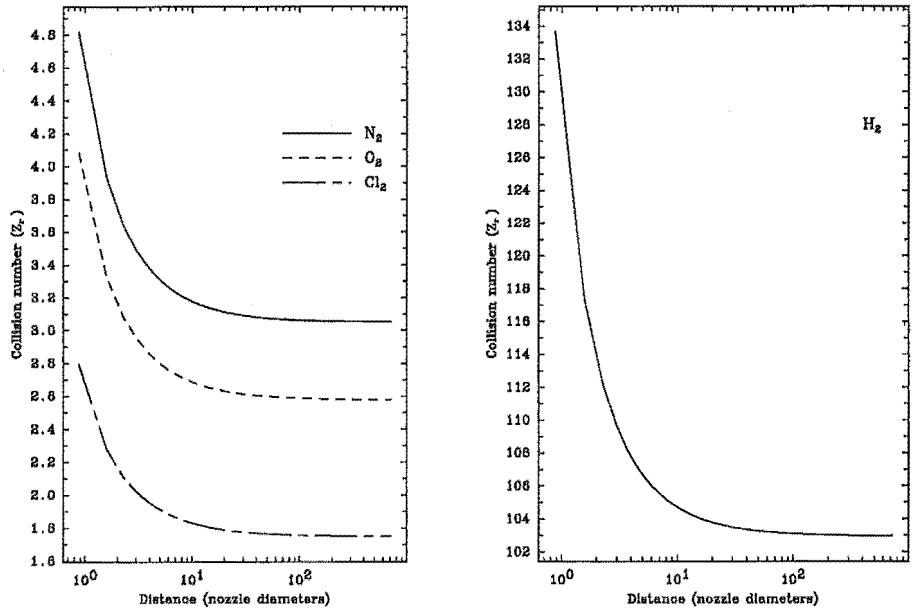

Figure 4.10: Rotational collision numbers as a function of distance from the nozzle exit for N_2, O_2, Cl_2 and H_2.

temperature becoming frozen relatively early in the expansion, close to the nozzle exit where the number density is still high. This is clearly illustrated in Figure 4.11, which shows the variation of rotational temperature as a function of axial distance expressed in terms of nozzle diameters for the species considered here. As can be seen, the rotational temperature of H_2 drops by only a factor of 2 and attains its terminal value after just a few nozzle diameters while the rotational temperatures of the other species continue to drop well into the expansion. By definition, ξ represents the fraction of inelastic collisions experienced by a molecule, indicating that only one in about every 67 collisions between hydrogen molecules leads to an exchange of energy between rotational and translation modes. The magnitude of the rotational collision number is largely determined by the value of the rotational–translational coupling parameter ξ, which may be considered to represent a measure of the efficiency of rotational to translational energy transfer.

Unfortunately, it is difficult to compare the data shown in Figures 4.8, 4.9 and 4.10 with most other studies of rotational relaxation in molecular beams. The accuracy of results presented in many papers which discuss the calculation of relaxation times and collision numbers in molecular beams is uncertain. While the majority of these communications generally employ sophisticated and reliable models to calculate the relaxation times, the expansion process is often described in a very simple manner using basic isentropic flow relations to evaluate the axial number density and translational temperature of the molecular beam [Yamazaki *et al*, 1981]. Such relations do not provide an accurate description of the expansion process and, as a consequence, rotational relaxation times

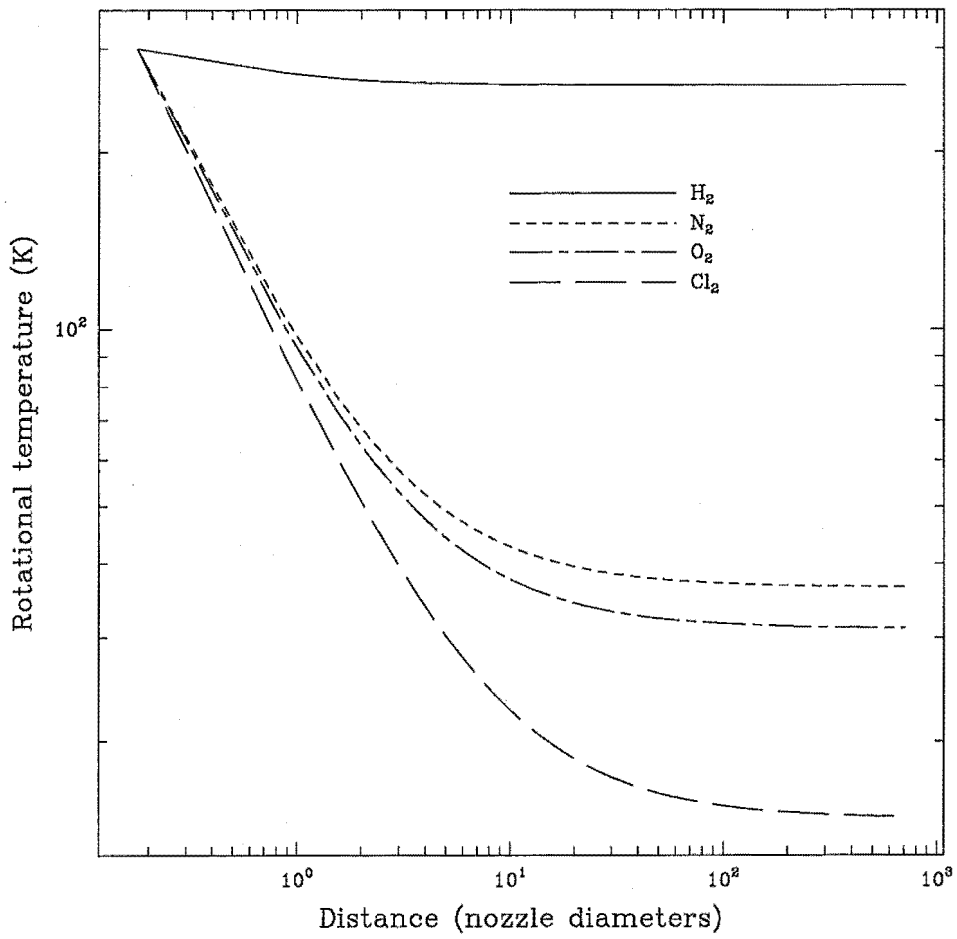

Figure 4.11: Rotational temperatures as a function of distance from the nozzle exit for N_2, O_2, Cl_2 and H_2.

calculated using number densities and translational temperatures determined in such a manner cannot be considered reliable.

The collision numbers presented in Figure 4.10 for N_2 and O_2 close to the nozzle exit where the translational temperature of the gas is not greatly different from that of the source, are in good agreement with the calculations of Parker [Parker, 1959] and the experimental results of Sessler [Sessler, 1958] and Greenspan [Greenspan, 1959]. The variation of $\mathcal{Z}_r$ with axial distance for N_2 is in qualitative agreement with the experimental results of Poulsen and Miller [Poulsen and Miller, 1977] for supersonic expansions of nitrogen–argon mixtures. The rotational collision numbers calculated for Cl_2 appear slightly high compared to the results of [Sittig, 1960] and [Bauer and Kosche, 1966] but are in reasonable agreement with Parker's results. The experimental data used to estimate ξ for Cl_2 was obtained from observations of shock front thickness and may not be entirely applicable to the molecular beam environment [Rabitz and Lam, 1975]. Experimental and theoretical

System	H_2	N_2	O_2	Cl_2
A (kg $m^{-1}s^{-1}K^{-1}$)	1.45×10^{-4}	6.97×10^{-6}	5.81×10^{-6}	2.83×10^{-6}

Table 4.5: Values of the parameter A in equation (4.19) calculated for $P_0 = 1$ atm and $T_0 = 300$ K.

studies indicate that rotational relaxation in Cl_2 is an efficient process, and the value for ξ of 0.58 may be somewhat conservative.

Studies for H_2 have generally been performed at higher temperatures than those considered here. The experimental data of Gallagher and Fenn [Gallagher and Fenn, 1974] for H_2 extends only down to 77 K and the Master Equation calculations of Rabitz [Rabitz and Lam, 1975] down to about 100 K. In both cases the calculated rotational collision numbers are considerably higher than those which might be expected from extrapolation of the data shown in Figure 4.10 for H_2 to higher temperatures. The results of Gallagher and Fenn suggest that the value of the rotational–translational coupling parameter for H_2 should possibly be closer to half the value stated in Table 4.4. The value of 0.015 was determined by comparing values of the terminal parallel translational temperature of the molecular beam calculated using the thermal conduction model with terminal temperatures measured by standard time–of–flight techniques. While it may be argued that the resolution of such techniques is insufficient to accurately measure the extremely narrow speed distribution of hydrogen, considerable care was taken to ensure that all possible sources of distortion to the time of flight signal were either eliminated or properly taken into account, and the value of ξ for H_2 is considered accurate to within $\pm$ 10%. It is hoped that work currently being pursued using a higher level of theory will help to clarify this situation.

It is evident from Figure 4.10 that log–log plots of rotational relaxation time verses axial distance are distinctly linear. Fitting these curves to a straight line yielded a linear least squares correlation coefficient of better than 0.99 in all cases. To a good approximation, the rotational relaxation time may therefore be calculated as a function of axial distance for any set of source conditions using the following expression:

$$\tau_r = A\frac{T_0}{P_0}\left(\frac{z}{d_0}\right)^2 ; \quad \frac{z}{d_0} > \left(\frac{1}{A}\right)^{1/2}\left(\frac{P_0}{T_0}\right)^{1/2}, \tag{4.19}$$

where z is the distance from the nozzle along the beam axis, d_0 is the nozzle diameter, P_0 and T_0 are the source pressure and temperature respectively, and A is a fitting parameter which is approximately constant over a moderate range of P_0 and T_0. The restriction imposed on the minimum value of z is relatively insignificant, corresponding to only a fraction of a nozzle diameter under most conditions. Values of A for the species considered in this investigation based on a source pressure of 1 atm and temperature of 300 K are given in Table 4.5. Calculations indicate that A is a weak function of P_0 and T_0, being inversely proportional to both quantities, but more sensitive to changes in the latter. For example, calculations for N_2 reveal that A changes by only 1% as a result of increasing P_0 from 1 atm to 2 atm, while increasing T_0 by a factor of two reduces the value of A given in Table 4.5 by approximately 5%. Equation (4.19) should be applied with some care and used as a guide only. It simply represents a convenient means of roughly estimating rotational relaxation times without the need for solving the differential equations used by the thermal conduction model to describe the expansion process.

4.3.4 Conclusion

The work presented in this section describes a relatively simple approach to the estimation of rotational relaxation times and collision numbers for non–polar molecules in a supersonic expansion based on the thermal conduction model. Results for the species considered are in general agreement with those of similar studies, providing some confidence in the derived expressions for the rotational relaxation time and the rotational collision number. The use of the derived expressions requires the complete solution of the thermal conduction model. The empirical expression given by equation (4.19) was obtained from an analysis of calculated relaxation time data as a function of axial distance and may be used to estimate relaxation times for any set of source conditions. The method described here is not restricted to diatomic species and may easily be applied to simple non–polar polyatomic molecules such as CO_2 and CH_4.

4.4 Monte Carlo calculation of rotational relaxation in small molecules

4.4.1 Introduction

The exchange of energy between translational and internal degrees of freedom in molecular collisions plays an important role in molecular processes, and has been an area of considerable theoretical and experimental interest for many years. The mechanism of rotational–translational energy transfer has not received nearly so much attention as that of vibrational–translational transfer, due to the greater influence of the latter process on the kinetics of chemical reactions. The study of rotational–translational energy transfer and rotational relaxation processes of molecules in supersonic expansions is, however, of particular interest for several reasons. The low collision energies attainable in supersonic expansions provide a unique environment ideally suited to the synthesis of weakly bound van der Waals clusters and the spectroscopy of complex molecules. From a spectroscopic point of view, it would therefore be highly desirable to be able to predict with some degree of accuracy the populations of individual rotational energy levels for molecules at any location within the expanding jet, while in general, there is the hope that an improved understanding of both rotational relaxation phenomena and the expansion process itself may be gained from such studies.

In the preceeding sections, the rotational relaxation of the homonuclear diatomic species H_2, N_2, O_2 and Cl_2 in a supersonic expansion were examined on the basis of the thermal conduction model [Klots, 1980; Cameron and Harland, 1991]. In this section, some initial calculations of rotational relaxation times and collision numbers using a direct simulation Monte Carlo procedure are presented, in which the exchange of energy between the rotational and translational degrees of freedom is assumed to be simply related to the fraction of inelastic collisions experienced by a molecule at a particular energy in terms of Klots rotational–translational coupling parameter [Klots, 1980]. The energy dependence of the rotational–translational coupling parameter is investigated for the homonuclear diatomic species stated above, and for the polyatomic molecules CO_2, OCS, NH_3, CH_4, CH_3Cl, and C_2H_4 using available experimental and theoretical data. The rotational and translational energy dependence of rotational relaxation times is examined for these species, and the energy dependent coupling parameter is incorporated into the thermal conduction model to investigate the breakdown of rotational and translational equilibrium in supersonic expansions of CO_2, OCS, and CH_3Cl.

4.4.2 Relaxation model

A number of classical dynamical and statistical theories have been developed for the investigation of relaxation phenomena in molecules of varying size and complexity. Dynamical calculations are generally observed to give results which differ considerably from those obtained using statistical theories, with the latter often badly over estimating the average energy changes in a collision. The use of full scale dynamical trajectory calculations is generally considered to be the most reliable means of investigating energy transfer or relaxation processes in a classical mechanical manner [Hippler *et al*, 1986]. In order for the full potential of such methods to be realized, however, it is necessary to have detailed information describing the entire potential surface for the collision system of interest. Lack of suitable potential energy surface data for many systems of interest coupled with the computational difficulties and time overhead associated with the use of such surfaces in full scale three dimensional trajectory calculations of relaxation times is sufficient to justify recourse to a phenomenological approach to the problem. The approach adopted here makes use of the direct simulation Monte Carlo method and available relaxation data to predict rotational relaxation times under any set of conditions.

The direct simulation Monte Carlo method is a technique specifically devised for the computer modelling of complex gas flow phenomena. Flows are modelled by storing the velocity components and spatial coordinates of a representative population of simulated molecules and allowing these molecules to collide and move in accordance with their physical properties. The crux of the direct simulation Monte Carlo technique is the manner in which molecular motion and intermolecular collisions are uncoupled. Simulations of this type essentially proceed by uncoupling molecular motion and intermolecular collisions over some time interval Δt_m such that Δt_m is small compared to the inverse of the mean collision frequency. At time t all molecules are allowed to move freely over the time interval Δt_m and collisions appropriate to this time span are then calculated by fixing the molecular positions.

The computation of a set of representative collisions is of crucial importance in the direct simulation Monte Carlo method. The total number of collisions N_t occurring in a uniform homogeneous gas during the time interval Δt_m is given by the expression

$$N_t = \frac{1}{2} N_m n \Delta t_m \overline{\sigma c_r}, \tag{4.20}$$

where N_m is the total number of simulated molecules present in the flow at time t, n is the number density, and σ is the collision cross section for a collision pair moving with relative speed c_r. The symmetry factor $1/2$ is included in equation (4.20) as there are two molecules whose properties are recalculated after each collision. If the number of collisions calculated over Δt_m is $N_m/2$, then all of the N_m simulated molecules will have experienced a change of state.

The product $\overline{\sigma c_r}$ in equation (4.20) represents the mean collision rate per unit density. The evaluation of this quantity will be time consuming, particularly if N_m is large, as is usually the case. To negate this problem, in the direct simulation Monte Carlo method each collision is given a *collision lifetime* Δt_c, determined by the expression

$$\Delta t_c = \frac{2}{N_m} (n \sigma c_r)^{-1}, \tag{4.21}$$

and collisions are then calculated until the sum of the collision lifetimes equals or just exceeds the value of Δt_m. Collision pairs are chosen by application of the acceptance–rejection method [Hammersley and Handscomb, 1964] with probability proportional to

σc_r and both molecules have their velocity components recalculated according to the conservation of energy and momentum.

Since its inception there has been some concern that the direct simulation Monte Carlo method does not provide a solution to the Boltzmann equation. The method has been shown to produce results consistent with the Boltzmann equation, but equivalence has not been proved. The technique was developed from the point of view of simulating *real* gas flows rather than for the explicit purpose of solving the Boltzmann equation. The method is simple to apply to a particular problem and conceptually straightforward. It is computationally more efficient than other similar simulation schemes [Nanbu, 1980; Nanbu, 1983] and has been demonstrated by Bird [Bird, 1963; Bird, 1970a] and others [Boyd and Stark, 1987] to give excellent results when applied to a wide range of complex gas flow problems.

The devised simulation method is based on the *energy sink* model proposed by Bird [Bird, 1970b; Bird, 1976a], and associates a single variable representing the total rotational energy summed over all rotational degrees of freedom with each simulated molecule. In a collision, the value of this variable is compared for each collision partner with the relative translational energy of the collision. If the rotational energy is not equal to the relative translational energy, a fraction of the energy difference is transferred between the rotational and translational modes in the direction which more nearly satisfies equilibrium according to the equation [Klots, 1980]

$$E_{t,f} = E_{t,i} + \xi \left(\frac{\mathcal{R}}{\mathcal{R}+1} \right) \left(k_b T_r - \frac{3}{5} E_{t,i} \right), \tag{4.22}$$

where $E_{t,i}$ and $E_{t,f}$ are the initial and final values of the relative translational energy, respectively, $\mathcal{R}$ is the number of rotational degrees of freedom, T_r is the effective rotational temperature, and ξ is the rotational–translational coupling parameter. The rotational–translational coupling parameter was introduced by Klots [Klots, 1980] as a means of incorporating rotational degrees of freedom into the thermal conduction model used for investigating the breakdown of equilibrium in supersonic expansions [Beijerinck and Verster, 1981; Cameron and Harland, 1991], and represents the fraction of collisions in which energy is transferred between the rotational and translational degrees of freedom of the colliding molecules.

As stated by Klots [Klots, 1980], the assumption that the rotational relaxation process can be properly described by a single value of the coupling parameter, independent of all other collision parameters, is somewhat naive and open to improvement. As ξ represents the fraction of inelastic collisions experienced by a molecule, it seems reasonable to assume that it will be proportional to the mean collision cross section, and it is therefore suggested that ξ may be suitably approximated by an expression of the form

$$\xi = \begin{cases} a\overline{\sigma} & \overline{\sigma} \leq a^{-1} \\ 1 & \text{otherwise} \end{cases} \tag{4.23}$$

where $\overline{\sigma}$ is the mean collision cross section and a is a constant scaling parameter for a particular collision system. According to the definition that ξ represents the fraction of inelastic collisions experienced by a molecule, it is required that $0 \leq \xi \leq 1$, and it is assumed that for energies below which $\overline{\sigma} > a^{-1}$, the coupling parameter is exactly equal to unity. In order to easily incorporate the functionality of ξ suggested by equation (4.23) into the thermal conduction model, calculated values of ξ are fitted to an expression of

the form

$$\xi = \begin{cases} (\beta T_m)^\alpha & T_m \geq \beta^{-1} \\ 1 & \text{otherwise} \end{cases} \tag{4.24}$$

where α and β are fitting parameters and T_m is the mean kinetic temperature. Collision cross sections are often approximated by functions of the form T_m^α and, in fact, the thermal conduction model using an attractive C_6 interaction potential, inherently uses collision cross sections proportional to $T_m^{-1/3}$.

4.4.3 Computational procedure

The Monte Carlo procedure for the calculation of rotational relaxation times is primed with the initial temperatures of the rotational and translational reservoirs, the initial pressure of the system, a tabulated interaction potential, the molecular mass of the gas, the cross section scaling parameter a, the number of rotational degrees of freedom, and a value specifying the time interval Δt_m at which the rotational and translational temperatures are to be sampled. The total number of sampling intervals is fixed at a value of 100.

The tabulated interaction potential consisted of up to 100 points, generally taken at regular intervals along the potential curve, and over a suitably wide range to ensure that little or no extrapolation of the supplied data was required. Cubic spline interpolation [Conte and de Boor, 1980] was then used to evaluate the interaction potential at any intermolecular separation from the supplied list of points. Extrapolation of the supplied potential data with the correct behaviour at large and small intermolecular separations was performed when necessary by fitting inverse power functions to each end of the interpolating function such that

$$V(r) = \begin{cases} \dfrac{c_1}{r^p} + c_2 & 0 < r \leq r_1 \\ \dfrac{c_3}{(r - c_4)^q} & r_n \leq r < \infty \end{cases} \tag{4.25}$$

where c_1, c_2, c_3 and c_4 are fitting parameters, and r_1 is the smallest and r_n the largest tabulated intermolecular separation. Values of the exponents p and q were generally chosen to be 12 and 6, respectively. Using a tabulated interaction potential in this way places no functional restrictions on the form of the potential and allows listed data to be taken directly from the literature if required. This method was used with considerable success by Simpson *et al* to accurately model ion mobilities in helium using interaction potentials calculated at as few as 12 intermolecular separations [Simpson *et al*, 1987; Simpson, 1988; Simpson *et al*, 1988]. A similar approach has been adopted by Viehland [Viehland and Mason, 1984] who used the somewhat more sophisticated method of Lagrange interpolation to calculate $V(r)$, although there appears to be little difference in terms of the results obtained using either interpolation scheme. The various advantages and disadvantages of these and other methods of interpolation are discussed in detail by Press *et al* [Press *et al*, 1986].

The number N_m of simulated molecules was set at 4096 for all of the calculations presented in this section. In general, there is a square law relationship between the error associated with an answer and the number of observations used in the determination of the answer in a Monte Carlo calculation. To reduce the error by a factor of k, it is therefore necessary to increase the number of observations by k^2. It was considered that 4096 simulated molecules was a sufficiently large number to produce answers with an

acceptably small standard error but not so large as to incur a significant overhead in the overall computation time.

The initial velocity components for each simulated molecule were randomly selected from a Maxwellian velocity distribution function of the form

$$f(v_x, v_y, v_z)\mathrm{d}v_x\mathrm{d}v_y\mathrm{d}v_z = \left(\frac{m}{2\pi k_b T_m}\right)^{\frac{3}{2}} \mathrm{e}^{-m(v_x+v_y+v_z)^2/2k_bT_m}\mathrm{d}v_x\mathrm{d}v_y\mathrm{d}v_z, \tag{4.26}$$

where m is the molecular mass and T_m is the translational temperature. The random selection of velocities from this distribution was performed using the method of Box and Muller [Press *et al*, 1986], which is generally considered to be the most efficient means of sampling from Gaussian distributions such as (4.26).

The distribution of rotational energies was approximated by a continuous probability distribution function of the form [Borgnakke and Larsen, 1975]

$$p(E_r)\mathrm{d}E_r \propto E_r^{(\mathcal{R}/2-1)}\mathrm{e}^{-E_r/k_bT_r}\mathrm{d}E_r, \tag{4.27}$$

where $\mathcal{R}$ is the number of rotational degrees of freedom and T_r is the effective rotational temperature. Values for the initial rotational energy of each simulated molecule were randomly selected from this distribution using a variation on the algorithm described by Press *et al* [Press *et al*, 1986] for the selection of random deviates from the Gamma distribution. While it may be somewhat unrealistic to describe the distribution of rotational energies in terms of a continuous function such as equation (4.27), it is computationally difficult and time consuming to sample from discrete distributions. Results obtained using equation (4.27) will be quite satisfactory in most circumstances.

The collision algorithm commences with the random selection of a pair of molecules with appropriate probability. For pairs which are accepted for a collision, the collision counter is advanced by unity, the time counter is advanced according to equation (4.21), and energy is transferred between the rotational and translational modes of the colliding molecules in accordance with equation (4.22).

Following the exchange of energy between the rotational and translational degrees of freedom, the post collision components (u_r^*, v_r^*, w_r^*) of the relative velocity vector $\mathbf{c}_r^*$ are calculated according to the following set of equations [Hirschfelder *et al*, 1954]

$$u_r^* = u_r\cos\chi + (v_r^2 + w_r^2)^{\frac{1}{2}}\sin\chi\sin\varepsilon \tag{4.28}$$

$$v_r^* = v_r\cos\chi + (c_r w_r\cos\varepsilon - u_r v_r\sin\varepsilon)(v_r^2 + w_r^2)^{-1/2}\sin\chi \tag{4.29}$$

$$w_r^* = w_r\cos\chi - (c_r v_r\cos\varepsilon + u_r w_r\sin\varepsilon)(v_r^2 + w_r^2)^{-1/2}\sin\chi \tag{4.30}$$

and scaled to account for the exchange of energy. The solution of these equations requires the evaluation of the classical deflection angle, χ, at the initial relative translational energy and the azimuth angle ε. The azimuth angle is uniformly distributed on the interval $\{0,2\pi\}$ and may be randomly selected according to the expression

$$\varepsilon = 2\pi R_f, \tag{4.31}$$

where R_f is a uniform random deviate on the interval $\{0,1\}$. The classical deflection angle is given by the integral

$$\chi = \pi - 2b\int_{r_m}^{\infty}\frac{1}{r^2}\left[1 - \frac{V(r)}{E} - \frac{b^2}{r^2}\right]^{-1/2}\mathrm{d}r, \tag{4.32}$$

where b is the impact parameter and r_m is the outermost solution of the equation

$$\left[1 - \frac{V(r)}{E} - \frac{b^2}{r^2}\right]^{1/2} = 0, \tag{4.33}$$

for an interaction potential $V(r)$. The impact parameter for the collision was chosen at random from the probability distribution

$$p(b)\mathrm{d}b = \frac{1}{\pi b_{max}^2} 2\pi b \mathrm{d}b, \tag{4.34}$$

with crude Monte Carlo selection [Hammersley and Handscomb, 1964]. Noting that the probability of obtaining a particular impact parameter is directly proportional to b, it is a straightforward matter to apply the transformation method [Hammersley and Handscomb, 1964] to equation (4.34) and show that

$$b = R_f^{1/2} b_{max}, \tag{4.35}$$

where R_f is a uniform random deviate on the interval $\{0,1\}$ and b_{max} is a cut-off impact parameter chosen such that it is large enough to include all significant events, but not so large as to produce too many uninteresting collisions. It is important to note that calculated rotational relaxation times will depend to some extent upon the choice of b_{max}, and its value must therefore be chosen with some care. In previous simulations of this type, the value of b_{max} was generally chosen in a somewhat arbitrary manner and held constant for all collisions [Hippler *et al*, 1986]. In this investigation, a separate and more suitable b_{max} was calculated for each collision on the basis of the collision cross section σ according to the expression

$$b_{max} = \frac{1}{\sqrt{\pi}} \sigma(c_r)^{1/2}, \tag{4.36}$$

where c_r is the relative speed of the collision pair. Collision cross sections were calculated according to the integral

$$\sigma^{(l)}(E) = 2\pi \int_0^\infty b(1 - \cos^l \chi)\mathrm{d}b, \tag{4.37}$$

for $l = 2$. Evaluation of (4.32) and (4.37) was performed using an extensively modified version of the program employed by O'Hara and Smith for the calculation of collision integrals [O'Hara and Smith, 1970; O'Hara and Smith, 1971].

It is important to emphasize that the deflection function described by equation (4.32) refers to elastic scattering while equations (4.28) to (4.30) are applicable to both elastic and inelastic collisions. The aim of the present model is to provide a reliable method for estimating rotational relaxation data without having to perform lengthy three dimensional trajectory calculations requiring detailed information about the entire potential surface for a particular collision system and the solution of a large set of coupled differential equations. Instead of calculating complete trajectories, the exchange of energy between the rotational and translational modes of the collision pair is assumed to be separable from the determination of the post collision velocity components. Energy is transferred between the rotational and translational modes according to equation (4.22) prior to the determination of the post collision velocity components, which are then scaled to ensure conservation of energy.

Due to the large number of collisions which must be examined, the evaluation of the double integral describing the collision cross sections clearly represents one of the more

time consuming aspects of the computational procedure. In order to reduce this computational overhead, collision cross sections were calculated at 256 intervals over a suitably wide energy range and fitted to Chebyshev polynomials [Abramowitz and Stegun, 1964; Press *et al*, 1986] prior to initiation of the Monte Carlo simulation. In this way, the solution of (4.37) was reduced to the evaluation of a simple polynomial expression, with a considerable saving in computation time. The energy range over which cross sections were fitted was taken as three standard deviations either side of the mean of the relative velocity distribution at the initial translational temperature. The probability of a velocity lying outside this range is less than 2.2×10^{-5} [Blank, 1982].

The rotational and translational temperatures were sampled at the specified interval Δt_m and stored until the end of the run, whereupon they were fitted to the first order relaxation equation

$$\frac{\mathrm{d}T_r}{\mathrm{d}t} = \frac{1}{\tau_r}(T_e - T_r) \tag{4.38}$$

or

$$T_r = T_e - (T_e - T_{r,0})\mathrm{e}^{-t/\tau_r}, \tag{4.39}$$

in which τ_r is the mean rotational relaxation time, T_e is the equilibrium temperature, T_r is the rotational temperature at time t and $T_{r,0}$ is the initial rotational temperature at time $t = 0$. The equilibrium temperature is defined for a non–equilibrium gas as the weighted average of the translational and rotational temperatures according to the expression

$$T_e = \frac{1}{\mathcal{R}+3}\left(3T_m + \mathcal{R}T_r\right), \tag{4.40}$$

assuming $\frac{1}{2}k_bT$ of energy per rotational degree of freedom.

To estimate collision cross section scaling parameters, the computational procedure was modified to solve the equation

$$\tau_r(a) = \tau_{r,expt}, \tag{4.41}$$

given an experimentally measured rotational relaxation time, $\tau_{r,expt}$, and two values of the scaling parameter, a, bridging the root. The value of the scaling parameter was then varied in an iterative manner using the algorithm of Dekker and Brent [Press *et al*, 1986] within the specified range until the calculated relaxation time converged to within $\pm 1\%$ of the experimental figure. Having determined the collision cross section scaling parameter, it is possible to calculate relaxation times under any set of conditions.

4.4.4 Results and discussion

Collision cross section scaling parameters and rotational relaxation times were calculated for the ten species given in Table 4.6. Relaxation times were determined by fitting the sampled rotational temperatures to equation (4.39) using a simple linear least squares algorithm. The quality of the obtained fits was generally found to be very good, resulting in linear least squares correlation coefficients of better than 0.95 in almost all cases. Poor correlation coefficients were invariably due to a bad choice of sampling interval, resulting in the rotational and translational degrees of freedom actually reaching equilibrium well before the end of the simulation. A sampling interval of approximately 0.1 mean collision times was found to be suitable for most calculations. Tabulated interaction potentials used in all of the calculations discussed below were constructed from the Lennard–Jones (12,6) parameters given by Hirschfelder *et al* [Hirschfelder *et al*, 1954].

Gas	a (m^{-2})	α	β (K^{-1})	Gas	a (m^{-2})	α	β (K^{-1})
H_2	3.40×10^{16}	-0.3348	2.924×10^{3}	O_2	6.81×10^{17}	-0.3827	3.499×10^{-2}
CH_4	1.05×10^{17}	-0.3842	2.372×10^{0}	CO_2	8.41×10^{17}	-0.3833	6.056×10^{-3}
NH_3	5.82×10^{17}	-0.3749	1.772×10^{-1}	CH_3Cl	6.50×10^{17}	-0.3315	6.981×10^{-3}
N_2	7.41×10^{17}	-0.3484	4.245×10^{-2}	OCS	6.06×10^{17}	-0.3698	7.036×10^{-3}
C_2H_4	1.15×10^{17}	-0.3831	7.563×10^{-1}	Cl_2	3.16×10^{17}	-0.3676	3.928×10^{-2}

Table 4.6: Calculated scaling and fitting parameters.

Values of the collision cross section scaling parameter for the species listed in Table 4.6 were determined from experimental and theoretical relaxation data found in the literature. Unfortunately it was often difficult to directly use the data given by some authors without making assumptions regarding the initial rotational temperature or degree of non–equilibrium between the rotational and translational degrees of freedom, as such information was not always clearly stated, the assumption presumably being that the relaxation time is independent of the initial degree of non–equilibrium.[3] In such situations it was necessary to choose a suitable initial rotational temperature on the basis of how the system was displaced from equilibrium. Rotational relaxation times have been most commonly measured by supersonic expansion, sound absorption, and shock tube techniques. As stated by Rabitz [Rabitz and Lam, 1975], the temperature departures associated with these three techniques are $T_r > T_m$, $T_r \sim T_m$, and $T_r < T_m$, respectively. It was found that the relaxation model is not well behaved when $T_r \sim T_m$, making it difficult to reliably use relaxation data obtained from sound absorption experiments for the estimation of scaling parameters.

The scaling parameter of 7.41×10^{17} m^{-2} calculated for N_2 was derived from the theoretical results of Mason and Monchick [Mason and Monchick, 1962] and represents an average of values determined at seven relaxation times over a translational temperature range from 100 K to 1000 K. The resulting values of the rotational–translational coupling parameter and the mean collision cross section $\overline{\sigma}$ at each of the seven temperatures are plotted in Figure 4.12. The plotted values of $\overline{\sigma}$ represent the average of some 10^4 cross sections calculated at energies sampled from the relative speed distribution at each temperature. The calculated variation of the coupling parameter is remarkably similar to the variation of the mean collision cross section with temperature over the range considered, providing some confidence in the validity of equation (4.23). Also plotted in Figure 4.12 is the curve fitted to the calculated values of ξ using equation (4.24).

Similarly, good agreement between the calculated variation of ξ and $\overline{\sigma}$ was found for CH_4 and C_2H_4 using the experimental data of Kelly and Hill [Kelly, 1957; Hill and Winter, 1968] and for O_2 based on the sound absorption measurements of Sessler and Greenspan [Sessler, 1958; Greenspan, 1959]. The value of the scaling parameter given for H_2 was estimated from the results of Gallagher and Fenn [Gallagher and Fenn, 1974] who determined relaxation times at several temperatures between 300 K and 1900 K from time of flight analysis of supersonic free jets and the ultrasonic measurements of Winter and Hill [Winter and Hill, 1967]. The scaling parameter for OCS was determined from the results of Unland and Flygare [Unland and Flygare, 1966], who determined rotational relaxation times for OCS from microwave double–resonance experiments over a wide range

[3] As will be discussed later, such an assumption is quite reasonable for most non–polar diatomic molecules, with the rotational relaxation time being only a weak function of the rotational temperature.

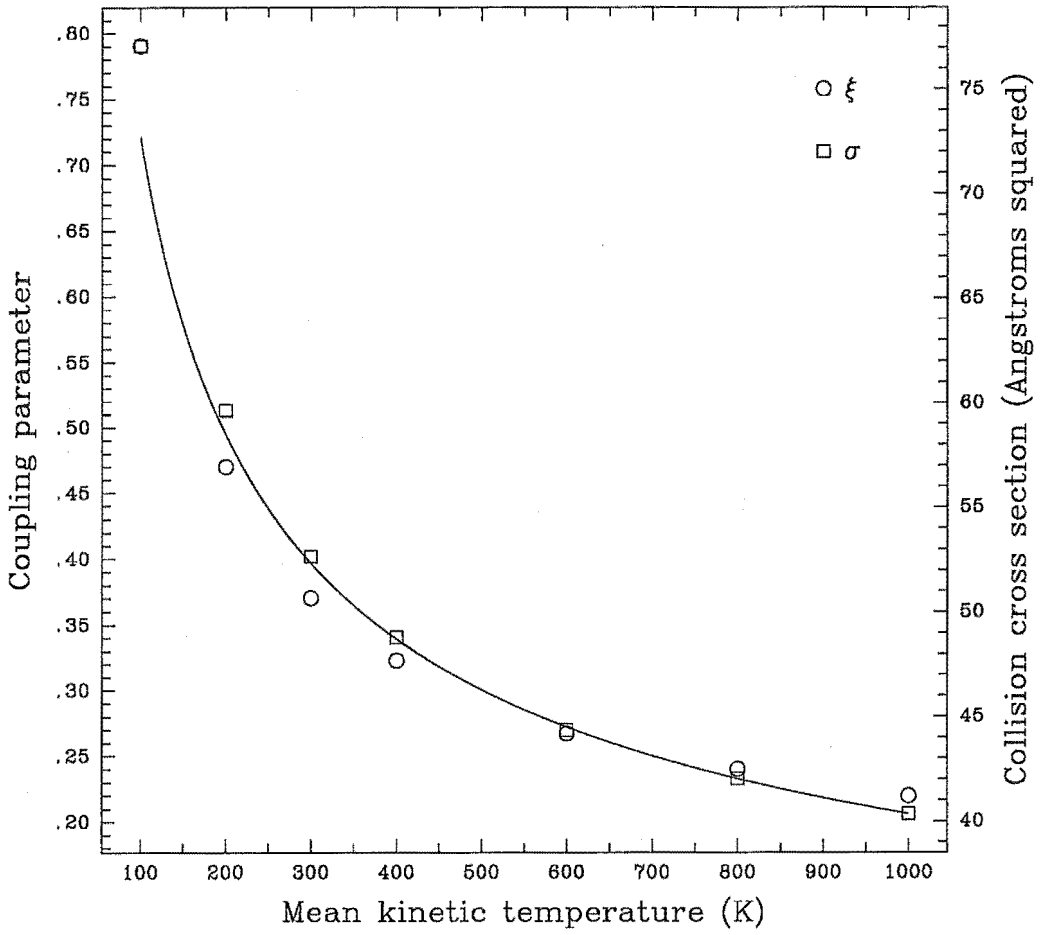

Figure 4.12: Collision cross sections and calculated values of ξ for N_2 from 100 K to 1000 K.

of pressures.

Calculations of the scaling parameter for the remaining species listed in Table 4.6 were made somewhat difficult due either to the lack of sufficiently accurate experimental data or considerable discrepancies between values of relaxation times stated by different authors. The value of 3.16×10^{17} m^{-2} for Cl_2 was determined from the experimental results of Sittig [Sittig, 1960], resulting in a calculated collision number of approximately 3.3 at 300 K. This figure is significantly less than that of 4.9 calculated by Parker [Parker, 1959] and the upper limit of 5.5 suggested by Anderson [Anderson and Hornig, 1958] from observations of shock front thickness. As stated by Miller [Miller and Andres, 1967], rotational collision numbers obtained from shock tube experiments are often observed to be slightly higher than may be expected. Due to the close coupling of the rotational and translational modes of most molecules, it is frequently difficult to separate the contributions of rotational relaxation from those of translational relaxation in such experiments, meaning that the information obtained, while generally precise, is not totally unambiguous. The rotational

energy levels of Cl_2 are considerably more closely spaced than those of N_2 or O_2 and since rotational–translational energy transfer is more efficient when the rotational levels of the species involved are closer, it seems reasonable to assume that rotational relaxation in Cl_2 should be somewhat more efficient than that of N_2 or O_2. It is therefore considered that the scaling parameter calculated for Cl_2 from the experimental results of Sittig is likely to be quite reasonable.

The scaling parameter of 5.82×10^{17} m^{-2} for NH_3 was estimated from the results of Jones *et al* [Jones *et al*, 1969]. Little work has been done on the rotational relaxation of NH_3, making it somewhat difficult to assess the reliability of the calculated parameter, although the resulting values of ξ seem quite reasonable ($\xi \approx 0.23$ at 300 K) considering the fact that the rotational energy levels in NH_3 are some 3 to 4 times less closely spaced than those of N_2. One point to note, however, is that vibrational–rotational energy transfer in NH_3 is a highly efficient process due to the low frequency *umbrella* motion peculiar to the NH_3 molecule, with $\mathcal{Z}_v \approx \mathcal{Z}_r$ at room temperature [Jones *et al*, 1969], where $\mathcal{Z}_v$ is the vibrational collision number. Consequently, it may not be possible to ignore vibrational motion in the calculation of rotational relaxation times for NH_3. Detailed information is available on the vibrational transition probabilities of many species, and the possibility of extending the model described here to include vibrational degrees of freedom is currently being investigated.

The value of 8.41×10^{17} m^{-2} determined for CO_2 was based on the thermal transpiration measurements of Malinauskas [Malinauskas *et al*, 1970] and results in coupling parameter values similar to those of OCS.

The scaling parameter of 6.50×10^{17} m^{-2} for CH_3Cl was calculated from the theoretical results of Mason and Monchick [Mason and Monchick, 1962] and should not be considered reliable. Mason and Monchick developed a simple expression relating the thermal conductivity of a polyatomic gas to its rotational relaxation time. Comparisons made with experimental data indicate that the expression produces good results for simple molecules such as homonuclear diatomics, but fails to provide an accurate description of the relaxation process for highly polar species. CH_3Cl is a highly polar molecule, having a dipole moment of 1.87 D, close to the value for H_2O (1.85 D) and significantly greater than that of HCl (1.08 D). The relaxation model described here, with its incorporation of a spherical potential, may not be applicable also.

Values of the fitting parameters α and β for equation (4.24) given in Table 4.6 were determined from a linear least squares fit of $\ln|\xi|$ versus $\ln|T_m|$. The calculated values of α are approximately the same for all of the species considered and are reasonably close to 1/3, reflecting the attractive C_6 component of the Lennard–Jones potentials used in all of the calculations. The value of β is observed to vary by several orders of magnitude from 10^{-3} for CO_2, OCS and CH_3Cl through to 10^3 for H_2. The reciprocal of β determines the temperature at which ξ for the molecule in question attains its maximum value of unity. For species such as CO_2 and OCS this temperature is about 150 K, while for H_2 it is approximately 3×10^{-4} K, emphasizing the extremely poor coupling between the rotational and translational modes in the H_2 molecule.

With the possible exception of CH_3Cl, the simulation procedure was found to reliably reproduce the majority of experimental and theoretical results used in the determination of the cross section scaling parameters, providing considerable confidence in the use of the model to predict rotational relaxation times at any set of initial conditions. Rotational collision numbers calculated using the direct simulation Monte Carlo procedure are presented in Figures 4.13 and 4.14 as a function of translational temperature from 50 K to 300 K for the species listed in Table 4.6. The rotational collision number is a useful and

frequently stated quantity in the discussion of rotational relaxation phenomena. It is a dimensionless quantity, defined simply as the product of the rotational relaxation time and the mean collision frequency:

$$\mathcal{Z}_r = \tau_r \nu, \tag{4.42}$$

and represents the average number of collisions required for a molecule initially perturbed from equilibrium to re-establish equilibrium between its rotational and translational degrees of freedom. The collision number is independent of density and thus provides a convenient means of comparing relaxation data measured under different conditions. With the exception of H_2 and some hydrides, the rotational energy level spacings of most molecules are quite small. Consequently, rotational–translational energy transfer is generally observed to be a relatively efficient process, with rotational collision numbers being in the range of 1 to 10 for most molecules at room temperature.

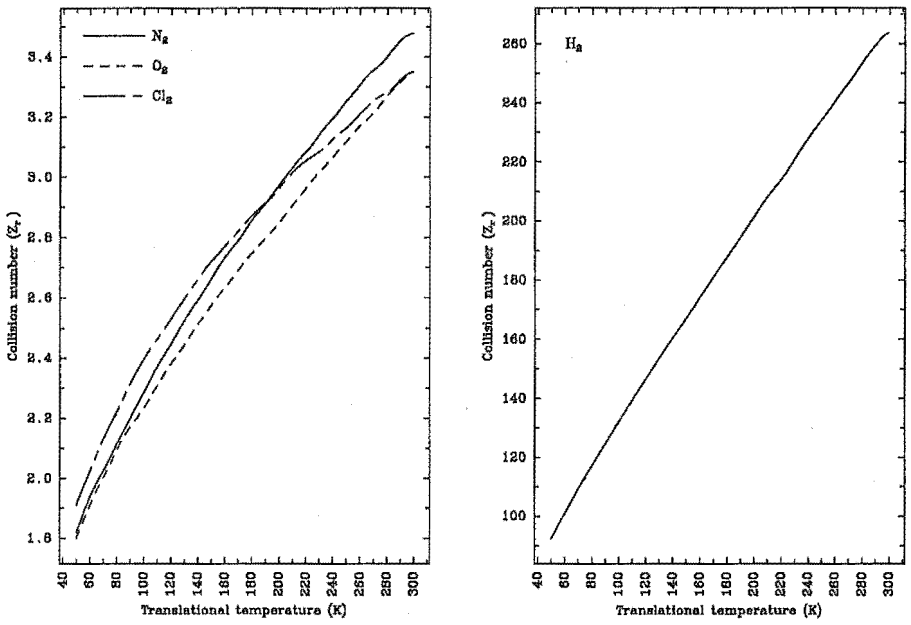

Figure 4.13: Variation of rotational collision number with translational temperature for N_2, O_2, Cl_2, and H_2.

The relaxation times used to determine the collision numbers illustrated in Figures 4.13 and 4.14 were calculated at a pressure of 1 atm with all of the energy associated with each simulated molecule initially contained in the translational modes so that the results could be directly compared with the theoretical predictions of Parker [Parker, 1959] and Zeleznik [Zeleznik, 1967]. The values of the collision cross section scaling parameter used for these calculations are given in Table 4.6 along with calculated values of the fitting parameters α and β used in equation (4.24). The data presented in Figures 4.13 and 4.14 were smoothed to remove from the calculated curves much of the noise incurred through the use of Monte

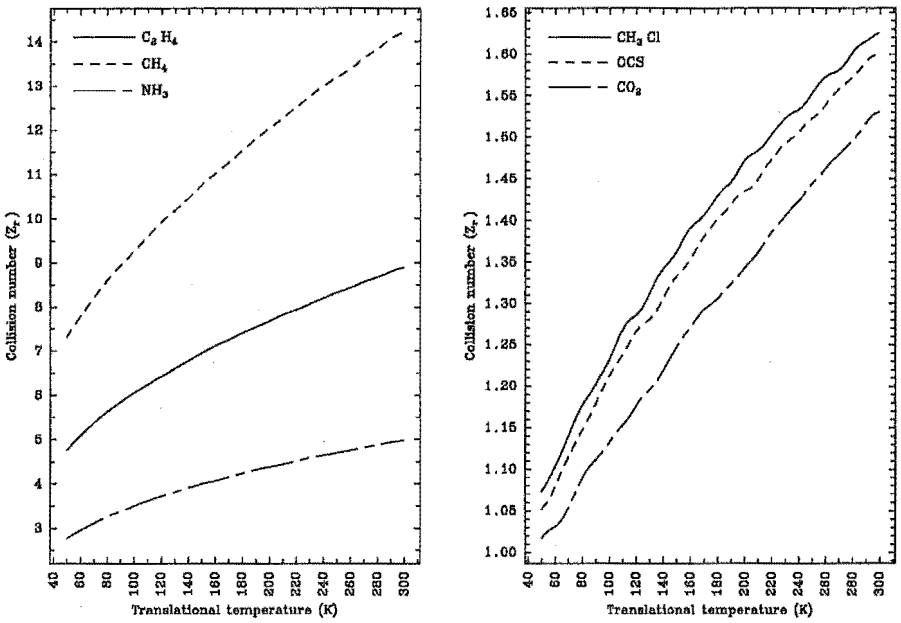

Figure 4.14: Variation of rotational collision number with translational temperature for C_2H_4, CH_4, NH_3, CH_3Cl, OCS, and CO_2.

Carlo methods. As can be seen, the calculated collision numbers increase with increasing translational temperature for all of the species considered. The results are all in qualitative agreement with the predictions of Parker, although, as discussed by Carnevale [Carnevale *et al*, 1967], the expression derived by Parker generally underestimates the dependence of the collision number on the translational temperature. The calculated variation of collision number with translational temperature for CH_3Cl is in reasonable agreement with results obtained using the expression derived by Zeleznik for pure polar gases. This result for CH_3Cl should be treated with some degree of caution. While the expression given by Zeleznik and the relaxation model employed here both predict that the rotational collision number of CH_3Cl monotonically increases with translational temperature, experimental measurements of rotational relaxation in other highly polar species such as HCl indicate that this may not be the case, with the rotational collision number being observed to pass through a local minimum [Baker and Brokaw, 1964; Baker and Brokaw, 1965].

The effect of rotational temperature on the relaxation time is illustrated in Figure 4.15 for CH_4 at a translational temperature of 300 K. In this case, the effect is very small, with the collision number decreasing by approximately 0.8 over the 1000 K rotational temperature range considered. Analogous calculations were performed for the other species listed in Table 4.6 and similar trends were observed in all cases, with the collision number decreasing slightly with increasing rotational energy. It was found that the rotational energy dependence was more significant for species such as CO_2 and OCS for which rotational relaxation is a highly efficient process, while for H_2 the effect was negligible. It should be

noted that relaxation times were not calculated between 250 K and 300 K due to the poor behaviour of the computational procedure when the initial departure from equilibrium is small. This effect can be seen in Figure 4.15, with the statistical noise increasing as the singularity at 300 K is approached. The data presented in Figure 4.15 has not been smoothed, unlike that in Figures 4.13 and 4.14.

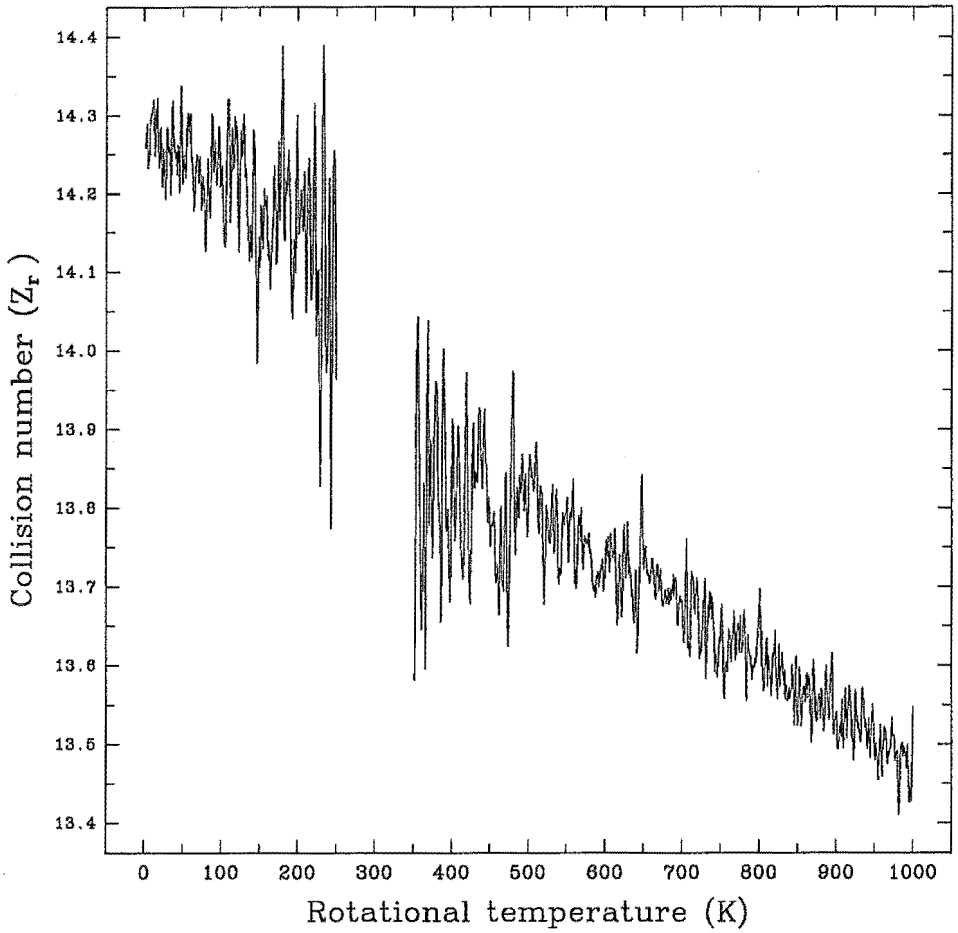

Figure 4.15: Variation of rotational collision number with rotational temperature for CH_4.

It would appear that the dependence of the rotational relaxation time on the rotational temperature becomes negligible for most systems when the fraction of elastic collisions falls below about 2%. The assumption that ξ is independent of the rotational energy is quite reasonable for non–polar or slightly polar molecules. The rotational relaxation time is largely determined by the total collision cross section, which is not significantly influenced by the rotational motion of such species. For highly polar molecules such as CH_3Cl, in which the total collision cross section can be significantly affected by the rotational motion of the molecule, the applicability of the model described here is questionable. Extremely large cross sections are observed for rotational–translational energy transfer

between strongly polar molecules due to the long range dipole–dipole interaction which dominates the scattering behaviour of such species and results in very large total collision cross sections and unusually large rotational inelastic cross sections.

Running on a MicroVAX 3100–30, the calculation of a single rotational relaxation time takes between 15 s and 60 s, depending upon the number of collisions examined. Figure 4.16 shows the number of collisions examined as a function of translational temperature from 1 K to 300 K for H_2 and N_2 with no initial rotational energy. The number of collisions examined is, in both cases, observed to gradually increase with temperature and then level out. Due to the inefficient and slow nature of rotational relaxation in H_2, the number of collisions examined at a given temperature is significantly greater for this species than for N_2.

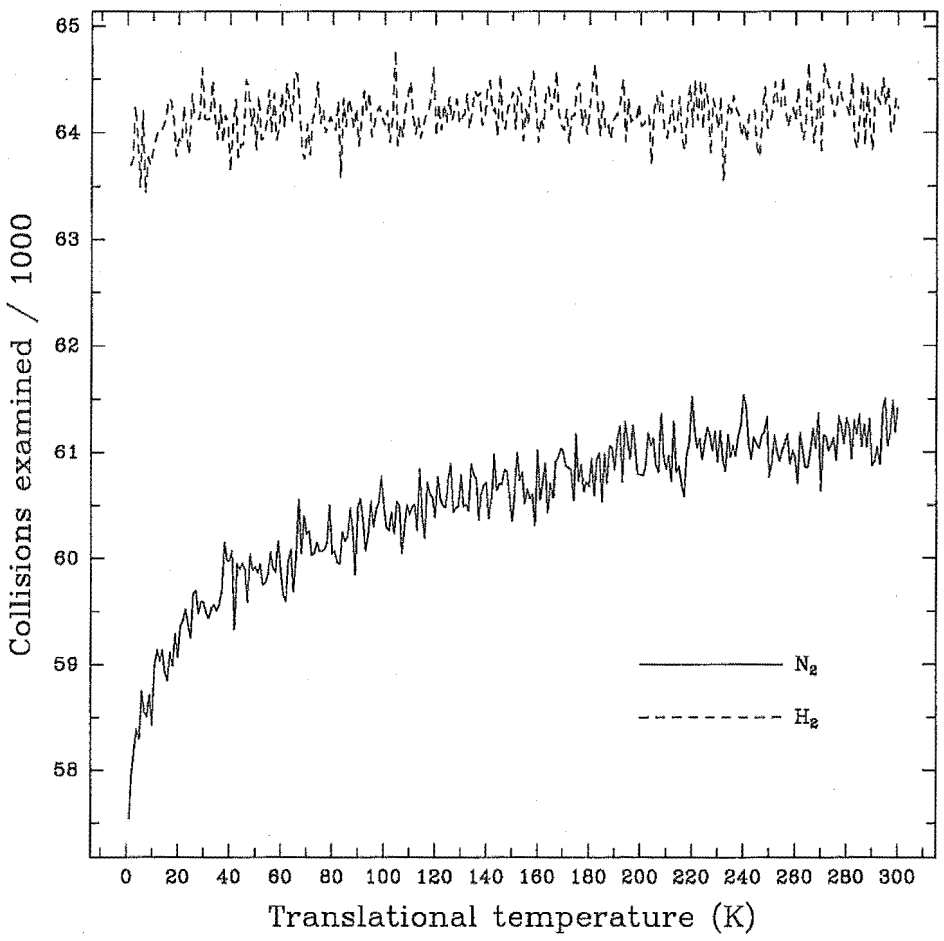

Figure 4.16: Number of collisions examined as a function of translational temperature for H_2 and N_2.

Until now, the rotational–translational coupling parameter ξ was assumed to be a constant, independent of all other collision parameters, and was generally estimated from a

System	P_0 (atm)	T_0 (K)	u_{calc} (m/s)	$T_{\parallel,calc}$ (K)	$T_{r,calc}$ (K)	ξ_{max}
CO_2	1	300	643	35.2	35.2	1.0
CH_3Cl	1	300	603	31.5	31.5	1.0
OCS	1	300	554	30.0	30.0	1.0

Table 4.7: Temperatures and flow velocities calculated using the thermal conduction model with the variation of ξ described by equation (4.24).

comparison of terminal translational and rotational temperatures measured in supersonic expansions with temperatures calculated using the thermal conduction model or the theory developed by Randeniya and Smith [Klots, 1980; Cameron and Harland, 1991; Randeniya and Smith, 1990]. In the model described here, ξ is assumed to be proportional to the mean collision cross section, according to equation (4.23). It is further suggested that the previously determined constant values of ξ, based on terminal temperatures measured in a supersonic expansion, represent the maximum attainable value of the coupling parameter, ξ_{max}, under such conditions. In order to make use of the results presented in this section for the prediction of expansion properties, it is therefore necessary to know or be able to estimate ξ_{max} for the species of interest. Reliable values of ξ_{max} have been determined for H_2, N_2, O_2, and CH_4 [Cameron and Harland, 1991; Randeniya and Smith, 1990][4], but for the remainder of the species listed in Table 4.6, there is little or no known experimental data on which to accurately estimate ξ_{max}. Huber-Wälchi *et al* [Huber-Wälchi and Nibler, 1982] observed a terminal rotational temperature of 40 K for C_2H_4 expanded through a 60 μm nozzle at 300 K with a source pressure of 0.6 atm. From this result ξ_{max} for C_2H_4 was estimated to be 0.18 $\pm$ 10%. The high efficiency of rotational relaxation observed for CO_2, CH_3Cl, and OCS suggests that ξ_{max} for these species may be close to unity, while values of 0.2 to 0.25 and 0.55 to 0.6 for NH_3 and Cl_2, respectively, are probably reasonable.

The results of thermal conduction model calculations performed for OCS, CO_2 and CH_3Cl using the values of α and β given in Table 4.6 to describe the temperature dependence of the coupling parameter according to equation (4.24) are presented in Table 4.7. The variation of rotational temperature with axial distance, expressed in terms of nozzle diameters, is shown in Figure 4.17 for CO_2 and OCS. All data were calculated for a source pressure of 1 atm at a temperature of 300 K with a nozzle diameter of 7×10^{-5} m. The rotational–translational coupling parameter was assumed to attain its maximum allowable value of unity in each case. The calculated variation of rotational temperature with axial distance for CH_3Cl was almost indistinguishable from that of OCS and is therefore not shown in Figure 4.17 for reasons of clarity. Similarly, the parallel component of the translational temperature was virtually identical to the rotational temperature in all cases, illustrating the close coupling of the translational and rotational degrees of freedom in these molecules.

The calculated final translational temperature of CH_3Cl is in excellent agreement with the value of 29 K measured by Aitken [Aitken *et al*, 1993] using the time–of–flight and deconvolution techniques described in §3.4. The calculated value of the flow velocity, however, was found to be some 10% greater than the measured value, indicating that the actual rotational temperature was approximately 170 K. It must therefore be con-

[4]It should be noted that the coupling parameter values given by Randeniya and Smith [Randeniya and Smith, 1990] implicitly include the number of rotational degrees of freedom and must therefore be scaled accordingly to obtain values comparable with those presented here.

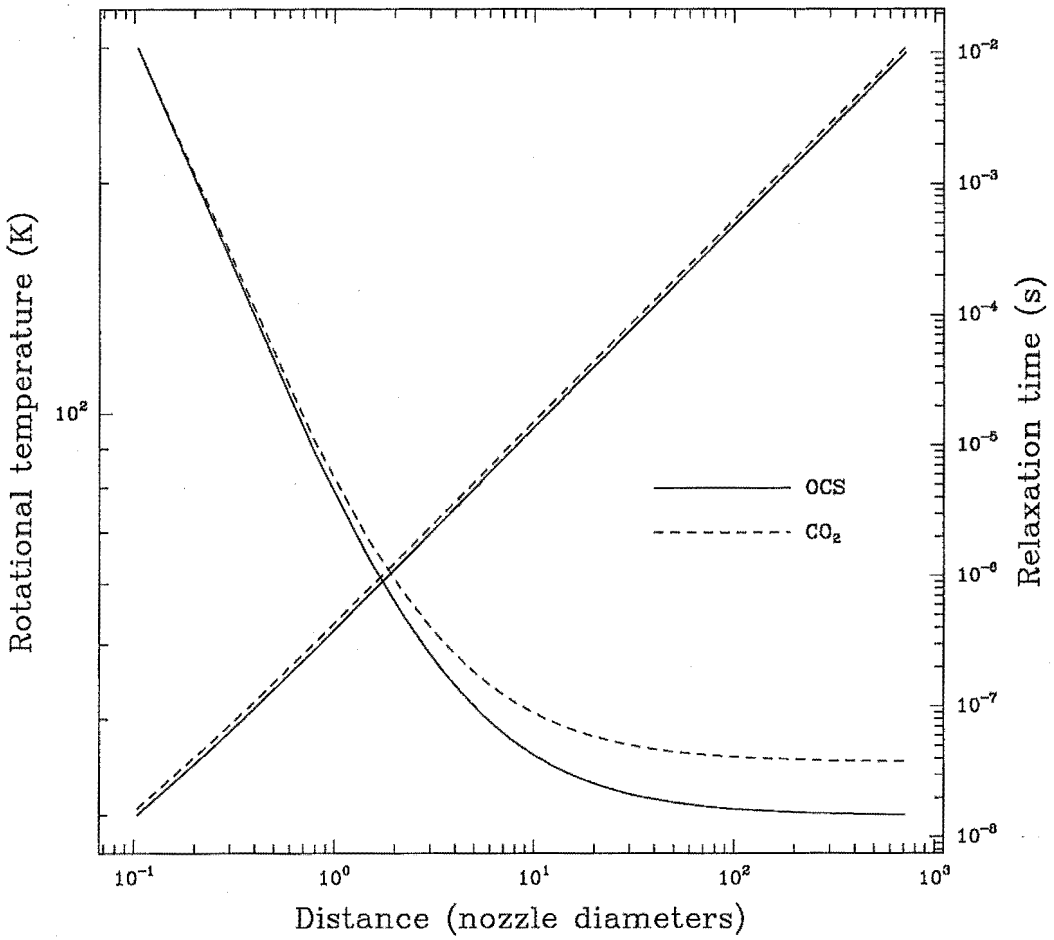

Figure 4.17: Rotational temperatures and relaxation times as a function of distance from the nozzle exit for OCS and CO_2.

cluded that the observed agreement between the calculated and measured temperatures was purely coincidental and that the supersonic expansion of such highly polar species cannot be accurately described by the thermal conduction model in its present form. In particular, it may be completely unrealistic to describe the distribution of rotational energies in terms of a single temperature. As was noted by Carman [Carman Jr., 1986], the rotational energy levels of CH_3Cl are widely spaced ($\mathcal{A}$ = 150000 MHz, $\mathcal{B}$ = 13293 MHz) and therefore non–equilibrium rotational distributions may be considerably more likely. Such deviations from Boltzmann distributions have been observed for rotational populations of a number of molecules in supersonic expansions [Kukolich *et al*, 1974; Maier *et al*, 1984]. In the thermal conduction model the rate of rotational–translational energy transfer is assumed to be proportional to the difference in temperature between the translational and rotational reservoirs. For highly polar symmetric top molecules, such as CH_3Cl with two very different rotational constants, it may be necessary to associate a

System	CO_2	CH_3Cl	OCS
A (kg $m^{-1}s^{-1}K^{-1}$)	7.078×10^{-6}	6.306×10^{-6}	6.314×10^{-6}

Table 4.8: Values of the parameter A in equation (4.43) calculated for $P_0 = 1$ atm and $T_0 = 300$ K.

separate rotational temperature with each unique rotational degree of freedom.

The calculated terminal parallel translational and rotational temperatures given in Table 4.7 for CO_2 and OCS seem reasonable. Previously reported thermal conduction model calculations for H_2, N_2 and O_2 were all found to be in good agreement with experimental measurements [Cameron and Harland, 1991; Huber-Wälchi and Nibler, 1982], and it is reasonable to assume that the computational procedure is reliable for species such as CO_2 and OCS.

Also shown in Figure 4.17 is the variation of the rotational relaxation time with distance from the nozzle exit for CO_2 and OCS calculated using the thermal conduction model. Log–log plots of rotational relaxation time in a supersonic molecular beam verses axial distance are distinctly linear and, as stated in §4.3, may be roughly estimated using an expression of the form

$$\tau_r = A\frac{T_0}{P_0}\left(\frac{z}{d_0}\right)^2 \; ; \; \frac{z}{d_0} > \left(\frac{1}{A}\right)^{1/2}\left(\frac{P_0}{T_0}\right)^{1/2}, \tag{4.43}$$

where z is the distance from the nozzle exit along the beam axis, d_0 is the nozzle diameter, P_0 and T_0 are the source pressure and temperature respectively, and A is a constant for a particular gas. Values of A for CH_3Cl, CO_2, and OCS are given in Table 4.8. Equation (4.43) should be used as a guide only, and it is important to emphasize this point. The equation is by no means accurate over a wide range of source conditions and simply represents a convenient method of estimating relaxation times in supersonic beams without the need for solving a complex set of equations describing the expansion process.

Rotational relaxation times in a bulb were also calculated for CO_2 using the Monte Carlo simulation procedure under analogous conditions of temperature and pressure to those employed for the calculation of relaxation times in a supersonic expansion using the thermal conduction model. The comparison, illustrated in Figure 4.18, shows that rotational relaxation is significantly faster in a bulb. While it is somewhat difficult to critically compare results obtained using the thermal conduction model with those of the direct simulation Monte Carlo procedure, it seems reasonable to expect that rotational relaxation will be less efficient in a supersonic molecular beam due to the lower collision frequency [Cameron and Harland, 1991] and the additional competing processes which redirect translational and internal energy into directed axial motion.

4.4.5 Conclusion

An approximate direct simulation Monte Carlo procedure has been developed for the investigation of rotational relaxation in homogeneous gases. The devised simulation procedure runs several orders of magnitude faster than full scale trajectory calculations of relaxation times and initial work indicates that the method gives good results for simple molecules such as homonuclear diatomic species and small non–polar polyatomic molecules such as CO_2, CH_4 and C_2H_4. Results for the polar species OCS and NH_3 also appear reasonable. The model fails to produce reliable results for highly polar species such as CH_3Cl, where it is quite unrealistic to ignore the effects of dipole–dipole interactions. For symmetric top

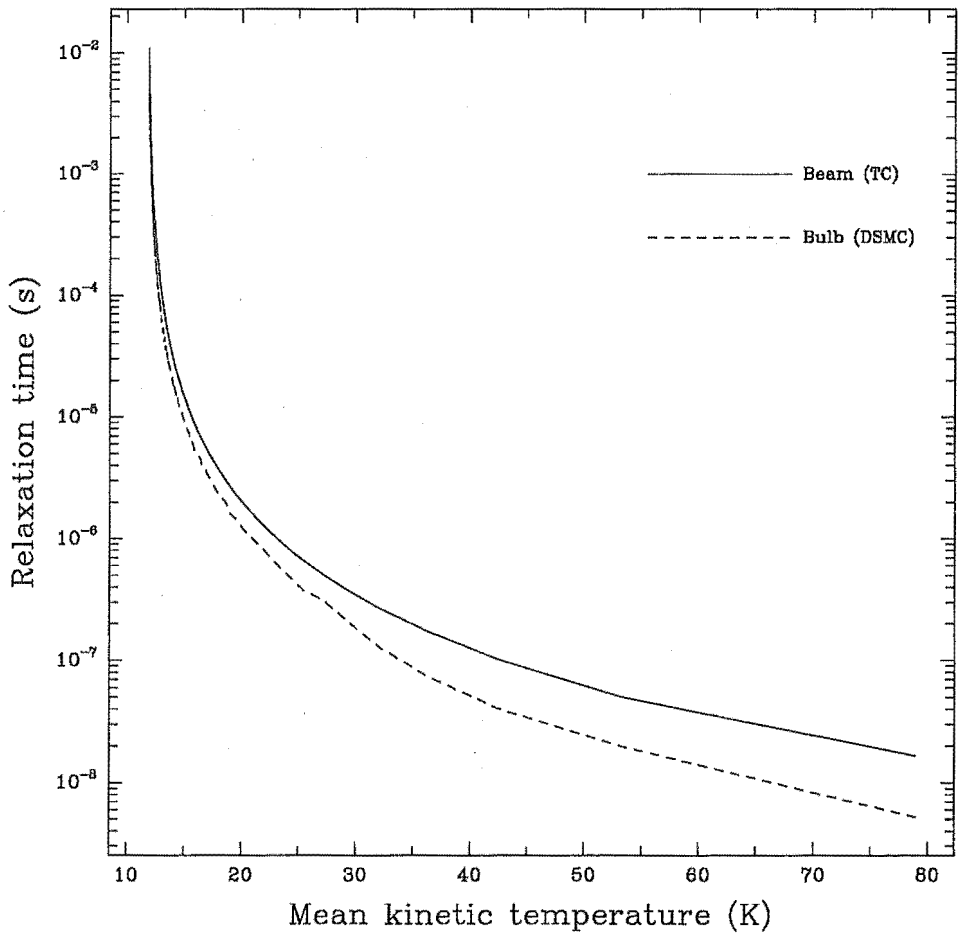

Figure 4.18: Comparison of rotational relaxation times for CO_2 in a bulb calculated using the Monte Carlo simulation procedure with relaxation times in a supersonic expansion estimated using the thermal conduction model.

molecules such as CH_3Cl, in which the two rotational constants A and B are significantly different, it is also somewhat unrealistic to assume that the coupling function ξ is the same for each unique rotational degree of freedom. The model described here may be extended to calculate separate relaxation times for each rotational degree of freedom having a unique coupling function, and it is hoped that work currently being pursued in this regard will improve the accuracy of the relaxation model for such species. The inclusion of dipole–dipole interactions is also being investigated.

Experimental and theoretical studies in the bulk have yielded valuable information on the overall rates of relaxation processes, although many important questions still remain largely unanswered. On the practical side, spectroscopist's in particular would like to know or be able to predict with some degree of accuracy not just the overall rate, but also the individual rates of state–state energy transfer processes. The model described in this section is by no means capable of calculating such detailed information, but provides a quick and convenient method of obtaining useful qualitative and quantitative information on many important aspects of rotational relaxation phenomena.

Chapter 5

Summary of results and directions for future work

The purpose of this chapter is to provide a brief summary of the results presented in §3 and §4, and to outline a number of possible suggestions for future work. It should be noted that most of the material contained in the following paragraphs has already been stated in the conclusions to the individual sections of §3 and §4. This material is combined here to provide the reader with a single cohesive summary of the experimental and theoretical investigations performed during the course of the research presented in this thesis and the significant findings of these investigations.

In §3.2 the intensities of supersonic beams of pure argon were measured as a function of source pressure and nozzle to skimmer separation in order to deduce a set of optimum operating conditions for the molecular beam apparatus. The beam intensity was observed to be strongly dependent upon the nozzle to skimmer separation, with the observed trends being attributed to a combination of skimmer interference effects and the scattering of jet particles by background gas in the expansion chamber. For all of the source pressures considered, the optimum nozzle to skimmer separation was found to lie between 200 and 300 nozzle diameters. Similar behaviour may be expected for gases other than argon, although further work would be required to confirm this prediction. There is little that can be done to reduce skimmer interference, but rather its effects must be minimized by way of experiment. While the results presented in §3.2 are by no means definitive, it is a straightforward matter to determine an optimum nozzle to skimmer separation for any gas under any set of source conditions using the methods described. The necessary measurements may be routinely performed at the start of any investigation to maximize the beam flux through the skimmer and thus optimize the signal–to–noise ratio for the experiment. Such measurements were performed at the beginning of all subsequent experimental investigations.

In §3.3 speed distributions were examined for supersonic beams of He, Ne, Ar, Kr, H_2, and N_2 using time–of–flight methods. The measured distributions were characterized in terms of a mean flow velocity u and a translational temperature $T_{||}$ by fitting them to an assumed form of the speed distribution function. Values of u and $T_{||}$ determined for the monatomic species were observed to be in excellent accord with theoretical predictions and the experimental results of other workers, indicating that the molecular beam apparatus was operating correctly with regard to the production of well defined, narrow velocity distributions. Flow velocities determined for the monatomic species were observed to be close to their thermodynamic limiting value, while those obtained for H_2 and N_2 were considerably lower than the limiting value due to the presence of internal degrees of free-

dom. For the monatomic species, the degree of translational cooling was observed to be inversely proportional to mass, suggesting that translational relaxation of atoms becomes more efficient with increasing molecular weight.

A quite general method for deconvolving badly convoluted supersonic molecular beam time–of–flight waveforms using Fourier transform and Wiener filtering techniques was presented in §3.4. The method makes no possibly invalid assumptions regarding the exact functional form of convolutions such as the chopper gating function or the response function of any detection electronics, but rather employs an overall system response function, estimated using accurate time–of–flight data, for the deconvolution of convoluted signals. The method was successfully applied to the deconvolution of highly distorted argon, krypton, CH_3Cl, and $CHCl_3$ time–of–flight waveforms measured in an unchopped pulsed supersonic molecular beam, affording considerable confidence in the reliability of the devised approach. Further work would be required to determine the dependence of the estimated response function on experimental conditions. The use of direct numerical deconvolution in the manner described is considerably more efficient than the use of moment methods or the fitting of a parameterized convolution to experimental data. The problem of noise superimposed on the measured signal may be negated through the use of Wiener filtering and the application of a simple low–pass filter.

The phenomena of velocity slip and temperature slip in supersonic expansions of gas mixtures were investigated in §3.5 for helium–neon, helium–argon and helium–krypton mixtures using time–of–flight methods. The observed trends were tentatively explained in terms of competing mass and translational relaxation effects. The results presented serve to illustrate that both velocity slip and temperature slip may be important effects, even for low seed mole fractions. It would be interesting to perform similar measurements for helium–xenon mixtures and for mixtures containing diatomic or polyatomic molecules. It would also be interesting to examine the behaviour of Δu and $\Delta T_{||}$ for somewhat less dilute mixtures than those considered. There are surprisingly few comprehensive studies of velocity slip and temperature slip in binary or multicomponent gas mixtures documented in the literature. The measurements required to obtain velocity slip and temperature slip data are straightforward and it would be interesting to investigate these phenomena in greater detail.

The kinetic theory analysis of velocity slip and temperature slip in binary gas mixtures is highly complicated, largely due to the possibility of three distinct binary collision types, each requiring a separate interaction potential. For gas mixtures containing more than two components, the situation will become still more complicated, with the number of possible binary collision types increasing in an almost exponential manner with increasing number of components. Consequently, although several reasonable semi-empirical expressions have been proposed to describe the observed behaviour, no generally valid correlation exits. The possibility of examining the phenomena of velocity and temperature slip using direct simulation Monte Carlo techniques with realistic interaction potentials is being investigated. Chatwani and Fieberg [Chatwani and Fieberg, 1981] have performed calculations of this type for monatomic binary mixtures using hard sphere and inverse ninth power law interaction potentials to describe the collision dynamics. The use of such potentials cannot be considered particularly realistic, however, and their results are probably not reliable.

In §3.6 cluster ion mass spectra were examined for supersonic expansions of pure argon and for expansions of seeded helium expansions containing SO_2, N_2O and H_2O, NO and NO_2, and NH_3. The recorded mass spectra indicated that most of the cluster species formed in the expanding jet incurred extensive fragmentation following electron impact

ionization. Fragmentation of ammonia clusters resulted in the formation of the protonated species $(NH_3)_n \cdot NH_4^+$ while for the SO_2 and mixed cluster systems a variety of cluster ion fragments were detected in addition to non–fragmented species. Intensity anomalies were observed for the species $(NH_3)_4 \cdot NH_4^+$ and $(NH_3)_{11} \cdot NH_4^+$, indicating that particularly stable geometric or electronic configurations exist for these ions. Cluster ion mass spectra were also briefly examined for several other gas mixtures. Using a gas mixture containing 500 Torr of CO_2 and 3500 Torr of helium it was possible to detect the cluster ions $(CO_2)_n^+$ $(2 \leq n \leq 8)$ while for a mixture containing 200 Torr of HCl and 3300 Torr of helium, only the $(HCl)_2^+$ dimer ion was detected. It is important to emphasize that the results presented in §3.6 cannot be used to obtain quantitative information regarding neutral cluster size distributions or to estimate the extent of any of the fragmentation processes described. The purpose of the study was simply to determine the types of clusters and cluster ions which may be prepared in the molecular beam apparatus prior to an investigation of cluster ion appearance potentials and fragmentation mechanisms.

In §3.7 appearance potentials were determined for the van der Waals cluster ions $(CO_2)_n^+$, $(N_2O)_n^+$ $(2 \leq n \leq 4)$ and $(NH_3)_nH^+$ $(1 \leq n \leq 8)$, and the cluster ion fragments $(N_2O \cdot O)^+$ and $(N_2O \cdot NO)^+$ using electron impact ionization. The appearance potentials obtained for $(CO_2)_n^+$, $(N_2O)_n^+$ $(2 \leq n \leq 4)$, $(N_2O \cdot NO)^+$ and $(NH_3)_nH^+$ $(1 \leq n \leq 3)$ were all found to be in general agreement with previously reported values while the appearance potentials of $(N_2O \cdot O)^+$ and $(NH_3)_n^+$ $(4 \leq n \leq 8)$ were examined for the first time. In contrast to the $(CO_2)_n^+$ and $(N_2O)_n^+$ systems, dissociation energies of the $(NH_3)_nH^+$ ions deduced from appearance potential measurements were observed to be in considerable disagreement with those obtained by ion–molecule methods, indicating that electron impact ionization measurements fail to sample the true adiabatic ionization thresholds of the latter species. Some knowledge of Franck–Condon factors for van der Waals clusters may therefore be required for the reliable interpretation of cluster ion appearance potentials. The most probable mechanism for the formation of the cluster fragment ions $(N_2O \cdot O)^+$ and $(N_2O \cdot NO)^+$ would appear to involve the ionization and fragmentation of one of the N_2O molecules in the neutral N_2O dimer without any significant perturbation of the accompanying molecule, although alternative mechanisms cannot be discounted. However, electron impact ionization efficiency curves provide significant mechanistic information where breaks are found and where comparisons with monomer measurements and data collected using other techniques are available. It is hoped that work currently being pursued in our laboratory using a more accurate instrument than that employed for the measurements described in §3.7 will help to clarify this situation. Appearance potentials have not been reported for many of the cluster ions and cluster ion fragments listed in Tables 3.8 and 3.10, and it would be interesting to investigate the thermochemical properties of these species. The SO_2 and NO_2 cluster systems may be of particular interest due to the important roles of the monomer species in atmospheric pollution.

In §4.2 the thermal conduction model was used to investigate the flow dynamics of supersonic beams for the monatomic species He, Ne, Ar and Kr, and the diatomic species H_2, N_2 and O_2. The model was modified to incorporate a variable flow velocity by the inclusion of an energy balance term. Temperature and flow velocity data obtained using the thermal conduction model were used to calculate collision frequencies and beam densities as a function of distance from the nozzle exit. Rotational–translational coupling parameters were determined for the diatomic species by fitting calculated values of u and $T_{\|}$ to experimental time–of–flight data. The excellent agreement obtained between the experimentally determined and calculated time–of–flight parameters for all of the species examined and the good agreement of the rotational–translational coupling parameter de-

termined for N_2 with that obtained by Randeniya and Smith [Randeniya *et al*, 1989] afford some confidence that the collision frequencies and particle densities calculated from the thermal conduction model using realistic collision cross sections and interaction potentials closely reflect the characteristics of a skimmed supersonic beam along the expansion axis. The possibility of extending the thermal conduction model or using direct simulation Monte Carlo methods to investigate supersonic expansions of simple gas mixtures is being pursued. A direct simulation Monte Carlo procedure was developed by Bird [Bird, 1976a] for the investigation of translational temperature relaxation in a homogeneous hard–sphere gas mixture. This procedure could be modified to include realistic interaction potentials and used to investigate supersonic expansions of monatomic gas mixtures. The results obtained from such calculations could be compared with time–of–flight data for gas mixtures and used to predict the magnitude of velocity slip and temperature slip which may be expected for the supersonic expansion of a particular mixture. Extension of Bird's direct simulation Monte Carlo procedure to include rotational degrees of freedom using an algorithm similar to that described in §4.4 for the investigation of rotational relaxation in small molecules may also be possible.

The work presented in §4.3 describes a relatively simple approach to the estimation of rotational relaxation times and collision numbers for non–polar molecules in a supersonic expansion based on the thermal conduction model. Results for the species considered were in general agreement with those of similar studies, providing some confidence in the derived expressions for the rotational relaxation time and the rotational collision number. The use of the derived expressions requires the complete solution of the thermal conduction model. The empirical expression given by equation (4.19) was obtained from an analysis of calculated relaxation time data as a function of axial distance and may be used to estimate relaxation times for any set of source conditions. The method described is not restricted to diatomic species and may easily be applied to simple non–polar polyatomic molecules such as CO_2 and CH_4.

An approximate direct simulation Monte Carlo procedure for the investigation of rotational relaxation in homogeneous gases was presented in §4.4. The devised simulation procedure runs several orders of magnitude faster than full scale trajectory calculations of relaxation times and initial work indicates that the method gives good results for simple molecules such as homonuclear diatomic species and small non–polar polyatomic molecules such as CO_2, CH_4 and C_2H_4. Results for the polar species OCS and NH_3 also appear reasonable. The model fails to produce reliable results for highly polar species such as CH_3Cl, where it is quite unrealistic to ignore the effects of dipole–dipole interactions. For symmetric top molecules such as CH_3Cl, in which the two rotational constants $\mathcal{A}$ and $\mathcal{B}$ are significantly different, it is also somewhat unrealistic to assume that the coupling function ξ is the same for each unique rotational degree of freedom. The model may be extended to calculate separate relaxation times for each rotational degree of freedom having a unique coupling function, and it is hoped that work currently being pursued in this regard will improve the accuracy of the relaxation model for such species. The inclusion of dipole–dipole interactions is also being investigated.

Experimental and theoretical studies in the bulk have yielded valuable information on the overall rates of relaxation processes, although many important questions still remain largely unanswered. On the practical side, spectroscopist's in particular would like to know or be able to predict with some degree of accuracy not just the overall rate, but also the individual rates of state–state energy transfer processes. The model described in §4.4 is by no means capable of calculating such detailed information, but provides a quick and convenient method of obtaining useful qualitative and quantitative information on many

important aspects of rotational relaxation phenomena.

Appendix A

Monte Carlo methods

A.1 Introduction

Monte Carlo methods comprise that branch of experimental mathematics which is concerned with the approximate solution of mathematical and physical problems by the simulation of random quantities: the solution being some parameter taken from a hypothetical population constructed using a random sequence of numbers. Monte Carlo methods have long be recognized as an extremely powerful technique for the solution of many problems, particularly those too complicated to be dealt with by a somewhat more classical approach. The Monte Carlo technique makes possible the simulation of any process that is influenced by random factors and the solution of any mathematical problem involving absolutely no chance whatsoever for which it is possible to artificially devise a probabilistic description of the situation. For this reason, Monte Carlo methods may be considered to represent a universal technique for the solution of mathematical problems.

The following sections of this appendix are intended to provide the reader with a brief introduction to the basic principles of Monte Carlo techniques. The material presented in these sections formed the basis of a seminar presented to the Chemistry Department staff, and many of the mathematical techniques described below were employed in the theoretical calculations presented in §4.2 to §4.4. Many books and review articles have been written about all aspects of the Monte Carlo technique. An excellent introduction to Monte Carlo methods is given by Hammersley and Handscomb [Hammersley and Handscomb, 1964] while an early article by von Neuman and Ulam [von Neuman and Ulam, 1949] provides an interesting historical insight into the development of the technique.

A.2 Types of Monte Carlo

Monte Carlo methods are capable of solving both probabilistic and deterministic problems. In the case of a probabilistic problem, such as that of neutron diffusion through matter, the simplest Monte Carlo approach is to observe random numbers chosen in such a way that they directly simulate the physical random process of the original problem and to then infer the desired solution from the behaviour of these random numbers. This type of approach is referred to as *direct simulation*. Although of little theoretical interest, direct simulation remains one of the principal forms of Monte Carlo because it arises so often in a wide variety of problems which are characterized by a fairly simple general structure overlaid with a mass of small and rather particular details. These problems are beyond the scope of general theory on account of the specific details, but are often easily simulated and such improvements as might be made by the application of some of the more sophisticated

Monte Carlo refinements described below are rarely worth the effort of their devising.

The idea behind the Monte Carlo approach to deterministic problems is to replace theory by experiment whenever the former falters. Specifically, consider a deterministic problem which can be formulated in theoretical terms, but cannot be solved by deterministic means. Being deterministic, such a problem has no direct association with random processes. However, when theory has exposed its underlying structure, it may be possible to recognize that this structure also describes some apparently unrelated random process, and hence it is possible to solve the deterministic problem by a Monte Carlo simulation of this concomitant probabilistic problem. The technique of solving a given problem by Monte Carlo simulation of a different problem is often called *sophisticated* Monte Carlo, to distinguish it from a straightforward simulation of the original problem.

An important point to note is that the statistical part of the amount of work required by the Monte Carlo method (be it sophisticated or otherwise) to achieve a given accuracy in computing one element of a solution is independent of the dimensionality of the problem. The computational effort required by most other numerical techniques is found to increase as the square or cube of the dimensionality.

A.3 Random numbers

The essential feature common to all Monte Carlo computations is that at some point it is necessary to substitute for a random variable a corresponding set of actual values which have the statistical properties of the random variable. These substituted values are called random numbers, on the grounds that they could have been produced by chance by some suitable random process. It is important to realize, however, that although the basic procedure of the Monte Carlo method is the manipulation of these random numbers, each such number is a potential source of added uncertainty in the final result, and consequently they should not be used in a prodigal manner; rather each part of the Monte Carlo experiment should be carefully scrutinized to see whether it cannot be replaced by exact mathematical theory contributing absolutely no uncertainty. Quite generally, good Monte Carlo practice uses each random number or combination of random numbers several times over whenever it is safe to do so, saving time and possibly increasing precision. Moreover, as experimental work provides an ever growing insight into the nature of the problem at hand and suggests appropriate theory, good Monte Carlo practice may be to this end self liquidating.

The generation of sequences of random numbers generally breaks down into the following two problems:

1. How to generate sequences of random numbers uniformly distributed on the interval $\{0, 1\}$; and

2. How to transform the uniform deviates into random variables having specified probability distributions.

A.3.1 Generation of uniform deviates

Uniform deviates are simply random numbers which lie within a specified range (typically 0 to 1), with any one number in the range being equally as probable as any other. They are, in other words, what most people consider random numbers to be. It is important to distinguish uniform deviates from other sorts of random numbers such as those drawn from a normal (Gaussian) distribution having a specified mean and standard deviation. These

other sorts of deviates are invariably generated by performing appropriate operations on one or more uniform deviates. Hence a reliable source of uniform deviates is an essential building block for any Monte Carlo work.

A sequence of truly random numbers is unpredictable and cannot therefore be reproduced. Such a sequence can be generated only by a random physical process such as radioactive decay, thermal noise in electronic devices, cosmic ray arrival times, and so on. In practice it turns out to be very difficult to construct physical generators which are fast enough for use in Monte Carlo calculations performed on modern computers (where thousands of floating–point random numbers may be required every second) and which are at the same time accurate and unbiased.

In calculations performed by modern computers it is most convenient to calculate a sequence of numbers one at a time as required using a completely specified rule devised in such a way that no reasonable statistical test will detect any significant departure from randomness. Such a sequence is called *pseudo–random*. The great advantage of a specified rule is that the sequence of numbers can be reproduced exactly for the purpose of computational checking.

It is a rather general property of all pseudo–random generators, including those in common usage today, that they are characterized by a period. That is, at some point the sequence of numbers produced by the generator will begin to repeat itself. The pseudo–random number generators used most widely today are D. H. Lehmer's *multiplicative congruential* or *linear congruential* generators [Press *et al*, 1986] which, given a modulus m, a multiplier a and some starting value r_i, produce successive pseudo–random numbers r_{i+1} by the formula

$$r_{i+1} = ar_i \pmod{m}. \tag{A.1}$$

A slight variation known as the *mixed congruential* generator requires, in addition, an additive constant or *increment* b:

$$r_{i+1} = ar_i + b \pmod{m}. \tag{A.2}$$

Not surprisingly, the two generators have similar properties. Their period can obviously be no greater than m. If m, a and b are chosen correctly then the period will be of maximal length, in which case all possible integers between 0 and $m-1$ will occur at some point, so that any initial choice of r_i is as good as any other: the sequence merely takes off from that point. The number m is usually equal to the word–size of the machine using the algorithm, this typically being $\sim 2^{32}$ for most modern computers. The linear congruential methods have the advantage of being very fast, requiring only a few operations per call, and hence their almost universal use. They are so good for practical computational purposes that there no longer exists any problem of having an adequate supply of random numbers. Thus the discovery of new methods for generating random or pseudo–random numbers is no longer of any practical importance, although it may be of considerable theoretical interest.

A.3.2 Non–uniform random numbers

The generation of non–uniform distributions is important in many applications where the physical phenomena being investigated are known to follow other distributions, the most common and important being the Gaussian (or normal) and exponential distributions for continuous variables, and the Poisson and binomial distributions in the case of discrete variables. Many other distributions may be required for special applications, and many

different techniques are known for generating them. Generally, values for any such distribution can be obtained by performing appropriate transformations on the values of some standard random variable (usually the uniform distribution on the interval $\{0,1\}$), and there are three main methods of operating with probability distributions which can be adapted to serve this purpose. These are based on direct functional transformation, the principle of compound probabilities [Dieter and Ahrens, 1973], and the procedure of rejecting some of the sampled values according to an appropriate test or rule. Only the first and last of these approaches will be considered here, with compound methods being somewhat complicated and difficult to discuss in general terms.

A.3.2.1 The transformation method

It is a simple matter to generate random numbers which have a uniform probability distribution function $p(x)\mathrm{d}x$ so that the probability of obtaining a number between x and $x + \mathrm{d}x$ is given by

$$p(x)\mathrm{d}x = \begin{cases} \mathrm{d}x & 0 \leq x \leq 1 \\ 0 & \text{otherwise} \end{cases} \tag{A.3}$$

where

$$\int_{\infty}^{\infty} p(x)\mathrm{d}x = 1. \tag{A.4}$$

Now, given some such uniform deviate x it is possible to take some prescribed function $y(x)$ of it, whereupon the resulting probability distribution of y, denoted by $p(y)\mathrm{d}y$, is determined by the fundamental law of probabilities to be

$$|p(y)\mathrm{d}y| = |p(x)\mathrm{d}x|\,, \tag{A.5}$$

or

$$p(y) = p(x)\left|\frac{\mathrm{d}y}{\mathrm{d}x}\right|. \tag{A.6}$$

This expression constitutes the basis of the transformation method. Hence, in order to generate some desired arbitrary distribution of y's with $p(y) = f(y)$ for some positive function f, whose integral is (A.4), it is necessary to solve the differential equation

$$\frac{\mathrm{d}x}{\mathrm{d}y} = f(y). \tag{A.7}$$

The solution of this differential equation is simply $x = F(y)$, where $F(y)$ is the indefinite integral of $f(y)$. The desired transformation which takes a uniform deviate into one distributed as $f(y)$ is therefore

$$y(x) = F^{-1}(x) \tag{A.8}$$

where $F^{-1}(x)$ is the inverse function of $F(x)$. Whether equation (A.8) is feasible to implement depends on whether the inverse function of the integral of $f(y)$ is itself feasible to compute, either numerically or analytically.

It is possible to generalize transformation methods to more than one dimension. If $x_1, x_2, \ldots, x_n$ are random deviates having a joint probability distribution

$$p(x_1, x_2, \ldots, x_n)\mathrm{d}x_1\mathrm{d}x_2 \ldots \mathrm{d}x_n, \tag{A.9}$$

and $y_1, y_2, \ldots, y_n$ are each functions of all the x's, then the joint probability distribution of the y's is

$$p(y_1, y_2, \ldots, y_n)\mathrm{d}y_1\mathrm{d}y_2 \ldots \mathrm{d}y_n = p(x_1, x_2, \ldots, x_n)\left|\frac{\partial(x_1, x_2, \ldots, x_n)}{\partial(y_1, y_2, \ldots, y_n)}\right|\mathrm{d}y_1\mathrm{d}y_2 \ldots \mathrm{d}y_n \tag{A.10}$$

where $|\partial(x_1, x_2, \ldots, x_n)/\partial(y_1, y_2, \ldots, y_n)|$ is the Jacobian determinant of the x's with respect to the y's.

A.3.2.2 The rejection method

The rejection method is illustrated in Figure A.1. It is a powerful and quite general technique for generating random deviates whose probability density function $p(x)\mathrm{d}x$ is known and computable. This method does not require that the cumulative distribution function

$$P(x) = \int_{-\infty}^{x} p(x)\mathrm{d}x \tag{A.11}$$

be readily computable, much less the inverse of this function, which was needed in the transformation method. The rejection method is attractive for use on computers, since rather complex distributions may be sampled by performing quite simple calculations.

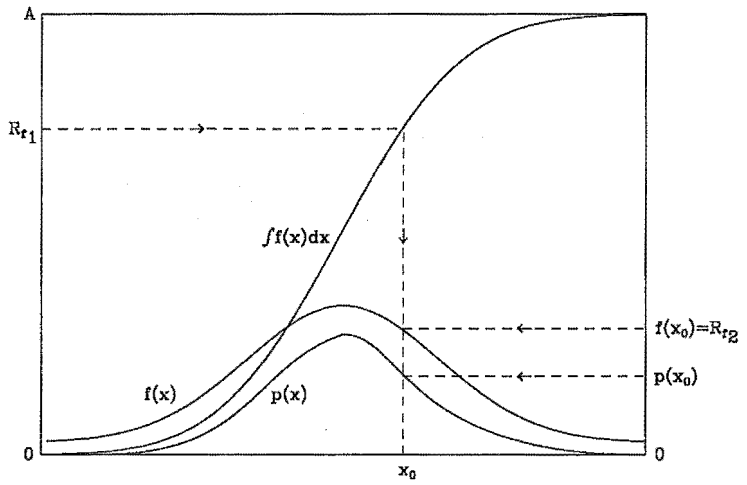

Figure A.1: The rejection method for generating random deviates.

The rejection method is based on a simple geometric argument. Say that it is necessary to generate random deviates from some probability distribution $p(x)\mathrm{d}x$. Consider the graph of this distribution. Assuming that $p(x)$ is normalized, the area under the curve in any range of x will correspond to the desired probability of generating an x in that range. Hence, if there exists some means of choosing a random point in two dimensions, with

uniform probability in the area under $p(x)$, then the x value of that random point will have the desired distribution.

Now consider any other curve $f(x)$ having *finite* area and lying everywhere above the original probability distribution. Imagine that it is possible to generate random points in two dimensions which are uniform under this function. Whenever a random point is outside the area under the original distribution $p(x)$ reject it, and whenever it lies inside the area under the original probability distribution accept it. The accepted points will be uniform in the accepted area, so that their x values therefore have the desired distribution. Note that the fraction of points rejected simply depends on the ratio of the area of the so–called *comparison function* $f(x)$ to the area of the original probability distribution function.

It remains only to suggest some means of choosing a uniform random point in two dimensions under the comparison function. By choosing a comparison function whose indefinite integral is known analytically, and is also analytically invertible to give x as a function of area under the comparison function to the left of x, it is possible to make use of a variant of the transformation method. Firstly, pick a uniform deviate between 0 and A, where A is the total area under $f(x)$, and use it to obtain the corresponding value of x. Then pick a uniform deviate between 0 and $f(x)$ as the y value for the two dimensional point. The resulting point (x, y) is uniformly distributed under the comparison function.

A.4 Variance-reduction

The main concern in all Monte Carlo work is to obtain a respectably small standard error in the final result with a minimum amount of effort. One way of reducing the uncertainty in an answer is simply to base it upon more observations. This is not a particularly economic course of action, however, since there is generally a square law relationship between the error in the final answer and the requisite number of observations. To reduce the error associated with the final answer by a factor of k it is therefore necessary to increase the sample size by k^2.

To escape a formidable or even impracticable amount of work it is profitable to change the original problem in such a way that the level of uncertainty in the solution is reduced. These so–called *variance–reducing* techniques, which lie at the core of all good Monte Carlo work, are techniques which reduce the coefficient of n^{-1} in the sampling variance of the final answer, where n is the sample size. These techniques depend on various devices, such as distorting the data so that the variance of the parent distribution is reduced, or making allowances for various causes of variation in the data. What all variance–reducing techniques have in common is that they do not introduce any bias into the estimation, thus making results more precise without sacrificing any reliability.

When Monte Carlo methods are to be used to solve a particular problem, attention is focussed on the following three main topics:

1. Choosing the model or probability process;

2. Generating sample values of any necessary random variables;

3. Designing and using variance–reducing techniques.

It is important to note that generally it is not possible to isolate variance–reduction from the first two topics, since the methods which can be used to reduce the variance are often sharply dependent upon the probability model and, in some cases, on the type of

approach used to generate values of the random variables. Also, the greatest gains in variance–reduction are very often made by exploiting specific details of the particular problem under study rather than by the routine application of any general principles. However, there do seem to be some general ideas on reducing variance which can be used in many problems.

Before going on to consider a few of the simpler and more commonly used variance–reducing techniques it is useful to draw attention to the fact that, in the formal sense at least, all Monte Carlo calculations are equivalent to integrations. This follows from the definition of a Monte Carlo calculation as producing a result F which is a function of random numbers r_i. If, for simplicity, it is assumed that the r_i are uniformly distributed on $\{0,1\}$, then the Monte Carlo result $F = F(r_1, r_2, \ldots, r_n)$ is an unbiased estimator of the multidimensional integral

$$I = \int_0^1 \ldots \int_0^1 F(x_1, x_2, \ldots, x_n) \mathrm{d}x_1 \mathrm{d}x_2 \ldots \mathrm{d}x_n, \tag{A.12}$$

or, stated another way, the integral I is equivalent to the expectation of F. This formal equivalence makes it possible to lay a firm theoretical justification for Monte Carlo techniques and also leads to many results of practical importance.

A.4.1 Stratified sampling

Mathematically, stratified sampling is based on the fundamental property that

$$\begin{aligned} I &= \int_0^1 f(u)\mathrm{d}u \\ &= \int_0^a f(u)\mathrm{d}u + \int_a^1 f(u)\mathrm{d}u, \quad 0 \le a \le 1 \end{aligned} \tag{A.13}$$

with the range of integration being broken into several pieces. The technique of stratified sampling involves dividing the full integration interval into several sub–intervals and choosing n_j points in the jth sub–interval of size $\{j\}$. Then, instead of adding the contributions from all points directly, partial sums are formed over each interval, and the partial sums are added, weighted proportionally to $\{j\}$ and inversely to n_j. This yields a result with the variance

$$s^2 = \sum_j \frac{\{j\}}{n_j} \int_{\{j\}} f^2(x)\mathrm{d}x - \sum_j \frac{1}{n_j} \left| \int_{\{j\}} f(x)\mathrm{d}x \right|^2, \tag{A.14}$$

which is merely the sum of the variances of the individual pieces. If the intervals $\{j\}$ and numbers n_j are chosen carefully so that the differences between the mean values of f in the various intervals are greater than the variations of f within the intervals, this can lead to a dramatic reduction in the variance, but it can also lead to a larger variance, so something must be known about the function f for this technique to be used most advantageously.

If nothing is known about the function, the best and simplest approach is to apply uniform stratification which can be shown not to increase the variance in any case and will in general decrease it if the expectation of the function is different in the different sub–regions. Uniform stratification is therefore a safe method, but any variance reduction may be arbitrarily small. In real calculations, additional complications may often arise. In many–dimensional integration, for example, it may not be at all straightforward to divide the integration region into sub–regions of known size.

A.4.2 Importance sampling

The general idea of importance sampling is to draw samples from a distribution other than the one suggested by the problem under consideration and to carry along an appropriate weighting factor which when multiplied into the final result corrects for having used the wrong distribution. Biasing is performed in such a way that the probability of samples being drawn from an interesting region is increased while the probability of sampling an uninteresting region is decreased.

Mathematically, importance sampling corresponds to a change of integration variable:

$$f(\mathbf{x})\mathrm{d}\mathbf{x} \longrightarrow f(\mathbf{x})\frac{\mathrm{d}G(\mathbf{x})}{g(\mathbf{x})}. \tag{A.15}$$

Points are chosen according to $G(\mathbf{x})$ instead of $f(\mathbf{x})$ and f is weighted inversely by $g(\mathbf{x}) = \mathrm{d}G(\mathbf{x})/d\mathbf{x}$. The relevant variance V is now $V(f/g)$ as opposed to $V(f)$ and will be small if g has been chosen to be close to f in shape.

In order to successfully apply importance sampling to a function f, a function g must be found such that:

1. $g(\mathbf{x})$ is a probability density function being everywhere non–negative and normalized so that its integral over the sampling region is unity.
2. $G(\mathbf{x})$, the integral of g, is known analytically.
3. Either the function $G(\mathbf{x})$ can be inverted analytically, or alternatively, it is possible to generate random numbers distributed according to g.
4. The ratio $f(\mathbf{x})/g(\mathbf{x})$ is as constant as possible so that the variance $V(f/g)$ is small compared with $V(f)$.

Importance sampling then involves randomly selecting values of G on $\{0,1\}$, solving for x, and evaluating $f(\mathbf{x})/g(\mathbf{x})$; taking the sum of these ratios as the result.

While importance sampling is one of the simplest and most useful variance reducing techniques, in practice it suffers from a number of drawbacks:

1. The class of functions g that are integrable and of which the integral can be inverted analytically is small, essentially consisting of the trigonometric functions, exponentials, and polynomials of low degree. Inversion can of course be done numerically, but this may be slow or inaccurate.
2. Multidimensional importance sampling is most awkward for all but the simplest functions.
3. Importance sampling is *unstable* in the sense that if the function g becomes very small, f/g will, along with the variance, become large. Therefore it is important to choose functions g which do not go through zero, or approach that value quickly.

A.4.3 Control variates

The method of control variates is similar to importance sampling in that it is again necessary to seek an integrable function g which approximates the original function f. Unlike importance sampling, however, the two functions are subtracted rather than divided. Mathematically, this technique is based on the linearity of the integral operator:

$$\int f(\mathbf{x})\mathrm{d}\mathbf{x} = \int \{f(\mathbf{x}) - g(\mathbf{x})\}\mathrm{d}\mathbf{x} + \int g(\mathbf{x})\mathrm{d}\mathbf{x}. \tag{A.16}$$

Now, given that the definite integral of g is known, the only uncertainty comes from the integral of $(f-g)$, which will have a smaller variance than f if g has been chosen carefully. The method of control variates is more reliable than importance sampling since zeros in g cannot induce singularities in $(f-g)$. Also, unlike importance sampling, it is not necessary to invert g in any way.

A.4.4 Antithetic variates

Usually Monte Carlo calculations make use of random numbers or points which are, in principle, independent of one another. The method of antithetic variates deliberately makes use of correlated points, taking advantage of the fact that such correlation may be negative as well as positive. If it is possible to choose points that are negatively correlated, then a substantial reduction in variance may be realized. This of course requires knowledge of the function under consideration, and it is not easy to lay down any general guidelines for accomplishing this negative correlation. Hammersley and Morton [Hammersley and Morton, 1956] discuss the technique of antithetic variates in some detail and give further references.

Appendix B

Physical constants and useful conversion factors

B.1 Frequently encountered physical constants

Constant	Symbol	Value	Dimensions
Avagadro number	N_A	$6.022169(40) \times 10^{23}$	mol^{-1}
Atomic mass unit	amu	$1.6605(11) \times 10^{-27}$	kg
Speed of light in a vacuum	c	$2.997925(10) \times 10^{8}$	$m\ s^{-1}$
Elementary charge	e	$1.6021917(70) \times 10^{-19}$	C
Boltzmann constant	k_b	$1.380622(59) \times 10^{-23}$	$J\ K^{-1}$
Bohr radius	a_0	$5.2918(81) \times 10^{-11}$	m
Planck constant	h	$6.6262(50) \times 10^{-34}$	J s
Gas constant	R	$8.31434(35) \times 10^{0}$	$J\ K^{-1}\ mol^{-1}$
Normal volume perfect gas	V_0	$2.24136(39) \times 10^{-2}$	$m^3\ mol^{-1}$
Pi	π	3.14159265359	
Base of natural logarithms	e	2.71828182846	

Table B.1: Frequently encountered physical constants. The numbers in parentheses indicate the standard deviation uncertainties in the last digits of the quoted value (see [Taylor *et al*, 1969]).

B.2 Useful conversion factors

1 atm	= 760 mm Hg
	= 760 Torr
	= 101.325 kPa
1 Torr	= 133.322 Pa
1 D	= 3.33564×10^{-30} C m
1 Å	= 1×10^{-10} m
1 cal	= 4.1840 J
1 eV	= 1.602189×10^{-19} J
	= 96.485 kJ mol^{-1}
	= 8065.5 cm^{-1}
	= 23.06 kcal mol^{-1}

	$= 2.42 \times 10^{14}$ Hz
	$= 1.161 \times 10^{4}$ K
	$= 3.68 \times 10^{-2}$ au
1 K	$= 1.380 \times 10^{-23}$ J
	$= 8.62 \times 10^{-5}$ eV
	$= 3.17 \times 10^{-6}$ au
	$= 6.95 \times 10^{-1}$ cm^{-1}
	$= 2.08 \times 10^{10}$ Hz
	$= 1.988 \times 10^{-3}$ kcal mol^{-1}
1 au	$= 2.72 \times 10^{1}$ eV
	$= 3.16 \times 10^{5}$ K
	$= 4.359 \times 10^{-18}$ J
1 kcal mol^{-1}	$= 4.33 \times 10^{-2}$ eV
	$= 5.03 \times 10^{2}$ K

Appendix C

Interaction potential parameters

C.1 Lennard–Jones (12,6) potential parameters

Tabulated spherical interaction potentials containing 100 equally spaced points were employed for the calculation of the collision cross sections required in §4.2 to §4.4 for the determination of collision frequencies and rotational relaxation times. The numerical methods used for extrapolation and interpolation of the tabulated potential data were described in §4.4. Collision cross sections for diatomic and polyatomic species were determined using a Lennard–Jones potential of the form

$$V(r) = 4\epsilon\left[\left(\frac{\sigma}{r}\right)^{12} - \left(\frac{\sigma}{r}\right)^{6}\right], \tag{C.1}$$

where σ is the value of r for which $V(r) = 0$ and ϵ is the maximum energy of attraction (or depth of the potential well), which occurs at $r = 2^{1/6}\sigma$. Values of σ and ϵ are listed in Table C.1 for all of the molecules examined in §4.2 to §4.4. Also listed in Table C.1 are values of the parameter Υ which were calculated according to the expression

$$\Upsilon = \left(\frac{C_6}{k_b}\right)^{1/3} \cdot \frac{1}{k_b}, \tag{C.2}$$

with $C_6 = 4\epsilon\sigma^6$ J m^6. This method of expressing the C_6 potential parameter was convenient for computational purposes and values of Υ form part of the required input to the computational procedure devised for the solution of the thermal conduction model (see §E.2).

Equation (C.1) is frequently referred to as the Lennard–Jones (12,6) potential. The inverse sixth–power attractive term of the potential faithfully represents the induced–dipole—induced–dipole interaction for most species while the choice of 12 as the index for the repulsive term is primarily one of mathematical convenience, and is by no means unique. The Lennard–Jones (12,6) potential provides a simple and realistic representation of the true interaction potential for non–polar molecules but is often unsatisfactory for the treatment of polar species.

C.2 Modified Buckingham potential parameters

For thermal conduction model calculations involving atomic species, the use of Lennard–Jones (12,6) potentials was found to produce results which were in reasonable accord only

System	ϵ (K)	σ (Å)	Υ (m^2 $K^{-2/3}$)
H_2	33.3	2.97	3.29579×10^4
CH_4	137	3.82	8.64901×10^4
NH_3	320	2.60	5.31614×10^4
N_2	91.5	3.68	7.18450×10^4
C_2H_4	205	4.23	1.21301×10^5
O_2	113	3.43	6.75117×10^4
CO_2	190	4.00	1.05756×10^5
CH_3Cl	855	3.375	1.25736×10^5
OCS	335	4.13	1.36201×10^5
SO_2	252	4.290	1.33654×10^5
Cl_2	357	4.12	1.38447×10^5

Table C.1: Lennard–Jones (12,6) potential parameters [Hirschfelder *et al*, 1954].

System	A (eV)	b (Å)	C_6 (au)	C_8 (au)	C_{10} (au)	Υ (m^2 $K^{-2/3}$)
He	498	4.5	1.46	14.2	182	1.566826×10^4
Ne	4308	4.7	6.55	57.2	698	2.584146×10^4
Ar	28440	4.0	67.7	1320	30000	5.629020×10^4
Kr	68080	3.94	135	2580	65500	7.085131×10^4

Table C.2: Potential parameters for the modified Buckingham potential [Tang and Toennies, 1977].

with experimental data. Superior agreement between theory and experiment was obtained for these species using a modified Buckingham potential of the form

$$V(r) = Ae^{-br} - \frac{C_6}{r^6} - \frac{C_8}{r^8} - \frac{C_{10}}{r^{10}}. \tag{C.3}$$

This five parameter potential function approximates the repulsive contribution to the interaction potential by an exponential term and takes into account both the induced dipole—induced–dipole and induced–dipole—induced–quadrupole interactions. Consequently equation (C.3) is somewhat more realistic than the Lennard–Jones model. The modified Buckingham potential is unrealistic in that it goes to $-\infty$ at the origin, but for most calculations this region of the potential is not considered. Values of the parameters A, b, C_6, C_8 and C_{10} in equation (C.3) are listed in Table C.2 for all of the monatomic species examined in §4.2. Also given are values of Υ calculated for these species using equation (C.2) and the modified Buckingham potential C_6 parameters.

Appendix D

Moments of the velocity distribution function

For the time–of–flight measurements described in §3.3, values of the flow velocity u and the parallel translational temperature $T_{||}$ were calculated using an iterative linear least squares algorithm to fit experimental time–of–flight data to the speed distribution function

$$f(v)\mathrm{d}v = Av^2\mathrm{e}^{-a(v-u)^2}\mathrm{d}v, \tag{D.1}$$

where $a = m/(2k_bT_{||})$ and A is a normalization constant defined such that the area under the distribution curve is unity. The use of a linear least squares procedure was considered necessary due to the presence of noise on many of the measured time–of–flight waveforms. The least squares method was straightforward to implement and generally produced satisfactory results.

In situations where the experimental data is sufficiently smooth and free from noise, it is also possible to extract values of u and $T_{||}$ by evaluating several moments of the speed distribution function. Ignoring the normalization constant A, the moments μ_n of the speed distribution function described by equation (D.1) are given by the general expression

$$\mu_n = \int_0^\infty v^n f(v)\mathrm{d}v = \int_0^\infty v^{n+2}\mathrm{e}^{-a(v-u)^2}\mathrm{d}v, \tag{D.2}$$

where n is an integer value on the range $\{-\infty, \infty\}$. The evaluation of the integral (D.2) may be simplified by introducing the change of integration variable $t = v - u$ to obtain

$$\mu_n = \int_{-u}^\infty (t+u)^{n+2}\mathrm{e}^{-at^2}\mathrm{d}t. \tag{D.3}$$

This integral may be readily evaluated to obtain the following expressions for the moments μ_n with $-2 \leq n \leq 2$

$$\mu_{-2} = \frac{\sqrt{\pi}}{2\sqrt{a}}\left(1 + \mathrm{erf}\left(a^{1/2}u\right)\right) \tag{D.4}$$

$$\mu_{-1} = \frac{1}{2a}\mathrm{e}^{-au^2} + \frac{u\sqrt{\pi}}{2\sqrt{a}}\left(1 + \mathrm{erf}\left(a^{1/2}u\right)\right) \tag{D.5}$$

$$\mu_0 = \frac{u}{2a}\mathrm{e}^{-au^2} + \frac{\sqrt{\pi}}{2\sqrt{a}}\left(u^2 + \frac{1}{2a}\right)\left(1 + \mathrm{erf}\left(a^{1/2}u\right)\right) \tag{D.6}$$

$$\mu_1 = \left(\frac{u^2}{2a} + \frac{1}{2a^2}\right)\mathrm{e}^{-au^2} + \frac{\sqrt{\pi}}{2\sqrt{a}}\left(\frac{3u}{2a} + u^3\right)\left(1 + \mathrm{erf}\left(a^{1/2}u\right)\right) \tag{D.7}$$

$$\mu_2 = \left(\frac{u^3}{2a} + \frac{5u}{4a^2}\right)\mathrm{e}^{-au^2} + \frac{\sqrt{\pi}}{2\sqrt{a}}\left(\frac{3}{4a^2} + \frac{3u^2}{a} + u^4\right)\left(1 + \mathrm{erf}\left(a^{1/2}u\right)\right). \tag{D.8}$$

The error function erf (x) represents the area bounded by the standard normal distribution function from 0 to x [Boas, 1983] and may be defined as

$$\mathrm{erf}\,(x) = \frac{2}{\sqrt{\pi}} \int_0^x \mathrm{e}^{-t^2}\,\mathrm{d}t. \tag{D.9}$$

The reciprocal of μ_0 represents the normalization constant A while the mean and variance of the distribution function are given by the expressions μ_1/μ_0 and $\mu_2/\mu_0 - (\mu_1/\mu_0)^2$, respectively.

From equations (D.4) to (D.8) it is possible to derive the following relationships between the moments μ_n $(-1 \leq n \leq 2)$ in terms of the quantities u and a

$$\mu_1 = \mu_0 u + \frac{\mu_{-1}}{a} \tag{D.10}$$

$$\mu_2 = \mu_1 u + \frac{3}{2}\frac{\mu_0}{a} \tag{D.11}$$

These expressions represent a pair of simultaneous equations which may be solved to obtain the following expressions for u and $T_{\|}$

$$T_{\|} = \frac{m}{k_b}\left[\frac{\mu_2}{\mu_0} - \frac{\mu_1^2}{\mu_0^2}\right] \tag{D.12}$$

$$u = 3\frac{\mu_1}{\mu_0} - 2\frac{\mu_2}{\mu_1} \tag{D.13}$$

For sufficiently smooth time–of–flight data sets containing a reasonably large number of points (≥ 256), equations (D.12) and (D.13) may be used to accurately calculate u and $T_{\|}$. The moments μ_n $(-1 \leq n \leq 2)$ of the measured distribution function may be readily evaluated using a simple numerical integration algorithm such as Simpsons rule [Press *et al*, 1986]. For very large data sets (≥ 2048 points) rectangular integration may suffice. It is important to emphasize, however, that any noise in the measured time–of–flight data will be amplified as a result of the numerical integration procedure, particularly in the evaluation of the positive moments μ_1 and μ_2.

Another quantity of interest which may be derived from the speed distribution function is the most probable speed v_{mp}. The most probable speed may be obtained by setting the first derivative of the speed distribution function to zero and solving for v on the interval $\{0, \infty\}$. Performing this operation on the speed distribution function described by equation (D.1) yields the following expression for v_{mp} in terms of u and $T_{\|}$

$$v_{mp} = \frac{u}{2} + \left(\frac{u^2}{4} + \frac{1}{a}\right)^{1/2}.$$

The most probable speed is generally observed to be very close to the value of u for supersonic expansions of most gases. In most situations the mean speed μ_1/μ_0 will be similar to u and v_{mp} also, particularly when the product $a^{1/2}u$ is large such that $\mathrm{erf}\left(a^{1/2}u\right) \approx 1$ and $\exp(-au^2) \approx 0$.

Appendix E

Software package design and user command summary

E.1 Software package design

During the course of the research presented in this thesis, a large quantity of computer software was developed both for analysing data and for performing a wide range of theoretical calculations. The majority of the procedures developed for the analysis and manipulation of data were combined into a single software package named UOCPROC (**U**niversity **o**f **C**anterbury data **proc**essing package). The UOCPROC package has been installed on the University of Canterbury Computer Services VAX cluster since 1991 and has proved popular with many users since that time. The purpose of the following paragraphs is to briefly describe the main features of the software package in terms of both functionality and design.[1]

The UOCPROC package may be defined as an interpreted language specifically designed for the manipulation and analysis of large quantities of scientific data. Data is loaded into the UOCPROC environment from specially formatted disk files and stored in uniquely named *buffers* which may be combined and manipulated using the wide range of mathematical operations and commands provided by the package. Dynamic allocation of memory is used to create and delete buffers as required, and to allow buffers of variable size to be efficiently combined and manipulated. The use of a sophisticated command interpreter provides flexible command line program control while the incorporation logical constructs (*if–then–else* constructs, *for* and *while* loops) allows sets of commands to be grouped and executed from command files. The package supports a wide variety of data types (integer, real double–precision, complex, byte and boolean) and provides a comprehensive interface to the NCAR graphics package [Clare *et al*, 1987] for the display of data. The UOCPROC package also provides a mechanism which allows advanced users to define their own personal commands. UOCPROC commands are specified in standard VAX/VMS format, generally taking at least one required parameter and often having several optional command qualifiers which may be used to override default values for the command.

The structure of the UOCPROC software package is illustrated in Figure E.1. Command tables are used to define the syntax for each command and to specify the computational procedure associated with each command. General UOCPROC commands are defined in the

[1] A complete description of the uocproc package is beyond the scope of this thesis. A copy of the entire software package, including documentation and source code, may be obtained from the author. The entire kit requires approximately 15000 blocks ($\sim$ 7.7 Mb) of disk space, ncar graphics version 3.00 or higher [Clare *et al*, 1987; Clare and Kennison, 1989], and Vax/vms v5.2 or higher.

UOCPROC command tables while users may define personal commands in their own copy of the *user command tables*. The UOCPROC command interpreter reads commands from the command line or from a specified command file and searches both the UOCPROC and *user* command tables for a match. Once the command syntax has been verified, the command is dispatched and the appropriate procedure is called. Control is returned to the main loop of the command interpreter upon normal completion of the called procedure or in the event of an error condition. Control of buffer allocation and error handling is performed by the *core* UOCPROC routines, which are coded to conform to the VAX procedure calling standard.

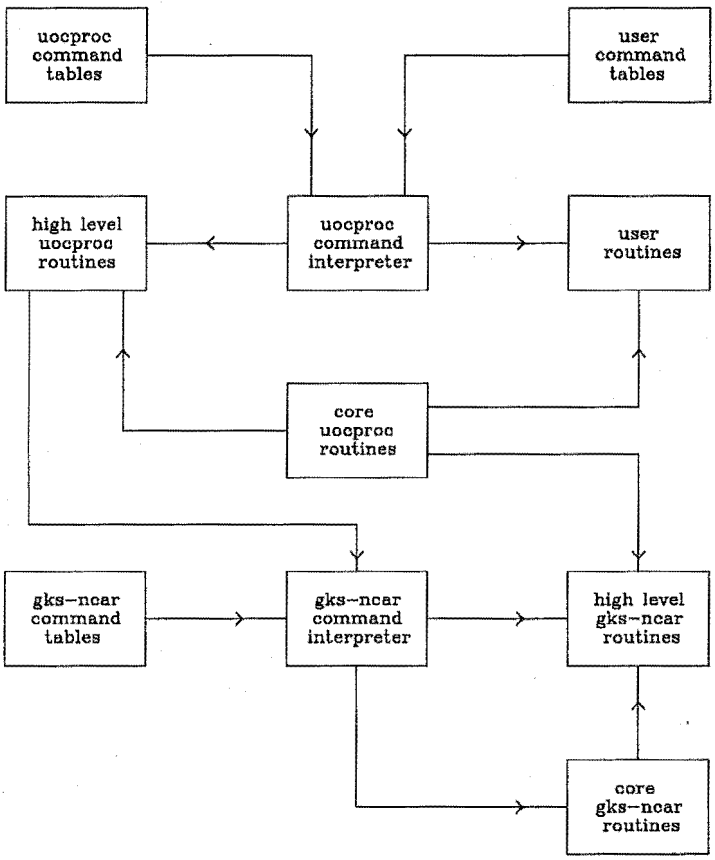

Figure E.1: Structure of the UOCPROC software package. The calculations described in §4 were implemented via the *user command interface*. All but five of the graphs and figures presented in this thesis were generated using the UOCPROC package.

Commands associated with the graphical display of data are defined in the *gks–ncar* command tables and are processed by the *gks–ncar* command interpreter. Graphing commands are provided for the construction of a variety of plot types, ranging from simple

two dimensional graphs through to complicated contour plots and three dimensional surface plots of regularly and irregularly spaced data. Commands are provided for histogram plotting and for the display of complicated two dimensional vector fields. The graphical interface also includes a crude picture drawing facility which may be used to construct simple diagrams consisting of lines, boxes, circles, ellipses, Bezier curves and text. A wide range of output devices are supported by the graphics software (including PostScript and X Windows) and support for new device drivers may be readily incorporated.

The UOCPROC graphical interface was used to produce all but five of the graphs and figures presented in this thesis while the computational procedures described in §4.2 to §4.4, and the Wiener filtering algorithm employed for the deconvolution of unchopped time–of–flight waveforms (§3.4) were implemented as personal UOCPROC commands defined in the *user command tables*.

E.2 Software package user command summary

The purpose of this section is to provide a brief description for several of the more important personal UOCPROC commands that are of relevance to the results presented in this thesis. In particular, the commands used for the solution of the thermal conduction model (§4.2 and §4.3), the Monte Carlo simulation of rotational relaxation in small molecules (§4.4), and the deconvolution of unchopped time–of–flight waveforms (§3.4) are discussed. The description of each command is broken down into several parts, including a general description of the command and a description of any command parameters and optional command qualifiers. Examples illustrating the use of each command are presented and discussed.

In addition to the computational procedures described in §4, many other procedures were developed and incorporated into the UOCPROC environment. These procedures included simple algorithms for the sorting and smoothing of data through to sophisticated procedures for the investigation of elastic scattering in crossed molecular beams and the calculation of rotational–translational energy transfer is atom–diatom collisions. The commands associated with these procedures are not described here as they are of little or no relevance to the results presented in this thesis, and many of the more complicated procedures require further work before they will be of any practical use. Programs used by Dr Harland for the theoretical calculation of ion mobilities and the fitting of experimental mobility data [Simpson, 1988] were also incorporated into the UOCPROC environment to provide a consistent, user–friendly interface.[2] A brief description of all personal UOCPROC commands may be obtained using the on-line help facility provided by the software package.

E.2.1 Tcm

The *tcm* command may be used to calculate the on–axis properties of an expanding jet according to the thermal conduction model. Mean collision frequency, flow velocity, number density, mean free path and translational temperatures are calculated as a function of distance from the nozzle exit. For diatomic and polyatomic species, the variation of rotational temperature with axial distance is calculated also [Cameron and Harland, 1991].

[2]The procedure developed by Simpson for the fitting of experimental mobility data [Simpson, 1988] was automated by the inclusion of a Monte Carlo multi–variable fitting algorithm.

Format

tcm $m\ T_0\ P_0\ \gamma\ \Upsilon\ \kappa\ \xi\ \mathcal{R}$

Parameters

m Specifies the mass of the expanding gas in units of g mol^{-1}.

T_0 Specifies the source temperature in degrees Kelvin.

P_0 Specifies the source pressure in pascals.

γ Specifies the heat capacity ratio C_p/C_v for the expanding gas.

Υ Specifies the C_6 potential parameter for the expanding gas in units of $m^2\ K^{-2/3}$.

κ Specifies the nozzle peaking factor for the expanding gas.

ξ Specifies the rotational–translational coupling parameter for the gas. This parameter will be zero for monatomic species.

$\mathcal{R}$ Specifies the number of rotational degrees of freedom possessed by the expanding gas. This parameter will be zero for monatomic species.

Command qualifiers

/output=file–name The */output* qualifier may be used to specify the name of an output file into which the results of the calculation are to be written. If no file name is specified then results will be written to *sys$output*.

/potential=file–name The */potential* qualifier may be used to specify the name of the file containing the tabulated interaction potential to be used in the calculation. If no file name is specified then the program will search the current directory for a file called *potential.dat*.

/range=real–value The */range* qualifier may be used to specify the maximum distance from the nozzle exit for which data is to be calculated. The distance is specified in metres. The default value for the maximum distance is 5×10^{-2} m.

/radius=real–value The */radius* qualifier may be used to specify the radius of the nozzle exit to be used in the calculation. The nozzle radius is specified in metres. The default value for the nozzle radius is 35 μm.

/step=real–value The */step* qualifier may be used to specify the integration step size to be used by the computational procedure for the solution of the differential equations employed by the thermal conduction model to describe the supersonic expansion process. The integration step size must be specified as a *reduced distance* (see [Cameron and Harland, 1991]). The default value for the integration step size is 1×10^{-6}.

/points=integer–value The */points* qualifier may be used to specify the number of equally spaced points along the expansion axis at which expansion properties are to be calculated and written to the output file. The distance between these points is equal to the maximum distance specified for the calculation divided by the specified number of points. The default number of points is 1024.

/hack=file-name The */hack* qualifier may be used to specify the name of an output file into which rotational relaxation data is to be written [Cameron and Harland, 1993d]. The */hack* qualifier is only applicable to calculations involving diatomic and polyatomic species. If no output file is specified then a file called *hack.dat* will be created. The */hack* qualifier cannot be used in conjunction with the */brief* qualifier and will be ignored if specified for a calculation involving a monatomic species.

/brief The */brief* qualifier may be used to instruct the computational procedure not to calculate any collisional properties. Only the temperature components and the flow velocity will be calculated. The */brief* qualifier cannot be used in conjunction with the */hack* qualifier.

/blarg The */blarg* qualifier may be used to calculate rotational relaxation data from an existing *tcm* output file. The */blarg* qualifier instructs the computational procedure to skip the solution of the thermal conduction model equations and move directly to the *hack* phase of the calculation. This qualifier is useful in situations where the */hack* qualifier was accidentally not specified for the initial calculation.

Examples

The following example illustrates the use of the *tcm* command with the */brief* qualifier. Temperature and flow velocity data are written to the file *argon.dat*. Default values are assumed for the radius of the nozzle exit, the range of the calculation, the integration step size, and the number of points along the expansion axis for which data is to be written to the output file.

```
tcm/pot=argon.pot/out=argon.dat/brief 40 300 101300 1.67 56290.2 1.98 0.0 0
```

The next example illustrates the use of the */hack* qualifier to obtain rotational relaxation data. Temperature and collisional data are calculated using default values for the radius of the nozzle exit, the range of the calculation, the integration step size, and the number of points along the expansion axis for which data is to be written to the output file. Rotational relaxation data is written to the file *relax.dat*. Temperatures and collisional data are calculated using the tabulated interaction potential file *n2.pot* and results are written to the output file *n2.dat*.

```
tcm/pot=n2.pot/hack=relax.dat/out=n2.dat 28 300 101300 1.4 71845.0 1.38 0.35 2
```

E.2.2 Properties

The *properties* command may be used to calculate the properties of a gas at a specified temperature and pressure. The number density, mean free path, mean speed, mean collision cross section and mean collision frequency are determined. For diatomic and polyatomic gases, the rotational relaxation time may be optionally evaluated.

Format

properties $T_\perp$ $T_\parallel$ m P_0

Parameters

$T_\perp$ Specifies the perpendicular translational temperature for the gas in degrees Kelvin.

$T_\parallel$ Specifies the parallel translational temperature for the gas in degrees Kelvin.

m Specifies the mass of the gas in units of g mol^{-1}.

P_0 Specifies the gas pressure in pascals.

Command qualifiers

/output=file-name The */output* qualifier may be used to specify the name of an output file into which the results of the calculation are to be written. If no file name is specified then results will be written to *sys$output*. If the specified output file already exists then data will be appended to the end of the file.

/potential=file-name The */potential* qualifier may be used to specify the name of the file containing the tabulated interaction potential to be used in the calculation. If no file name is specified then the program will search the current directory for a file called *potential.dat*.

/samples=integer-value The */samples* qualifier may be used to specify the number of randomly selected velocities to be used for the estimation of the mean collision quantities. The default number of velocities sampled is 1024. This default value is possibly somewhat low and may not produce particularly accurate results.

/delete The */delete* qualifier may be used to instruct the computational procedure to delete the scratch file *aco.opf* upon successful completion of the *properties* calculation. The *aco.opf* file contains information regarding the calculation of collision cross section interpolation parameters and may be quite large, depending on the quality of the tabulated interaction potential data. Use of the */delete* qualifier is strongly recommended in situations where large numbers of *properties* calculations are performed consecutively.

/list The */list* qualifier may be used in conjunction with the */relax* qualifier to obtain a listing of rotational and translational temperatures as a function of time during the Monte Carlo calculation of rotational relaxation times (see [Cameron and Harland, 1993a]). One hundred points of data are written to *sys$output* in four columns. The first column indicates the time elapsed since the start of the simulation while the second, third and fourth columns indicate the translational, rotational and overall temperatures, respectively.

/statistics The */statistics* qualifier may be used to obtain timing information for the various phases of the *properties* calculation. The first phase of the calculation involves the determination of collision cross section interpolation data. Following the calculation of this data, the number density, mean collision cross section, mean speed, mean collision frequency and mean free path are determined. The third phase of the calculation involves the evaluation of rotational relaxation data, and will only be performed if the */relax* qualifier was specified. Timing information is written to *sys$output*.

/relax=(Δt,$\mathcal{R}$,a,$T_{r,0}$) The */relax* qualifier may be used to specify information required for the calculation of rotational relaxation data. Information is specified as a list of four values, which are defined as follows:

Δt_m Specifies the time interval at which rotational and translational temperatures are to be sampled. The sampling interval must be expressed as a multiple of the mean collision time [Cameron and Harland, 1993a]. A value of 1×10^{-1} mean collision times is generally adequate.

$\mathcal{R}$ Specifies the number of rotational degrees of freedom possessed by the molecule for which the relaxation data is to be calculated.

a Specifies the collision cross section scaling parameter in units of m^{-2} [Cameron and Harland, 1993a].

$T_{r,0}$ Specifies the initial rotational temperature of the system in degrees Kelvin.

Examples

The following example illustrates a UOCPROC command procedure for the calculation of collisional and rotational relaxation data for CH_4 from 1 K to 300 K. Data are calculated using the tabulated interaction potential file *ch4.pot* and written to the output file *ch4.dat*. The integer variable *count* is used to specify the translational temperature while the real variable *factor* is used to define the value of the collision cross section scaling parameter for the system. A large number of velocities are sampled to ensure accurate results and the */delete* qualifier is used to conserve disk space.

```
declare/scalar count 1
!
!
let factor := 1.05e+17
!
for count 1 to 300 do
   properties/del/pot=ch4.pot/samples=16384/out=ch4.dat/rel=(0.1,3,factor,0.0) -
   count -
   count 16 101300
end for
!
!
exit
```

The next example illustrates the use of the */statistics* qualifier to obtain timing information for each phase of a *properties* calculation. Collisional and rotational relaxation data are calculated for N_2 at 300 K for a pressure of 1 atm. The real variable *factor* is used to define the value of the collision cross section scaling parameter for the system and a large number of velocities are sampled to ensure accurate estimates for the mean collision quantities. No output file is specified for the calculation, causing collisional data to be written to *sys$output*.

```
set verify
!
set trace
!
!
let factor := 7.41e+17
!
properties/del/statistics/pot=n2.pot/samples=16384/rel=(0.1,2,factor,0.0) -
300 -
300 28 101300
!
!
exit
```

The output produced by the above command is listed below. From the timing information it can be seen that the calculation of the mean collision quantities (phase 2) required the most computational effort. The time required for the completion of phase 2 is directly

proportional to the number of velocities used to estimate the mean collision quantities while the times required for the completion of phases 1 and 3 may be influenced by many factors, including the quality of the tabulated interaction potential data and the efficiency of rotational relaxation for the system being investigated [Cameron and Harland, 1993a].

```
Timing information:
~~~~~~~~~~~~~~~~~~~
Phase 1 took:  6.51000E+01 ms
Phase 2 took:  1.96400E+02 ms
Phase 3 took:  1.50400E+02 ms


Number density              :  2.44569E+25
Mean collision cross-section:  5.26579E-19
Twice mean speed            :  1.34510E+03
Collision frequency         :  7.58796E+09
Mean free path              :  7.76490E-08
Rotational relaxation time  :  4.61252E-10  ( 9.99938E-01, 61151 )
```

Dimensions of the number density, mean collision cross section, mean speed, collision frequency, mean free path and rotational relaxation time listed above are m^{-3}, m^2, m s^{-1}, s^{-1}, m and s, respectively. The two values enclosed in parentheses following the rotational relaxation time indicate the linear least squares correlation coefficient for the calculation and the total number of collisions examined.

E.2.3 Wiener

The *wiener* command may be used to construct a Weiner filter for a specified response function. The resultant filter may then be used to deconvolve the effects of the response function from convolved experimental data [Cameron and Harland, 1993b].

Format

wiener *input–buffer output–buffer* ϕ

Parameters

input–buffer Specifies the name of the complex buffer containing the Fourier transform of the response function.

output–buffer Specifies the name of the output buffer which is to contain the Weiner filter. If the buffer does not already exist then it will be automatically created.

ϕ Specifies the noise–to–signal ratio to be used for the construction of the Weiner filter.

Example

The following example illustrates a UOCPROC command procedure for the the deconvolution of experimental time–of–flight data using the Wiener filtering technique described by Cameron and Harland [Cameron and Harland, 1993b]. The theoretical and experimental data sets (*theo.uoc* and *expt.uoc*) are loaded into the real buffers *ifx* and *igx* which are then combined into the complex buffers f and g, respectively. The Fourier transforms of f and g are evaluated and g is low–pass filtered to remove any noise using a simple filtering function with a cut-off frequency determined by the value of the variable *fc*. A Wiener filter is constructed from f and used to estimate the system response function h. The estimated response function is then used to deconvolve g.

```
set verify
!
!
! Define a few variables
!
let wphi := 1.0e-09
!
let fs := 2.0e+04 ! sampling frequency (Hz)
let fc := 1.0e+03 ! low-pass filter cut-off frequency (Hz)
!
!
let xfrac := fs / 2 / fc
!
!
! Read in the theoretical and experimental data sets
!
read theo.uoc ifx ! theoretical distribution
read expt.uoc igx ! convoluted experimental data
!
declare/scalar/integer xsize 1024 ! input buffer size
!
declare/real fx xsize 1 1
declare/real fy xsize 1 1
declare/real gx xsize 1 1
declare/real gy xsize 1 1
!
add fx ifx fx
add gx igx gx
!
!
! Construct complex buffers for the two data sets
!
combine/rectangular fx fy f
combine/rectangular gx gy g
!
!
! Transform the data into the Fourier domain
!
fft f
fft g
!
!
! Extract the real (modulus) and imaginary (phase) components of the
! transformed data
!
extract f fm fp
extract g gm gp
!
!
! Write out the real components of the transformed data
!
write fm fm
write gm gm
!
!
```

```
! Construct a simple low-pass filter consisting of a single cosine lobe
!
declare/real lm xsize 1 1
declare/real lp xsize 1 1
!
evaluate/symmetric lm rect(x * xfrac / xsize) * cos(pi * x * xfrac / xsize)
!
combine lm lp l
!
!
! Use the low-pass filter to remove any high frequency components from
! the experimental data set
!
multiply g l g
!
!
! Construct a Wiener filter from the theoretical data set using a small
! fraction of the maximum amplitude for phi
!
statistics/max=fmax fm
!
let phi := fmax * wphi
!
wiener f h phi
!
!
! Determine an estimate for the system response function by deconvolving
! the theoretical distribution from the experimental data
!
multiply g h h
!
!
! Extract the real component of the estimated response function (in the
! frequency domain) and write it to disk
!
extract/rectangular h hx hy
!
write hx hx
!
!
! Test the estimated response function by using it to deconvolve the
! experimental data set
!
extract h hm hp
!
statistics/max=hmax hm
!
let phi := hmax * wphi
!
wiener h w phi
!
multiply g w w ! the actual deconvolution
!
!
! Transform the deconvolved data back into the time domain and write the
```

```
! real component to disk
!
ifft w
!
extract/rectangular w wx wy
!
write wx wx
!
!
exit
```

References

Abramowitz, M. and Stegun, I.A. (1964), *Handbook of mathematical functions*, Vol. 55 of Applied Mathematical Series, Dover Publications.

Abuaf, N., Anderson, J.B., Andres, R.P., Fenn, J.B. and Miller, D.R. (1966), 'Studies of low density supersonic jets', *Proceedings of the 5th international symposium on rarefied gas dynamics*, Vol. 2, p. 1317.

Abuaf, N., Anderson, J.B., Andres, R.P., Fenn, J.B. and Marsden, D.G. (1967), *Science*, Vol. 155, p. 997.

Aitken, C.G., Blunt, D.A. and Harland, P.W. (1993). Unpublished results.

Alcalay, J.A. and Knuth, E.L. (1969), 'Molecular-beam time-of-flight spectroscopy', *Rev. Sci. Instrum.*, Vol. 40, No. 3, March, p. 438.

Anderson, J.B. (1974), *Molecular beams and low density gas dynamics*, Dekker, New York, Chap. 1.

Anderson, J.B. and Fenn, J.B. (1965), 'Velocity distributions in molecular beams from nozzle sources', *Phys. Fluids*, Vol. 8, No. 5, May, p. 780.

Anderson, W.H. and Hornig, D.F. (1958), Technical Report, Metcalf Research Laboratory, Brown University, May.

Anderson, J.B., Andres, R.P. and Fenn, J.B. (1966), 'Supersonic nozzle beams', *Adv. Chem. Phys.*, Vol. 10, p. 275.

Arshadi, M.R. and Futrell, J.H. (1974), 'Studies in high–pressure mass spectrometry. V. Thermodynamics of solvation reactions. NH_4^+–NH_3', *J. Phys. Chem.*, Vol. 78, No. 15, p. 1482.

Baker, C.E. and Brokaw, R.S. (1964), 'Thermal conductivities of gaseous H_2O, D_2O, and the equimolar H_2O–D_2O mixture', *J. Chem. Phys.*, Vol. 40, p. 1523.

Baker, C.E. and Brokaw, R.S. (1965), 'Thermal conductivities of ordinary and isotopically substituted polar gases and their equimolar mixtures', *J. Chem. Phys.*, Vol. 43, p. 3519.

Bartell, L.S. (1966), 'Diffraction studies of clusters generated in supersonic flow', *Chemical Reviews*, Vol. 86, No. 3, June, p. 491. and references therein.

Bauer, H.J. and Kosche, H. (1966), 'Rotational relaxation in CO compared with other diatomic gases', *Acustica*, Vol. 17, p. 96.

Becker, E.W. and Bier, K. (1954), 'Production of an intense, partially monochromatized molecular beam of hydrogen by means of a laval jet', *Z. Naturforsch*, Vol. 9, p. 975.

Becker, E.W., Bier, K. and Henkes, W. (1956), 'Strahlen aus kondensierten Atomen und Molekeln im Hochvakuum', *Z. Phys.*, Vol. 146, p. 333.

Beijerinck, H.C.W. and Verster, N.F. (1981), 'Absolute intensities and perpendicular temperatures of supersonic beams of polyatomic gases', *Physica*, Vol. 111c, p. 327.

Bird, G.A. (1963), 'Approach to translational equilibrium in a rigid sphere gas', *Phys. Fluids*, Vol. 6, p. 1518.

Bird, G.A. (1970a), 'Breakdown of translational and rotational equilibrium in gaseous expansions', *AIAA Journal*, Vol. 8, No. 11, November, p. 1998.

Bird, G.A. (1970b), *Proceedings of the 7th international symposium on rarefied gas dynamics.*

Bird, G.A. (1976a), *Molecular gas dynamics*, Oxford engineering science series, Clarendon press, Oxford.

Bird, G.A. (1976b), 'Transition regime behaviour of supersonic beam skimmers', *Phys. Fluids*, Vol. 19, No. 10, October, p. 1486.

Blank, L. (1982), *Statistical procedures for engineering, managment, and science*, McGraw Hill, Tokyo, 1 ed.

Boas, M.L. (1983), *Mathematical methods in the physical sciences*, Wiley, New York, 2 ed.

Bohme, D.K., Hemsworth, R.S. and Rundle, H.W. (1973), 'Chemical equilibrium of $NH_2^- + H_2 \rightleftharpoons H^- + NH_3$ and the determination of $D_0^o(NH_2\text{–}H)$', *J. Chem. Phys.*, Vol. 59, p. 77.

Borgnakke, C. and Larsen, P.S. (1975), 'Statistical collision model for Monte Carlo simulation of a polyatomic gas mixture', *J. Comp. Phys.*, Vol. 18, p. 405.

Boyd, I.D. and Stark, J.P.W. (1987), 'A comparison of the implementation and performance of the Nanbu and Bird direct simulation Monte Carlo methods', *Phys. Fluids*, Vol. 30, No. 12, December, p. 3661.

Bracewell, R.N. (1986), *The Fourier transform and its applications*, McGraw–Hill, Sinapore, 2 ed.

Buck, U. and Meyer, H. (1984), 'Scattering analysis of cluster beams: Formation and fragmentation of small Ar_n clusters', *Phys. Rev. Letters*, Vol. 52, No. 2, January, p. 109.

Cameron, B.R. (1990), August. Departmental seminar, Chemistry Department, University of Canterbury.

Cameron, B.R. and Harland, P.W. (1991), 'Flow dynamics of supersonic molecular beams and the measurement of rotational-translational coupling parameters for N_2 and H_2', *J. Chem. Soc. Faraday Trans.*, Vol. 87, No. 8, April, p. 1069.

Cameron, B.R. and Harland, P.W. (1993a), 'Monte carlo calculation of rotational relaxation in small molecules', *J. Chem. Soc. Faraday Trans.* In press.

Cameron, B.R. and Harland, P.W. (1993b), 'Deconvolution of unchopped time–of–flight waveforms', *Rev. Sci. Instrum.* In press.

Cameron, B.R. and Harland, P.W. (1993c). Unpublished results.

Cameron, B.R. and Harland, P.W. (1993d), 'Application of the thermal conduction model to rotational relaxation in molecular beams', *J. Chem. Soc. Faraday Trans.*, Vol. 89, No. 12, June, p. 1903.

Cameron, B.R., Aitkin, C.G. and Harland, P.W. (1993), 'Appearance potentials of small cluster ions and their fragments', *J. Chem. Soc. Faraday Trans.* Submitted for publication.

Campargue, R. (1984), 'Progress in overexpanded supersonic jets and skimmed molecular beams in free-jet zones of silence', *J. Phys. Chem.*, Vol. 88, p. 4466.

Campbell, E.E.B. and Tittes, A. (1990), 'Observation of highly excited electronic states of $(CO_2)_m$ clusters', *Chem. Phys. Letters*, Vol. 165, No. 4, January, p. 289.

Carman Jr., H.S. (1986), *Molecular beam reactions of oriented molecules*, Ph.D. thesis, Rice University, Texas, U.S.A., April.

Carman Jr., H.S., Harland, P.W. and Brooks, P.R. (1986), 'Reaction of K atoms with oriented CF_3Br', *J. Phys. Chem.*, Vol. 90, p. 944. and references therein.

Carnevale, E.H., Carey, C. and Larson, G. (1967), 'Ultrasonic determination of rotational collision numbers and vibrational relaxation times of polyatomic gases at high temperatures', *J. Chem. Phys.*, Vol. 47, p. 2829.

Ceyer, S.T., Tiedemann, P.W., Mahan, B.H. and Lee, Y.T. (1979), 'Energetics of gas phase proton solvation by NH_3', *J. Chem. Phys.*, Vol. 70, No. 1, January, p. 14.

Chatwani, A. and Fieberg, M. (1981), 'Source expansion of monatomic gas mixtures', *Proceedings of the 14th international symposium on rarefied gas dynamics*, Vol. 2, p. 785.

Clare, F. and Kennison, D. (1989), NCAR *graphics guide to new utilities*, National Center for Atmospheric Research, Scientific Computing Division, P.O. Box 3000, Boulder, CO 80307–3000.

Clare, F., Kennison, D. and Lackman, B. (1987), NCAR *graphics user's guide*, National Center for Atmospheric Research, Scientific Computing Division, P.O. Box 3000, Boulder, CO 80307–3000.

Conte, S.D. and de Boor, C. (1980), *Elementary numerical analysis*, McGraw Hill, Tokyo, 3 ed.

Coolbaugh, M.T., Peifer, W.R. and Garvey, J.F. (1989), 'Ion-molecule chemistry within doubly charged ammonia clusters', *Chem. Phys. Letters*, Vol. 156, No. 1, March, p. 19.

Cooley, J.W. and Tukey, J.W. (1965), 'An algorithm for the machine calculation of complex Fourier series', *Math. Comput.*, Vol. 19, April, p. 297.

Cooper, A.L. and Bienkowski, G.K. (1966), 'An asymptotic theory for steady source expansion of a binary gas mixture', *Proceedings of the 5th international symposium on rarefied gas dynamics*, Vol. 1, p. 861.

Dawson, P.H. (1976), *Quadrupole mass spectrometry and its applications*, Elsevier, Amsterdam.

Dibeler, V.H. and Reese, R.M. (1966), 'Mass spectrometric study of the photoionization of small molecules', *Advan. Mass Spectrometry*, Vol. 3, p. 471.

Dieter, U. and Ahrens, J.H. (1973), *Computing*, Vol. 11, p. 137.

Douglas, J.F., Gasiorek, J.M. and Swaffield, J.A. (1984), *Fluid mechanics*, Pitman publishing limited.

Dreyfuss, D. and Wachman, H.Y. (1982), 'Measurments of relative concentrations and velocities of small clusters (n≤40) in expanding water vapour flows', *J. Chem. Phys.*, Vol. 76, No. 4, February, p. 2031.

Duquette, G., Ellis, T., Scoles, G., Watts, R.O. and Klein, M.L. (1978), 'An intermolecular potential for $(NH_3)_2$', *J. Chem. Phys.*, Vol. 68, p. 2544.

Engelhardt, R., Lorenz, T., Bergmann, K., Mietzner, T. and Palczewski, A. (1985), 'Shape analysis of the velocity distribution in supersonic Ar beams: comparison between experiment and theory', *Chem. Phys.*, Vol. 95, p. 417.

Flaim, T.A. and Ownby, P.D. (1971), 'Bayard–Alpert ion gauge sensitivities to various gases', *J. Vac. Sci. Technol.*, Vol. 8, p. 661.

Gallagher, R.J. and Fenn, J.B. (1974), 'Rotational relaxation of molecular hydrogen', *J. Chem. Phys.*, Vol. 60, No. 9, May, p. 3492.

Gentry, W.R. and Giese, C.F. (1975), 'High-precision skimmers for supersonic molecular beams', *Rev. Sci. Instrum.*, Vol. 46, No. 1, January, p. 104.

Gentry, W.R. and Giese, C.F. (1977), 'Resolved single-quantum rotational excitation in HD + He collisions: First results from a unique pulsed molecular beam apparatus', *J. Chem. Phys.*, Vol. 67, p. 5389.

Goodliffe, A.L., Jenkens, H.D.B., Martin, S.V. and Waddington, T.C. (1971), 'The proton affinity of gaseous ammonia, the charge distribution on the NH_4^+ ion and the lattice energies of NH_4Cl, NH_4Br and NH_4I', *Mol. Phys.*, Vol. 21, p. 761.

Greenspan, M. (1959), 'Rotational relaxation in nitrogen, oxygen, and air', *J. Acoust. Soc. Am.*, Vol. 31, p. 155.

Haberland, H., Tully, F.P. and Lee, Y.T. (1972), *Proceedings of the 8th international symposium on rarefied gas dynamics.*

Haberland, H., Buck, U. and Tolle, M. (1985), 'Velocity distributions of supersonic nozzle beams', *Rev. Sci. Instrum.*, Vol. 56, No. 9, September, p. 1712.

Habets, A.H.M. (1977), Ph.D. thesis, Eindhoven University of Technology, Eindhoven.

Hagena, O.F. (1964), *Z. Angew. Phys.*, Vol. 17, p. 542.

Hagena, O.F. (1981), 'Nucleation and growth of clusters in expanding nozzle flows', *Surface Sci.*, Vol. 106, p. 101.

Hamel, B.B. and Willis, D.R. (1966), 'Kinetic theory of source flow expansion with application to the free jet', *Phys. Fluids*, Vol. 9, No. 5, May, p. 829.

Hammersley, J.M. and Handscomb, D.C. (1964), *Monte Carlo methods*, Wiley, New York.

Hammersley, J.M. and Morton, K.W. (1956), 'A new Monte Carlo technique: antithetic variates', *Proc. Camb. Phil. Soc*, Vol. 52, p. 449.

Harland, P.W. and McIntosh, B.J. (1985), 'Enthalpies of formation for the isomeric ions H_xCCN^+ and H_xCNC^+ ($x = 0 - 3$) by "monochromatic" electron impact on C_2N_2, CH_3CN and CH_3NC', *Int. J. Mass Spectrom. and Ion. Phys.*, Vol. 67, p. 29.

Harland, P.W., MacNeil, K.A.G. and Thynne, J.C.J. (1970), *Dynamic mass spectrometry*, Hayden and Sons, London. Chapt. 8.

Harland, P.W., Carman Jr., H.S., Phillips, L.F. and Brooks, P.R. (1990), 'Electron transfer to oriented molecules: K + CF_3I and K + CH_3I', *J. Chem. Phys.*, Vol. 93, p. 1089.

Harland, P.W., Carman Jr., H.S., Phillips, L.F. and Brooks, P.R. (1991), 'Effects of molecular orientation on electron–transfer collisions', *J. Phys. Chem.*, Vol. 95, p. 8137. and references therein.

Hayes, J.M. (1987), 'Analytical spectroscopy in supersonic expansions', *Chem. Rev.*, Vol. 87, p. 745.

Hill, G.L. and Winter, T.G. (1968), 'Effect of temperature on the rotational and vibrational relaxation times of some hydrocarbons', *J. Chem. Phys.*, Vol. 49, p. 440.

Hippler, H., Schranz, H.W. and Troe, J. (1986), 'Trajectory calculations of intermolecular energy transfer in SO_2–Ar collisions. 1. Method and representative results', *J. Phys. Chem.*, Vol. 90, No. 23, p. 6158.

Hiraoka, K. and Mori, T. (1989), 'Formation and stabilities of cluster ions Ar_n^+', *J. Chem. Phys.*, Vol. 90, No. 12, June, p. 7143. and references therein.

Hiraoka, K., Nakajima, G. and Shoda, S. (1988), 'Determination of the stabilities of $CO_2^+ \cdot (CO_2)_n$ clusters with n = 1–6', *Chem. Phys. Letters*, Vol. 146, No. 6, May, p. 535.

Hirschfelder, J.O., Curtiss, C.F. and Bird, R.B. (1954), *Molecular theory of gases and liquids*, John Wiley and Sons Inc.

Houle, F.A. and Beauchamp, J.L. (1979), 'Photoelectron spectroscopy of methyl, ethyl, isopropyl, and t-butyl radicals. Implications for the structures of the radicals and their corresponding carbonium ions', *J. Am. Chem. Soc.*, Vol. 101, p. 4067.

Huber-Wälchi, P. and Nibler, J.W. (1982), 'CARS spectroscopy of molecules in supersonic free jets', *J. Chem. Phys.*, Vol. 76, No. 1, January, p. 273.

Illies, A.J. (1988), 'Thermochemistry for the gas phase ion–molecule clustering of $CO_2^+CO_2$, $SO_2^+CO_2$, $N_2O^+N_2O$, $O_2^+CO_2$, NO^+CO_2, $O_2^+N_2O$, NO^+N_2O, and NO^+N_2O: Description of a new hybrid drift tube/ion source with coaxial electron beam and ion exit apertures', *J. Phys. Chem.*, Vol. 92, No. 10, p. 2889.

Illies, A.J., McKee, M.L. and Schlegal, H.B. (1987), 'Ab initio study of the CO_2 dimer and the CO_2 ion complexes $(CO_2)_2^+$ and $(CO_2)_3^+$', *J. Chem. Phys.*, Vol. 91, No. 13, p. 3489.

John, J.E.A. (1969), *Gas dynamics*, Allyn and Bacon, Boston.

Johnston, H.L. and McCloskey, K.E. (1940), 'Viscosities of several common gases between 90 K and room temperature', *J. Phys. Chem*, Vol. 44, p. 1038.

Jones, G.G. and Taylor, J.W. (1978), 'A photoionization study of carbon dioxide dimers in a supersonic molecular beam', *J. Chem. Phys.*, Vol. 68, No. 4, February, p. 1768.

Jones, D.G., Lambert, J.D., Suksena, M.P. and Stretton, J.L. (1969), 'Rotational and vibrational relaxation in gaseous ammonia', *Trans. Faraday Soc.*, Vol. 65, p. 965.

Kamke, B., Kamke, W., Herrmann, R. and Hertel, I.V. (1989), 'Exciton absorption and intramolecular Penning ionization of small molecular clusters 1: $(N_2O)_n$ and $C_6H_5CN \cdot (N_2O)_n$', *Z. Phys. D. – Atoms, Molecules and Clusters*, Vol. 11, p. 153.

Kantrowitz, A. and Grey, J. (1951), 'A high intensity source for the molecular beam. Part 1. Theoretical', *Rev. Sci. Instrum.*, Vol. 22, No. 5, May, p. 328.

Kasper, S.F. and Franklin, J.L. (1972), 'Ion–molecule reactions in the system CO_2–CH_4', *J. Chem. Phys.*, Vol. 56, p. 1156.

Kay, B.D., Raymond, T. and Rice, J. (1986), 'Time–of–flight characterisation of pulsed supersonic helium free–jet expansions', *Rev. Sci. Instrum.*, Vol. 57, No. 9, September, p. 2266.

Keesee, R.G. and Castleman, A.W. (1986), 'Thermochemical data on gas–phase ion–molecule and clustering reactions', *J. Phys. Chem. Ref. Data*, Vol. 15, p. 1011.

Kelly, B.T. (1957), 'Ultrasonic velocity, absorption, and rotational dispersion in methane', *J. Acoust. Soc. Am.*, Vol. 29, p. 1005.

Kennard, E.H. (1958), *Kinetic theory of gases*, McGraw–Hill, New York.

Kern, D.R., David, R. and Cosma, G. (1985), 'Low–energy helium nozzle beam', *Rev. Sci. Instrum.*, Vol. 56, p. 369.

Kiode, A. and Kihara, T. (1974), 'Intermolecular forces for D_2, N_2, O_2, F_2 and CO_2', *Chem. Phys.*, Vol. 5, p. 34.

Kiser, R.W. (1965), *Introduction to mass spectrometry and its applications*, Prentice–Hall, Englewood Cliffs, New Jersey.

Klots, C.E. (1980), 'Rotational relaxation in sonic nozzle expansions', *J. Chem. Phys.*, Vol. 72, No. 1, p. 192.

Klots, C.E. and Compton, R.N. (1978), 'Electron attachment to van der Waals polymers of carbon dioxide and nitrous oxide', *J. Chem. Phys.*, Vol. 69, No. 4, August, p. 1636.

Kukolich, S.G., Oates, D.E. and Wang, J.H.S. (1974), 'Rotational energy distribution in a nozzle beam', *J. Chem. Phys.*, Vol. 61, p. 4686.

Lee, Y.T., McDonald, J.D., LeBreton, P.R. and Hershbach, D.R. (1969), 'Molecular beam reactive scattering apparatus with electron bombardment detector', *Rev. Sci. Instrum.*, Vol. 40, p. 1402.

Levine, R.D. and Bernstein, R.B. (1974), *Molecular reaction dynamics*, Oxford.

Levy, D.H. (1981), 'Van der Waals molecules', *Adv. Chem. Phys.*, Vol. 47, No. 323.

Lias, S.G., Shold, D.M. and Ausloos, P. (1980), 'Proton–transfer reactions involving alkyl ions and alkenes. Rate constants, isomerization processes, and the derivation of thermochemical data', *J. Am. Chem. Soc.*, Vol. 102, p. 2540.

Lifshitz, C. and Louage, F. (1989), 'Magic numbers in kinetic energy releases for unimolecular decompositions of $(NH_3)_nH^+$ ion clusters', *J. Phys. Chem.*, Vol. 93, No. 15, July, p. 5633.

Linn, S.H. and Ng, C.Y. (1981), 'Photoionization study of CO_2, N_2O dimers and clusters', *J. Chem. Phys.*, Vol. 75, No. 10, November, p. 4921.

Liverman, M.G., Beck, S.M., Monts, D.L. and Smalley, R.E. (1979), 'Fluorescence excitation spectrum of the ^1A_u $(n\pi^*) \leftarrow^1 A_g$ $(0-0)$ band of oxalyl fluoride in a pulsed supersonic free jet', *J. Chem. Phys.*, Vol. 70, No. 1, January, p. 192. and references therein.

Lubman, D.M., Rettner, C.T. and Zare, R.N. (1982), 'How isolated are molecules in a molecular beam?', *J. Phys. Chem.*, Vol. 86, No. 7, p. 1129.

Maier, M., Luftman, H.S. and Winn, J.S. (1984), 'Translational and rotational cooling in supersonic beams of OCS seeded in Ar', *J. Phys. Chem.*, Vol. 88, p. 5167.

Malinauskas, A.P., Gooch Jr., J.W., Annis, B.K. and Fuson, R.E. (1970), 'Rotational collision numbers of N_2, O_2, CO, and CO_2 from thermal transpiration measurements', *J. Chem. Phys.*, Vol. 53, p. 1317.

Marrone, P.V. (1967), 'Temperature and density measurements in free jets and shock waves', *Phys. Fluids*, Vol. 10, No. 3, March, p. 521.

Mason, E.A. and Monchick, L. (1962), 'Heat conductivity of polyatomic and polar gases', *J. Chem. Phys.*, Vol. 36, No. 3, March, p. 1622.

Mautner, M. and Field, F.H. (1977), 'Proton affinities and cluster ion stabilities in CO_2 and CS_2. Application in Martian ionispheric chemistry', *J. Chem. Phys.*, Vol. 66, No. 10, May, p. 4527.

McDowell, C.A. (1963), 'The ionization and dissociation of molecules', in McDowell, C.A. (Ed.), *Mass spectrometry*, McGraw-Hill, New York, Chap. 12.

McGinty, D.J. (1970), 'Vapour phase homogeneous nucleation and the thermodynamic properties of small clusters of argon atoms', *J. Chem. Phys.*, Vol. 55, No. 2, July, p. 580.

McKee, M.L. (1990), 'A theoretical study of $(N_2O)_2^+$, $(CO_2)_2^+$ and $N_2O^+CO_2$. Comparison of the two–center–three–electron bond and the ion–dipole complex', *Chem. Phys. Letters*, Vol. 165, No. 2, January, p. 265.

Miller, D.R. and Andres, R.P. (1967), 'Rotational relaxation of molecular hydrogen', *J. Chem. Phys.*, Vol. 46, No. 9, May, p. 3418.

Miller, D.R. and Andres, R.P. (1968), *Proceedings of the 6th international symposium on rarefied gas dynamics*, Vol. 2, p. 1385.

Milne, T.A., Beachey, J. and Greene, F. (1972), 'Possible errors in vapour composition determinations due to dimer formation in noneffusive expansions', *J. Chem. Phys.*, Vol. 57, p. 2221.

Morrison, J.D. (1963), 'On the optimum use of ionization efficiency data', *J. Chem. Phys.*, Vol. 39, p. 200.

Murphy, H.R. and Miller, D.R. (1984), 'Effects of nozzle geometry on kinetics in free jet expansions', *J. Phys. Chem.*, Vol. 88, p. 4474.

Nanbu, K. (1980), 'Direct simulation scheme derived from the Boltzmann equation. I. Monocomponent gases', *J. Phys. Soc. Jpn.*, Vol. 49, p. 2042.

Nanbu, K. (1983), 'Interrelations between various direct simulation methods for solving the Boltzmann equation', *J. Phys. Soc. Jpn.*, Vol. 52, p. 3382.

von Neuman, J. and Ulam, S. (1949), 'The monte carlo method', *J. Am. Stat. Assoc.*, Vol. 44, No. 247, p. 351.

Ng, C.Y. (1983), 'Molecular beam photoionization studies of molecules and clusters', *Adv. Chem. Phys.*, Vol. 52, p. 263.

Ng, C.Y., Trevor, D.J., Tiedemann, P.W., Ceyer, S.T., Kronebusch, P.L., Mahan, B.H. and Lee, Y.T. (1977), 'Photoionization of dimeric polyatomic molecules: Proton affinities of H_2O and HF', *J. Chem. Phys.*, Vol. 67, p. 4235.

O'Hara, H. and Smith, F.J. (1970), 'The efficient calculation of the transport properties of a dilute gas to a prescribed accuracy', *J. Comp. Phys.*, Vol. 5, p. 328.

O'Hara, H. and Smith, F.J. (1971), *Phys. Comm.*, Vol. 2, p. 328.

Ono, Y., Linn, S.H., Prest, H.F., Gress, M.E. and Ng, C.Y. (1980), 'Molecular beam photoionization study of carbon disulfide, carbon disulfide dimer and clusters', *J. Chem. Phys.*, Vol. 73, p. 2523.

Parker, J.G. (1959), 'Rotational and vibrational relaxation in diatomic gases', *Phys. Fluids*, Vol. 2, No. 4, July, p. 449.

Paulson, J.F., Dale, F. and Mosher, R.F. (1964), 'Production of $C_2O_4^+$ in an ion–molecule reaction', *Nature*, Vol. 204, p. 377.

Pauly, H. and Toennies, J.P. (1968), *Methods of experimental physics*, Vol. 7A, Academic Press, New York, p. 227.

Payzant, J.D., Cunningham, A.J. and Kebarle, P. (1973), 'Gas phase solvation of the ammonium ion by NH_3 and H_2O and stabilities of mixed clusters $NH_4^+(NH_3)_n(H_2O)_w$', *Can. J. Chem.*, Vol. 51, p. 3242.

Poulsen, P. and Miller, D.R. (1977), 'The energy balance and free–jet expansions of polyatomics', in Potter, J.L. (Ed.), *Rarefied gas dynamics*, American Institute of Aeronautics and Astronautics, New York, p. 899.

Press, W.H., Flannery, B.P., Teukolsky, S.A. and Vetterling, W.T. (1986), *Numerical recipes: the art of scientific computing*, Cambridge University Press.

Rabitz, H. and Lam, S.H. (1975), 'Rotational energy relaxation in molecular hydrogen', *J. Chem. Phys.*, Vol. 63, No. 8, October, p. 3532.

Ramsey, N.F. (1956), *Molecular beams*, Oxford University Press, New York.

Randeniya, L.K. and Smith, M.A. (1990), 'A study of molecular supersonic flow using the generalized Boltzmann equation', *J. Chem. Phys.*, Vol. 93, No. 1, July, p. 661.

Randeniya, L.K., Zeng, X.K., Smith, R.S. and Smith, M.A. (1989), 'Temperature dependence of termolecular association reactions $N_2^+ + 2N_2 \longrightarrow N_4^+ + N_2$ and $O_2^+ + 2O_2 \longrightarrow O_4^+ + O_2$ occurring in free jet expansions below 20 K', *J. Phys. Chem.*, Vol. 93, No. 24, p. 8031.

Rosenstock, H.M., Draxl, K., Steiner, B.W. and Herron, J.T. (1977), *J. Phys. Chem. Ref. Data 6, Suppl. 1*, Vol. 70.

Saenger, K.L. (1981), 'Pulsed molecular beams: A lower limit on pulse duration for fully developed supersonic expansions', *J. Chem. Phys.*, Vol. 75, No. 5, September, p. 2467.

Schafer, T.P., Siska, P.E., Parson, J.M., Tully, F.P., Wong, Y.C. and Lee, Y.T. (1970), 'Crossed molecular beam study of $F + D_2$', *J. Chem. Phys.*, Vol. 53, p. 3385.

Schildcrout, S.M. and Franklin, J.L. (1969), 'High–pressure mass spectra and ion chemsitry of carbon dioxide', *J. Chem. Phys.*, Vol. 51, p. 4055.

Scoles, G. (Ed.) (1988), *Atomic and Molecular Beam Methods*, Oxford.

Searles, S.K. and Kebarle, P. (1968), 'Ion–solvent–molecule interactions in the gas phase. Enthalpies and entropies for the reactions $NH_4^+(NH_3)_{n-1} + NH_3 \rightleftharpoons NH_4^+(NH_3)_n$', *J. Phys. Chem.*, Vol. 72, p. 742.

Sessler, G. (1958), *Acustica*, Vol. 8, p. 395.

Shinohara, H., Nishi, N. and Washida, N. (1988), 'Experimental evidence of the magic number stability of the hydrated ammonia cluster ions $(H_2O)(NH_3)_{0-4}NH_4^+$', *Chem. Phys. Letters*, Vol. 153, No. 5, December, p. 417.

Simpson, R.W. (1988), *Theoretical and experimental studies of ion transport and ion–molecule reactions*, Ph.D. thesis, University of Canterbury, New Zealand.

Simpson, R.W., Maclagan, R.G.A.R. and Harland, P.W. (1987), '*Ab initio* calculation of the mobility of F^- in helium', *J. Phys. B: At. Mol. Phys.*, Vol. 20, p. 2723.

Simpson, R.W., Maclagan, R.G.A.R. and Harland, P.W. (1988), 'Interaction potentials and mobility calculations for the HeO^+ system', *J. Chem. Phys.*, Vol. 87, p. 5419.

Sittig, E. (1960), *Acustica*, Vol. 10, p. 81.

Stein, G.D. (1985), 'Cluster beam sources: Predictions and limitations of the nucleation theory', *Surface Sci.*, Vol. 156, p. 44.

Stephan, K., Futrell, J.H., Peterson, K.I., Castleman Jr., A.W. and Märk, T.D. (1982a), 'An electron impact study of carbon dioxide dimers in a supersonic molecular beam: Appearance potentials of $(CO_2)_2^+$, $(CO.CO_2)^+$, and $(Ar.CO_2)^+$', *J. Chem. Phys.*, Vol. 77, No. 5, September, p. 2408.

Stephan, K., Futrell, J.H., Peterson, K.I., Castleman Jr., A.W., Wagner, H.E., Djuric, N. and Märk, T.D. (1982b), 'An electron impact study of ammonia clusters in a supersonic molecular beam: Appearance potentials of NH_4^+, $(NH_3)_2^+$, $(NH_3)_2H^+$, $(NH_3)_3^+$, $(NH_3)_3H^+$ and $(NH_2NH_3)^+$', *J. Mass Spec. and Ion Phys.*, Vol. 44, p. 167.

Stogryn, D.E. and Hirschfelder, J.O. (1959), 'Contribution of bound, metastable, and free molecules to the second virial coefficient and some properties of double molecules', *J. Chem. Phys.*, Vol. 31, p. 1531.

Tang, K.T. and Toennies, J.P. (1977), 'A simple theoretical model for the van der Waals potential at intermediate distances. 1. Spherically symmetric potentials', *J. Chem. Phys.*, Vol. 66, No. 4, February, p. 1496.

Tann, L.P. and Linnett, J.W. (1976), 'Proton transfer from NH_4^+ to NH_3; Floating spherical Gaussian orbital calculations', *J. Chem. Soc., Chem. Commun.*, Vol. 10, p. 364.

Tarr, S.M., Schiavone, J.A. and Freund, R.S. (1981), 'Long–lived high Rydberg molecules formed by electron impact: H_2, D_2, N_2, and CO', *J. Chem. Phys.*, Vol. 74, p. 2869.

Taylor, B.N., Parker, W.H. and Langenberg, D.N. (1969), *Rev. Mod. Phys.*, Vol. 41, p. 375.

Toennies, J.P. and Winkelmann, K. (1977), 'Theoretical studies of highly expanded free jets: Influence of quantum effects and a realistic intermolecular potential', *J. Chem. Phys.*, Vol. 66, p. 3965.

Tomoda, S. and Kimura, K. (1983), 'Proton–transfer potential–energy surfaces of the water dimer cation $(H_2O)_2^+$ in the $1^2A''$ and $1^2A'$ states', *Chem. Phys.*, Vol. 82, p. 215.

Troitskii, V.S. (1962), 'The mean free path of molecules in a molecular beam', *Soc. Phys. JETP (Engl. Transl.)*, Vol. 14, p. 281.

Unland, M.L. and Flygare, W.H. (1966), 'Direct measurement of rotational relaxation', *J. Chem. Phys.*, Vol. 45, No. 7, October, p. 2421.

van den Bergh, H.E., Faubel, M. and Toennies, J.P. (1973), 'Measurement of differential cross sections for individual rotational quantum transitions in the scattering of lithium (1+) ions by molecular hydrogen at E_{cm} = 0.6 eV', *Faraday Disc. Chem. Soc.*, Vol. 55, p. 203.

Viehland, L.A. and Mason, E.A. (1984), 'Repulsive interactions of closed–shell ions with He and Ne atoms: Comparison of beam and transport measurements', *J. Chem. Phys.*, Vol. 80, p. 416.

Wei, S., Tzeng, W.B. and Castleman Jr., A.W. (1990a), 'Dissociation dynamics: Measurements of decay fractions of metastable ammonia cluster ions', *J. Chem. Phys.*, Vol. 93, No. 4, August, p. 2506.

Wei, S., Tzeng, W.B. and Castleman Jr., A.W. (1990b), 'Kinetic energy release measurements of ammonia cluster ions during metastable decomposition and determination of cluster ion binding energies', *J. Chem. Phys.*, Vol. 92, No. 1, January, p. 332.

Willis, D.R., Hamel, B.B. and Lin, J.T. (1972), 'Development of the distribution function on the centerline of a free jet expansion', *Phys. Fluids*, Vol. 15, p. 573.

Wincel, H. (1972), 'Ion–molecule reactions in ammonia at high pressures', *Int. J. Mass Spectrom. Ion Phys.*, Vol. 9, p. 267.

Winter, T.G. and Hill, G.L. (1967), 'High–temperature ultrasonic measurements of rotational relaxation in hydrogen, deuterium, nitrogen, and oxygen', *J. Acoust. Soc. Am.*, Vol. 42, p. 848.

Wolf, J.F., Staley, R.H., Koppel, I., Toagepera, M., Melver Jr., R.T., Beauchamp, J.L. and Taft, R.W. (1977), 'Gas–phase basicities and relative proton affinities of compounds between water and ammonia from pulsed ion cyclotron resonance thermal equilibria measurements', *J. Am. Chem. Soc.*, Vol. 99, p. 5417.

Yamazaki, S., Taki, M. and Fujitani, Y. (1981), 'Rotational relaxation in free jet expansion for N_2 from 300 to 1000 K', *J. Chem. Phys.*, Vol. 74, p. 4476.

Yamdagni, R. and Kebarle, P. (1976), 'Gas–phase basicities and proton affinities of compounds between water and ammonia and substituted benzenes from a continuous ladder of proton transfer equilibria measurements', *J. Am. Chem. Soc.*, Vol. 98, p. 1320.

Young, W.S. (1973), 'Distortions of time-of-flight signals', *Rev. Sci. Instrum.*, Vol. 44, No. 6, June, p. 715.

Zeleznik, F.J. (1967), 'Rotational relaxation in polar gases', *J. Chem. Phys.*, Vol. 47, p. 3410.

Zemansky, M.W. (1984), *Heat and thermodynamics*, McGraw–Hill, 4 ed.

Index